

---

**Mesoscopic concepts in  
soft condensed matter physics**  
**From wind-blown sand to biopolymer solutions**

---

Von der Fakultät für Physik und Geowissenschaften

der Universität Leipzig

genehmigte

DISSERTATION

zur Erlangung des akademischen Grades

Doctor Rerum Naturalium

Dr. rer. nat.,

vorgelegt,

von Marc Lämmel

geboren am 31.05.1985 in Zschopau

Gutachter: Prof. Dr. Klaus Kroy

Prof. Dr. Ralf Stannarius

Tag der Verleihung: 16. September 2019



Europäische Union

Europa fördert Sachsen.



Europäischer Sozialfonds

I gratefully acknowledge the financial support from the European Union through the European Social Funds (ESF program “Wissens- und Know-How-Transfer”), the German Exchange Service “Deutscher Akademischer Austauschdienst” (DAAD “Kurzzeitstipendium” and RISE program), the National Science Foundation (NSF grant No. PHY-1125915), and the Max Planck Institute for the Physics of Complex Systems (MPI Visitors Program). My studies and research were further supported by the graduate school “Leipzig School of Natural Sciences – Building with Molecules and Nano-objects (BuildMoNa),” and the German–Israeli Foundation for Scientific Research and Development (GIF grant No. 1143-60.8/2011).

# Outline

Science becomes particularly appealing when it makes contact with our own experience. Many systems that fall into this category are subsumed under the notion *soft condensed matter*. They are soft, because their macroscopic characteristics can be probed at energy, length, and time scales amenable to us humans. Typical examples of soft-matter systems range from polymer solutions, colloidal suspensions, liquid crystals, surfactants, foams, to granulates.<sup>1,2</sup> Often, their macroscopic phenomenology is described in terms of coarse-grained quantities, like average particle concentrations, fluxes, transport coefficients, response functions, etc., which obey macroscopic (hydrodynamic) laws that rest on general physical principles, most prominently mass, momentum, and energy conservation. Dealing with such averaged quantities, these laws may represent drastic idealizations of the system, because they inevitably wipe out its heterogeneous microstructure, as, for instance, characteristic for granular media and polymer solutions. And indeed, such fluctuations often crucially influence the macroscopic properties of the soft materials and, in particular, their dynamic response. To estimate the consequential corrections to the macroscopic laws, one has to resort to a microscopic description. One is then left with a complicated many-body problem that can only be tackled numerically, by means of computer simulations. An alternative approach that goes beyond the macroscopic level of description is based on mesoscopic (pseudo-)objects and quantities that take relevant fluctuations into account, while ignoring most of the “uninteresting” microscopic degrees of freedom. For the systems considered in this thesis, identifying such mesoscopic entities turns however out to be quite subtle and is often guided by some intuition and by the particular investigated problem. In this regard, the approach used here is conceptually somehow related to the notion of quasi particles or Cooper pairs, say, which were introduced as abstract mesoscopic entities in order to explain complicated many-body phenomena, like the effective mass of an electron traveling through a semiconductor or the superconductivity properties that arise from an electron-pair condensate.

Throughout this thesis, the concept of mesoscopicity is employed to theoretically investigate and discuss two groups of soft-matter systems: (i) aeolian sand transport and the ensuing structure formation and (ii) entangled solutions of stiff biopolymers. They both give rise to numerous relevant and ubiquitous phenomena we encounter in our everyday lives. When you take a walk along the beach on a windy day, you may, for instance, watch the irregular meandering of wind-blown sand clouds and the formation of wavy sand ripples. This transport process shapes arid regions on Earth and other extraterrestrial bodies. Biopolymers, on the other side, are responsible for the mechanical properties of our cells and tissue. When you pull on your skin

---

<sup>1</sup>M. Kleman and O. D. Lavrentovich, *Soft matter physics: an introduction* (Springer Science & Business Media, 2007).

<sup>2</sup>M. Doi, *Soft matter physics* (Oxford University Press, 2013).

or stretch your muscles, you probe the mechanics of the cytoskeleton, which is the polymeric meshwork inside our cells. Despite their obvious phenomenological dissimilarity, both sand transport and biopolymer solutions feature a peculiar mesoscale structure that emerges from their underlying microscopic physics and that carries over to the diverse macroscopic properties. A common theme of the presented theoretical approaches is thus the attempt to identify effective mesoscopic degrees of freedom that govern the macroscopic physics but are largely insensitive to the many details of the complex microphysics.

Part I of the thesis discusses *aeolian sand transport* and the ensuing formation of a whole hierarchy of sand structures, ranging from delicate ripple patterns to vast dune fields.<sup>3</sup> The very transport process itself is of distinct stochastic nature, mainly due to the inherently erratic collisions of the hopping grains with the sand bed. Describing the transport statistics and dynamics thus requires a sound understanding of these bed collisions and the ensuing splash process of the bed grains. In a first step, we address this task by developing an analytical splash model that is based on the collision geometry and fundamental physical principles, like momentum and energy conservation. It predicts the full rebound and ejection statistics and it gives rise to a first emergent mesoscopic length scale, namely the average hop height of splashed bed grains. This height turns out to be of particular relevance for the mesoscale structure of the wind-driven transport layer, as it echoes the presence of two qualitatively different types of grain trajectories: short trajectories of the low-energy ejected bed grains and long trajectories of fast grains that create the ejecta during their successive bed collisions. This insight gives rise to a so-called two-species approximation to the complicated transport statistics. Its main concept is illustrated in Fig. 1a. For wind-dependent averages, like the height-integrated mass flux, we find this approach to be in better agreement with various wind-tunnel data than the conventional mean-field (*i.e.*, single-trajectory) models. However, since our splash model provides us with the full splash statistics, we are actually able to go beyond the two-species approximation and to derive an analytical description of the full mesostructure of the transport layer. This statistical approach allows us to identify various emergent mesoscopic length scales, like the mean hop length, the characteristic transport-layer height, or, most eminently, the so-called saturation length. The latter is the characteristic length needed for the transport process to respond to a perturbation in wind strength or sand availability. It is of particular relevance, as it is expected to essentially correspond to the minimum size of a sand dune.

The aforementioned concept of mesoscopicity—and the necessity of taking some of the nontrivial fluctuations into account—is best illustrated for the wind-strength dependence of the saturation length. It has been discussed very controversially in the literature, with apparently contradictory proposals for its wind dependence. Here, we are able to reconcile them using coarse-grained computer simulations that rest on our splash model. In particular, we show that intermittent turbulent wind fluctuations, which are paramount in the field, drastically influence the dependence of the transient transport on the average wind strength. To understand the field data, these fluctuations have to be taken into account and must not be dismissed.

Besides the stochastic bed collisions and the intermittent turbulent wind-speed variations, it is the polydispersity of the irregular sand grains that crucially influences the transport physics. The mesoscale heterogeneities arising from this polydispersity are responsible for the formation

---

<sup>3</sup>For convenience, citations are omitted in the rest of this outline. Please consult the main text of the thesis for references to the relevant literature.



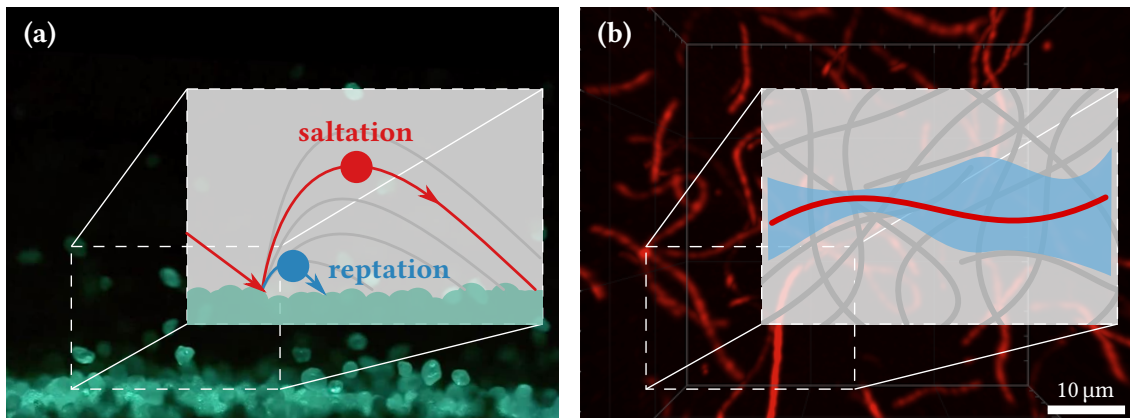


Figure 1: Mesoscopic concepts employed in this thesis. **(a)** Aeolian sand transport is characterized by a broad distribution of grain trajectories. Due to the hopping grains' bed collisions, it exhibits a bimodal structure, which suggests to approximate the whole ensemble (indicated by the grey trajectories) by two representative species. The corresponding mesoscale transport modes “saltation” and “reptation” represent that the long wind-blown trajectories and the passive ejecta, respectively. The background image shows a snapshot of wind-blown sand grains taken in the wind tunnel at the Thermocinetique Nantes Laboratory (image credit: BBC; kindly provided by Alexandre Valance). **(b)** The physics of a pure solution of biopolymers is dominated by their entanglements. They constrain the thermal motion of a test filament (red), effectively confining it to a tube-like cage (blue) that is collectively formed by surrounding filaments (gray). The microscopic image in the back shows an F-actin solution, with a fraction of 1/1000 of the filaments being fluorescently labeled (image credit: Evelin Jaschinski).

of a particular bedform, called megaripples. They stand out from normal sand ripples and dunes due to the characteristic—typically bimodal—grading of the sand they are made from. We thus suggest wind-driven sorting of polydisperse sand as a prerequisite for the megaripple formation: fine-grain winnowing (due to erosion) leaves behind a surface lag of coarse grains from which the megaripples are formed. The coarse grains moreover provide an armoring layer that makes the megaripples particularly robust against wind gusts, allowing them to become much larger than the fragile and highly transient normal ripples made from nearly monodisperse sand. The combination of sand polydispersity, the heterogeneous mesostructure of aeolian sand transport, and the turbulent wind fluctuations is thus key to the megaripples' formations, evolution, and their stability. From our splash model for to poly- or bidisperse sand mixtures, we first identify the creep-like motion of the coarse bed grains that are mobilized by fast fine-grain impacts as the important transport process responsible for the megaripple formation. Secondly, we explain the accumulation of coarse surface lag by means of an erosion-driven sand-sorting model. And thirdly, we analyze a number of field observations and measurements, which reveal that the megaripples have a lot in common with (isolated) sand dunes. Indeed, their morphology, dynamics, and stability turn out to be well understood from a “reptation-dune” model.

Emergent mesoscopic length scales will also play a central role in Part II of the thesis, where we discuss the physics of *biopolymer solutions*. A very prominent paradigm of such a length scale

is the persistence length of a semiflexible polymer. It is defined as the characteristic contour length over which the local polymer direction is randomized. In physical terms, it is a measure for the polymer's bending stiffness—and it thus abstractly represents the microscopic chemical binding structure of the adjacent monomers of the filamentous macromolecule. The value of the persistence length thereby echoes the balance between enthalpic and entropic free energy contributions, which is of central importance for the biopolymer physics. While the enthalpic bending rigidity favors a straight rod-like shape, entropic free-energy contributions originating from thermal contour fluctuations favor a coiled polymer conformation. From a slightly different perspective, one might say that the zero-temperature limit of the polymer (which actually is a rigid rod) is “dressed up” by thermal bending fluctuations—quite similar to the saturation length for the aeolian sand transport that is dressed up by intermittent wind fluctuations in the field.

An even richer mesoscale structure appears as we go from the isolated single polymer to entangled solutions of many polymers. Since the polymers cannot pass through each other, they are topologically constrained to a region in phase space that can only be reached by geometrically allowed polymer fluctuations once the system has been prepared (if these constraints are assumed to be conserved). More precisely, neighboring polymers of a test polymer form a tube-like confinement cage that impedes the test polymer's bending fluctuations. This is the principal idea of the tube model for entangled semiflexible polymer solutions, illustrated in Fig. 1b. Only polymer segments shorter than some characteristic length, called the entanglement length, can equilibrate within this tube, longer fluctuation modes are topologically impeded. The bending free energy that is stored in these impeded modes is now argued to be responsible for the mechanical response of the solutions. This again underscores the pertinence of the (thermal) fluctuations that can be incorporated into a mesoscopic concept—the tube—, which in turn serves as a very handy concept for predicting the macroscopic properties. It allows us to investigate the influence of imposed nematic order and an externally applied shear deformation on the mesoscale packing structure. Eventually, we discuss the viscoelastic response of entangled biopolymer solutions. As a main conclusion, we argue that nonaffine contributions and frictional (or sticky) polymer contacts may be responsible for various experimental observations that cannot be predicted by the standard affine tube model, especially for the nonlinear rheology that exhibits a softening–stiffening transition as a function of the polymer concentration, polymer length, deformation rate, and various solvent properties. In these regards, the purely entangled solutions exhibit close similarities to (transiently) crosslinked polymer networks, as we detail in the last section of the thesis.

In terms of publications, it is fair to say that I was far more productive in the field of aeolian sand transport than in that of biopolymers. As a consequence, Part I happened to become slightly longer, while Part II is more like a short literature review that might serve as a solid starting point for future work. For the same reason, I found it appropriate to include a not yet finished study about the viscoelastic response of biopolymer solutions to the last section. It proposes a new modeling perspective that aims to explain some of the above mentioned rheological phenomena on the basis of the mesoscale structure of entangled biopolymer solutions.

# Contents

<b>Contents</b>	<b>v</b>
<b>I Aeolian sand transport and megaripple formation</b>	<b>1</b>
1 Introduction	3
2 The splash process	11
3 Aeolian sand transport	29
4 Structure formation	85
5 Outlook	103
Bibliography	107
<b>II Solutions of stiff biopolymers</b>	<b>127</b>
6 Introduction	129
7 Entangled solutions	135
8 Viscoelastic response	161
Appendix	177
Bibliography	189

<b>Acknowledgments</b>	<b>201</b>
<b>Wissenschaftlicher Werdegang</b>	<b>202</b>
<b>Bibliographische Beschreibung</b>	<b>203</b>

## **Part I**

# **Aeolian sand transport and megaripple formation**



# Introduction

Sand is the most ubiquitous example for granular matter. Defined as a loose assembly of grains of sizes between about 100 microns to a few millimeters [1], its physics is determined by the collective behavior of athermal, dissipatively interacting particles<sup>1</sup> and its rich phenomenology shares features of solids, liquids, and gases [3]. Here, dissipation can originate from the inelastic grain deformations, from a viscous solvent, and from the sliding friction between contacting grains [4–6]. The main reason for the non-trivial behavior of granular media is that the typical grain size ( $>1\ \mu\text{m}$ , in order to be athermal) is often only a few orders of magnitude below the size of the considered system, so that their heterogeneous microstructure becomes noticeable on macroscopic scales and hydrodynamic approaches that rest on the system's large-scale homogeneity are not generally applicable. Moreover, the inelastic interactions tend to create mesostructures, *e.g.*, via inelastic collapse, jamming, etc. This gives rise to a hierarchy of scales that determines the statistics and dynamics of granular systems. Solid-like properties of a granular material, for instance, emerge on the mesoscopic scale, when mechanical load is transmitted along contact chains that extend throughout the whole granular packing [7, 8]. Such force chains can cause a pressure dip under the apex of a static sand pile [9, 10] and lead to dangerously large local pressure peaks at the wall of a silo. Since thermal fluctuations are not sufficient to move the grains, granular systems are usually trapped—or jammed [11–14]—in metastable states far from equilibrium [15]. Jamming due to the mesoscopic contact networks formed by a granular packing is also responsible for its complex viscoelastic and plastic dynamical response when driven by imposed stresses [16–22]. Another famous example for a very peculiar property of granulates is the volume increase upon shearing, called dilatancy, due to which wet beach sand becomes dry as it is deformed under your feet.

The heterogeneous nature of granular media also plays an important role for the physics of aeolian sand transport, which is the wind-driven erratic grain hopping you can occasionally observe on a windy day at the beach. This highly stochastic non-equilibrium process attracts

---

<sup>1</sup>Athermal means that the macroscopic grains do not undergo Brownian motion. The reader might, however, question the combination “athermal” and “dissipatively interacting”: the microscopics responsible for the dissipation (due to dry/viscous friction or grain deformation) is of course of thermal nature, leading to an increase of the overall entropy as the granulate cools down via collisions [2].

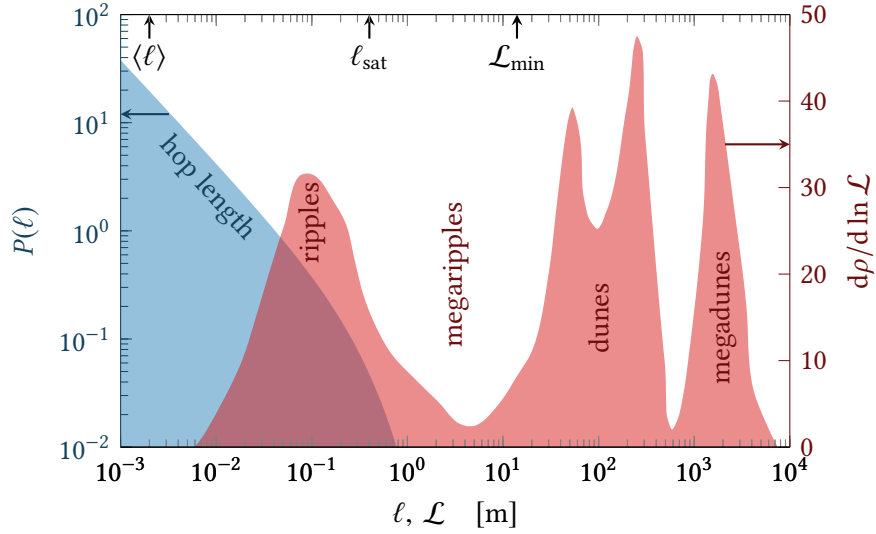


Figure 1.1: Hierarchy of scales associated with aeolian sand transport. The typical hop-length distribution  $P(\ell)$  (blue, our theoretical prediction of Ref. [52] with model parameters obtained by fitting field data by Namikas [53] for the vertical sand flux) is compared to field data for the length  $\mathcal{L}$  of various aeolian bedforms gathered in one histogram (red,  $\rho$  is the relative area fraction, adapted from Ref. [41]). The strong length-scale separation between the mean hop length  $\langle \ell \rangle$  and the saturation length  $\ell_{\text{sat}}$  is plainly echoed by the void between ripples and dunes—only megaripples that are made from polydisperse sand can populate this otherwise forbidden wavelength gap. The arrows at the top axis show the theoretically expected values for  $\langle \ell \rangle$ , the lower bound of  $\ell_{\text{sat}}$ , and the ensuing minimum dune size  $\mathcal{L}_{\text{min}} \approx 35\ell_{\text{sat}}$  predicted for typical dune sand [52]. (Note that  $\ell_{\text{sat}}$  diverges near the transport threshold, as we discuss in Chap. 3.)

the physicist’s interest, for various reasons. It combines the hybrid gas-, fluid-, and solid-like character of granular media due to the strong density variations, from very dilute in the upper part of the transport layer to randomly packed in the sand bed [23, 24]. Further, it is responsible for a whole hierarchy of the most accessible and widely observed examples of spontaneous structure formation in the desert. Ranging from fragile sand ripples and long-lived megaripples [25–30] over dunes [31, 32] and megadunes (or draas) [33–36] to vast dune fields [37–39], these structures span orders of magnitude in size, from a few centimeters to kilometers [40–42] (see Fig. 1.1). They inevitably emerge whenever a (turbulent) flow meets loose grains. Not only deserts and beaches are decorated with such aeolian features, they can also be found on snowscapes [25]. Also wavy patterns on riverbeds have been shown to be essentially down-scaled cousins of desert dunes [43–46]. And even the sandy surfaces of our extraterrestrial neighbors Venus, Mars, Saturn’s moon Titan, and the very recently observed comet 67P/Churyumov-Gerasimenko are evidently shaped by wind, with abundant morphometric structures that share many features with their relatives on Earth, despite the different ambient conditions [1, 47–51]. (See Sec. 1.2, for a brief discussion of our current understanding about the aeolian transport on Mars.)

Besides the creation of this impressive hierarchy of sand waves, the sediment movement by a turbulent flow is also responsible for a number of interesting ecologically and economically



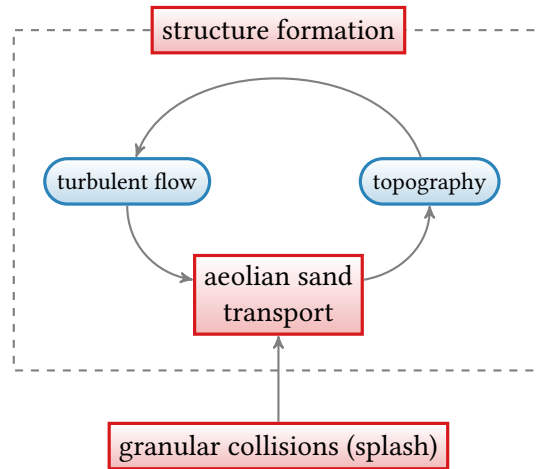


Figure 1.2: Bottom-up approach to aeolian structure formation.

relevant geological phenomena, like desertification [1], erosion [54, 55], dust proliferation [56–59], hazardous shifting sands [42, 60–62], and, ultimately, rock structure and composition [63, 64]. Its far-reaching implications and manifold applications clearly make aeolian sand transport an important interdisciplinary topic that concerns physics, meteorology, geology, and even chemistry and biology [1, 42].

## 1.1 Bottom-up approach to aeolian structure formation

Modern desert geomorphology is inextricably linked with the name of R. A. Bagnold, a British engineer and veteran of both world wars, whose pioneering field journeys and laboratory investigations back in the 1930s and 40s have inspired many researches ever since. The exploratory approach by Bagnold and many of his successors was—and still is—essential to gain insight into the phenomenology of the fascinating wind-created features in the desert and of the various processes responsible for their emergence. A systematic theoretical understanding, however, calls for a bottom-up approach that starts from the grain-scale physics and goes all the way up to the wind-shaped sand structures. Thanks to the vast experimental and theoretical progress made over the last decades, we are now in the position to follow such an ambitious program. Its principal structure is outlined in Fig. 1.2.

At the basis of this hierarchy is the dissipative collisions of the sand grains—more precisely, the collisions between hopping grains and bed grains. During this splash process, an impacting grain can bounce off the bed grains and eject some of them if it is sufficiently fast. Crucially controlled by mesoscopic contact network in the bed-grain packing, these highly stochastic bed collisions give rise to a characteristic mesoscopic structure of the lower region of the transport layer, where the statistics of the grain trajectories turns out to follow remarkably universal laws, as we detail in Chaps. 2 and 3. The combination of the dissipative splash with the interaction between hopping grains and the turbulent air flow is the fundamental mechanism at the grain scale of aeolian sand transport. When the momentum (or energy) transferred from the air to the grains is balanced by the dissipation rate due to the bed collisions, the transport becomes

stationary, whereas any imbalance will give rise to transients, during which the sand transport rate relaxes towards its steady-state value. Such changes in the mass of the blown sand go along with erosion or deposition of sand, which means they change the topography. The topography, in turn, alters the (space- and time-dependent) turbulent flow field, which feeds back to the local transport conditions. This interplay between transport, topography, and flow field gives rise to an important mesoscopic structure of aeolian sand transport (not the only one, as we will discuss in Chap. 4) and is at the core of aeolian structure formation at the meso- and macroscopic scales, as illustrated by the dashed box in Fig. 1.2.

One of the main goals of this first part of the thesis, finally reached in Chap. 4, is to develop a theoretical description for so-called megaripples—wind-created structures of a few decimeters up to meters in length that are made from polydisperse sand, usually of bimodal grain-size distribution [26, 27, 29, 40, 41]. They are formed under erosive wind conditions that lead to a deflation lag of coarse grains, which build an armoring layer that stabilizes the sand bed and makes the wind-shaped structures resistant to pervasive wind gusts. Megaripples can therefore become older and larger than normal ripples made from unimodal sand (*cf.*, Fig. 1.1). Although coarse grains at the bed surface are not transported efficiently by the wind, they move downwind with the help of fine-grain bombardment—a transport mode called creep or reptation [40, 65, 66]. A physically sound description of the transport of polydisperse sand is thus vital to the understanding of the formation and evolution of megaripples. Following the hierarchy of Fig. 1.2, we first take a closer look into the physics of the bed collisions in Chap. 2, with a particular emphasis on bidisperse sand mixtures. In Chap. 3, this splash description is used to develop two closely related transport models for wind-blown monodisperse sand. The first one divides the grain trajectories into two species corresponding to wind-blown fast saltating and ejected reptating bed grains, very much reminiscent of a bidisperse-sand approximation to megaripples. The second approach goes beyond this extended mean-field picture and derives the whole distribution of trajectories from the splash statistics. In Chap. 4, we finally consider a model for erosive wind-driven sand sorting, which predicts coarse bed grains to accumulate at the surface, and combine it with the results for the bidisperse bed collisions in order to describe the megaripples that are made from the coarse deflation lag. As the typical reptation length of these bigger bed grains is on the order of their own size, megaripples are characterized by a strong scale separation between the responsible transport process and the ripple size, similar to what holds for large sand dunes. And indeed, megaripples and sand dunes share various features and can be well modeled along the same lines, when one plugs in the correct length scale characterizing the underlying transport process, as we demonstrated in Ref. [67] (attached to Chap. 4), where we established a “reptation-dune” description for the megaripples.

In the remainder of this introduction, I would like to give a short overview of the relevant literature and the recent experimental and theoretical achievements related to aeolian sediment transport.

## 1.2 A short survey of the literature

Written more than 75 years ago, Bagnold’s classic text book “The Physics of Blown Sand and Desert Dunes” [40] must be considered as the bible in the context of wind-blown sand transport and the related structure formation. It provides a comprehensive view of the rich phenomenology

and the underlying physics and is an excellent starting point to familiarize yourself with this subject. Bagnold's treatise starts with the grain-scale mechanism of the transport process and the crucial interplay between wind and the hopping grains, with many references to his own seminal wind tunnel studies. His overview on the formation, morphology, and dynamics of sand ripples, megaripples (called ridges by Bagnold), and dunes has become the basis for various branches of geomorphological research established over the past decades.

Scientific progress after Bagnold's influential work is for example documented in the books "Wind as a geological process on Earth, Mars, Venus and Titan" by R. Greeley and J. D. Iversen [1], "Aeolian Sand and Sand Dunes" by K. Pye and H. Tsoar [42], and "Physics and Modelling of Wind Erosion" by Y. Shao [56]. The first one stands out from this collection due to its particular focus on extraterrestrial aeolian features, which are discussed by the authors in various contexts ranging from the grain-scale physics (especially, the transport threshold), over the morphology of aeolian bedforms, to abrasion, erosion, and dust transport. The analysis by Greeley and Iversen is mainly guided by phenomenological aspects and field observations, quite similar to the approach by Pye and Tsoar, two researchers with a strong background in sedimentology and geomorphology, whose book covers the properties and formation of aeolian sediments, the formation and dynamics of aeolian bedforms, and outreaching topics like the anthropogenic impact on dune areas and the vegetation and stabilization of dunes. (Further details on sedimentology and dust can also be found in K. Pye's classic book "Aeolian dust and dust deposits" [68].) Shao's book has a clear focus on the underlying physical principles and on theoretical modeling. Being closest to his own research, the chapters on aeolian erosion, dust emission, and dust transport definitely provide a profound introduction to these subjects.

Aeolian sediment transport is a topic of active research. The quite substantial recent experimental and theoretical progress has been gathered in various review articles [45, 46, 57, 69–73]. An important motivation for the present research clearly comes from the elaborate experimental techniques [73], ranging from particle tracking and laser Doppler velocimetry [23, 74–77] over low/high pressure wind tunnels [73, 78] to long-term records in the field [79–81]. Over the last years, field measurements on our own planet have been substantially complemented by data for aeolian features observed on extraterrestrial bodies, most prominently on Mars, either remotely taken by orbiters or acquired during landing missions [47–50]. The combination of these manifold observations with profound theoretical modeling approaches and extensive computer simulations have paved the road towards a comprehensive understanding of the statistical and dynamical characteristics of the transport process and its mesoscopic nature, which manifests itself in the heterogeneous structure of the transport layer and in the sand patterns that emerge from the seemingly chaotic grain-scale process.

**Structure formation.** Theoretical attempts have been very successful in describing the formation and evolution of aeolian sand dunes and their subaqueous analogs [45, 46, 57, 69, 72]. The main reason for this success is the strong scale separation between the grains' average hop length and the typical size of the dune. In fact, a simple mean-field continuum model [82, 83] that maps the complex grain hopping onto a single representative grain trajectory has provided very accurate and non-trivial predictions about many interesting features of sand dunes, such as their non-universal shapes, their minimum size as a function of the atmospheric conditions, their growth and migration dynamics, etc. [43, 84–88] But such a highly coarse-grained model is

unlikely sufficient to yield much insight regarding the structure formation on the very scale that was deliberately washed out in its formulation. That the length of the typical grain trajectory sets the wavelength of these smaller ripple patterns was already hypothesized by Bagnold [40], later called into question by (apparently too simplistic) modeling approaches [89], and only recently substantiated by means of full-fledged grain-scale computer simulations that clarified the seemingly mysterious interplay between the high- and low-energy grain populations in the transport layer [90]. Classifying the ensemble of trajectories into such two species has also been proven instrumental for an accurate, yet technically manageable, analytical description of the transport process [91, 92]. We will come back this approach in Chap. 3.

**Grain collisions and splash.** On the grain-scale level, good progress has been achieved from the concentrated effort to systematically investigate the dissipative grain collisions and the various mechanisms contributing to the total force exerted on the hopping grains. Chapter 2 starts with a commented list of the relevant works on grain collisions and, in particular, on the splash process when wind-blown grains hit the sand bed. Regarding the force contributions, it is fair to say that gravity and drag largely dominate the grain trajectories [57]. Other secondary hydrodynamic forces, like Archimedes, added-mass, Basset, Magnus, and Saffman force are much smaller and often neglected in transport models. A concise overview of these contributions can be found in Ref. [70].

**Electrostatic interactions.** In addition to the hydrodynamics, electrostatic interactions can influence the grain trajectories. The electrification of wind-blown sediment has been observed in various wind-tunnel [93] and field [94–96] experiments. It is usually traced back to the triboelectric charging during grain collisions of different size (including the bed or a wall [97]), with smaller grains becoming negatively charged [98]. Combined with the size-dependent hop heights [99–105], the charges are separated in the transport layer and build up an electric field. An alternative explanation relates the charge separation to the collisions of grains that are polarized by an external [106] and/or their own [107–110] electric field. The resulting electric forces are argued to be of high relevance for both the entrainment process and the suspension of light dust particles [57, 71], but they may also enhance the transport of the normal sand grains [77, 111, 112]. On the other side, triboelectric charging may lead to attractive forces between the grains, making them less susceptible to the wind, especially on extraterrestrial surfaces where the chemical properties of the grains make them more likely to become charged [113]. Despite the recent progress, the triboelectric charging process itself remains still purely understood, its manifold consequences call for further systematic experimental studies and theoretical attempts.

**Wind fluctuations.** Similarly, various questions regarding the important influence of intermittent turbulent wind fluctuations (see Sec. 3.5.2) on the transport process and the structure formation [57, 70] are yet unanswered. This becomes particularly evident for wind strengths fluctuating around the transport threshold, where the measurements repeatedly sample the initiation and cessation process [114] (Sec. 3.5.5). The latter is characterized by a distinct hysteresis, *i.e.*, stronger winds are required to initiate the transport than to sustain it. The gap between the two threshold wind strengths is believed to be especially pronounced on Mars and is therefore held responsible for the current activity of Martian aeolian sand features despite the relatively low aver-

age wind strength [115–118]. Also under terrestrial conditions, the highly non-linear dependence of, *e.g.*, the transport rate [119] or the size of aeolian sand dunes [120] and (mega)ripples [79] on the wind strength leads to nontrivial effects, namely that their time averages can deviate markedly from their values taken at the average wind strength. So, any field measurement is decorated with systematic “errors” due to the pervasive wind fluctuations, and theoretical models should account for them in terms of fluctuation-induced renormalizations of their predictions [52, 119, 121]. Despite the recent effort made in controlled wind-tunnel experiments [122, 123], extensive field studies [124–126], and theoretical modeling approaches [127–130], our insight into the complicated interplay between the wind-speed variations and the transiently responding transport and its consequences for the sand patterns observed in the field is still rudimentary. Unraveling the impact of the wind variations on the structure formation would require a large number of long-term records, only sparsely available today. From a theoretical perspective, the combination of intermittent wind fluctuations with the stochastic nature of the transport itself seems particularly interesting and challenging [124, 131, 132]. Future studies should also investigate this complex interplay between such fluctuations and the heterogeneity arising from a distribution of grain sizes [101] (see also Sec. 3.5.5).

**Sand polydispersity.** Natural sand is always polydisperse, because it is created by quite chaotic processes, like turbulent transport, breaking up crustal rock and crushing by weathering, erosion, abrasion, etc. [42] These processes are expected to give rise to log-normal [133] or, after the sand has been transported by wind, to log-hyperbolic [134] grain-size distributions, as indeed frequently observed in the field [135]. The sand’s polydispersity plays a crucial role for several phenomena already mentioned above: megaripples, for instance, are characterized by bimodal grain-size distributions [80] and large enough grain-size ratios are thought to be needed for efficient triboelectric charging [93]. While the transport of mixed sand has been studied in various field [100, 101, 105] and wind-tunnel [99, 102, 104, 136] experiments, the physics governing the transport of sand mixtures is relatively poorly understood. Some modeling approaches [101, 137–139] have accounted for distributed grain sizes. But, a purely qualitative discussion by Martin and Kok [105], who aimed at disentangling the various contributions to the size-dependence of the height-resolved transport characteristics, reveals that solid systematic predictions are still lacking. A major challenge is surely a reasonable parametrization of the bed collisions in coarse-grained models. The theoretical approach we proposed in Ref. [140] may help to bridge this divide in the future (see Chap. 2).

**Aeolian sand transport and structure formation on Mars.** The numerous field surveys and wind-tunnel studies on our own planet have been complemented by orbiter and rover missions on Mars, which allowed for detailed investigations of the abundant aeolian features. As we will discuss in Chap. 3, the more dilute atmosphere and lower gravity on Mars leads to long grain trajectories [141], so that Martian dunes [85, 142], ripples, and megaripples [140] are larger than their terrestrial analogs. Another consequence of the particular atmospheric conditions on Mars is that the threshold wind strength at which aeolian sand transport sets in is about one order of magnitude larger than on Earth [1, 85] (see Sec. 3.5.5 of Chap. 3). The high threshold implies that relatively strong storms are required to create and evolve the sand structures. As mentioned above, this limitation might be relaxed by the prevalent wind fluctuations, together

with a pronounced hysteresis effect due to the very small threshold wind strength at which once initiated transport ceases [85, 116, 128]. Combined with intermittent turbulent wind fluctuations, the hysteresis has been argued to be responsible for the numerous currently active (*i.e.*, migrating, growing/shrinking) aeolian features observed on Mars, despite the average wind is expected to be below the fluid threshold [115–118, 128, 143–146]. Anyhow, Martian wind gusts seem to be strong enough to cause rather frequent dust storms and to keep the observed sand structures at some locations similarly active as on Earth [117, 145, 146]. Large ripple-like patterns referred to as “transverse aeolian ridges” (TARs) in the literature [48], are very robust against storms and seem to be immobile over years—a property they share with the biggest gravel-covered megaripples on Earth [147–149]. The pronounced hysteresis of the transport was also put forward as an explanation for the formation of ripples from grains that are so fine that they are expected to be entrained directly into suspension by the wind—once lifted by a short gust, the fine sand might form ripples as long as the wind strength remains above the much lower impact threshold [118].

The mechanism of sustained transport after a burst-like gust was recently called into question by Sullivan and Kok [150]. Referring to wind tunnel experiments [40, 132] that indicate that such temporary transport quickly ceases once the upwind sand supply is turned off (see pp. 31–32 of Ref. [40]), they argued that the self-sustained transport at lower wind strengths is rather unlikely. As one reads through the aforementioned recent articles (*e.g.*, Refs. [117, 145, 146]), one might get the impression that the apparent contradiction between the present wind conditions on Mars and the observed activity of various aeolian features could be a result of a deep-rooted misconception: it is widely argued that sand grains of some *representative* size cannot be transported at the *typical* wind strength. However, both the wind and the susceptibility for sand grains to be transported (and mobilized) are of immanently stochastic character—the grains, for instance, vary in size, roughness, and geometry or their location at the sand bed (protruding form vs. sheltered by other bed grains, located at the ripple trough vs. crest), which may be subsumed into an effective grain-size distribution. While the wind fluctuations dominate the actual transport mode on Earth (*e.g.*, “saltation streamers” follow the turbulence structures of local high energy density [131, 151]), the wide gap between the fluid and impact thresholds on Mars gives more weight to the heterogeneity of the sand itself. As a consequence of the sand dispersity, transport can be initiated at relatively low wind speeds—close to the impact threshold of the average grain—by mobilizing only a certain fraction of the bed grains. When these grains gain enough kinetic energy during their flight to eject some of the immobile bed grains during the bed collisions, steady transport is possible [150]. A comprehensive investigation of the activity of aeolian sand transport and the ensuing structure formation on Mars should thus combine the sand and intermittent wind statistics with the transport physics. Despite the numerous publications that touch this problem (see, for instance, the computer simulations proposed by Dupont *et al.* [131]), such an approach, with application to the particular Martian atmospheric conditions, is still lacking.

## The splash process

Dissipative collisions between hopping grains and the sand bed are at the core of aeolian sand transport. A physically sound parametrization of this splash process is thus an integral part of any transport model, while providing itself an interesting and theoretically challenging phenomenon that combines various outstanding properties of granular matter. It is determined by two elementary physical ingredients: dissipative inter-particle contacts and the collision geometry between the incident grain and the bed grains. What makes it theoretically appealing (and challenging) is its stochastic character and, in particular, the complicated impact-driven ejection of the bed grains, which depends on the irregular bed geometry and the momentum/energy distribution along contact chains in the granular packing.

The splash process has been intensively studied in wind-tunnel experiments for saltating sand [136, 152–157], ice/snow [158–160], mustard seeds [158], and plastic beads [157], and by shooting sand [27, 161], glass [162], steel [163], and plastic grains [164–167] into a quiescent bed packing. While the impact speed and impact angle of the saltating grains in the wind tunnel can be influenced only indirectly, namely via the wind strength [155, 159] and the bed slope [153], they can be varied systematically in the shot experiments, which allow to analyze the influence of these variables on various observables, like the rebound/ejection speed, the rebound/ejection angle, the total/vertical restitution, and the number of ejected grains. In most experiments that have been performed in the past, the sand samples were approximately monodisperse with a mean grain diameter between 100 and 600  $\mu\text{m}$ . Rice *et al.* [136] used polydisperse sand, which they dyed according to three size fractions in order to analyze the influence of the impactor–bed grain-size ratio on the splash statistics during the saltation process. Nishida *et al.* [168] performed collision experiments for impactor–bed combinations of various densities and sizes. Besides the experimental effort, further insight has been gained from discrete-element computer simulations in two [161, 169–175] and three dimensions [174, 176], and, more recently, also for polydisperse granulates [175, 177–181]. To interpret these manifold observations and to make them applicable for analytical and numerical transport models, various coarse-grained theoretical models have been proposed in the past [139, 140, 160, 182–187]. However, guided by experiments and computer simulations, some of them rest on rather simplistic parametrizations for the rebound and the ejection process, namely via effective macroscopic restitution coefficients

and an effective energy/momentum balance [139, 166, 183], whereas only few approaches aim at deriving the splash properties from the underlying physics, determined by the dissipative grain collisions and the impactor–bed geometry [160, 184–186]. Moreover, the splash models often lack simple predictions that can be directly used to fit the data or applied in transport models, and most attempts are restricted to monodisperse sand, while we know that the influence of poly-/bidispersity on the transport is essential for, say, the formation of megaripples [26, 27, 29, 40, 41]. We took this as a motivation to propose a new splash model [140] that allows for arbitrary size ratios between the incident grain and the hit bed grains. Besides this major achievement, our formalism enabled us to derive a number of simple analytical results describing the splash statistics, like the velocity distribution of the rebounded impactor and the number and velocity distribution of the ejected bed grains. The full model is presented in the article attached at the end of this chapter.

## 2.1 The basic physics of the splash process

The microscopic basis of the splash process is the inelastic deformation of and the friction between the contacting grains, which are conveniently described by normal and tangential restitution coefficients. In principle, they both depend on the relative velocity and the size of the colliding particles [188, 189], which can be approximately resolved by viscoelastic models (*i.e.*, a Hookian/Hertzian spring plus a dash pot), as done in various simulations [169, 171, 173, 174, 176, 181]. However, the minor quantitative corrections introduced by these dependencies can be neglected to fair accuracy [184], because most splash properties are dominated by the collision geometry [182]. In fact, it was shown in Refs. [140, 160] that the rebound statistics obtained in experiments and simulations can be accurately described within such a simple approach, and that the bed-grain ejection crucially depends on the energy/momentum splitting cascade in the grain packing [160, 184, 186], but not so much on the details of the velocity restitution at the grain contacts. As a direct consequence, both the ejection statistics and thus the lower region of the transport layer exhibit a universal structure, as for instance reflected by the grain-velocity or hop-height distributions (see Chap. 3).

In general, the bed collisions can be quantified in terms of the so-called splash function [65, 160]

$$P(\boldsymbol{v}', \boldsymbol{v}'_1, \boldsymbol{v}'_2, \dots | \boldsymbol{v}), \quad (2.1)$$

which is the probability density function for the rebound velocity  $\boldsymbol{v}'$  and the ejection velocities  $\boldsymbol{v}'_1, \boldsymbol{v}'_2, \dots$  of the mobilized bed grains that reach a certain height (on the order of the grain size) above the bed for a given the impact velocity  $\boldsymbol{v}$ . For both conceptual and practical reasons, the splash process is usually divided into the rebound of the impacting grains and the ejection of the bed grains. Equation (2.1) is then split up into a rebound probability of the form  $P_{\text{reb}}(\boldsymbol{v}' | \boldsymbol{v})$  and a velocity distribution  $P_{\text{ej}}(\boldsymbol{v}'_1 | \boldsymbol{v})$  of the ejected grains, while the number  $N$  of ejected grains is approximated by its average, given by a function  $N(\boldsymbol{v})$  of the impact velocity. Often, it is even more convenient to rewrite the velocities in terms of their absolute values and corresponding impact/rebound/ejection angles and to discuss the pairwise dependencies between these quantities separately.



Coarse-grained models for the grain splashing typically start with the overall energy and momentum balance [56, 139]

$$\frac{1}{2}m\boldsymbol{v}^2 = \frac{1}{2}m(\boldsymbol{v}')^2 + \frac{1}{2}\sum_n m_n(\boldsymbol{v}'_n)^2 + E_{\text{bed}}, \quad (2.2a)$$

$$m\boldsymbol{v} = m\boldsymbol{v}' + \sum_n m_n\boldsymbol{v}'_n + \boldsymbol{p}_{\text{bed}} \quad (2.2b)$$

between the impact and the sum of the rebound, ejection, and some bed contributions, given by the dissipated energy  $E_{\text{bed}}$  lost to the sand bed and the total momentum  $\boldsymbol{p}_{\text{bed}}$  taken up by the bed. Here,  $m$  and  $m_n$  refer to the masses of the impactor and the  $n$ -th ejected bed grain. The common ansatz to get rid of the unknown dissipation term is to assume  $E_{\text{bed}} \propto (m/2)\boldsymbol{v}^2$  with some numerical prefactor that is obtained by fitting the model predictions to experiments or simulations. Kok and Renno [139] used a “friction-free” version of Eqs. (2.2), with  $E_{\text{bed}} = 0$  and  $\boldsymbol{p}_{\text{bed}} = 0$ , to estimate whether energy or momentum provides the stronger constraint on the total number of ejected grains. To this end, they replaced  $\boldsymbol{v}'_n$  by the average ejection velocity and all velocity vectors in Eq. (2.2b) by their absolute values. While the first approximation is uncritical, the interpretation of the scalar momentum balance seems highly dubious. Very recently, Comola and Lehning [187] used the same approach, but argued that, due to the shallow impacts typical for saltation, the horizontal components of the momenta largely exceed the vertical ones, such that the latter may be neglected in the momentum balance. This again is highly questionable and neglects the essential character of the bed collisions, namely that they convert the horizontal momentum of the impacting grains into vertical movement of both the rebounded and ejected grains. Based on their simplification, Kok and Renno found that saltation is dominantly constrained by the scalar momentum balance. Combined with the assumed proportionality  $v' \propto v$  between rebound and impact speed and the (empirically suggested) constant ejection velocity  $v'_n = v_{\text{ej}}$  that does not depend on  $v$ , this immediately yields an affine law  $N \propto (v - v_{\text{bed}})/v_{\text{ej}}$  for the number of ejected grains, which is indeed in agreement with collision experiments [164–167] and computer simulations [161, 169, 171, 174]. Despite this apparent success, some caution seems in order, because it is often hard to decide whether  $N$  depends affinely on  $v$  or follows some (weak) power law [166], and, moreover, the energy budget analyzed in the experiments and simulations suggests that an energy balance in fact holds [167, 190]. Instead of the weakly founded and somehow misleading coarse-grained momentum balance, the statics of the ejecta should rather be traced back to the collision chains in the bed packing [160]. This was, for instance, done by Ho *et al.* [186], who used a fragmentation model to describe the energy splitting at each grain contact in the packing. This gives rise to a log-normal energy distribution for the ejected grains, in excellent agreement with wind-tunnel experiments performed by the same authors. In Ref. [140] (attached below this section), we used this approach to predict the number of ejected grains and their mean velocity as a function of the impact speed and the impact angle. The good agreement with collision experiments again supports the energy-fragmentation picture. An important consequence of this branching process is the very weak influence of the impact energy on the energy distribution for the ejected bed grains. The average energy transmitted to a bed grain is then roughly given by the minimum kinetic energy for which the fragmentation cascade ends, which is on the order  $mag$ , with  $m$  being the grain mass,  $a$  its diameter, and  $g$  the gravitational acceleration. Defining the ejected grains as those that reach at least a minimum height of their own size, their average ejection height is then found to be on the order of  $10a$

and largely independent of the impact velocity. In Chap. 3, the log-normal ejection-energy (or ejection-height) distribution and the average ejection height will serve as the fundamental starting point for formulating a model for aeolian sand transport that resolves the whole distribution of grain trajectories.

**Grain-scale modeling and splash parametrization for aeolian sand transport**

Marc Lämmel, Kamil Dzikowski, and Klaus Kroy\*

*Institut für Theoretische Physik, Universität Leipzig, Postfach 100920, 04009 Leipzig, Germany*

Luc Oger† and Alexandre Valance‡

*Institut de Physique de Rennes, CNRS UMR 6251, Université de Rennes I, 35042 Rennes, France*

(Received 21 October 2016; published 3 February 2017)

The collision of a spherical grain with a granular bed is commonly parametrized by the splash function, which provides the velocity of the rebounding grain and the velocity distribution and number of ejected grains. Starting from elementary geometric considerations and physical principles, like momentum conservation and energy dissipation in inelastic pair collisions, we derive a rebound parametrization for the collision of a spherical grain with a granular bed. Combined with a recently proposed energy-splitting model [Ho *et al.*, *Phys. Rev. E* **85**, 052301 (2012)] that predicts how the impact energy is distributed among the bed grains, this yields a coarse-grained but complete characterization of the splash as a function of the impact velocity and the impactor-bed grain-size ratio. The predicted mean values of the rebound angle, total and vertical restitution, ejection speed, and number of ejected grains are in excellent agreement with experimental literature data and with our own discrete-element computer simulations. We extract a set of analytical asymptotic relations for shallow impact geometries, which can readily be used in coarse-grained analytical modeling or computer simulations of geophysical particle-laden flows.

DOI: [10.1103/PhysRevE.95.022902](https://doi.org/10.1103/PhysRevE.95.022902)**I. INTRODUCTION**

Granular flows are ubiquitous in nature and frequently encountered in everyday life. Their profound understanding is a necessary prerequisite for designing and improving processing steps in industry as well as for predicting hazards like rockfall, avalanches, or devastating shifting sands. In particular, the grain hopping excited by strong winds shapes arid regions on Earth or other astronomical bodies, thereby creating a whole hierarchy of structures that span orders of magnitude in size. The collisions of the hopping grains with the sand bed result in a dissipative rebound and grain splashing. These are essential features that need to be understood to predict aeolian transport and the whole ensuing structure formation.

Since Bagnold's [1] pioneering investigations back in the 1940s, grain-bed collisions have been studied in wind tunnels [2–7], by shooting steel or plastic beads onto a quiescent granular bed [8–14], and in (event-driven) computer simulations [15–19]. The general aim is to parametrize the complex stochastic process by the so-called *splash function* [20]. It provides the average velocity of the rebounding grain after the collision and the average number and the velocity distribution of bed particles ejected in the splash, given the velocity of the impacting particle and the size ratio of the impacting particle to the bed particles. Unequal grain sizes are of interest, because field observations indicate that aeolian structure formation may be linked to grains sorting, as observed in megaripples [21–23].

For their theoretical understanding, a robust and reliable parametrization for the splash function of bidisperse granulates could be of great help. To establish such a parametrization based on physical arguments and mathematical modeling was a major motivation for the study reported below.

We divide the presentation into two parts, according to the two physical processes at work during the splash process, the rebound of the impacting grain and the impact-driven ejection of bed grains. The first process appears to be both conceptually and technically less complex, as it can, in a reasonable approximation, be reduced to a two-body scattering problem. This can be analyzed straightforwardly by means of a combination of elementary geometric considerations and basic physical principles, like momentum conservation. In the first part of Sec. II, we show how various rebound observables, e.g., rebound angles and coefficients of restitution, their dependence on impact angle and impactor-bed grain-size ratio, and their distributions can be obtained from such an approach. Then we illustrate that the predictions compare well with experimental data available from the literature and with our own discrete-element computer simulations. The second process, grain splashing from the bed, is a full-fledged many-body problem that is much harder to grasp and requires a smart ansatz to formalize the complex momentum propagation through the disordered grain packing. It is analyzed in Sec. III, based on a fragmentation model that is applied to the energy-splitting process in the bed, as recently proposed by Ho *et al.* [24]. The combination of the results from Secs. II and III constitutes a complete and self-contained description of the splash process with various potential applications, as outlined in the concluding section.

**II. REBOUND PROCESS**

The starting point of our analysis of the impacting grain's rebound is a purely geometric picture, where the bed packing is approximated by a bumpy wall of infinite mass. To account for finite-mass effects on the energy dissipation during

\*klaus.kroy@uni-leipzig.de

†luc.oger@univ-rennes1.fr

‡alexandre.valance@univ-rennes1.fr

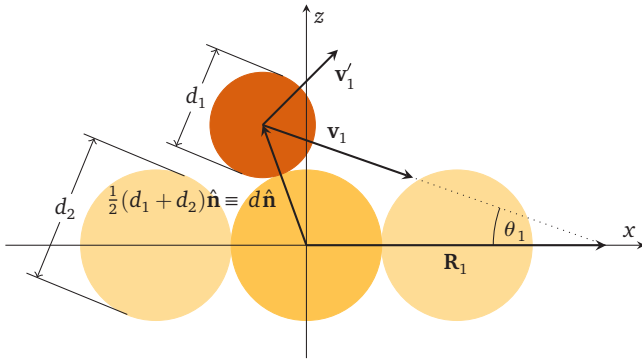


FIG. 1. The two-dimensional collision model. The spherical impactor of diameter  $d_1$  strikes the homogeneous flat bed with impact velocity  $\mathbf{v}_1$  and bounces off the target bed grain of diameter  $d_2$  located at the origin. Without the bed grains, the impactor would cross the  $x$  axis at  $\mathbf{R}_1$ . The rebound velocity  $\mathbf{v}'_1$  is computed using two independent coefficients of restitution for the tangential and normal component of  $\mathbf{v}_1$  according to Eq. (6). As a consequence, the rebound speed is proportional to the impact speed,  $|\mathbf{v}'_1| \propto |\mathbf{v}_1|$ , which can thus be scaled out, so it suffices to characterize the impactor by its impact angle  $\theta_1$  only.

the rebound, we introduce effective bead-bead restitution coefficients that have the same form but different values as the “microscopic” restitution coefficients characterizing binary collisions. Introducing a phenomenologically motivated dependence on the impactor-bed grain-size ratio allows for a simple and transparent discussion of the geometry that yields manageable analytical predictions.

For pedagogical reasons, we first present a two-dimensional version of our rebound model that can straightforwardly be extended to three dimensions. As the predictions turn out to be relatively insensitive to the dimensionality, the simpler two-dimensional version suggests itself as the more promising starting point for most practical purposes. It can easily be solved analytically and provides asymptotic scaling laws for various quantities of interest.

### A. Two-dimensional collision model

Our formal description of the rebound process is similar to the two-dimensional model proposed by Rumpel [25], who considered a regular packing of identical spheres hit by an impactor of the same size as the bed grains. As a first generalization, we account for different diameters  $d_1$  and  $d_2$  of the impactor and the bed grains, respectively. In the following, all lengths are given in units of the mean diameter  $d \equiv (d_1 + d_2)/2$ , so  $d_1 + d_2 = 2$ . We denote the impact velocity by  $\mathbf{v}_1$  and label all postcollision quantities by a prime. The collision geometry and the main quantities that we use to describe the rebound are summarized in Fig. 1. The rebound velocity of the impinging particle, for instance, reads  $\mathbf{v}'_1$ . For given impact velocity  $\mathbf{v}_1$ , the statistical distribution

$$P(A|\mathbf{v}_1) = \overline{\delta\{A - f[\mathbf{v}'_1(\mathbf{v}_1, \hat{\mathbf{n}})]\}} \\ = \frac{1}{d_2} \int_{x_0}^{x_0+d_2} dx \delta\{A - f[\mathbf{v}'_1(\mathbf{v}_1, \hat{\mathbf{n}})]\} \quad (1)$$

with mean

$$\overline{A}(\mathbf{v}_1) = \int dA AP(A|\mathbf{v}_1) = \frac{1}{d_2} \int_{x_0}^{x_0+d_2} dx f[\mathbf{v}'_1(\mathbf{v}_1, \hat{\mathbf{n}})] \quad (2)$$

of an observable function  $A = f(\mathbf{v}'_1)$  of the rebound velocity is obtained by averaging over all possible impact positions  $x$ . We have taken them to be uniformly distributed over the width  $d_2$  of one bed grain. The implicit  $x$  dependence of  $f$  originates from the normal unit vector  $\hat{\mathbf{n}} \equiv \hat{\mathbf{n}}(x)$  of the bed surface that is obtained from the collision condition

$$\hat{\mathbf{n}} = \mathbf{R}_1 - t\mathbf{v}_1 \quad (3)$$

between the bed grain located at the origin and the impactor that would cross the  $x$  axis at  $\mathbf{R}_1 = (x, 0)$  at time  $t = 0$ , see Fig. 1. The collision time  $t = \mathbf{R}_1 \cdot \mathbf{v}_1 / |\mathbf{v}_1|^2 + (1/|\mathbf{v}_1|^2)[(1 - \mathbf{R}_1^2)|\mathbf{v}_1|^2 + (\mathbf{R}_1 \cdot \mathbf{v}_1)^2]^{1/2}$  is obtained by inserting Eq. (3) into  $\hat{\mathbf{n}}^2 = 1$ , which yields the normal vector

$$\hat{\mathbf{n}} = (\mathbb{1} - \hat{\mathbf{v}}_1 \hat{\mathbf{v}}_1) \cdot \mathbf{R}_1 - \sqrt{1 - \mathbf{R}_1 \cdot (\mathbb{1} - \hat{\mathbf{v}}_1 \hat{\mathbf{v}}_1) \cdot \mathbf{R}_1} \hat{\mathbf{v}}_1 \quad (4)$$

on the bed-grain surface at the collision point, where  $\hat{\mathbf{v}}_1 \equiv \mathbf{v}_1/|\mathbf{v}_1|$  denotes the normalized velocity vector. This impact direction is most conveniently characterized in terms of the impact angle  $\theta_1$  as  $\hat{\mathbf{v}}_1 = (\cos \theta_1, \sin \theta_1)$ . Besides the (relative) bed coarseness  $d_2$ , the impact angle  $\theta_1$  crucially affects the value of the leftmost impact position  $x_0$  in Eqs. (1) and (2). Determining  $x_0$  from the contact condition between the impactor and the bed grain located at the origin requires us to discriminate between shallow and steep impact angles. For shallow impact trajectories, the smallest value of  $x_0$  is obtained for a trajectory that is tangential to the left neighbor of the central grain; for steep trajectories, it is determined by the impact position at which the impactor hits the two bed grains at once. This yields

$$x_0 = \begin{cases} \csc \theta_1 - d_2, & 2 \sin \theta_1 < d_2, \\ \cot \theta_1 \sqrt{1 - (d_2/2)^2} - d_2/2, & \text{else.} \end{cases} \quad (5)$$

Note that the value of the scaled bed grain diameter  $d_2$  ranges from 0 to 2, corresponding to big and small impactors, respectively.

Before we can evaluate the integrals in Eqs. (1) and (2), we have to specify the (implicit)  $x$  dependence of the function  $f[\mathbf{v}'_1(\mathbf{v}_1, \hat{\mathbf{n}})]$ . To this end, we model the momentum dissipation

$$\mathbf{v}'_1(\mathbf{v}_1, \hat{\mathbf{n}}) = [-\alpha \hat{\mathbf{n}} \hat{\mathbf{n}} + \beta(\mathbb{1} - \hat{\mathbf{n}} \hat{\mathbf{n}})] \cdot \mathbf{v}_1 \quad (6)$$

during the rebound in terms of the effective restitution coefficients

$$\alpha = \frac{1 + \epsilon}{1 + \mu} - 1 \quad \text{and} \quad \beta = 1 - \frac{(2/7)(1 - \nu)}{1 + \mu} \quad (7)$$

for the normal and the tangential velocity component of the rebounding grain, respectively. The expressions for  $\alpha$  and  $\beta$  are derived for two inelastically colliding spheres of mass ratio  $\mu$ , where the total momentum is taken to be conserved and the energy dissipation is determined by the *microscopic* restitution coefficients  $\epsilon$  and  $\nu$  for the normal and tangential component of the relative surface velocity of the collision partners. (The latter can be taken to be material parameters, independent of the grain sizes and impact speed.) We outline this classical calculation in Appendix A. To account for the nontrivial

grain-size dependence of the energy dissipation in the bed, we freely interpret the grain-mass ratio as an effective parameter that interpolates between the exactly known asymptotic scaling  $\mu \sim d_1^3/d_2^3$  [26] for small grain-size ratios  $d_1/d_2 \ll \pi/2$  and a phenomenological value that accounts for the high number of excited bed grains for large  $d_1/d_2 \rightarrow \infty$ . In the first case, energy transfer to the packing becomes negligible, so the rebound process reduces to a binary collision. In the second case, for large impactors ( $d_1/d_2 \gg 1$ ), the large number of excited bed grains makes the collision highly dissipative, for which we impose the limit  $\mu \sim \epsilon$ , so the normal rebound velocity vanishes ( $\alpha \rightarrow 0$ ). The expression

$$\mu = \epsilon d_1^3 / (d_1^3 + \epsilon d_2^3), \quad (8)$$

provides a plausible parametrization that fulfills both of these conditions.

Inserting Eq. (4) for the normal vector  $\hat{\mathbf{n}}$  into Eq. (6) and recalling that  $\mathbf{R}_1 = (x, 0)$ , we get the wanted dependence of  $f[\mathbf{v}'_1(\mathbf{v}_1, \hat{\mathbf{n}})]$  on the impact position  $x$ . In particular, for the identity function  $f[\mathbf{v}'_1(\mathbf{v}_1, \hat{\mathbf{n}})] = \mathbf{v}'_1(\mathbf{v}_1, \hat{\mathbf{n}})$ , we obtain the components

$$\begin{aligned} \frac{v'_{1x}}{|\mathbf{v}'_1|} &= -\alpha \cos \theta_1 + (\alpha + \beta)x^2 \sin^2 \theta_1 \cos \theta_1 \\ &\quad + (\alpha + \beta)x \sin^2 \theta_1 \sqrt{1 - x^2 \sin^2 \theta_1}, \end{aligned} \quad (9a)$$

$$\begin{aligned} \frac{v'_{1z}}{|\mathbf{v}'_1|} &= \alpha \sin \theta_1 - (\alpha + \beta)x^2 \sin^3 \theta_1 \\ &\quad + (\alpha + \beta)x \sin \theta_1 \cos \theta_1 \sqrt{1 - x^2 \sin^2 \theta_1}, \end{aligned} \quad (9b)$$

of the rebound velocity  $\mathbf{v}'_1 = (v'_{1x}, v'_{1z})$ . It follows that the rebounding grain continues moving downward into the bed after the first collision if  $1/(1 + \beta/\alpha) < x^2 \sin^2 \theta_1 - x \cos \theta_1 \sqrt{1 - x^2 \sin^2 \theta_1}$ . In this case, it thus collides with an adjacent second bed grain. In the remainder of the current section, we neglect such secondary collisions for simplicity, which allows us to derive analytically manageable expressions for the asymptotic scaling of various averages. Further below, it is demonstrated that only marginal errors are incurred by this approximation.

### 1. Shallow impacts ( $\theta_1 \ll \pi/2$ ).

To facilitate the following analysis, we now make the  $x$  dependence of the function  $f$  in Eq. (1) explicit and identify  $f(x) = f[\mathbf{v}'_1(\mathbf{v}_1, \hat{\mathbf{n}})]$ . The  $x$  integral in Eq. (1) can be evaluated if all branches  $f_i^{-1}$  of the inverse of  $f(x)$  are known. For shallow impacts,  $\theta_1 \ll \pi/2$ , there exists only a single branch and the rebound distribution evaluates to

$$P(A|\mathbf{v}_1) \sim \begin{cases} \frac{1}{d_2} \left| \frac{df^{-1}}{dA} \right|, & 0 < \csc \theta_1 - f^{-1}(A) < d_2, \\ 0, & \text{else,} \end{cases} \quad (10)$$

where we inserted the first line of Eq. (5) for  $x_0$ . As an example for an interesting observable, consider the rebound angle, i.e.,  $f(x) = \theta'_1 = \arctan(v'_{1z}/v'_{1x})$ . Replacing  $x$  in Eq. (9) by the shifted coordinate  $x + d_2 - \csc \theta_1$ , we obtain its exact shallow-impact asymptotics  $\theta'_1 \sim (1 + \alpha/\beta)\sqrt{2(d_2 - x)\theta_1} - \theta_1$ . Inserting this into Eq. (10), we calculate the statistical

distribution

$$P(\theta'_1|\theta_1) \sim \begin{cases} \frac{\beta^2(\theta_1 + \theta'_1)}{(\alpha + \beta)^2 d_2 \theta_1}, & 0 < \frac{\beta(\theta_1 + \theta'_1)}{(\alpha + \beta)\sqrt{2d_2\theta_1}} < 1, \\ 0, & \text{else,} \end{cases} \quad (11)$$

and mean

$$\bar{\theta}'_1 \sim (2/3)(1 + \alpha/\beta)\sqrt{2d_2\theta_1} - \theta_1. \quad (12)$$

of the rebound angle. The same procedure can be applied to the total and the vertical restitution  $e \equiv |\mathbf{v}'_1|/|\mathbf{v}_1|$  and  $e_z \equiv v'_{1z}/|v_{1z}|$ , respectively. For small  $\theta_1$ ,  $e \sim \beta - (\beta^2 - \alpha^2)(d_2 - x)\theta_1/\beta$  and  $e_z \sim -\beta + (\alpha + \beta)\sqrt{2(d_2 - x)\theta_1}$  follows from Eq. (9) after shifting the  $x$  coordinate by  $\csc \theta_1 - d_2$ . Inserting these asymptotically exact results into Eq. (10) yields

$$P(e|\theta_1) \sim \begin{cases} \frac{\beta}{(\beta^2 - \alpha^2)d_2\theta_1}, & 0 < \frac{\beta(\beta - e)}{(\beta^2 - \alpha^2)d_2\theta_1} < 1, \\ 0, & \text{else,} \end{cases} \quad (13)$$

$$\bar{e} \sim \beta - (\beta^2 - \alpha^2)d_2\theta_1/(2\beta), \quad (14)$$

and

$$P(e_z|\theta_1) \sim \begin{cases} \frac{(e_z + \beta)\theta_1}{(\alpha + \beta)^2 d_2}, & 0 < \frac{e_z + \beta}{(\alpha + \beta)\sqrt{2d_2/\theta_1}} < 1, \\ 0, & \text{else,} \end{cases} \quad (15)$$

$$\bar{e}_z \sim -\beta + (2/3)(\alpha + \beta)\sqrt{2d_2/\theta_1}. \quad (16)$$

### 2. Steep impacts ( $\theta_1 \approx \pi/2$ )

For steep impacts, similar relations can be derived by expanding the observables  $\theta'_1$ ,  $e$ , and  $e_z$ , introduced above, in the impact angle  $\theta_1$  up to linear order around  $\pi/2$ . This strategy provides analytical expressions for their mean values, obtained by averaging over the impact position  $x$ , but gives no access to their distributions. The reason is that the  $x$  dependence  $A = f(x)$  of an observable  $A$  is now nonlinear (in contrast to the shallow-impact expansions), which precludes the inversion  $x = f^{-1}(A)$ , required in Eq. (1). Reasonable approximations of the distributions can nevertheless be obtained by expanding  $f(x)$  up to first or second order in  $x$ , as documented in Appendix B together with further technical details of the steep-impact expansion. Here, we only quote the first-order asymptotics of the mean rebound angle, the mean total restitution, and the mean vertical restitution, respectively:

$$\begin{aligned} \bar{\theta}'_1 &\sim \pi - \theta_1 + \sin^{-1}(d_2/2)\sqrt{4/d_2^2 - 1}(\theta_1 - \pi/2) \\ &\quad + \tan^{-1}\left(\frac{\beta/\alpha}{\sqrt{4/d_2^2 - 1}}\right)\sqrt{4/d_2^2 - 1}(\theta_1 - \pi/2), \end{aligned} \quad (17)$$

$$\begin{aligned} \bar{e} &\sim (1/4)\sqrt{4\alpha^2 + (\beta^2 - \alpha^2)d_2^2} \\ &\quad + \frac{\alpha^2}{(\beta^2 - \alpha^2)d_2} \tanh^{-1}\left[\frac{\beta^2 - \alpha^2}{4\alpha^2 + (\beta^2 - \alpha^2)d_2^2}\right], \end{aligned} \quad (18)$$

$$\bar{e}_z \sim \alpha - (\alpha + \beta)d_2^2/12. \quad (19)$$

### 3. Full numerical solution

The numerical solution of the proposed rebound model is illustrated in Fig. 2, where  $\bar{\theta}'_1$ ,  $\bar{e}$ , and  $\bar{e}_z$  are plotted against the impact angle  $\theta_1$  and the impactor-bed grain-size ratio  $d_1/d_2$ .

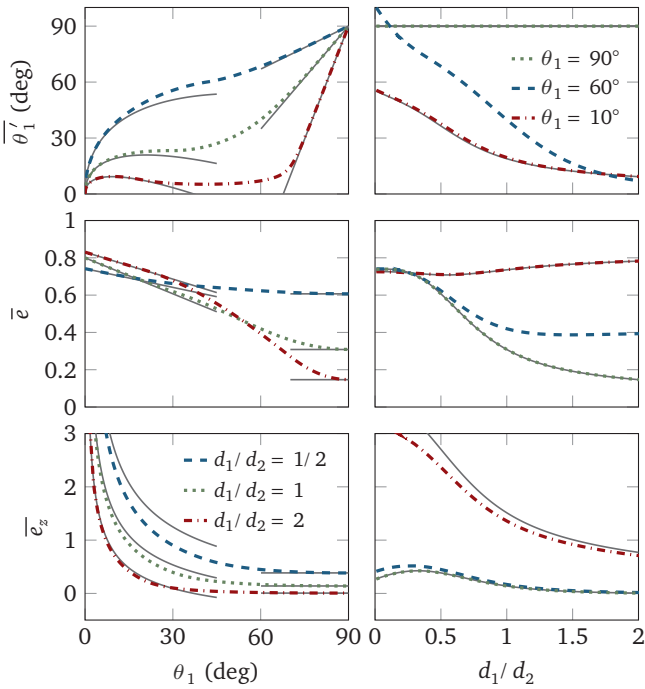


FIG. 2. The two-dimensional collision model predicts the mean rebound angle  $\theta'_1 = \arctan(v'_{1z}/v'_{1x})$ , the total restitution  $e \equiv |\mathbf{v}'_1|/|\mathbf{v}_1|$ , and the vertical restitution and  $e_z \equiv v'_{1z}/|v_{1z}|$  as a function of the impact angle  $\theta_1$  and the impactor-bed grain-size ratio  $d_1/d_2$  from an average over the possible impact positions of the regularly packed bed. Solid lines represent the asymptotic scaling relations, Eqs. (12), (14), (16), and (17)–(19) derived for shallow and steep impacts, respectively. The microscopic restitution coefficients are  $\epsilon = 0.75$  and  $\nu = 0$ .

The plots reveal that the asymptotic relations for shallow and steep impacts, Eqs. (12), (14), (16), and (17)–(19), shown as dashed lines, indeed provide useful expressions if  $\theta_1 < 20^\circ$  and  $\theta_1 > 80^\circ$ , respectively. Note that small impactors with a large-enough impact angle are scattered backwards (i.e., to the left in Fig. 1) for most possible impact positions, yielding a mean rebound angle larger than  $90^\circ$ , as it is the case for the  $60^\circ$  impacts shown in the upper right panel of Fig. 2 (green curve).

So far, we kept the two-dimensional formulation as simple as possible in order to derive the above analytical relations. One might suspect this approach to be too simplistic and therefore prone to some unphysical artifacts. To obtain a more realistic rebound description, we therefore account for a second recoil from the bed grains, thereby suppressing negative (or too large) rebound angles. This refinement provides only minor quantitative corrections that can approximately be subsumed into a moderate renormalization of the microscopic restitution coefficients  $\epsilon$  and  $\nu$ , as illustrated in Sec. IID, where we compare the various model versions with experimental data and our computer simulations. More significant consequences on the rebound statistics are obtained from a three-dimensional extension of our model that we present in the following section.

### B. Three-dimensional collision model

To extend the above toy model to three dimensions, we represent the bed surface by a periodic hexagonal plane

packing of spheres. On contact, the vector connecting the centers of the impacting grain and the bed grain with lattice coordinates  $(i, j)$  reads

$$\mathbf{R}_{lij} \equiv [\mathbf{R}_1 - (i + j/2)d_2\mathbf{e}_x - (\sqrt{3}/2)jd_2\mathbf{e}_y]. \quad (20)$$

Replacing its 2D analog  $\mathbf{R}_i$  by this expression, all equations of Sec. IIA stay the same for the 3D model version. But now, the average is over three parameters: two dimensions of initial position and the horizontal angle of incidence, which by symmetry needs to vary by  $\pi/3$ .

To compare with experiments employing a single camera, we have to replace the rebound velocity with its projection

$$\mathbf{v}'_{1,iz} = (\mathbb{1} - \mathbf{q}\mathbf{q}) \cdot \mathbf{v}'_1, \quad \mathbf{q} \equiv \mathbf{v}_1 \times \mathbf{e}_z / |\mathbf{v}_1 \times \mathbf{e}_z|, \quad (21)$$

on the plane viewed by the camera, for which we assume that it is always the plane of incidence (i.e., spanned by  $\mathbf{v}_1$  and the  $z$  axis). As already pointed out above, such a collision can result in a rebound velocity that points downwards, thus leading to secondary collisions. Altogether, we thus end up with four versions of our geometrical collision model: two or three dimensional, each with one or two bed collisions, which we label in the following as 2D, 2D2, 3D, and 3D2, respectively. To keep the following analysis and comparison with numerical and experimental data manageable, we will not explicitly consider the 3D model version, because it would neither provide any qualitatively new insight nor is it computationally much more efficient, as we have to evaluate both the 3D and the 3D2 version numerically, anyway.

To evaluate the difference between the two- and the three-dimensional descriptions, we compare the distribution  $P(\theta'_1|\theta_1)$  of the rebound angle  $\theta'_1$  for given impact angle  $\theta_1$  and  $d_1/d_2$  in Fig. 3. The plot reveals that both approaches yield rather similar distributions, suggesting that the much simpler 2D version suffices in most applications. Only for shallow impacts, we find that the two- and three-dimensional approaches differ qualitatively: While the graph of the 2D distribution has a triangular shape, as we also expect from the asymptotic Eq. (11), its 3D analog appears to be smoothed, with a considerable contribution of large rebound angles. The latter is a consequence of the fact that an impactor can reach relatively low—and thus quite steep—parts of a 3D packing when it approaches the trough formed by three neighboring bed grains. This three-dimensional effect can also be rationalized by considering the 2D slices that cut through the regular three-dimensional packing. They appear to be highly irregular, characterized by strong variations of the size of the solid disks and intermittent voids. It should thus be possible to effectively simulate the effects due to the three-dimensional collision geometry by introducing some surface irregularity into the two-dimensional bed. This idea is addressed in the next section.

### C. Effective disordered two-dimensional bed

To effectively simulate the irregularities encountered along two-dimensional cuts through a three-dimensional bed, we introduce a distribution  $p(s_d, s_v)$  of the reduced disk and void size  $s_d$  and  $s_v$ , respectively. Here  $s_d d_2$  is the actual size of the effective two-dimensional bed grains at the surface and  $s_v d_2$



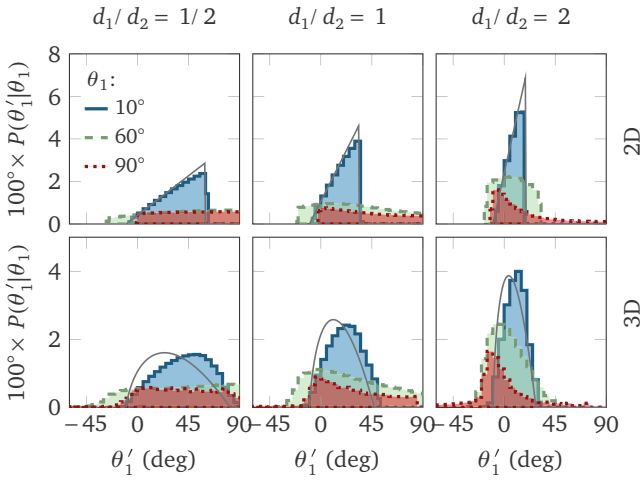


FIG. 3. The rebound angle distribution  $P(\theta'_1|\theta_1)$  as obtained from the 2D and 3D version of our model. The qualitative differences are most significant for small impact angles  $\theta_1$  and can be traced back to the irregular packing of two-dimensional slices through a regular three-dimensional granular packing. We effectively account for this effect by introducing a uniform distribution of void sizes between neighboring bed grains in the 2D model. Thereby, we can analytically determine the asymptotic form of  $P(\theta'_1|\theta_1)$  for shallow impacts, Eq. (30) (dashed lines in the lower panels), which reproduces the bell shape obtained from the numerically evaluated full 3D model rather than the triangular shape predicted by Eq. (11) (dashed lines in the upper panels). The microscopic restitution coefficients are  $\epsilon = 0.75$  and  $\nu = 0$ .

the void size between them. For each pair  $(s_d, s_v)$ , the bed may be considered a regular lattice with periodicity  $(s_d + s_v)d_2$ . The distribution and mean of an observable  $A(\mathbf{v}_1)$  that characterizes the rebound of an impactor of velocity  $\mathbf{v}_1$  now read

$$P(A|\mathbf{v}_1) = \int ds_d ds_v \frac{p(s_d, s_v)}{(s_d + s_v)d_2} \times \int_{x_0 - s_v d_2}^{x_0 + s_d d_2} dx \delta\{A - f[\mathbf{v}'_1(\mathbf{v}_1, \hat{\mathbf{n}})]\} \quad (22)$$

and

$$\bar{A}(\mathbf{v}_1) = \int ds_d ds_v \frac{p(s_d, s_v)}{(s_d + s_v)d_2} \int_{x_0 - s_v d_2}^{x_0 + s_d d_2} dx f[\mathbf{v}'_1(\mathbf{v}_1, \hat{\mathbf{n}})], \quad (23)$$

respectively. The integrals in Eqs. (22) and (23) average over the void to the left of the bed grain hit by the impactor, whereby the range of the possible impact positions  $x$  is determined by

$$x_0 = \begin{cases} \csc\theta_1 - s_d d_2, & 2 \sin\theta_1 < (s_d + s_v)d_2, \\ \cot\theta_1 \sqrt{1 - [(s_d + s_v)d_2/2]^2} - (s_d - s_v)d_2/2, & \\ \text{else.} & \end{cases} \quad (24)$$

As the  $s$  dependence of  $x_0$  obviously complicates the calculation of the double integral in Eq. (22), it is useful to bring it into a more transparent form. Following the formalism introduced in Sec. II A, we again make the  $x$  dependence of the function  $f(x) = f[\mathbf{v}'_1(\mathbf{v}_1, \hat{\mathbf{n}})]$  in Eq. (22) explicit. The  $x$  integral evaluates to the sum  $\sum_i |df_i^{-1}/dA|$  over all branches

$f_i^{-1}$  of the inverse of  $f$ . In general, the support of each  $f_i^{-1}$  is not the whole image  $f([x_0 - s_v d_2, x_0 + s_d d_2])$  of  $f$  but only a subset of it. The integral thus becomes

$$P(A|\mathbf{v}_1) = \sum_i \int ds_d ds_v \frac{p(s_d, s_v)}{(s_d + s_v)d_2} \left| \frac{df_i^{-1}}{dA} \right| \chi_i(A), \quad (25)$$

where the characteristic function  $\chi_i(A)$  is one if  $A$  is in the support of  $f_i^{-1}$  and zero otherwise. Note that  $\chi_i(A)$  depends implicitly on  $s$ , as  $\text{supp } f_i^{-1}$  is a subset of the  $(s_v, s_d)$ -dependent image  $f([x_0 - s_v d_2, x_0 + s_d d_2])$ .

To determine the distribution  $p(s_d, s_v)$  is again a purely geometrical, though complex, problem, which is further complicated by the fact that, for a two-dimensional cut through a three-dimensional packing,  $s_d$  and  $s_v$  are not independent of each other. Here, we thus propose a rather simplistic approach that can be easily used to derive a number of results. Testing them against experiments, computer simulations, and (in particular) the full 3D model introduced above eventually allows us to assess the quality of our simplified model for  $p(s_d, s_v)$ . First, we neglect the correlations between  $s_d$  and  $s_v$  and assume that the effect of the bed surface irregularities is sufficiently characterized by a fixed bed grain size  $d_2$  and a uniform void-size distribution:

$$p(s_d, s_v) \approx \delta(s_d - 1) \begin{cases} 1/(b - a), & a < s_v < b, \\ 0, & \text{else.} \end{cases} \quad (26)$$

The complex dependence on the grain-size ratio and the impact angle is thereby delegated to the values of  $a$  and  $b$  that serve to parametrize the effect of the three-dimensional scattering geometry in terms of the two-dimensional void size. In general, the minimum void size  $b$  can take negative values but must be larger than  $-1$ , as the target grain becomes completely screened by its left neighbor for  $s_v = -1$ . The maximum void size  $b$  can basically take arbitrarily large values.

The precise geometry for higher impact angles is somewhat involved. However, the comparison between the two- and three-dimensional approaches in Fig. 3 reveals that the rebound statistics differ qualitatively only for shallow impacts, whereas for steeper impact angles the simple two-dimensional framework already seems to capture the main characteristics of the impact statistics for the three-dimensional geometry quite well. We thus restrict the following analysis to very shallow impacts.

### 1. Shallow impacts ( $\theta_1 \ll \pi/2$ )

For shallow impacts, the expressions for the minimum and maximum void size take the simple form

$$a \sim -1, \quad b \sim -1 + \sqrt{3}, \quad (27)$$

respectively, independent of the grain-size ratio and impact angle. The target bed grain is completely screened for the minimum  $s_v = a$ , while the impactor is tangent to the next neighbor in front of the trough-forming bed grains for the maximum  $s_v = b$ .

As the inverse  $f^{-1}$  of  $f(x)$  consists of only a single branch, both  $f$  and  $f^{-1}$  are monotonic functions and the effect of the characteristic function  $\chi_1(A) = 1$  is equivalent to the interval

condition  $-s_v d_2 < f^{-1}(A) < s_d d_2$ , for which the rebound distribution in Eq. (25) becomes

$$P(A|\mathbf{v}_1) \sim \frac{1}{d_2} \left| \frac{df^{-1}}{dA} \right| \int_{s_0}^{\infty} ds_d \int_{-s_0}^{\infty} ds_v \frac{p(s_d, s_v)}{s_d + s_v} \quad (28)$$

with  $s_0 \equiv f^{-1}(A)/d_2$ . Here we shifted the  $x$  coordinate by  $x_0 = \csc\theta_1 - d_2$ , as given in the first line of Eq. (24). The

latter requires that  $2 \sin \theta_1 < (1 + s_v)d_2$ , which is actually not always fulfilled, because  $s_v$  becomes as small as  $a = -1$ , according to Eq. (27). For small  $\theta_1$ , however, we argue that the so-introduced error is inconsequential compared to the approximation of the void- and disk-size distributions. Inserting the uniform void size-distribution, Eq. (26), with the asymptotic estimates of  $a$  and  $b$  given in Eq. (27), we can perform the  $s_v$  integration to obtain the following compact form of the rebound distribution:

$$P(A|\mathbf{v}_1) \sim \begin{cases} \frac{|df^{-1}/dA|}{\sqrt{3}d_2} \ln \frac{\sqrt{3}d_2}{d_2 - f^{-1}(A)}, & 0 < d_2 - f^{-1}(A) < \sqrt{3}d_2, \\ 0, & \text{else.} \end{cases} \quad (29)$$

Substituting the shallow-impact scaling of the rebound angle  $\theta'_1 \sim (1 + \alpha/\beta)\sqrt{2(d_2 - x)}\theta_1 - \theta_1$ , the total restitution  $e \sim \beta - (\beta^2 - \alpha^2)(d_2 - x)\theta_1/\beta$ , and the vertical restitution  $e_z \sim -\beta + (\alpha + \beta)\sqrt{2(d_2 - x)}/\theta_1$  for  $f(x)$  yields the distributions

$$P(\theta'_1|\theta_1) \sim \begin{cases} \frac{\beta^2(\theta_1 + \theta'_1)}{(\alpha + \beta)^2 \sqrt{3}d_2\theta_1} \ln \frac{2(\alpha + \beta)^2 \sqrt{3}d_2\theta_1}{\beta^2(\theta_1 + \theta'_1)^2}, & 0 < \frac{\beta(\theta_1 + \theta'_1)}{(\alpha + \beta)\sqrt{3}d_2\theta_1} < 2, \\ 0, & \text{else,} \end{cases} \quad (30)$$

$$P(e|\theta_1) \sim \begin{cases} \frac{\beta}{(\beta^2 - \alpha^2)\sqrt{3}d_2\theta_1} \ln \frac{(\beta^2 - \alpha^2)\sqrt{3}d_2\theta_1}{\beta(\beta - e)}, & 0 < \frac{\beta(\beta - e)}{(\beta^2 - \alpha^2)\sqrt{3}d_2\theta_1} < 1, \\ 0, & \text{else,} \end{cases} \quad (31)$$

$$P(e_z|\theta_1) \sim \begin{cases} \frac{(e_z + \beta)\theta_1^2}{(\alpha + \beta)^2 \sqrt{3}d_2\theta_1} \ln \frac{2(\alpha + \beta)^2 \sqrt{3}d_2\theta_1}{(e_z + \beta)^2 \theta_1^2}, & 0 < \frac{(e_z + \beta)\theta_1}{(\alpha + \beta)\sqrt{2}\sqrt{3}d_2\theta_1} < 1, \\ 0, & \text{else,} \end{cases} \quad (32)$$

respectively. The corresponding mean values

$$\overline{\theta'_1} \sim (4/9)(1 + \alpha/\beta)\sqrt{2\sqrt{3}d_2\theta_1} - \theta_1, \quad (33)$$

$$\bar{e} \sim \beta - (\beta^2 - \alpha^2)\sqrt{3}d_2\theta_1/(8\beta), \quad (34)$$

$$\bar{e}_z - \beta + (4/9)(\alpha + \beta)\sqrt{2\sqrt{3}d_2/\theta_1}. \quad (35)$$

are of the form of the corresponding expressions for the two-dimensional bed in Eqs. (12), (14), and (16), with a renormalized dimensionless bed grain size  $d_2$ .

Although our analytical expressions rely on quite drastic simplifications, their agreement with the full model is good enough for computing qualitatively reliable predictions of the rebound statistics. As an illustration, we compare the approximate relation for the rebound angle distribution, Eq. (30), with the numerical solution of the 3D model for three different grain-size ratios in Fig. 3.

#### D. Comparison with simulations and experiments

We now test the predictions of the various versions of our model against experiments and computer simulations. In summary, we find that the simplest two-dimensional approach, even without a second collision, suffices to fit the rebound averages for monodisperse granulates, i.e., as long as  $d_1/d_2 = 1$ , whereas the dependence of these averages on  $d_1/d_2$  can only qualitatively be reproduced by the two-dimensional models, while quantitative predictions actually require some three-dimensional information about the bed packing.

We start with the collision experiments by Beladjine *et al.* [11], who shot plastic beads into a bed of similar beads to obtain the mean rebound angle  $\overline{\theta'_1}$ , the total restitution  $\bar{e}$ , and the vertical restitution  $\bar{e}_z$  as a function of the impact angle. As shown in Figs. 4(a)–4(c), the numerically evaluated two- and three-dimensional model versions compare well with these data. For each version, the values of the (effective) microscopic restitution coefficients  $\epsilon$  and  $\nu$ , which are used as global fit parameters, are listed in Table I.

The dependence of the splash properties on the grain-size ratio was addressed in only very few experimental studies so far. Willetts and Rice [3], for instance, used dune sand that is characterized by a unimodal grain-size distribution ranging from about 150 to 600  $\mu\text{m}$ , which they split into three fractions—fine, medium, and coarse—to investigate the influence of the size of the impactor on the rebound. From their data we infer the grain-size ratios  $d_1/d_2 \approx 0.73, 1, \text{ and } 1.4$ , whereby we identified  $d_1$  with the mean diameter of the fine, medium, or coarse grain fraction and  $d_2$  with the overall mean. The authors recorded the collision process in a wind tunnel during saltation, i.e., when the grains are driven by the wind. Altering the bed inclination, they were able to tune the impact angle  $\theta_1$  of the fast hopping grains and thereby to investigate its influence on the mean rebound angle  $\overline{\theta'_1}$  and the total restitution  $\bar{e}$ . Again, we globally fit these data using  $\epsilon$  and  $\nu$  as free fit parameters. The result, shown in Figs. 4(d) and 4(e), reveals that the influence of the varying grain size is convincingly reproduced by both the two- and three-dimensional approach. To improve the qualitative agreement between the data and the 3D model version, we here manually set the grain-size ratios



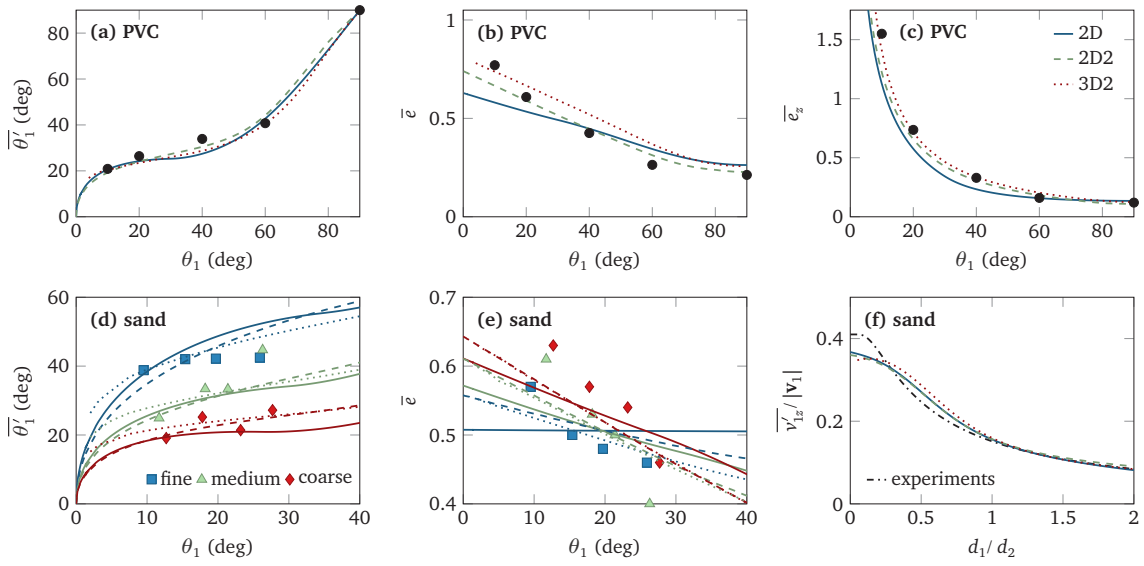


FIG. 4. Comparison with literature data. [(a)–(c)] The two-dimensional model with (2D2) and without (2D) a second bed collision compared to the full three-dimensional version (3D2) and experimental data by Beladjine *et al.* [11] (dots) obtained for plastic PVC beads. Each model version is fitted to the data for the mean rebound angle  $\bar{\theta}'_1$ , the total restitution  $\bar{\epsilon}$ , and the vertical restitution  $\bar{\epsilon}_z$  as a function of the impact angle  $\theta_1$  using the microscopic restitution coefficients  $\epsilon$  and  $\nu$  as global fit parameters. [(d) and (e)] Similar model fits to the wind-tunnel data by Willetts and Rice [3] (symbols), who discriminated among fine, medium, and coarse grain fractions of the used sand sample to analyze their measurements. (f) Also the empirical relation  $\bar{v}'_{1z}/|\mathbf{v}_1| = 0.41(1 - 10^{-0.2d_2/d_1})$  for grain-size dependence of the mean vertical rebound velocity for fixed impact angle  $\theta_1 = 14^\circ$ , proposed by Ellwood *et al.* [27] to fit their collision experiments with natural sand, is qualitatively well reproduced. Values of the microscopic restitution coefficients  $\epsilon$  and  $\nu$  for all shown fits are given in Table I.

to  $d_1/d_2 = 0.75, 1$ , and  $1.25$ , which corresponds to a slightly smaller polydispersity of the sand sample than expected from the measured grain-size distribution.

A few years before Willetts and Rice, Ellwood *et al.* [27] used sieved natural sand to measure the vertical rebound speed  $v'_{1z}$  for a fixed impact angle  $\theta_1 = 14^\circ$  and various size ratios  $d_2/d_1$ . From their data, they extracted an empirical formula  $\bar{v}'_{1z}/|\mathbf{v}_1| = 0.41(1 - 10^{-0.2d_2/d_1})$  that we compare in Fig. 4(f) with the predictions of the two- and three-dimensional versions of our collision model. Up to minor quantitative deviations in the limit of fine impactors,  $d_1/d_2 < 0.2$ , all model versions are found to be in very good qualitative agreement with the empirical formula, which strongly supports our choice for the

TABLE I. Values of the microscopic restitution coefficients  $\epsilon$  and  $\nu$  employed to fit the collision experiments with plastic beads by Beladjine *et al.* [11], with natural sand by Willetts and Rice [3] and Ellwood *et al.* [27], and our discrete-element simulations [9,28] by our two-dimensional model with (2D2) and without (2D) a second bed collision and its three-dimensional extension with a second bed collision (3D2).

	Plastic [11]	Sand [3]	Sand [27]	Simulations
2D	$\epsilon$ 0.70	0.94	0.46	0.67
	$\nu$ -0.83	-1.2	-0.86	-1.5
2D2	$\epsilon$ 0.58	0.84	0.53	0.53
	$\nu$ -0.24	-0.98	-1.4	-1.1
3D2	$\epsilon$ 0.58	0.86	0.68	0.79
	$\nu$ -0.24	-0.97	-1.6	-0.69

dependence of the restitution coefficients  $\alpha$  and  $\beta$  on the mass ratio  $d_1^3/d_2^3$  in Eqs. (7) and (8).

As all the currently available experimental data are limited to rather confined parameter ranges—in particular, laboratory studies on the influence of the grain-size ratio are still lacking—we also test our model predictions against computer simulations that allow us to freely tune these parameters. Details about the discrete-element method that is employed to simulate the collision of an impacting bead with a three-dimensional packing of beads of varying size can be found in Refs. [9,28]. The dissipative collision between two beads at contact are quantified in terms of a friction coefficient and a normal restitution coefficient, which we set to 0.3 and 0.8, respectively. As we found the rebound properties to be independent (within the statistical error bars) of the impact speed  $|\mathbf{v}_1|$ , we average all observables over the used  $|\mathbf{v}_1| = 20, 30$ , and  $40$  m/s. Figure 5 shows the so-obtained mean rebound angle  $\bar{\theta}'_1$ , the total restitution  $\bar{\epsilon}$ , and the vertical restitution  $\bar{\epsilon}_z$  as a function of the impact angle  $\theta_1$  and the impactor–bed grain-size ratio  $d_1/d_2$  and compares them with the corresponding predictions of the two- and three-dimensional version of our collision model. Again, we used the (effective) microscopic restitution coefficients  $\epsilon$  and  $\nu$  as global fit parameters for each model version. Their values are listed in Table I. Besides such average quantities, the simulations provide us with the full rebound statistics. As an example, we compare in Fig. 6 the distribution of the rebound angle with the numerical solution of the three-dimensional model version with a second collision and the asymptotic relation for shallow impacts derived from the two-dimensional effective approach with a uniform void-size distribution, introduced in Sec. II C.

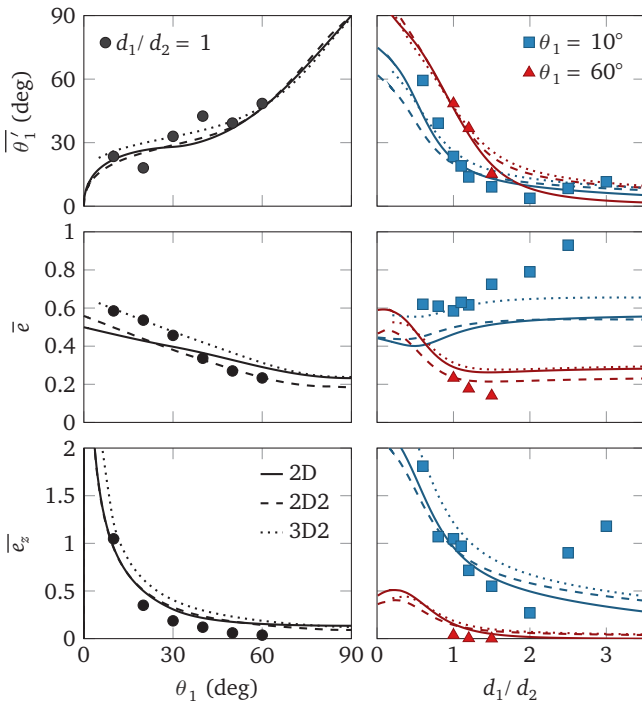


FIG. 5. Comparison with computer simulations: averaged rebound characteristics as a function of the impact angle  $\theta_1$  and the grain-size ratio  $d_1/d_2$ , as predicted by the 2D and 3D model versions and compared with computer simulations that describe the collision of an impacting bead with a 3D packing using a discrete-element method [9,28].

### III. BED GRAIN EJECTION

We finally turn to the theoretical description of the actual splash, the ejection of bed grains by the impacting particle. High-speed videos of the collision process reveal that bed grains are not directly knocked out of the assembly by the impactor, but that they rather leave from a relatively large area of the bed, shortly after the impinging grain already bounced off (see, e.g., [11]). This suggests a partial fluidization of the bed caused by the momentum and energy transfer through the initially quiescent grain packing.

Valance and Crassous [14] modeled this process theoretically by a numerical scheme that could be extended to binary mixtures. They further proposed an alternative energy diffusion approach that is easier to analyze, which could also serve as a starting point for further studies. As yet another approach, one could consider the force propagation along *force chains* in a granular bed. Thereby one can, for example, account for the pressure dip beneath the apex of a sand pile produced by depositing grains from a nozzle. Its occurrence depends on the history of the granular packing (i.e., the preparation of the pile) and can be suppressed by strong disorder and intergrain friction [29]. This behavior can be linked to two different mathematical descriptions of the stress propagation in static granular media, corresponding to hyperbolic or elliptic differential equations. The former gives rise to a type of ray propagation along force chains and the second to “diffusive” stress fields similar to those

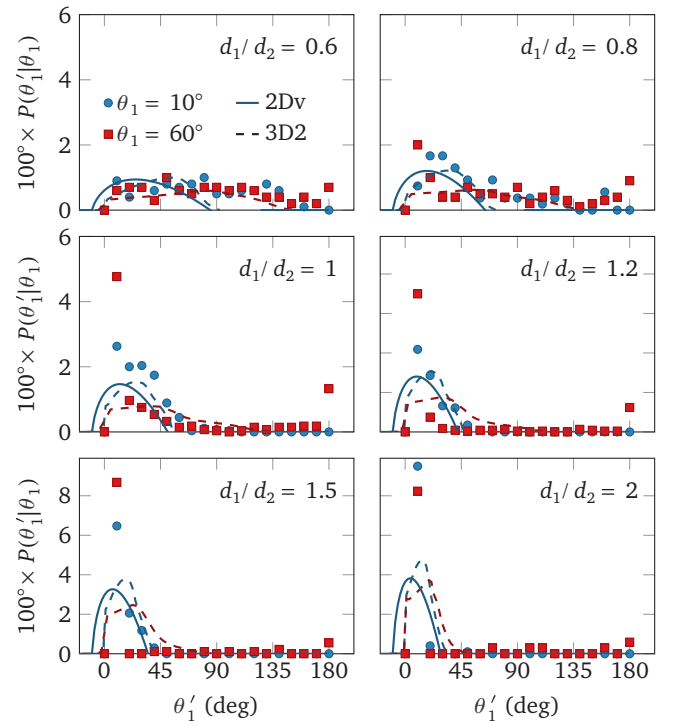


FIG. 6. Comparison with computer simulations: rebound angle distribution from the discrete-element simulations (symbols) compared to the three-dimensional collision model (3D2) of Sec. II B and the asymptotic scaling relation Eq. (29) for shallow impacts obtained from the effective two-dimensional model (2Dv) with a uniform void-size distribution.

in homogeneous elastica (see, e.g., the lecture notes by Bouchaud [30] for an overview). One can actually derive these macroscopic relations from simple force balances on the grain contact level. However, this is only possible for a static packing under the influence of gravity, where the weight is transferred downwards from one grain layer to the other. For momentum propagation the situation is far more complex: The grains move and may therefore change the contact network, and one has to account for momentum changes of all collision partners. A possible starting point might be the force chain splitting approach by Bouchaud and coworkers [30–32], who proposed simple rules to create scattering paths through a quenched random packing. Originally interpreted as static force chains, the very same paths might tentatively be used to model momentum propagation, which is highly suggested by the experiments by Clark and colleagues, who analyzed the force distribution [33,34] and the flow field [35] in a granular bed hit by a large intruder. Particularly striking are the videos of these experiments, see also Ref. [36] for an example and a brief review of this work. The quasistatic modeling approach by Bouchaud *et al.* was criticized, e.g., by Wyart [37], for its lack of floppy modes, which turn out to be essential for a proper understanding of the response of granular packings to weak forces, in particular, for the characteristic power-law distribution of small forces in the network. In our case, however, we may tentatively argue that the force exerted by the fast impacting grain is large and the tail of the weak

contact forces is inconsequential for the splash, for which gravity has to be overcome.

The approach we want to pursue here is mainly inspired by the above-described picture of the branching force chains. We follow Ho *et al.* [24], who estimated the velocity distribution of the ejected particles by mapping the cascade of collisions in the packing to a fragmentation process. As they were interested in the generic shape of this distribution, they assumed that in each collision, the kinetic energy is equally distributed among two target grains without any losses. The energy transferred to a particle at the end of a chain of  $k$  collisions is thus given by the fraction  $(1/2)^k$  of the energy transferred to the bed. The latter could be estimated by  $(1 - \bar{e}^2)E_1$ , where  $\bar{e}$  denotes the mean total restitution, as introduced in the previous section, and  $E_1 = (m_2/2)v_1^2$  is the kinetic energy of the impactor. The collisions in the packing can easily be made dissipative by replacing the energy-splitting factor  $1/2$  by a smaller effective restitution coefficient, but this would not affect the structure of the final result. Ho *et al.* argued that the following fragmentation process can be used to describe the collision cascade: The energy is split into two fractions of equal size. Next, one of the resulting fractions is selected randomly and again split into two. Then, one of the three fractions is selected and split, and so on. It is well known that the energy fractions created through such a procedure are Poisson distributed with a parameter  $\lambda$  determined by the total number of splitting events. For the splash process, this number is given by the total input energy divided by the minimum ejection energy, i.e.,  $(1 - \bar{e}^2)E_1/(m_2gd_2)$ . For typical impact speeds ( $>10\sqrt{gd_1}$ ) and not-too-small grain-size ratios ( $d_1/d_2 > 0.5$ ),  $\lambda$  is large enough so the Poisson distribution can be approximated by a normal distribution. This eventually yields a log-normal distribution

$$P(E_2|E_1) = \frac{1}{\sqrt{2\pi}\sigma E_2} \exp\left[-\frac{(\ln E_2 - \mu)^2}{2\sigma^2}\right] \quad (36)$$

for the energy  $E_2$  of the ejected particles, where

$$\begin{aligned} \sigma &= \sqrt{\lambda} \ln 2, \\ \mu &= \ln[(1 - \bar{e}^2)E_1] - \lambda \ln 2, \\ \lambda &= 2 \ln[(1 - \bar{e}^2)E_1/E_{d_2}], \end{aligned} \quad (37)$$

and  $E_{d_2} \equiv m_2gd_2$  is the minimum transferred energy for a bed particle to be counted as ejecta. It was shown in Ref. [24] that Eq. (36), rewritten in terms of the ejection velocity  $|\mathbf{v}'_2| = \sqrt{2E_2/m_2}$ , is in excellent agreement with simulations of a discrete collision model and even with wind-tunnel measurements of saltating particles. Both the simulations and the experiments were performed with unimodal sand, i.e.,  $d_1/d_2 = 1$ , and with values for the parameter  $\lambda$  varying between 8 and 17. However, even for grain-size ratios below 0.5, corresponding to  $\lambda$  on the order of 1, the minor quantitative errors incurred by the log-normal approximation would not appreciably affect the following qualitative predictions.

We here test Eq. (36), together with Eq. (37), against the laboratory data by Beladjine *et al.* [11]. From these relations,

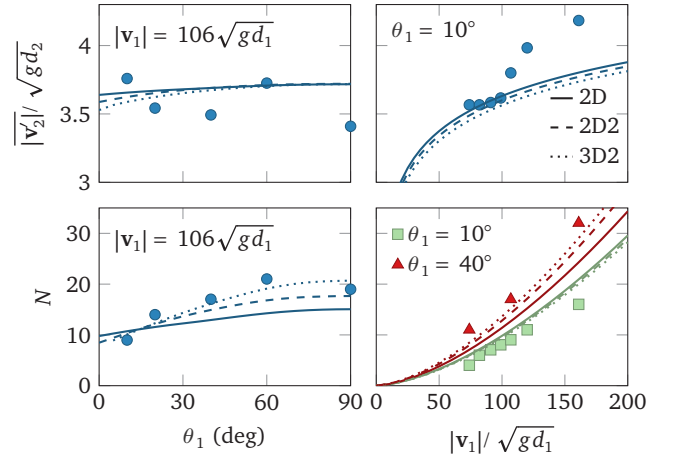


FIG. 7. Comparison with experimental literature data: The measured key characteristics of the ejected particles in the splash caused by an impacting grain can be reproduced by the fragmentation model by Ho *et al.* [24] if combined with our collision model from Sec. II. To compare the mean ejection velocity  $|\mathbf{v}'_2|$ , Eq. (38), and the number  $N$  of ejected grains, Eq. (39), over a wide range of impact angles  $\theta_1$  and impact speeds  $|\mathbf{v}_1|$  with the experiments by Beladjine *et al.* [11] (symbols), we inserted the values of the microscopic restitution coefficients  $\epsilon$  and  $\nu$  listed in Table I. The fraction  $\gamma$  of the impact energy lost in the bed was used as fit parameter, which yields  $\gamma = 0.049, 0.055,$  and  $0.062$  for the 2D, 2D2, and 3D2 versions of the collision model, respectively.

we can calculate the mean ejection velocity

$$\begin{aligned} \overline{|\mathbf{v}'_2|} &= \int_{E_{d_2}}^{\infty} dE_2 \sqrt{2E_2/m_2} P(E_2|E_1) \Big/ \int_{E_{d_2}}^{\infty} dE_2 P(E_2|E_1) \\ &= \frac{\operatorname{erfc}[(\ln E_{d_2} - \mu - \sigma^2/2)/(\sqrt{2}\sigma)]}{\operatorname{erfc}[(\ln E_{d_2} - \mu)/(\sqrt{2})]} \sqrt{2} e^{\mu/2 + \sigma^2/8}, \end{aligned} \quad (38)$$

from the reduced ensemble of mobilized grains with energy  $E_2 \geq E_{d_2}$ . We thereby obtain its dependence on the impact angle and the impact speed, which we compare with the experimental data in Fig. 7. Recalling that the shown curves are *not fitted* to the data, as there is no free parameter left in Eq. (38), we find the agreement very satisfactory—only for the highest impact speeds the theory seems to underestimate the measured ejection velocities. Moreover, the plot reveals that  $|\mathbf{v}'_2|$  depends only very weakly on the choice of the model version used to compute the total restitution  $\bar{e}$ , which underscores that the fragmentation approach indeed robustly captures the underlying physics.

The fragmentation model as such does not provide us with a prediction for the total number  $N$  of ejected particles, which is an important coarse-grained measure of the splash function and frequently used in transport models to parametrize the splash. But, following the same lines as for the mean ejection speed, we may combine it with the rebound properties obtained in Sec. II to estimate  $N$  and its dependence on impact speed, impact angle, and grain-size ratio. Subsuming the energy losses in the bed packing into the numerical prefactor  $\gamma$ , the energy that goes into the mobilized (not necessarily ejected)

grains can be written as  $\gamma(1 - \bar{e}^2)E_1$ . Divided by the average energy  $\bar{E}_2$  of one mobilized grain it yields the total number of mobilized grains, from which we obtain the number

$$\begin{aligned} N &\approx \gamma \frac{(1 - \bar{e}^2)E_1}{\bar{E}_2} \int_{E_{d_2}}^{\infty} dE_2 P(E_2|E_1) \\ &= \gamma \frac{(1 - \bar{e}^2)E_1}{2\bar{E}_2} \operatorname{erfc}\left(\frac{\ln E_{d_2} - \mu}{\sqrt{2}\sigma}\right), \end{aligned} \quad (39)$$

of ejected grains. In the second step, we used the log-normal energy distribution, Eq. (36), from which we also estimate the average energy

$$\begin{aligned} \bar{E}_2 &= e^{\mu + \sigma^2/2} \\ &= E_{d_2} [(1 - \bar{e}^2)E_1/E_{d_2}]^{1 - (2 - \ln 2)\ln 2}, \end{aligned} \quad (40)$$

of a mobilized grain. The small exponent  $1 - (2 - \ln 2)\ln 2 \approx 0.1$  implies that the mean ejection energy is actually on the same order as its minimum value  $E_{d_2}$ .

In Ref. [14],  $\gamma$  was estimated from an energy-diffusion model, which allows us to trace back the large energy losses in the bed to a simple geometrical effect: Only a very small fraction of the downward propagating impact energy is scattered back towards the bed surface by collisions in the bed packing. This means that, even for elastically colliding bed grains, typical values of  $\gamma$  are expected to be on the order of a few percentages. In fact, the values predicted by the diffusion model without energy dissipation varied between 0.05 and 0.2 for small to large impact velocities. In the lower panels of Fig. 7, Eq. (39) is tested against the plastic-bead experiments by Beladjine *et al.*, where the total restitution  $\bar{e}$  is taken from the collision models presented in Sec. II and  $\gamma$  is used as fit parameter. Depending on the model version,  $\gamma$  varies between 0.052 and 0.071, which is on the same order as estimated in Ref. [14] for moderate impact speeds.

#### IV. A READY-TO-USE ANALYTICAL SPLASH PARAMETRIZATION

In this section, we propose an exemplary list of relations that can be used to compute all needed splash properties for shallow impacts, as it is, for example, required in coarse-grained simulations of aeolian particle transport. From Sec. II C and Figs. 3 and 6, we conclude that the bumpiness of the bed surface yields only minute fluctuations in the total restitution coefficient, whereas the rebound angle varies significantly and may therefore be held responsible for the stochastic nature of the particle trajectories. We therefore fix the total restitution coefficient to its mean  $\bar{e}$ , as given by the shallow-impact asymptotics in Eq. (14), and use Eq. (30) for the rebound-angle distribution  $P(\theta'_1|\theta_1)$ . For both expressions, we employ the same values for the microscopic restitution coefficients  $\epsilon$  and  $\nu$ , taken from, say, the fits for the 2D model version as given in Table I. (To unify the various modeling approaches, the bed grain size  $d_2$  Eq. (30) may be replaced by  $9d_2/(4\sqrt{3})$ , so it yields the same asymptotic relation for the mean rebound angle as the 2D model version. This has only marginal consequences for the shape of the rebound-angle distribution.)

An interesting measure that is typically required as input for coarse-grained particle transport simulations [17,38,39] is

the rebound probability  $P_{\text{reb}}(\mathbf{v}_1)$ . Within our approach, it can be defined as the probability that the vertical rebound speed of the impacting grain is larger than  $\sqrt{2gd_1}$ . With Eqs. (14) and (30) it becomes

$$\begin{aligned} P_{\text{reb}}(\mathbf{v}_1) &= \int d\theta'_1 P(\theta'_1|\theta_1) \Theta(\bar{e}|\mathbf{v}_1| \sin \theta'_1 - \sqrt{2gd_1}) \\ &= 1 - \frac{1 + \ln \xi}{\xi}, \end{aligned} \quad (41)$$

with

$$\xi \equiv \frac{2\sqrt{2}(\alpha + \beta)^2 d_2 \theta_1}{\beta^2(\theta_1 + \sqrt{2gd_1}/|\mathbf{v}_1|)^2}, \quad (42)$$

which is indeed in good qualitative agreement with the parametrization  $P_{\text{reb}}(\mathbf{v}_1) \propto 1 - \exp(-|\mathbf{v}_1|/v_c)$  proposed by Anderson and Haff [17] based on their grain-scale computer simulations of the splash process. However, the magnitude of  $P_{\text{reb}}$  predicted by Eq. (41) is slightly smaller than expected, because our single-collision approximation for  $P(\theta'_1|\theta_1)$ , Eq. (30), yields a significant fraction of negative rebound angles. Comparing this analytical estimate with the numerical solution that accounts for a second bed collision (i.e., version 3D2) in Fig. 6 reveals that one should shift the analytical rebound-angle distribution to strictly positive values, namely as  $\theta'_1 \mapsto \theta'_1 + \theta_1$ , to account for this effect in a simple way. The full splash parametrization is completed by Eq. (39), with  $\gamma = 0.06$ , and Eq. (36), which determine the number of ejected particles and their velocity distribution, respectively.

#### V. SUMMARY

In this contribution, we aimed at a manageable parametrization of the splash function, which rests on basic physical principles, like momentum conservation and energy dissipation through inelastic pair collisions of the grains. To this end, we started from a geometrical description of the collision of a spherical grain with a regular granular packing. We introduced semiphenomenological expressions for the gain-size-dependent normal and tangential restitution coefficient for such a grain-bed collision. These two coefficients depend on two microscopic restitution coefficients  $\epsilon$  and  $\nu$ , for the normal and tangential velocity losses during the inelastic grain-grain collisions, which serve as fit parameters in the model. This approach eventually yields the rebound velocity of an impacting grain as a function of the impact velocity and the impactor-bed grain-size ratio. We completed our parametrization of the splash function by combining this framework for the rebound with the energy-splitting model by Ho *et al.* [24], which predicts how the impact energy is distributed among the bed grains. It thereby gives access to the velocity distribution of the ejected bed grains and allows us to estimate how their total number scales with impact angle, impact speed, and grain-size ratio.

We have shown that the proposed two- and three-dimensional versions of our collision model yield very similar predictions for typical observables of interest, like the mean rebound angle, the mean total, and the mean vertical restitution. In general, we found that each model version can be convincingly fitted to various experiments and computer



simulations if we use  $\epsilon$  and  $\nu$  as free fit parameters. Excellent agreement is obtained, in particular, for the two-dimensional model that accounts for secondary collisions with the bed. This is an important observation as this model version is simple and computationally relatively cheap, which makes it suitable for practical applications. Moreover, the two-dimensional approach allows for analytical asymptotic relations for shallow impacts, as shown in Sec. II A 1. This limit is of particular relevance, because the trajectories of wind-blown hopping grains are characterized by very small impact angles on the order of  $10^\circ$  [1]. Hence, the simple asymptotics might be used, for instance, in coarse-grained aeolian transport simulations that cannot afford to resolve the granular structure of the sand bed. The three- and two-dimensional models yield almost the same dependence on the impact angle and the grain size ratio for the analyzed averages. Only their distributions can differ qualitatively, the three-dimensional approach yielding smoother shapes for shallow impacts, as illustrated in Fig. 3. We showed that this shortcoming of the two-dimensional models can be overcome by an extension with a uniform distribution of void spaces between neighboring surface grains. Thereby good agreement with the full three-dimensional model and with our discrete-element simulations could be achieved, as shown for the rebound-angle distribution in Fig. 6. Combined with the energy-fragmentation model by Ho *et al.* [24] for the statistics of the ejected bed particles, the simple two-dimensional impact model yields a ready-to-use parametrization for the splash. It therefore provides an excellent starting point for modeling aeolian structure formation. This, however, requires some extensions of our parametrization, including the drag and lift forces due to the driving turbulent flow. Moreover, the inclusion of additional model ingredients, like the disaggregation of dust agglomerates due to collisions [40] or cohesive, hydrodynamic, and electrostatic interactions [41,42], could give rise to a much richer phenomenology. They are of particular relevance for understanding extraterrestrial granular structures, as observed on Mars [40] or, most recently, on a Jupiter comet [43]. Dedicated theoretical approaches and experimental work [44], might help to extend our model to such phenomena in the future.

#### ACKNOWLEDGMENTS

This research was supported by a Grant from the GIF, the German-Israeli Foundation for Scientific Research and Development. We also acknowledge the hospitality of the KITP in Santa Barbara and the MPI-PKS in Dresden, where this work was started, and financial support by the National Science Foundation under Grant No. NSF PHY-1125915, the Max Planck Institute for the Physics of Complex Systems Visitors Program, and the German Academic Exchange Service (DAAD) through a Kurzzstipendium (for M.L.) and the RISE program (for K.D.). M.L. thanks Maik Weßling for fruitful discussions during the early stages of this project.

#### APPENDIX A: INELASTIC BINARY COLLISIONS

We briefly outline the usual parametrization of an inelastic collision of two spheres in terms of the normal and tangential restitution coefficients  $\epsilon$  and  $\nu$ , which account for dissipation

of kinetic energy during the grain contact. The energy loss by relative motion in normal direction originates from grain deformations, and the tangential loss characterizes the reduction of the relative velocity of the grain surfaces at the contact point due to friction. The exact value of  $\nu$ , which characterizes the tangential slip on particle contact, is hard to estimate, and we might, for simplicity, assume that the colliding spheres roll past each other, corresponding to  $\nu = 0$ . However, comparing the model predictions obtained with experimental data in Sec. II D, we find that  $\nu$  has to be negative to fit the data, which means that the relative surface velocity (or the spin of the impactor) has formally to be reversed. Exact results for the normal restitution  $\epsilon$  of perfect spheres are reviewed, e.g., in Ref. [26]. For viscoelastic Hertzian beads, one obtains that  $\epsilon$  decreases with the impact speed and the size of the colliding grains. Corresponding marginal quantitative corrections to our discussion would not change the overall qualitative picture.

The surface velocities of the colliding grains are determined by the relative velocity of the centers of two colliding spheres and their rotational velocities. The full calculation can be found in classical textbooks (see, e.g., the book by Brilliantov and Pöschel [26]), so we only give the result for the velocity  $\mathbf{v}'_1$  of the first grain after the collision,

$$\begin{aligned} \mathbf{v}'_1 = & \mathbf{v}_1 - \frac{M}{m_1}(1 + \epsilon)(\hat{\mathbf{n}} \cdot \mathbf{v}_{12})\hat{\mathbf{n}} - \frac{M}{m_1} \frac{1 - \nu}{1 + q} (\mathbb{1} - \hat{\mathbf{n}}\hat{\mathbf{n}}) \cdot \mathbf{v}_{12} \\ & + \frac{1}{2} \frac{M}{m_1} \frac{1 - \nu}{1 + q} \hat{\mathbf{n}} \times (d_1\omega_1 + d_2\omega_2). \end{aligned} \quad (\text{A1})$$

Here  $d_{1,2}$  are the diameters of the two spherical grains,  $m_{1,2}$  their masses, and  $\mathbf{v}_{1,2}$  their velocities before the collision, which define  $\mathbf{v}_{12} \equiv \mathbf{v}_1 - \mathbf{v}_2$ . The unit vector  $\hat{\mathbf{n}}$  is parallel to the line that connects the centers of the spheres at contact. The effective mass is  $M \equiv m_1 m_2 / (m_1 + m_2)$  and the parameter  $q \equiv (M/4)(d_1^2/I_1 + d_2^2/I_2)$  depends on the moments of inertia  $I_{1,2}$  of the two grains. For spheres,  $I_{1,2} = m_{1,2} d_{1,2}^2 / 10$  and thus  $q = 5/2$ .

Assuming that the colliding grains do not rotate and that the second grain is at rest before the collision,  $\omega_{1,2} = 0$  and  $\mathbf{v}_2 = 0$ , as is the case when an impactor hits the granular packing, Eq. (A1) reduces to

$$\begin{aligned} \mathbf{v}'_1 = & \left[ 1 - \frac{M}{m_1}(1 + \epsilon) \right] \hat{\mathbf{n}}\hat{\mathbf{n}} \cdot \mathbf{v}_1 \\ & + \left[ 1 - \frac{M}{m_1} \frac{1 - \nu}{1 + q} \right] (\mathbb{1} - \hat{\mathbf{n}}\hat{\mathbf{n}}) \cdot \mathbf{v}_1. \end{aligned} \quad (\text{A2})$$

For grains of similar size,  $d_1 \approx d_2$ ,  $M \approx m_1/2$ , and thus

$$\mathbf{v}'_1 \approx \left[ \frac{1 - \epsilon}{2} \hat{\mathbf{n}}\hat{\mathbf{n}} + \frac{1 + 2q + \nu}{2 + 2q} (\mathbb{1} - \hat{\mathbf{n}}\hat{\mathbf{n}}) \right] \cdot \mathbf{v}_1. \quad (\text{A3})$$

For small impactors,  $m_1 \ll m_2$ , we may approximate  $M \sim m_1$ , which yields

$$\mathbf{v}'_1 \sim \left[ \epsilon \hat{\mathbf{n}}\hat{\mathbf{n}} + \frac{\nu + q}{1 + q} (\mathbb{1} - \hat{\mathbf{n}}\hat{\mathbf{n}}) \right] \cdot \mathbf{v}_1. \quad (\text{A4})$$

**APPENDIX B: 2D COLLISION MODEL: STEEP IMPACTS**

For steep impact, the impact position  $x_0$  is given by the second line of Eq. (5) and the integral in Eq. (1) simplifies to  $P(A|\mathbf{v}_1) \sim (1/d_2)|df^{-1}/dA|$  if the rebound condition  $-d_2 < 2f^{-1}(A) - \sqrt{4-d_2^2} \cot \theta_1 < d_2$  is fulfilled and  $P(A|\mathbf{v}_1) \sim 0$  otherwise. We start with the rebound angle  $f(x) = \theta'_1$ , which we expand in the impact angle  $\theta_1$  around  $\theta_1 = \pi/2$ ,

$$\theta'_1 \sim \tan^{-1} \left[ \frac{\alpha - (\alpha + \beta)x^2}{(\alpha + \beta)x\sqrt{1-x^2}} \right] - (\theta_1 - \pi/2) + \frac{\alpha\beta + \alpha^2 + (\beta^2 - \alpha^2)x^2}{2\alpha^2 + 2(\beta^2 - \alpha^2)x^2} \sqrt{\frac{4-d_2^2}{1-x^2}} (\theta_1 - \pi/2). \quad (\text{B1})$$

For convenience, we here substituted the shifted impact position  $x + \sqrt{1 - (d_2/2)^2} \cot \theta_1$  for the argument of  $f(x)$ , so  $x$  takes values between  $-d_2/2$  and  $d_2/2$ . Integrating over this impact interval, we obtain Eq. (17) of the main text for the mean rebound angle  $\bar{\theta}'_1$ . Although Eq. (B1) cannot be solved for  $x$ , as required for the rebound angle distribution a closer look at Eq. (B1) reveals that it can be approximated by its first-order  $x$  expansion  $\theta'_1 \sim \pi/2 - (1 + \beta/\alpha)x - [1 - (1 + \beta/\alpha)\sqrt{1 - (d_2/2)^2}](\theta_1 - \pi/2)$ . This, in turn allows us to (roughly) estimate its inverse  $f^{-1}(\theta'_1)$  and thus the asymptotic distribution of the impact angle. Within this crude approximation, the latter evaluates to a uniform distribution,

$$P(\theta'_1|\theta_1) \sim \begin{cases} \frac{\alpha}{(\alpha+\beta)d_2}, & -d_2 < \frac{2\alpha(\theta_1+\theta'_1-\pi)}{\alpha+\beta} + \sqrt{4-d_2^2}(\theta_1-\pi/2) < d_2, \\ 0, & \text{else.} \end{cases} \quad (\text{B2})$$

Note that the mean rebound angle  $\bar{\theta}'_1 \sim \pi/2 - [1 - (1 + \beta/\alpha)\sqrt{4-d_2^2}](\theta_1 - \pi/2)$  obtained from this approximate distribution differs from the correct asymptotic scaling relation given in Eq. (17).

Following the same idea, we obtain the  $x$  dependence

$$e \sim \sqrt{\alpha^2 + (\beta^2 - \alpha^2)x^2} - (\beta^2 - \alpha^2)x \sqrt{\frac{1 - (d_2/2)^2}{\alpha^2 + (\beta^2 - \alpha^2)x^2}} (\theta_1 - \pi/2) \quad (\text{B3})$$

of the total restitution coefficient. Integrated over the impact position  $x$ , it yields the result for  $\bar{e}$  given in Eq. (18) of the main text. Again, the distribution of  $e$  can analytically only be estimated from an approximate form of Eq. (B3), e.g., from the parabola  $e \sim \alpha + (\alpha/2)(\beta^2/\alpha^2 - 1)[x^2 - x\sqrt{4-d_2^2}(\theta_1-\pi/2)]$ , which yields

$$P(e|\theta_1) \sim \begin{cases} \frac{1}{d_2} \sqrt{\frac{2\alpha}{(\beta^2-\alpha^2)(e-\alpha)}}, & 0 < \frac{8\alpha(e-\alpha)}{\beta^2-\alpha^2} < d_2^2 - \sqrt{4-d_2^2}(\theta_1-\pi/2), \\ \frac{1}{d_2} \sqrt{\frac{\alpha/2}{(\beta^2-\alpha^2)(e-\alpha)}}, & -1 < \frac{8\alpha(e-\alpha)/(\beta^2-\alpha^2)-d_2^2}{\sqrt{4-d_2^2}(\theta_1-\pi/2)} < 1, \\ 0, & \text{else,} \end{cases} \quad (\text{B4})$$

up to linear order in  $\theta_1 - \pi/2$ . The first line represents the impact range  $-d_2/2 < x < \sqrt{1 - (d_2/2)^2}(\theta_1 - \pi/2)$  where the inverse of  $e(x)$  has two branches; the second line corresponds to the single-branch region  $\sqrt{1 - (d_2/2)^2}(\theta_1 - \pi/2) < x < d_2/2$ .

Finally, we consider the steep-impact limit for the vertical restitution coefficient

$$e_z \sim \alpha - (\alpha + \beta)x^2 + (\alpha + \beta)x(\sqrt{4-d_2^2} - \sqrt{1-x^2})(\theta_1 - \pi/2). \quad (\text{B5})$$

Integrating over the impact positions  $x$ , we obtain its mean  $\bar{e}_z$ , given in Eq. (19). Again, Eq. (B5) can be approximated by its second-order  $x$  expansion  $e_z \sim \alpha - (\alpha + \beta)x^2 + (\alpha + \beta)x(\sqrt{4-d_2^2} - \sqrt{1-x^2})(\theta_1 - \pi/2)$ , from which we derive the estimate

$$P(e_z|\theta_1) \sim \begin{cases} \frac{1}{2d_2\sqrt{(\alpha+\beta)(e_z-\alpha)}}, & -1 < \frac{d_2^2/2+2(e_z-\alpha)/(\alpha+\beta)}{(1-\sqrt{4-d_2^2})(\theta_1-\pi/2)} < 1, \\ \frac{1}{d_2\sqrt{(\alpha+\beta)(e_z-\alpha)}}, & \frac{d_2^2/2+2(e_z-\alpha)/(\alpha+\beta)}{(1-\sqrt{4-d_2^2})(\theta_1-\pi/2)} > 1 \quad \text{and } e_z < \alpha, \\ 0, & \text{else} \end{cases} \quad (\text{B6})$$

for the distribution of  $e_z$ .

- [1] R. A. Bagnold, *The Physics of Blown Sand and Desert Dunes* (Methuen, London, 1941).  
 [2] B. Willetts and M. Rice, *Acta Mech.* **63**, 255 (1986).  
 [3] B. B. Willetts and M. a. Rice, *Earth Surf. Process. Landforms* **14**, 719 (1989).

- [4] I. K. McEwan, B. B. Willetts, and M. A. Rice, *Sedimentology* **39**, 971 (1992).  
 [5] M. A. Rice, B. B. Willetts, and I. K. McEwan, *Sedimentology* **42**, 695 (1995).  
 [6] M. A. Rice, B. B. Willetts, and I. K. McEWAN, *Sedimentology* **43**, 21 (1996).

- [7] Z. Dong, X. Liu, F. Li, H. Wang, and A. Zhao, *Earth Surf. Process. Landforms* **27**, 641 (2002).
- [8] S. Mitha, M. Tran, B. Werner, and P. Haff, *Acta Mech.* **63**, 267 (1986).
- [9] L. Oger, M. Ammi, a. Valance, and D. Beladjine, *Eur. Phys. J. E* **17**, 467 (2005).
- [10] J. Crassous, D. Beladjine, and A. Valance, *Phys. Rev. Lett.* **99**, 248001 (2007).
- [11] D. Beladjine, M. Ammi, L. Oger, and A. Valance, *Phys. Rev. E* **75**, 061305 (2007).
- [12] L. Oger, M. Ammi, a. Valance, and D. Beladjine, *Comput. Math. Appl.* **55**, 132 (2008).
- [13] M. Ammi, L. Oger, D. Beladjine, and A. Valance, *Phys. Rev. E* **79**, 021305 (2009).
- [14] A. Valance and J. Crassous, *Eur. Phys. J. E* **30**, 43 (2009).
- [15] B. T. Werner and P. K. Haff, *Sedimentology* **35**, 189 (1988).
- [16] R. S. Anderson and P. K. Haff, *Science* **241**, 820 (1988).
- [17] R. S. Anderson and P. K. Haff, *Acta Mech.* **1 (Suppl.)**, 21 (1991).
- [18] F. Rioual, A. Valance, and D. Bideau, *Europhys. Lett.* **61**, 194 (2003).
- [19] F. Bourrier, F. Nicot, and F. Darve, *Granul. Matter* **10**, 415 (2008).
- [20] J. E. Ungar and P. K. Haff, *Sedimentology* **34**, 289 (1987).
- [21] H. Yizhaq, O. Isenberg, R. Wenkart, H. Tsoar, and A. Karnieli, *Isr. J. Earth Sci.* **57**, 149 (2009).
- [22] H. Yizhaq, I. Katra, O. Isenberg, and H. Tsoar, *Aeolian Res.* **6**, 1 (2012).
- [23] G. Qian, Z. Dong, Z. Zhang, W. Luo, and J. Lu, *Sedimentology* **59**, 1888 (2012).
- [24] T. D. Ho, P. Dupont, A. Ould El Moctar, and A. Valance, *Phys. Rev. E* **85**, 052301 (2012).
- [25] D. a. Rumpel, *Sedimentology* **32**, 267 (1985).
- [26] N. V. Brilliantov and T. Pöschel, *Kinetic Theory of Granular Gases* (Oxford University Press, Oxford, 2010).
- [27] J. M. Ellwood, P. D. Evans, and I. G. Wilson, *J. Sediment. Res.* **45**, 554 (1975).
- [28] L. Oger and A. Valance (unpublished).
- [29] C. Goldenberg and I. Goldhirsch, *Nature* **435**, 188 (2005).
- [30] J.-P. Bouchaud, [arXiv:cond-mat/0211196v2](https://arxiv.org/abs/cond-mat/0211196v2).
- [31] J.-P. Bouchaud, P. Claudin, D. Levine, and M. Otto, *Eur. Phys. J. E* **4**, 451 (2001).
- [32] J. Socolar, D. Schaeffer, and P. Claudin, *Eur. Phys. J. E* **7**, 353 (2002).
- [33] A. H. Clark, L. Kondic, and R. P. Behringer, *Phys. Rev. Lett.* **109**, 238302 (2012).
- [34] A. H. Clark, A. J. Petersen, L. Kondic, and R. P. Behringer, *Phys. Rev. Lett.* **114**, 144502 (2015).
- [35] A. H. Clark, L. Kondic, and R. P. Behringer, *Phys. Rev. E* **93**, 050901 (2016).
- [36] M. Schirber, *Physics* **5**, 137 (2012).
- [37] M. Müller and M. Wyart, *Annu. Rev. Condens. Matter Phys.* **6**, 177 (2015).
- [38] B. Andreotti, *J. Fluid Mech.* **510**, 47 (2004).
- [39] J. F. Kok and N. O. Renno, *J. Geophys. Res.* **114**, D17204 (2009).
- [40] R. Sullivan, R. Arvidson, I. F. Bell, R. Gellert, M. Golombek, R. Greeley, K. Herkenhoff, J. Johnson, S. Thompson, P. Whelley, and J. Wray, *J. Geophys. Res.* **113**, 2156 (2008).
- [41] J. F. Kok, E. J. R. Parteli, T. I. Michaels, and D. B. Karam, *Rep. Prog. Phys.* **75**, 106901 (2012).
- [42] J. Merrison, *Aeolian Res.* **4**, 1 (2012).
- [43] N. Thomas, H. Sierks, C. Barbieri, P. L. Lamy, R. Rodrigo, H. Rickman, D. Koschny, H. U. Keller, J. Agarwal, M. F. A'Hearn, F. Angrilli, A.-T. Auger, M. A. Barucci, J.-L. Bertaux, I. Bertini, S. Besse, D. Bodewits, G. Cremonese, V. Da Deppo, B. Davidsson, M. De Cecco, S. Debei, M. R. El-Maarry, F. Ferri, S. Fornasier, M. Fulle, L. Giacomini, O. Groussin, P. J. Gutierrez, C. Güttler, S. F. Hviid, W.-H. Ip, L. Jorda, J. Knollenberg, J.-R. Kramm, E. Kührt, M. Küppers, F. La Forgia, L. M. Lara, M. Lazzarin, J. J. L. Moreno, S. Magrin, S. Marchi, F. Marzari, M. Massironi, H. Michalik, R. Moissl, S. Mottola, G. Naletto, N. Oklay, M. Pajola, A. Pommerol, F. Preusker, L. Sabau, F. Scholten, C. Snodgrass, C. Tubiana, J.-B. Vincent, and K.-P. Wenzel, *Science* **347**, aaa0440 (2015).
- [44] K. R. Rasmussen, A. Valance, and J. Merrison, *Geomorphology* **244**, 74 (2015).





# Aeolian sand transport

This chapter focuses on the theoretical approaches to aeolian sand transport. It starts with a short discussion of the mesoscopic length scales that determine its physics. In Secs. 3.2–3.4, various modeling attempts are reviewed—from hydrodynamic mean-field approaches, over computer simulations that resolve the individual grains, to more recent models that aim at capturing the statistical nature of the transport process. Section 3.5 provides some supplementary information, mainly summarizing the text-book knowledge of the physics of aeolian transport. My own contributions to these attempts are attached at the end of this chapter.

## 3.1 Characteristic length scales

Aeolian sand transport is characterized by a hierarchy of emergent mesoscales. Clearly, the splash process, analyzed in the previous chapter, is an inherent grain-scale process, as it crucially depends on the collision geometry and the local packing structure of the bed grains. Yet, it was shown to give a robust universal mesostructure in the grain hopping. Namely, for monodisperse granulates of (mean) diameter  $a$ , one finds from theoretical estimates [140, 186] the typical ejection height to be on the order of  $10a$ , and only weakly dependent on the impact energy, in good agreement with experiments [136, 166, 167]. This ejection height can be taken as the characteristic height of a small surface layer, densely crowded with splashed grains. Due to their large number, they take up a significant part of the wind's momentum, thereby drastically reducing the wind speed in this lower region of the transport layer. This phenomenon was first observed by Bagnold, who found from his wind-tunnel measurements that the wind speed at a certain height  $z_f$  took nearly the same value, independent of the externally imposed wind strength (determined by, say, the fan frequency for the wind tunnel). Typical values of the height  $z_f$  of this focus, as Bagnold called it, are on the order of  $10a$  to  $40a$  [40, 191], indeed roughly coinciding with the mean hop height of the splashed bed grains. This height might thus be considered a first pertinent emerging mesoscopic length scale of the transport process. The average trajectory height of all moving grains is in fact on the very same order of magnitude as  $z_f$ , corresponding to an average trajectory length  $\langle l \rangle \approx 10z_f \approx 10^2 a$  [23, 52, 73, 191, 192], because the large population of the low-energy ejecta dominates this mean value. A comprehensive

statistical discussion [52] however reveals a somewhat richer picture, with longer trajectories being exponentially suppressed at a independent characteristic height  $H$  of the transport layer. The latter is again found to be weakly dependent on the wind strength, but with typical values on the order of  $H \approx 10^2 a$ , roughly corresponding to a grain trajectory of length on the order of  $L \approx (\sigma - 1)a$ , where the linear scaling in the buoyancy-reduced sand–air density ratio  $\sigma - 1 \approx 2 \cdot 10^3$  is expected from the drag–gravity force balance [52] (see Sec. 3.5.3, below). A more accurate characterization of the aeolian transport layer therefore involves two emergent mesoscales, the focus height and the overall characteristic height of the transport layer. The first arises from the splash geometry alone, as described in the previous section. The can be traced back to the finite lifetime of the hopping grains or to the limiting momentum balance between the driving wind and the driven sand grains.

As already announced in Sec. 1.1, yet another emergent mesoscale is responsible for the size selection in the ensuing structure formation: the saturation transients through which the system relaxes to stationary transport. The minimum size of a dune—which is actually a smooth heap—is determined by the so-called saturation length  $\ell_{\text{sat}}$ , which is the typical relaxation length of the transport process [83, 193] (see Sec. 4.1, for an explanation). It takes typical values on the order of a few meters. The saturation transients however crucially depend on the sand’s polydispersity: Compared to the long transients for the nearly monodisperse dune sand, the coarse grain fraction of a strongly polydisperse sand exhibits a much shorter saturation length, on the order of a few millimeters. The reason is that these big grains are transported by so-called “reptation” (or creep) that is driven by impacts of “saltating” (i.e., hopping) fine grains. Compared with normal sand dunes, the minimum size of megaripples that are made from poly-/bidisperse sand is thus strongly reduced by about two orders of magnitude (see Ref. [67], appended to the present chapter).

The central notion of saturation transients was originally introduced by Sauermann *et al.* [82]. These authors predicted  $\ell_{\text{sat}}$  to decay with increasing wind strength  $\tau$ , whereas later studies argued that it might either be independent [32, 194] of  $\tau$  or even grow monotonically [195, 196] in  $\tau$ . Based on coarse-grained computer simulations of the transport process, we were recently able to resolve the apparent conflict between these diverse proposals [52] (attached at the end of the present chapter). Our theory predicts  $\ell_{\text{sat}}$  to be almost constant and to follow the characteristic length of the grain trajectories for almost all wind strengths. Physically, mobile grains are abundant and their acceleration to the stationary speed limits the adaptation to an increase in wind strength (“drag regime”). Only for wind strengths  $\tau$  very close to the threshold value  $\tau_t$ , where the transport is increasingly limited by the number of splashed bed grains [82] (“impact regime”),  $\ell_{\text{sat}}$  indeed features a singularity of the form  $\ell_{\text{sat}} \propto 1/(\tau - \tau_t)$ . The divergence seems indeed to be confirmed in recent wind-tunnel experiments by Selmani *et al.* [197]. In their analysis, these authors split the saturation process into two subprocesses, representing the initial aerodynamic grain mobilization and the subsequent transport relaxation. The wind-strength dependence of the total saturation length, obtained as the sum of the response lengths associated with the two subprocesses, seems to be close to our prediction in Ref. [52]. Out in the field, the situation is more complicated, due to the pervasive turbulent wind-speed fluctuations. The “bare” saturation length is thus renormalized by the intermittent wind fluctuations. They smear out the singularity at  $\tau = \tau_t$  and bring the observed “dressed” saturation length close to the wind-dependent minimum dune length measured in the field [194]

The relation of the various length scales—the average hop length  $\langle l \rangle$ , the characteristic

trajectory length  $L$ , as obtained from the overall height of the aeolian transport layer, and the saturation length  $\ell_{\text{sat}}$ —to the only elementary scale, the grain size  $a$ , can be summarized as

$$\langle l \rangle \approx 10^2 a, \quad L \approx (\sigma - 1)a, \quad \ell_{\text{sat}} \approx Lf(\tau/\tau_t - 1). \quad (3.1)$$

In the last relation we introduced a scaling function  $f$  that depends on the ratio between the wind shear stress  $\tau$  and the threshold shear stress  $\tau_t$  needed to sustain the transport. It fulfills the asymptotic scaling relations  $f(x \ll 1) \sim 1/x$  and  $f(x \gg 1) \approx \text{const}$ .

Equation (3.1) illustrates that the transport process itself is characterized by a hierarchy of length scales extending over more than three orders of magnitude. This is the reason why the very process of the wind-blown grain hopping can dictate the size of such large objects like sand dunes. Any reliable model for aeolian sand transport has to account for this hierarchy. To what extent depends of course on the practical problems it should be applied to. Aeolian sand dunes, for instance, feature a strong scale separation between the emerging structure and the underlying grain-scale processes, whereas sand ripples and megaripples, with typical sizes comparable to the length of an average grain trajectory, are mesoscale structures that crucially depend on the mesoscale physics. Numerous field and laboratory studies and extensive grain-scale computer simulations performed over the last decades supply us with lots of high-resolution data that provide a great playground for developing and testing refined models that resolve the mesoscale structure of the transport process to various degrees. It thus comes as little surprise that many theoretical approaches to aeolian sand transport have been proposed in the literature, with an increasing tendency over the last recent years towards resolving more of its complex mesoscale structure. These models are concisely outlined and discussed in the standard text books and the recent review articles listed in Sec. 1.2 of Chap. 1; an extensive review, can, for example, be found in the book by Pye and Tsoar [42]. Here, I would like to briefly retrace the development over the past decades from the early mean-field approaches to the recent attempts that aim at the transport statistics.

## 3.2 Hydrodynamic mean-field approaches

Since the seemingly erratic grain hopping is a complex many-body problem, all analytical approaches to aeolian sand transport share some mean-field character, in the sense that they idealize the broad distribution by some manageable tamed ensemble [52, 91, 92, 195, 198–203] or, in the simplest, true mean-field case, by a single representative trajectory [40, 82, 204–210]. The idea to map the complex grain hopping onto one “characteristic path” of the saltating grains goes, once again, back to Bagnold [40], who estimated its shape assuming that the representative grain starts vertically from the sand bed and reaches a height given by the focus height that he observed from the wind-speed profiles. Combined with the shape of the measured wind profiles, he computed the length of this characteristic path. From the marked focus in these wind profiles, in turn, Bagnold already knew that the blown grains extract momentum from the air, which is partly dissipated during the bed collisions, but he had not yet the mathematical tools to explicitly account for such a feedback in a model. It took a few more years, till Kawamura [204] and Owen [205] translated Bagnold’s insights into comprehensive mathematical models for stationary and (in Kawamura’s case) transient aeolian sand transport. Using the concept of the representative trajectory together with the local (*i.e.*, height-dependent) grain–air momentum

balance, Owen was able to estimate the wind speed above and inside the transport layer. He therefor hypothesized that stationary transport requires the turbulent shear stress exerted on the bed grains to be pinned to the critical value at which these bed grains are mobilized by the wind, an assumption widely used in analytical transport models [82, 92, 211]. Indeed, recent numerical studies support this hypothesis at low-wind conditions, while the exact value of the air-borne shear stress slightly decreases with increasing wind strength, when the impact-driven splash becomes more and more efficient [57]. To obtain the shape of the representative trajectory from the equations of motion, Owen followed Bagnold and set the horizontal component of the initial velocity to zero and estimated its vertical component from a global (*i.e.*, height-integrated) grain–air energy balance. That the latter holds, is a consequence of the stationary-transport assumption that the excess energy gained by the average grain during one hop is completely lost to the bed during its rebound.

Later on, wind-tunnel studies revealed that the average saltating grain does not leave the bed vertically, but under an angle below  $90^\circ$ , suggesting that more elaborate transport models should somehow account for the complex splash process. Sørensen [199, 200] and Sauermann *et al.* [82] proposed particularly successful examples for such analytical models that resolve the grain scale physics using (semi-)empirical splash parametrizations. Besides the accurate agreement for the stationary transport properties, like the wind-dependent sand mass flux, these improved models, in particular the one by Sauermann *et al.*, also make predictions for the transient behavior, *i.e.*, the time- and space-dependent flux with its characteristic saturation time and length, introduced in Sec. 3.1, above. In fact, Sauermann *et al.*'s simple continuum model has provided very accurate and non-trivial predictions for various features of sand dunes, such as their non-universal shapes and their (dynamic) shape transition, their minimum size as a function of the atmospheric conditions, their growth and migration dynamics, etc. [43, 83–88, 120, 142, 193, 212] But these mean-field approaches do, of course, not provide any information about the heterogeneous nature of the transport layer, as reflected by the statistics of the hop-heights, hop-lengths, and velocities of the blown grains, which is the information needed to explain the structure formation on the very scale of the grain trajectories.

### 3.3 Grain-scale and coarse-grained computer simulations

Such limitations can be easily overcome in numerical approaches. Besides the broad distribution of trajectories they can resolve, they also allow for extended and more accurate descriptions of the grain–air interactions and the bed collisions. As computational approaches to the collision process are significantly challenged by its erratic nature, various attempts have been proposed to equip the transport models with a computationally cheap splash parametrization, either derived from theoretical arguments [65, 98] or taken from experiments [161, 210, 213] and computer simulations [66, 169]. For the latter, the simulation data for collisions of an impacting grain with a quiescent granular packing is fitted by a splash parametrization that is then used in the aeolian-transport simulations, thus (often) neglecting the influence of the wind drag on the splash process. Only rather recently, the available computer performance allowed for simulating the saltation process with grain-resolved impactor-bed collisions [24, 214], which revealed detailed insight into the formation of sand ripples [90], the influence of midair collisions on the transport rate [215], the transport transients [196], and the hysteresis for transport initiation and cessation [132]

and the related hydrodynamic and collisional bed grain mobilization [216]. However, such full-fledged discrete-element methods are still extremely time-consuming and thus not suitable to systematically test a broad range of model parameters. For this reason, coarse-grained numerical approaches that do not explicitly resolve the bed grains have been extensively used over the last decades to investigate the influence of electrostatic interactions [93], distributed sand-grain sizes [98, 131], (local) wind-speed fluctuations [98, 131], and varying wind strengths [129] on aeolian sand transport. They have further proven helpful in studying the transport layer's grain-scale structure [23, 217, 218] and stochastic character [203], its transient properties and dynamic fluctuations [219, 220], the difference between a rigid and an erodible sand bed [210], and how the grain paths depend on ambient conditions [141, 213, 221]. The latter provides a particularly relevant contribution to explain the wind-driven structure formation on extraterrestrial bodies, like Mars, Venus, Saturn's moon Titan (see, *e.g.*, Ref. [47, 48] and references given there), or, very recently, Jupiter's comet 67P/Churyumov-Gerasimenko [51].

### 3.4 Transport statistics

Besides the full-fledged grain-scale and the reduced coarse-grained computer simulations, recent analytical models have also aimed at going beyond the drastically reduced mean-field models. A particularly useful improvement into this direction rests on the insight we discussed in the previous chapter, namely that the splash process is comprised of two major sub-processes: the rebound of the impacting grain and ejection of bed grains caused by this impact. With this two-fold structure in mind, so-called two-species models have been developed to describe the transport statistics [91, 92, 199] and the structure formation on the grain scale [198, 222]. They divide the distribution of trajectories into two transport modes usually named saltation and reptation, which represent fast continuously rebounding grains and slow ejected bed grains, respectively. Although this classification was already introduced by Bagnold, the numerous numerical studies on the splash process and on aeolian transport (see, *e.g.*, [65, 66]) together with its application to aeolian sand ripples [89] made it very popular at the end of the 1980s and the early 1990s. At this time, Sørensen [199] made a first attempt to introduce the two populations into an analytically tractable transport model. As shown in Ref. [200] for a reduced single-trajectory version, its overall structure allows to accurately fit various wind-tunnel data for the sand transport rate, but to the cost of using three independent fit parameters instead of a sound parametrization of the splash process. A slightly different approach was proposed by Andreotti [91], who started from a full-fledged  $n$ -generations model to derive a reduced two-species framework, for which he took the wind-dependent characteristics (hop time and length) of the saltating grain fraction from the numerically solved full model. From these two contributions by Sørensen and Andreotti we found that an analytically tractable two-species formalism with a reduced number of physically meaningful fit parameters was still missing in the literature and we thus presented our own version [92], attached at the end of the present chapter. It further stands out from the earlier attempts due to its strong influence by the continuum saltation model by Sauermaun *et al.* [82], from which we borrowed the hydrodynamic approach to the transport physics. Combined with the recent empirical insights into the splash process, we were able to formulate a simple analytical and thus computationally cheap model that is, at the same time, in excellent agreement with various wind-tunnel data. Alternative approaches to overcome

the limitations of the mean-field approaches have been proposed by Jenkins *et al.* [201], who used kinetic gas theory to derive analytical expressions for various height-dependent transport quantities, and by Pähtz and coworkers [195, 211, 223], who traced the mesostructure back to model coefficients that relate various averages and correlations to each other, reminiscent of macroscopic hydrodynamic laws.

Notwithstanding this considerable progress, most of the mentioned approaches have focused on averaged quantities, while the investigation of the full distribution of trajectories in the transport layer was initiated only very recently. This goes along with the limited number of experimental data on the transport statistics. Based on their high-resolution data gained in wind-tunnel experiments, Ho *et al.* [186] showed that the velocity distribution of the hopping grains largely reflects the splash statistics. Taking up this insight, we used our splash model, introduced in the previous chapter, to develop a transport model that accounts for the full distribution of the grain trajectories [52] (attached at the end of the present chapter). It allows to derive various height-resolved mesoscale properties, like the sand mass concentration and flux, the grain and air velocity, the grain-velocity distributions, etc., which are in excellent agreement with coarse-grained computer simulations and field and wind-tunnel observations. On the basis of this model, we were able to reconcile the long-standing debate on the wind dependence of the saturation length  $\ell_{\text{sat}}$ , as outlined in Sec. 3.1.

## 3.5 The physics of aeolian sand transport

In the remainder of this chapter, I would like to briefly introduce some of the salient features of the physics of aeolian sediment transport. In most publications, they are assumed familiar to the reader, and everybody who wants to enter this field might hopefully benefit from the following short overview. The remarks on the theoretical description of the (atmospheric) wind, the discrimination between dust and sand, the various transport modes and threshold conditions for mono- and bidisperse sand transport are rather general and not restricted to the aeolian transport on Earth. Instead, connections will be drawn to the sediment transport under water and on extraterrestrial surfaces whenever possible.

### 3.5.1 The atmospheric turbulent boundary layer

Atmospheric wind is a turbulent boundary layer flow. It is characterized by a very large Reynolds number  $Re = Hu/\nu \gg 1$ , where  $H$  is the typical height of the boundary layer,  $u$  the characteristic wind speed, and  $\nu$  the kinematic viscosity of the flowing fluid, which is in our case air. For the order-of-magnitude estimates  $H \approx 1$  km,  $u \approx 1$  m/s,  $\nu \approx 10^{-5}$  m<sup>2</sup>/s, we find  $Re$  to be in the order  $10^8$  under atmospheric conditions (in a wind tunnel of height  $H = 1$  m, we get  $Re \approx 10^5$ ). On atmospheric scales, viscous effects are thus completely irrelevant for the space- and time dependent wind velocity  $\mathbf{u}(\mathbf{r}, t)$ . The usual starting point to estimate  $\mathbf{u}(\mathbf{r}, t)$  is then the purely turbulent Reynolds-averaged Navier-Stokes (RANS) equations

$$\partial_t \bar{\mathbf{u}} + (\bar{\mathbf{u}} \cdot \nabla) \bar{\mathbf{u}} = \frac{1}{\rho} (\nabla \cdot \boldsymbol{\tau} - \nabla p + \mathbf{f}), \quad (3.2)$$

for the time-averaged fluid velocity,

$$\bar{\mathbf{u}}(\mathbf{r}, t) = \frac{1}{T} \int_0^T d\tilde{t} \mathbf{u}(\mathbf{r}, t + \tilde{t}) \quad (3.3)$$

with some coarse-graining time interval  $T$ , for which the time derivative of the “slow variable”  $\bar{\mathbf{u}}$  in Eq. (3.2) is defined as the difference  $\partial_t \bar{\mathbf{u}}(\mathbf{r}, t) = [\mathbf{u}(\mathbf{r}, t + T) - \mathbf{u}(\mathbf{r}, t)]/T$ . The terms on the right hand side of Eq. (3.2) represent the total force exerted on a fluid parcel, where  $\rho$  is the fluid’s mass density,  $\boldsymbol{\tau} = -\rho \overline{\delta \mathbf{u} \delta \mathbf{u}}$  the Reynolds stress tensor arising from the velocity fluctuations  $\delta \mathbf{u} = \mathbf{u} - \bar{\mathbf{u}}$ ,  $p$  the pressure, and  $\mathbf{f}$  a body force.

We now consider a boundary layer flow in  $x$ -direction over a surface given by the plane  $z = 0$ . In the absence of external forces ( $\mathbf{f} = 0$ ) and under stationary ( $\partial_t = 0$ ), homogeneous ( $\partial_x = \partial_y = 0$ ) conditions, the RANS equations (3.2) reduce to  $d\tau_{xz}/dz = d\tau_{yz}/dz = 0$  and  $d\tau_{zz}/dz = dp/dz$ . As the wind-driven sand transport takes place in the thin surface layer, whose height is much smaller than the total height  $H$  of the system, but still large enough that viscous effects can be ignored, we can neglect the pressure’s  $z$ -dependence and get

$$d\tau/dz = 0 \quad \text{or} \quad \tau = \text{const.} \quad (3.4)$$

Combined with Prandtl’s mixing length closure

$$\tau_{xz} = \rho(\kappa z)^2 (du/dz)^2, \quad (3.5)$$

it yields the famous logarithmic law of the wall,

$$u(z) = \frac{u_*}{\kappa} \ln(z/z_0), \quad (3.6)$$

with  $\kappa \approx 0.4$  being the von Kármán constant and  $z_0$  the roughness length. For a quiescent sand bed of grains of diameter  $a$ ,  $z_0$  takes phenomenological values on the order of  $a/10$ . In Eq. (3.6), we introduced the shear velocity  $u_*$ , defined through

$$\tau_{xz} = \rho u_*^2. \quad (3.7)$$

It thus provides a direct measure for the strength of the turbulent fluctuations of the fluid velocity,  $u_* \approx |\overline{\delta \mathbf{u}}|$ . As a consequence of Eq. (3.4), the strength of the turbulent boundary flow is completely characterized by a single quantity, namely the value of  $\tau_{xy}$  or  $u_*$ .

In the literature, the wind strength is usually quantified in terms of  $u_*$ . To get an idea how its values are translated into the phenomenological wind force, Table 3.1 gathers values corresponding to the widely used Beaufort scale, together with the typical size of the grains that can be transported by such winds.

### 3.5.2 Intermittency

In Eq. (3.5) of the previous section, we introduced a mixing-length closure to the boundary layer problem. It rests on the assumption that the turbulent velocity field is self-similar, thus exhibiting no particular length scale over which the flow speed, say, increases as a function of the wall distance. Instead, one expects that the distance from the wall itself determines this characteristic

Wind force	Description	$u(10\text{ m})$ [km/h]	$u_*$ [m/s]	$a$ [ $\mu\text{m}$ ]	Specifications
0	Calm	0	0.00	—	Smoke rises vertically.
1	Light Air	1	0.01	—	Direction shown by smoke drift but not by wind vanes.
2	Light Breeze	6	0.05	—	Wind felt on face; leaves rustle; wind vane moved by wind.
3	Gentle Breeze	12	0.1	70	Leaves and small twigs in constant motion; light flags extended.
4	Moderate Breeze	20	0.17	130	Raises dust and loose paper; small branches moved.
5	Fresh Breeze	29	0.25	270	Small trees in leaf begin to sway; crested wavelets form on inland waters.
6	Strong Breeze	38	0.32	470	Large branches in motion; whistling heard in telegraph wires; umbrellas used with difficulty.
7	Near Gale	50	0.42	810	Whole trees in motion; inconvenience felt when walking against the wind.
8	Gale	62	0.52	1300	Twigs break off trees; generally impedes progress.
9	Strong Gale	75	0.64	1800	Slight structural damage (chimney pots and slates removed).
10	Storm	89	0.75	2600	Seldom experienced inland; trees uprooted; considerable structural damage
11	Violent Storm	103	0.87	3500	Very rarely experienced; accompanied by widespread damage.
12	Hurricane	118	1.00	4500	Devastation.

Table 3.1: Wind strengths categorized according to the Beaufort scale [224]. The wind force is defined via the wind velocity  $u(10\text{ m})$  at 10 m height; given is the minimum level of  $u(10\text{ m})$  for each wind force. For the corresponding value of the shear velocity  $u_*$ , computed from Eq. (3.6) with  $z_0 = 20\text{ }\mu\text{m}$ , sand of maximum grain size  $a$  can be transported, as predicted by the threshold estimate  $u_*^2 \approx 0.01(\sigma - 1)ga$  (see Sec. 3.5.5), with  $\sigma \approx 2.2 \cdot 10^3$  being the grain-air density ratio and  $g \approx 10\text{ m/s}^2$  the gravitational acceleration. (Specifications are taken from Ref. [224].)



length, given by  $\kappa z$  in Eq. (3.5), the underlying picture being that the local flow properties at height  $z$  are determined by eddies of size  $z$  (because they are of highest energy density compared to other eddies rolling over the wall). However, turbulence is in fact not self-similar at all scales, but intermittent [225], which means that the flow is characterized by alternating phases of gust-like activity and intermediate calm (stationary wind). While the wind speed fluctuates markedly over long times, a temporary calm leads to a completely flat wind-speed protocol on short times. This scale-dependent structure manifests the broken self-similarity of the flow field. The associated gust and waiting times are found to follow power-law statistics [226, 227]. This phenomenology is reminiscent of self-organized criticality [228], dressed with some minimum “detection” threshold [229]. The analogy describes the gust events as avalanches triggered by some permanent active driving, where the heterogeneous nature of the system determines the avalanches statistics. Further, intermittency yields nontrivial statistics for the velocity increments  $\delta u(\ell)$  over a distance  $\ell$  (or corresponding time intervals). They exhibit nonuniversal exponents of their moments that emanate from distributions with fat exponential (or stretched exponential) tails [230]. The shape of these distributions of  $\delta u(\ell)$  can be quantified in terms of so-called superstatistics [231], namely as a superposition of (infinitely many) normal distributions with variances that, in turn, follow a log-normal distribution [232, 233]. For large  $\ell$ , comparable to the system size, the intermittent features vanish and the statistics becomes ultimately Gaussian [234]. Assuming that the lateral components  $u_x$  and  $u_y$  of the wind velocity are normally distributed, their absolute value  $w \equiv (u_x^2 + u_y^2)^{1/2}$  then follows a Rayleigh distribution, which is a special form of the Weibull distribution

$$P(w) = (k/\mu)(w/\mu)^{k-1}e^{-(w/\mu)^k}, \quad (3.8)$$

namely for the shape parameter  $k = 2$  [235]. Long-term wind data are thus often fitted to a Weibull distribution, where typical values for  $k$  range from 1.2 to 2, but can become as large as 8.7 [234, 236].

Intermittency, and the turbulent wind-speed statistics in general, has a direct impact on the transport statistics and, thus, also on the structure formation in the field [57, 70] (see Sec. 1.2). It becomes particularly notable in the vicinity of the threshold wind strength of grain motion discussed in the following.

### 3.5.3 Forces on wind-blown grains

Apart from the microscopic details of the splash, which depend on the material properties of the colliding grains, the transport physics is dominated by gravity and the turbulent drag between the fluid (in our case, air) and the grains. In general, the drag force  $F_D$  on a spherical grain of diameter  $a$  immersed in a fluid of density  $\rho$  and kinematic viscosity  $\nu$ , is related to the relative fluid–grain velocity  $\Delta \mathbf{v} = \mathbf{u} - \mathbf{v}$  as

$$F_D(\Delta \mathbf{v}) = \frac{1}{2}\rho C_D(Re)\frac{\pi}{4}a^2|\Delta \mathbf{v}|\Delta \mathbf{v}. \quad (3.9)$$

Viscous contributions enter via the drag coefficient  $C_D(Re)$  that depends on the (grain-scale) Reynolds number  $Re = |\Delta \mathbf{v}|a/\nu$ . It obeys the two asymptotic scaling relations

$$C_D(Re) \sim \begin{cases} Re_c/Re & (Re \ll Re_c) \\ C_D^\infty = \text{const.}, & (Re \gg Re_c) \end{cases} \quad (3.10)$$

Reference	$\alpha$	$\varphi$
Dallavalle [238]	1	0
Cheng 1997 [239]	3/2	0
Ferguson & Church 2004 [240]	2	0
Jiménez & Madsen 2003 [241]	2	1/2

Table 3.2: Literature values for the parameters  $\alpha$  and  $\varphi$  of the phenomenological drag coefficient in Eq. (3.12).

where  $Re_c = 24$  denotes the critical Reynolds number above which a region of closed streamlines forms behind a sphere [237]. As  $Re$  increases, the scaling of  $F_D$  in  $\Delta\mathbf{v}$  thus changes from linear, for purely viscous Stokes friction ( $Re \ll Re_c$ ), to quadratic, for purely turbulent Newton friction ( $Re \gg Re_c$ ). Balancing the gravitational force  $(\pi/6)(\rho_g - \rho)ga^3$  on a grain of density  $\rho_g$  with the drag given in Eq. (3.9) for a quiescent fluid ( $\mathbf{u} = 0$ ), yields the settling velocity

$$v_\infty = \sqrt{\frac{4(\sigma - 1)ga}{3C_D(Re)}} \sim \begin{cases} (\sigma - 1)ga^2/(18\nu) & (Re \ll Re_c) \\ \sqrt{(\sigma - 1)ga}, & (Re \gg Re_c) \end{cases} \quad (3.11)$$

where we inserted the asymptotic relations from Eq. (3.10) with  $Re_c = 24$  and used the empirical observation  $3C_D^\infty/4 \approx 1$ .

With the typical order-of-magnitude estimates  $|\Delta\mathbf{v}| \approx |\mathbf{u}| \approx 1$  m/s for the wind speed,  $a \approx 10^{-4}$  m for sand, and  $\nu \approx 10^{-5}$  m<sup>2</sup>/s for air, we obtain  $Re \approx 10$ , which is on the order of  $Re_c$ . We thus have to resort to a phenomenological law for  $C_D(Re)$  that interpolates between the two limits in Eq. (3.10). Various such attempts can be found in the literature, many of them of the common form

$$C_D(Re) = \left[ (1 - \varphi)^{1/\alpha} (C_D^\infty)^{1/\alpha} + (\varphi C_D^\infty + Re_c/Re)^{1/\alpha} \right]^\alpha. \quad (3.12)$$

The values for the exponent  $\alpha$  and the coefficient  $\varphi \in [0, 1]$  used in models for aeolian sand transport are usually taken from one of the references listed in Table 3.2. Phenomenological corrections due to the irregular shape of the sand grains are also incorporated in  $C_D$ . While the general drag relations that follow from Eq. (3.12) can be easily used in numerically solved models, analytical approaches and estimates often use the purely viscous linear [200, 204, 205] or turbulent quadratic [82, 92, 209] velocity–drag relation.

As already noted in Chap. 1, electrostatic interactions [57, 77, 111, 112] may have a significant impact on the wind-blown transport, in particular for fine dust grains [57, 71], while the other secondary hydrodynamic forces, like Archimedes, added-mass, Basset, Magnus, Saffman, are much smaller and often neglected in transport models [70]. The Archimedes force is the total force exerted by the fluid (*i.e.*, the air) on a grain if it were of the same density as the fluid. For a resting fluid, it reduces to the buoyancy force, and in this form it is taken into account in most transport models. The added-mass force originates from the acceleration of the fluid around a moving particle (in contrast to drag force that assumes a stationary flow), the Basset force accounts for a lagging response between the change of the particle velocity and the change of the drag (*i.e.*, a non-trivial memory kernel), the Magnus force describes the influence of the grain spin, and the Saffman force the lift due to a velocity gradient. With magnitudes on the order of 1% [57], only the Magnus force seems to play a role for the shape of some trajectories [242, 243].

### 3.5.4 Transport modes

Depending on the grain size, sediment is transported by typical atmospheric winds in terms of three transport modes: suspension, saltation, and reptation. This classification goes back to Bagnold [40] (he used the notion creep instead of reptation) and is widely used in the literature. I here give a quick overview of the phenomenology of these regimes, before I outline the main physical mechanisms responsible for them, below.

**Suspension.** Once mobilized, fine dust grains of size below  $70\ \mu\text{m}$  go directly into suspension. For typical atmospheric conditions on Earth, one usually discriminates between long-term (several days) and short-term (several hours) suspension for grain sizes below  $20\ \mu\text{m}$  and in the range  $20$  to  $70\ \mu\text{m}$ , respectively [56].

**Saltation.** Medium sized sand grains in the size range from about  $70\ \mu\text{m}$  to a millimeter are efficiently transported by typical winds. This mode is called saltation, referring to the seemingly erratic grain hopping. The physics of this transport mode is crucially determined by the splash process, when the hopping grains collide with the bed. At stationary transport, the momentum transmitted from the wind onto the grains has to be balanced by the momentum loss during these dissipative collisions and ejected bed grains have to compensate for the loss of moving grains that are trapped in the bed.

**Reptation and the role of polydispersity.** As the grains get larger in size, sand becomes less and less susceptible to aeolian transport. Under typical atmospheric conditions on Earth, grains bigger than about one millimeter are hardly transported by saltation at all, because this requires petty strong winds (see Table 3.1). However, such big grains can nevertheless move downwind due to short intermittent gusts and/or by the help of impacting smaller grains.

### 3.5.5 The thresholds of grain motion

The physics responsible for the emergence of the observed transport modes can be best understood in terms of various thresholds of the grain motion. In the following, I first introduce some dimensionless quantities that are instrumental to the formulation of the relevant transport conditions. These are (i) the criterion for turbulent particle suspension, (ii) the fluid and (iii) impact thresholds for bed-grain mobilization, and (iv) the reptation threshold for bidisperse-sand transport.

Based on the two fundamental forces acting on the blown sand grains, fluid drag and gravity, we can describe our system using six physical quantities: the gravitational acceleration  $g$ , the diameter  $a$  and mass density  $\rho_g$  of the grains, and the mass density  $\rho$ , kinematic viscosity  $\nu$ , and shear stress  $\tau$  of the fluid. Since we have only three fundamental units (*e.g.*, mass, length, and time), we may select three quantities and construct three dimensionless ones. A common choice<sup>1</sup>

---

<sup>1</sup>Some authors [213] prefer to use the unit system  $a$ ,  $\rho_g$ , and  $(1 - \rho/\rho_g)g$ , emphasizing the properties of the grains, not the fluid. It yields some trivial, yet sometimes confusing, differences in the definitions of the drag coefficient and the particle Reynolds number. The latter, for examples, is then  $\sqrt{(1 - \rho/\rho_g)ga^3}/\nu$ , while the combination in Eq. (3.1) is interpreted as a Stokes number  $St = \sigma Re$ .

	Earth	Venus	Mars	Titan	Water
$g$ [kgm/s <sup>2</sup> ]	9.8	8.9	3.7	1.4	9.8
$\sigma$	$2.2 \cdot 10^3$	$4.5 \cdot 10^1$	$1.5 \cdot 10^5$	$1.9 \cdot 10^2$	2.7
$\nu$ [m <sup>2</sup> /s]	$1.5 \cdot 10^{-5}$	$2.5 \cdot 10^{-7}$	$6.5 \cdot 10^{-4}$	$1.2 \cdot 10^{-6}$	$10^{-6}$
$a_m$ [ $\mu\text{m}$ ]	75	75	120	330	95
$Re_g(a_m)$	6	50	1	80	4

Table 3.3: Properties of planetary environments. Typical values for the gravitational acceleration  $g$ , the fluid–grain density ratio  $\sigma$ , the atmosphere’s kinematic viscosity  $\nu$  on Earth, Venus, Mars, and Titan taken from Ref. [78] and under water from Ref. [85]. The optimum grain size  $a_m$  and particle Reynolds number  $Re_g(a_m)$  of sand that is most easily mobilized by a turbulent flow is estimated from Eqs. (3.16), with the reference value  $a_m = 75 \mu\text{m}$  for sand on Earth, and (3.13), respectively.

is to use  $a$ ,  $\rho$ , and  $g$  as units, and to introduce the grain–air mass density ratio  $\sigma$ , the particle Reynolds number  $Re_g$  (sometimes, also called Galileo number  $Ga$ ) and the Shields number  $S$ :

$$\sigma = \rho_g/\rho, \quad Re_g = \sqrt{(\sigma - 1)ga^3}/\nu, \quad S = \frac{\tau}{(\rho_g - \rho)ga} = \frac{u_*^2}{(\sigma - 1)ga}, \quad (3.13)$$

where we used Eq. (3.7) to replace the shear stress  $\tau$  by the shear velocity  $u_*$  in the last relation. Note that  $(\sigma - 1)g$  is the buoyancy-reduced gravitational constant.

The value of  $Re_g$  provides an estimate that indicates whether the typical flow–grain interaction is of viscous or turbulent character. For a spherical particle, the onset of turbulence manifests itself in the closed streamlines that are formed behind the sphere, when the Reynolds number is on the order of the critical Reynolds number  $Re_c \approx 24$  [237]. Typical values of  $Re_g$  for aeolian sand transport on Earth, Venus, Mars, Titan, and for aqueous transport on Earth are listed in Table 3.3. They all fall into the intermediate regime, where  $Re_g$  is on the same order as  $Re_c$ , which means that both viscous and turbulent effects contribute to the fluid–grain interaction, as we already noticed below Eq. (3.10).

**Dust’s susceptibility to wind.** Dust is often defined through its grain size, namely smaller than  $70 \mu\text{m}$ . Physically, this limit refers to the fact that such fine grains are transported in suspension. Suspension requires the turbulent vertical velocity fluctuations of the wind to be larger than the grains’ settling velocity  $v_\infty$ , *i.e.*, the so-called Rouse number  $v_\infty/(\kappa u_*)$  has to be much smaller than unity [56]. Here,  $\kappa u_*$  is the strength of the Lagrangian vertical velocity fluctuations [244], with  $\kappa = 0.4$  the van Kármán constant, introduced in Sec. 3.5.1. Using Eq. (3.11) for the settling velocity and the asymptotic scaling in Eq. (3.10) for  $C_D(Re_g)$ , this criterion yields a suspension threshold

$$S_s = 4\kappa^2/[3C_D(Re_g)] \approx \kappa^2 Re_g/Re_c. \quad (Re_g \ll Re_c) \quad (3.14)$$

Here, some caution is in order: instead of a well-defined threshold,  $S_s$  rather marks a crossover region, as also reflected by the notions of long-term and short-term suspension. For values

of  $Re_g$  on the order of  $Re_c \approx 24$  and larger,  $S_s$  becomes so large that these grains are never suspended—they are not dust, but sand grains.

**Sand’s susceptibility to wind: the fluid threshold.** Besides the potential of being suspended in air, dust can equally well be defined by the wind’s ability to mobilize it from the ground, which makes its discrimination from sand more explicit. With a typical size of about  $100 \mu\text{m}$ , sand grains are very susceptible to being mobilized and transported by the wind—much larger granules and pebbles are simply too heavy, smaller dust particles are prone to cohesive inter-particle forces (e.g., van der Waals, Coulomb, capillary, and chemical binding forces [56]) and trapped in the viscous sublayer [85, 245]. To put this reasoning into a predictive quantitative model, various approaches have been proposed in the literature. They all share a similar starting point: the force balance between the fluid drag exerted on the bed grain, the weight of this grain, and some cohesive inter-particle forces. Following these lines, Iversen and coworkers [1, 246, 247] were the first to formulate a semi-empirical model, which, however, suffers from a number of ad-hoc assumptions and fudge expressions they introduced in order to match experimental data. Later on, Shao and Lu [248] proposed a much simpler formulation, for which they showed that it fits the data equally well. A physically well-founded—and therefore the most convincing—approach was brought up by Claudin and Andreotti [85], who allowed for both viscous and turbulent contributions to the drag and estimated the strength of the cohesive forces from a surface tension arising at the grain–grain contact area.

The minimum flow strength needed to mobilize the bed grains is quantified by the threshold (or critical) Shields number  $S_{\text{tf}}$ , with the subscript “tf” referring to the threshold of motion driven by the fluid. It corresponds to the threshold shear stress  $\tau_{\text{tf}}$  via Eq. (3.13). A often used heuristic and empirically motivated approximation the cohesive inter-particle forces to depend linearly [56] (or, based on a surface-tension argument, only slightly stronger [85]) on the grain size and to be independent of the ambient conditions, for which the force balance takes the form [85]

$$S_{\text{tf}}(Re_g, a/a_m) = S_{\text{tf}}^0(Re_g) \left( 1 + \frac{a_m^2}{3a^2} \right). \quad (3.15)$$

The first term  $S_{\text{tf}}^0(Re_g)$  on the right is the threshold Shields number in the absence of cohesive forces. It arises from the force balance between the turbulent drag and gravity of the pivoting bed grain—recall that the Shields number is defined as the ratio between drag and grain weight [245], Eq. (3.13). As both viscous and turbulent contributions to the total drag determine the numerical value of  $S_{\text{tf}}^0$ , it is a function of the Reynolds number  $Re_g$ , with the two asymptotic values  $S_{\text{tf}}^0(Re_g \ll Re_c) \approx 0.14$  and  $S_{\text{tf}}^0(Re_g \gg Re_c) \approx 0.04$  in the purely viscous and turbulent limits, respectively [70], and a weak minimum around  $Re_g \approx Re_c$  [245]. The bracketed term in Eq. (3.15) represents the cohesive inter-particle forces, where

$$a_m \propto 1/\sqrt{(\rho_g - \rho)g} \quad (3.16)$$

is the grain size, for which the threshold shear stress  $\tau_{\text{tf}} \equiv (\sigma - 1)gaS_{\text{tf}}$  attains a minimum. Grains of size  $a_m$  are thus most easily mobilized by the flow.

Inserting literature data for  $\rho_g$ ,  $\rho$ , and  $g$ , together with the empirically observed grain size  $a_m \approx 75 \mu\text{m}$  for sand on Earth [1, 85, 249], Eq. (3.16) yields values for  $a_m$  on Venus, Mars, Titan,

and for aqueous transport on Earth, which are listed in Table 3.3. From these numbers, we may conclude that typical aeolian sand on Mars and Titan is slightly coarser than on Earth. Indeed, images taken by exploration rovers show that typical grain sizes at the Martian surface vary between 90 and 300  $\mu\text{m}$  [85, 144] (for further references, see [57]). Recent experiments that simulate the threshold conditions on Titan in a high-pressure wind tunnel also suggest a relatively large value for  $a_m$  on the order of 200  $\mu\text{m}$  [249], yet a bit below our rough estimate in Table 3.3.

Note that the force-balance argument applied in Eq. (3.15) to estimate the conditions for bed grain mobilization is of inherent mean-field nature. In particular, only the average wind drag was considered. One might, however, wonder whether the intermittent turbulent fluctuations of the driving fluid (see Sec. 3.5.2) would alter the drawn picture of the mobilization process and thereby lead to significant quantitative corrections. Indeed, recent flume studies by Valyrakis and coworkers [250–253] showed that the strength and duration of the gust events, during which the drag force exceeds a critical value, determine the bed-grain dislodgement by a turbulent flow. These authors formulated criteria for the initiation of the grain movement in terms of the fluctuating drag force [250, 251] and the fluctuating flow power [253] integrated over the duration of a gust. This suggests that the grain mobilization is determined by the momentum (time-integrated force or “impulse”) or the energy (time-integrated power) that is transferred to the grain, instead of the average force (shear stress) exerted on it. As a consequence, the intermittent wind-strength fluctuations crucially determine the transport near the threshold conditions [114], making it itself intermittent [124, 131, 132, 254]. The gust-energy distribution, for instance, is then expected to exhibit power-law statistics, facilitating burst-like transport even when the mean wind strength is well below the mobilization threshold [132].

**Kicked bed grains: the impact threshold.** Besides the described direct aeoro-/hydrodynamic entrainment, bed grains can also be mobilized by the impacts of other hopping grains. This leads to the so-called impact or dynamic threshold. It corresponds to the wind strength that is needed to sustain the transport, as opposed to the above introduced fluid or static threshold, which characterizes the wind strength needed to initialize the transport. We quantify the wind strength at the impact threshold by the Shields number  $S_t$  (corresponding to the threshold shear stress  $\tau_t$ ), which is always below the fluid threshold<sup>2</sup>,  $S_t \leq S_{tf}$ . For thin atmospheres, like on Earth or Mars, the hopping grains efficiently transmit momentum from the fluid to the sand bed, whereby they concentrate it spatially around their impact location. This leads to a large local grain-borne shear stress (*i.e.*, a large momentum per area is transmitted to the bed grains). As a consequence, these impacts help to sustain the transport and there is a significant gap between the two threshold values  $S_t$  and  $S_{tf}$ . It yields a marked hysteresis of the transport around these threshold values, as thoroughly analyzed in recent wind-tunnel experiments [132], field measurements [255], and numerical simulations of coarse-grained transport models [256, 257]. For very dense atmospheres, where the drag dominates the grain’s inertial force, the momentum transport due to the grains is very inefficient and the direct fluid entrainment becomes more efficient than the grain collisions,  $S_t \approx S_{tf}$  [57, 85]. The hysteresis then diminishes.

<sup>2</sup>The opposite,  $S_t > S_{tf}$ , cannot hold, because, at the impact threshold  $S_t$ , the total stress acting on the bed grains comprises both fluid and grain contributions, so the impacting grains can only provide an additional effect. This is of course not the case if one compares the pure fluid entrainment with the mobilization due to grain impacts only, *i.e.*, without the fluid contribution, as done in Ref. [85].

The observed phenomenology can be rationalized as follows. The weight of the bed grains is effectively reduced by flow-induced lift and drag forces. At the fluid threshold ( $S = S_{\text{ff}}$ ), this reduced weight has to vanish, so the bed grains start to move. Following Bagnold (Chap. 7 of Ref. [40]), the force balance for a bed grain exposed to the shearing flow of strength  $S$  yields

$$\text{effective weight} \propto (\rho_{\text{g}} - \rho)ga^3(1 - S/S_{\text{ff}}). \quad (3.17)$$

It is this remaining weight (*viz.*, the corresponding potential energy) that prevents the bed grains from becoming mobile—and the grain impacts have to compensate for it in order to sustain the transport. As argued by Duran and Andreotti [70], the number of ejected grains per impact is constrained to a fixed value to sustain the transport at the impact threshold ( $S = S_{\text{t}}$ ). This number of ejected grains is proportional to

$$\frac{\text{impact energy}}{a \cdot (\text{effective weight})} \propto \frac{\sigma S}{1 - S/S_{\text{ff}}}. \quad (3.18)$$

Here, we plugged in Eq. (3.17) and used that the kinetic impact energy scales as  $\rho_{\text{p}}u^2$ , with  $u$  the typical wind speed, which, in turn, is proportional to the shear velocity,  $u \propto u_* \equiv \sqrt{S(\sigma - 1)ga}$ , according to Eq. (3.13). For  $S = S_{\text{t}}$ , the right hand side of Eq. (3.18), is equal to the constant scaled number  $n_{\text{t}}$  of ejected grains, which incorporates all suppressed factors of proportionality and the relative energy loss during the collisions. This yields [70]

$$S_{\text{t}} = \frac{S_{\text{ff}}}{1 + (\sigma/n_{\text{t}})S_{\text{ff}}} \sim \begin{cases} S_{\text{ff}} & (\sigma S_{\text{ff}} \ll n_{\text{t}}) \\ n_{\text{t}}/\sigma & (\sigma S_{\text{ff}} \gg n_{\text{t}}) \end{cases} \quad (3.19)$$

Empirically, one finds for aeolian transport on Earth  $S_{\text{ff}} \approx 0.01$  and  $S_{\text{ff}}/S_{\text{t}} \approx 1.5$  [57, 85], thus  $n_{\text{t}} \approx 40$ . For aqueous transport on Earth ( $\sigma \approx 2.6$ ) and aeolian transport on Venus ( $\sigma \approx 40$ ) we thus expect the fluid and impact threshold to essentially coincide, whereas aeolian transport on Earth ( $\sigma \approx 2.2 \cdot 10^3$ ) and Mars ( $\sigma \approx 2.2 \cdot 10^5$ ) is characterized by a marked hysteresis [216, 221]. The large wind-strength ratio between fluid and impact entrainment on Mars has been argued to be responsible for the numerous currently active aeolian features, from ripples over so-called TARs (transverse aeolian ridges) to large dunes that cover large parts of the Martian surface, despite the average wind is expected to be below the fluid threshold [115–118]. However, one should also note that both the sand's polydispersity and the pertinent wind fluctuations may lead to a non-zero sand transport even though the average wind is below the transport threshold of the average sand grain (see also Chap. 5). Such subthreshold conditions are moreover required to form megaripples from bidisperse sand, where the coarse-grain fraction is transported through reptation [67]. This regime is considered in the next paragraph.

**Bi- and polydisperse sand: the reptation threshold.** From the above discussion, we learned that the combination of grain weight and cohesive forces leads to a window of grain sizes that are susceptible to being mobilized by typical atmospheric winds. For bidisperse sand, this grain-size range can become significantly wider, because the bombardment of fine saltating grains can drive bigger bed grains into reptation. As in Eq. (3.18), we determine the minimal wind strength needed to eject a coarse bed grain of diameter  $a_{\text{c}}$  by a fine impactor of diameter  $a_{\text{f}}$  from the

energy balance

$$\frac{(\text{reduced mass}) \cdot (\text{fine-grain impact energy})}{a_c \cdot (\text{coarse-grain effective weight})} \propto \frac{(a_f/a_c)^7 \sigma S_{\text{ff}} \tau / \tau_{\text{ff}}^f}{1 - \tau / \tau_{\text{ff}}^c}, \quad (a_f \ll a_c) \quad (3.20)$$

which is pinned to a constant numerical value, reflecting the relative energy loss during the splash. The reduced mass on the left hand side accounts for the momentum and energy balance for collisions of two grains of unequal size; for  $a_f \ll a_c$ , it reduces to  $(a_f/a_c)^3$ , inserted here. Instead of the Shields number  $S$ , we expressed the wind strength in terms of the shear stress  $\tau$ , because the unit  $(\rho_g - \rho)ga$  underlying the definition of  $S$  depends on a particular choice of the grain size  $a$ , which would make the formulas for polydisperse sand unnecessarily complicated. We also introduced the threshold stress values  $\tau_{\text{ff}}^f$ ,  $\tau_{\text{ff}}^c$  for the fine and coarse grain fraction, respectively. Denoting the constant value of Eq. (3.20) at the coarse grains' reptation threshold  $\tau = \tau_r^c$  by  $n_r$  and using  $\tau_{\text{ff}}^f = (a_f/a_c)\tau_{\text{ff}}^c$ , we obtain

$$\tau_r^c = \frac{\tau_{\text{ff}}^c}{1 + (a_f/a_c)^6 (\sigma/n_r) S_{\text{ff}}}. \quad (3.21)$$

Note that  $n_t$ , introduced in Eq. (3.19), represents the number of splashed bed grains needed to sustain the stationary saltation transport, whereas the value of  $n_r$  is not bounded by such a constraint. The coarse reptating grains do not contribute to the maintenance of the saltation process, so we expect  $n_r \ll n_t$ . As a consequence, there exists a distinguished reptation regime,  $\tau_r^c < \tau_{\text{ff}}^c$ , where the fine-grain bombardment drives the big-grain movement. Figure 3.1a shows this wind-strength regime as a function of the grain-size ratio  $a_f/a_c$ .

Equation (3.21) is only valid for bidisperse sand, *i.e.*, for two distinct grain sizes. Natural sand is however polydisperse, characterized by a continuum distribution. This means that the size of the saltating fine grains  $a_f$  is determined by the actual wind strength  $\tau$ , namely as the size of the biggest grains transported in terms of saltation, *i.e.*,  $\tau_t^f = \tau$  or

$$a_f/a_c = \tau / \tau_t^c. \quad (3.22)$$

Combining Eq. (3.21) and (3.22), we can draw the following conclusion: for a given wind strength  $\tau$ , grains of maximum size  $a_f$  are transported by saltation, coarser ones reptate, whereby the maximum size of the latter is determined by Eq. (3.21) with  $\tau_r^c = \tau$ , yielding  $a_f/a_c = \text{const}$ . The size range of such reptating grains is illustrated in Fig. 3.1b.

When comparing this prediction with field data, one should keep the following complication in mind. Since the saturation length and the associated saturation time increase with the grain size, the intermittent turbulent wind gusts might be too short to transport big grains efficiently, even though the average wind strength might exceed their threshold value  $\tau_t^c$ . Instead of performing high jumps, these big grains will be transported by reptation, during the short gusts. In the field, the grain-size range of the reptating coarse-grain fraction can thus be significantly broader than estimated in Fig. 3.1. Very recently, Martin and Kok [105] reported a similar effect for grain-size-resolved field measurements. They observed that even very coarse grains (up to about 0.6 . . . 1.0 mm, almost insensitive to the prevailing average wind strength) were transported, but with much shorter trajectories than observed for the fine grains. Indeed, they argued that a significant contribution to this trend comes from the longer response time and the fact that



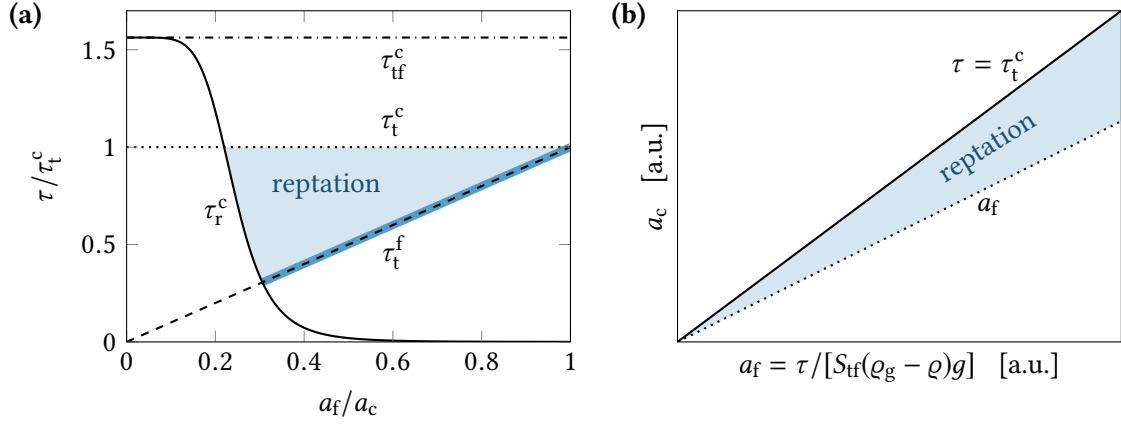


Figure 3.1: Sand polydispersity and the reptation transport. **(a)** For a given fine–coarse grain-size ratio  $a_f/a_c$ , the reptation regime (shaded area) extends over a range of wind strengths  $\tau$ . It is bounded by the saltation thresholds  $\tau_t^{f,c}$  of the fine and coarse grains (dashed and dotted lines, respectively) and the reptation threshold  $\tau_r^c$  of the coarse grains (solid line). Namely, fine grains saltate ( $\tau > \tau_t^f$ ), while coarse grains reptate ( $\tau_r^c < \tau < \tau_t^c$ ). The grain-size dependence of  $\tau_r^c$ , given in Eq. (3.21), is determined by the momentum and energy balance for a binary collision between a saltating fine grain and a coarse bed grain. With typical conditions for wind-blown sand in mind, we here used  $(\sigma/n_r)S_{ff} = 5000$ , in agreement with the estimate proposed in Ref. [67] (appended to Chap. 4). The upper bound of the window may be shifted from the impact threshold  $\tau_t^c$  towards the fluid threshold  $\tau_{ff}^c \approx 1.5\tau_t^c$  (dash-dotted line) when the coarse grains do not self-sustain their once initiated transport, meaning that they do not saltate despite  $\tau > \tau_t^c$ . **(b)** For a continuum grain-size distribution and a given wind strength  $\tau$ , the size  $a_f$  of the biggest saltating grains is determined by  $\tau_t^f = \tau$ . Bigger grains can be transporter by reptation (shaded area) if their reptation threshold is below the wind strength ( $\tau > \tau_r^c$ ). Via Eq. (3.13), this upper bound is given by  $a_c \propto a_f$ , with a numerical prefactor on the order of 2.1 . . . 3.9, as estimated in Ref. [67]. In panel **(a)**, the reptation regime for a continuum grain-size distribution collapses onto the dark thick line, as can be readily seen from  $a_f/a_c = \tau/\tau_t^c$ , which follows from  $\tau_t^f = \tau$  and, again, Eq. (3.13).

the “probability of promotion to saltator status decreases dramatically with increasing particle size”. A systematic theoretical investigation of this complicated interplay between the grain-size-dependent dynamic transport physics and the wind-speed fluctuations is still lacking, but seems to be a promising project for future studies.

## A two-species continuum model for aeolian sand transport

M Lämmel, D Rings and K Kroy<sup>1</sup>

Institute for Theoretical Physics—University of Leipzig, Postfach 100 920,  
04009 Leipzig, Germany

E-mail: [klaus.kroy@uni-leipzig.de](mailto:klaus.kroy@uni-leipzig.de)

*New Journal of Physics* **14** (2012) 093037 (24pp)

Received 15 May 2012

Published 20 September 2012

Online at <http://www.njp.org/>

doi:10.1088/1367-2630/14/9/093037

**Abstract.** Starting from the physics on the grain scale, we develop a simple continuum description of aeolian sand transport. Beyond popular mean-field models, but without sacrificing their computational efficiency, it accounts for both dominant grain populations, hopping (or ‘saltating’) and creeping (or ‘reptating’) grains. The predicted stationary sand transport rate is in excellent agreement with wind tunnel experiments simulating wind conditions ranging from the onset of saltation to storms. Our closed set of equations thus provides an analytically tractable, numerically precise and computationally efficient starting point for applications addressing a wealth of phenomena from dune formation to dust emission.

<sup>1</sup> Author to whom any correspondence should be addressed.



Content from this work may be used under the terms of the [Creative Commons Attribution-NonCommercial-ShareAlike 3.0 licence](https://creativecommons.org/licenses/by-nc-sa/3.0/). Any further distribution of this work must maintain attribution to the author(s) and the title of the work, journal citation and DOI.

**Contents**

<b>1. Introduction</b>	<b>2</b>
<b>2. Basic notions of aeolian sand transport and the two-species parametrization</b>	<b>4</b>
<b>3. Implementing the two-species framework</b>	<b>8</b>
3.1. Sand density: two-species mass balance . . . . .	8
3.2. Wind velocity field: two-species turbulent closure . . . . .	9
3.3. Transport kinetics: two-species transport velocities . . . . .	11
3.4. Stationary sand flux: the two-species transport law . . . . .	12
<b>4. Discussion</b>	<b>12</b>
4.1. The two-species flux balance . . . . .	13
4.2. One-species limits . . . . .	13
4.3. Comparison with experiments . . . . .	15
<b>5. Conclusions</b>	<b>17</b>
<b>Acknowledgments</b>	<b>18</b>
<b>Appendix A. Solving the Prandtl turbulent closure</b>	<b>18</b>
<b>Appendix B. The two-species approach for the wind profile</b>	<b>18</b>
<b>Appendix C. Reptation velocity</b>	<b>20</b>
<b>Appendix D. The coefficients of the transport law</b>	<b>22</b>
<b>References</b>	<b>23</b>

**1. Introduction**

Wind-driven sand transport is the most noticeable process shaping the morphology of arid regions on the Earth, Mars and elsewhere. It is responsible for the spontaneous creation of a whole hierarchy of self-organized dynamic structures from ripples over isolated dunes to devastating fields of shifting sands. It also contributes considerably to dust proliferation, which is a major determinant of our global climate. There is thus an urgent need for mathematical models that can efficiently and accurately predict aeolian sand fluxes. However, the task is very much complicated by the complex turbulent flow of the driving medium (e.g. streaming air) and the erratic nature of the grain hopping it excites [1]. Yet, it is by now well understood that this hopping of grains accelerated by the wind has some characteristic structure [2]. Highly energetic ‘saltating’ grains make a dominant contribution to the overall mass transport. When impacting on the sand bed, they dissipate some of their energy in a complex process called splash, ejecting a cloud of ‘reptating’ grains [3, 4]. A snapshot of this splash would show a whole ensemble of trajectories corresponding to a distribution of jump lengths from short, over intermediate, to large hops. However, grain-scale studies and theoretical considerations have indicated that a reduced description in terms of only two idealized populations (sometimes called saltons and reptons) should indeed be able to provide a faithful parametrization of the complex aeolian sand transport process and the ensuing structure formation [2, 5]. A rule of thumb to say which grains in a real splash pertain to idealized population of saltating or reptating grains is whether or not their jump height exceeds a threshold of about a few grain diameters.

A drawback of the two-species description has been that it is still conceptually and computationally quite demanding. For reasons of simplicity and computational efficiency, many theoretical studies have therefore chosen to reduce the mathematical description even further, to mean-field-type ‘single-trajectory’ models [6]. This may be justified for certain purposes, e.g. for the mathematical modelling of aeolian sand dunes, which are orders of magnitude larger than the characteristic length scales involved in the saltation process and thus not expected to be very sensitive to the details on the grain scale. Their formation and migration is thought to predominantly depend on large-scale features of the wind field and of the saltation flux, chiefly the symmetry breaking of the turbulent flow over the dune and the delayed reaction of the sand transport to the wind [7]. Moreover, the reptating grains, although they are many, are generally thought to contribute less to the overall sand transport, because they have short trajectories and quickly get trapped in the bed again. Therefore, it seems admissible to concentrate on the saltating particles. On this basis, numerically efficient models for one effective grain species that can largely be identified with the saltating grain fraction have been constructed. The Sauermann model [8] is a popular and widely used example of such mean-field continuum models. One-species models have become a very successful means of gaining analytical insight into [9–14] and to conduct efficient large-scale numerical simulations of [15–19] the complex structure formation processes caused by aeolian transport. The reduction to a single representative trajectory makes the one-species models analytically tractable and computationally efficient. However, it is also responsible for some weaknesses concerning both the way in which the two species are subsumed into one [5] and how they feed back onto the wind [12]. These entail imperfections in the model predictions, most noticeably a systematic overestimation of the stationary flux at high wind speed (see figure 5). Therefore, the one-species models have been criticized for their lack of numerical accuracy and internal consistency [5, 20]. There is also a number of interesting phenomena that cannot be quantitatively modelled within a one-species model, because they specifically depend on one of the two species, or on their interaction, or because the two species are not merely conceptually but also physically different.

As three important representatives of such phenomena, we name dust emission from the desert, ripples and megaripples. Dust is created, exposed to the wind and emitted by aeolian sand transport, and saltating and reptating particles play quite different roles in these processes [1, 21]. For example, fragmentation processes might be driven by the bombardment of high-energy saltating grains [22], but not by the slower reptating grains. In contrast, the emission of dust hidden from the wind underneath the top layer of grains in a sand bed could arguably be linked to the absolute number of reptating grains dislodged from the bed. The reptating grain fraction and its sensitivity to the local slope of the sand bed are, moreover, held responsible for the spontaneous evolution of aeolian ripples [1, 2, 4, 23–29]. But the number of reptating particles depends on the strength of the splash caused by the saltating grains. This interdependence of the reptating and saltating species becomes even more transparent when the two species correspond to visibly different types of grains. This is the case for megaripples, which have wavelengths in the metre range and form on strongly polydisperse sand beds in a process accompanied by a pronounced grain sorting [30–32]. The mechanism underlying their formation and evolution is still not entirely understood, but it seems that the highly energetic bombardment of small saltating grains drives the creep of the larger grains armouring the ripple crests. The mentioned grain-sorting emerges due to the grain-size-dependent hop lengths.

The demand for more faithful descriptions of aeolian sand transport has recently spurred notable efforts to eliminate the deficiencies of the one-species models [11, 12, 33] or to develop a numerically efficient two-species model [5]. It also motivated the development of the model described in detail below, as we felt that the problem has not yet been cured at its root. In our opinion, many of the amendments proposed so far have targeted the symptoms rather than the disease by invoking some *ad hoc* assumptions. It was our aim to modify the sand transport equations from bottom-up, based on a careful analysis of the physics on the grain scale and including the feedback of the two dissimilar grain populations on the turbulent flow. In this way, we derived a conceptually simple, analytically tractable and numerically efficient two-species model with only two phenomenological fit parameters. They serve to parametrize the complicated splash process and take very reasonable values if the predicted flux law is fitted to measured data. Compared with the time when the first continuum sand transport models were formulated, we could build on more detailed experimental and theoretical knowledge of the grain-scale physics [5, 34–39] and rely on more comprehensive empirical information about the wind shear stress and sand transport to test our predictions [40–43].

The plan of the paper is as follows. We first summarize some of the pertinent basic notions of turbulent flows and aeolian sand transport and introduce the two-species formalism. Then we implement the two-species physics on the level of the sand flux in section 3.1 and on the level of the turbulent closure for the wind in section 3.2. In sections 3.3 and 3.4, we address the most interesting observables, namely the speed and the average number of hopping grains, and the saturated sand flux. We finally compare our results with other models and experiments in section 4, before concluding in section 5.

## 2. Basic notions of aeolian sand transport and the two-species parametrization

Our analysis of the two-phase flow of air and sand is similar, in spirit, to the Sauermann model [8]. The Sauermann model is a continuum or hydrodynamic model. Rather than with the positions and velocities of individual grains it deals with spatio-temporal fields of these quantities, namely the local mass density  $\varrho(\vec{x}, t)$  and sand transport velocity  $\vec{v}(\vec{x}, t)$ . It is of mean-field type since it reduces both fields to the mean quantities  $\rho(x, t)$ ,  $v(x, t)$  for a single representative trajectory, characterizing the conditions along the wind direction (the  $x$ -direction), with the distribution of airborne grains in the vertical direction (the  $z$ -direction) integrated out. Note that  $\rho$  therefore is an area density, obtained by integrating the volume density  $\varrho$  over  $z$ . (The vertical grain distribution is a crucial element of the modified turbulent closure, however, which accounts for the feedback of the sand onto the wind.) In this paper, we deal exclusively with the saturated sand flux, i.e. the sand flux along the wind direction over a flat sand bed and under stationary wind conditions. What we call the flux  $q = \rho v$  is actually a vertically integrated flux, or a sand transport rate [8]. The central aim is to derive a constitutive relation  $q(\tau)$ , giving the stationary flux at a given shear stress  $\tau$ .

In the following, the strong mean-field approximation of the one-species models is somewhat relaxed, and reptating, and saltating particles with densities  $\rho^{\text{rep}}$ ,  $\rho^{\text{sal}}$  and transport velocities  $v^{\text{rep}}$ ,  $v^{\text{sal}}$  are treated separately. The flux is split up accordingly

$$q = q^{\text{rep}} + q^{\text{sal}} = \rho^{\text{sal}} v^{\text{sal}} + \rho^{\text{rep}} v^{\text{rep}}. \quad (1)$$

Introducing the dimensionless mass fraction  $\varphi \in [0, 1]$  of saltating grains relative to the total number of mobile grains, the (integrated) densities of the mobile grains can be written in the

form

$$\rho^{\text{sal}} = \varphi\rho \quad \text{and} \quad \rho^{\text{rep}} = (1 - \varphi)\rho. \quad (2)$$

Accordingly, the flux balance and the relative contribution of reptating and saltating grains to the flux read as

$$q = \rho v = \rho [\varphi v^{\text{sal}} + (1 - \varphi)v^{\text{rep}}] \quad \text{and} \quad q^{\text{rep}}/q^{\text{sal}} = (\varphi^{-1} - 1)v^{\text{rep}}/v^{\text{sal}}. \quad (3)$$

The fluxes depend on the wind velocity field, which, in turn, depends on the grain–wind feedback. To make progress in this respect, the (steady) shear stress  $\tau$  in the saltation layer is split into two components carried by the airborne grains ('g') and the air ('a') itself, respectively,

$$\tau = \tau_{\text{g}}(z) + \tau_{\text{a}}(z) = \text{const}. \quad (4)$$

This idea, introduced by Owen [44], which amounts to an effective two-fluid representation of the wind and the airborne sand, was used in many analytical models [5, 8, 11, 45] and confirmed by numerical simulations [6, 37–39, 46]. In the two-species model, we moreover keep track of the two species of mobile grains in (4). Similar to the flux division introduced in (1), we further split the grain-borne shear stress

$$\tau_{\text{g}}(z) = \tau_{\text{g}}^{\text{rep}}(z) + \tau_{\text{g}}^{\text{sal}}(z). \quad (5)$$

Concerning the feedback of the grains on the wind, it turns out that the wind velocity profile  $u(z)$  is predominantly determined by the reptating grain fraction and thus by the functional form of  $\tau_{\text{g}}^{\text{rep}}(z)$ , while the number and trajectories of the saltating grains hardly affect the wind profile at all. Physically, this makes sense, since the saltating particles form a very disperse gas compared with the dense reptating layer. Also note that the reptating grains, which lose all their momentum upon impact, are responsible for the momentum loss of the flow field. The wind profile may thus be computed in a reduced one-species scheme, as explained in section 3.2 and appendix B.

Under steady conditions, a common simplifying assumption is that the airborne stress near the ground ( $z = 0$ ) can be identified with the threshold shear stress  $\tau_{\text{t}}$  required to mobilize grains from the ground [44],

$$\tau_{\text{a}}(0) \approx \tau_{\text{t}}. \quad (6)$$

If it were larger or smaller, an increasing or decreasing number of grains would be mobilized, respectively, resulting in an unsteady flow. This idea is indeed supported by empirical observations, which find that the number of ejected grains increases (almost linearly) with the impact speed, not their ejection velocity or jump height [34, 35, 47, 48]. The feedback of the grains on the wind thus essentially fixes the air shear stress at the ground (and, if  $\tau \approx \tau_{\text{t}}$ , also above) to the threshold value  $\tau_{\text{t}}$ . To be precise,  $\tau_{\text{t}}$  is called the impact threshold, to emphasize that it is easier to lift grains from the splash cloud than to lift completely immobile grains from the ground [1]. But, for the sake of simplicity, we do not bother to make this distinction here, nor do we speculate about possible small deviations of  $\tau_{\text{a}}(0)$  from  $\tau_{\text{t}}$  under steady conditions [12, 33]. Combining (4) and (6), we may express the shear stress contributed by the grains near the ground as

$$\tau_{\text{g}}(0) = \tau_{\text{g}}^{\text{rep}}(0) + \tau_{\text{g}}^{\text{sal}}(0) = \tau - \tau_{\text{t}}. \quad (7)$$

Both stress contributions are defined as the product of the vertical sand flux  $\phi^i$  and the horizontal velocity difference  $v^i - v_0^i$  upon impact,  $\tau_{\text{g}}^i(0) = (v^i - v_0^i)\phi^i$ . The vertical sand flux

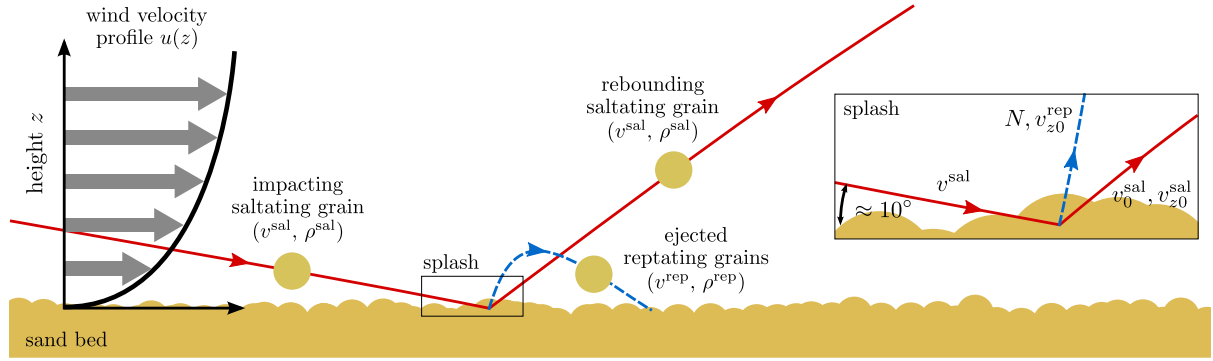


**Figure 1.** The two-species picture of aeolian sand transport maps the ensemble of mobile grains onto two representative species. High-energy (‘saltating’) grains accelerated by the wind (arrows in the wind-speed profile indicating the wind velocity) rebound upon impact and eject some low-energy (‘reptating’) grains in a splash. Sand transport is quantified in terms of the transport velocities,  $v^{\text{sal}}$  and  $v^{\text{rep}}$ , and mean densities,  $\rho^{\text{sal}}$  and  $\rho^{\text{rep}}$ , of the two species. The momentum balance of the splash process (inset, see section 3.1) is effectively encoded in the impact velocity  $v^{\text{sal}}$ , the horizontal and vertical rebound velocities of the saltating grain,  $v_0^{\text{sal}}$  and  $v_{z0}^{\text{sal}}$ , respectively, and the number  $N$  and velocity  $v_{z0}^{\text{rep}} = v_0^{\text{rep}}$  of the ejected reptating grains (neglecting a small horizontal velocity component, for simplicity).

$\phi^i$  is given by the horizontal (height integrated) flux  $q^i$  divided by the grains’ mean hop length,  $\phi^i \propto q^i = \rho^i v^i$ . Here,  $i$  represents the species indices ‘rep’ or ‘sal’. Following Sauermann *et al* [8], we assume parabolic grain trajectories with initial horizontal and vertical velocity components  $v_0^i$  and  $v_{z0}^i$ , respectively, and obtain

$$\phi^i = g\rho^i/(2v_{z0}^i), \quad \tau_g^i(0) = g\rho^i(v^i - v_0^i)/(2v_{z0}^i), \quad i = \text{rep, sal.} \quad (8)$$

Since the average ejection angle of the reptating particles is known to be about  $80^\circ$  [34],  $v_0^{\text{rep}} \approx 0$  and we identify the total ejection speed of the reptating grains with its vertical component  $v_{z0}^{\text{rep}}$ . The impact angle of saltating grains is known to be almost independent of the wind strength and to take typical mean values of about  $10^\circ$  [49], so that we can identify the total impact speed with the horizontal speed  $v^{\text{sal}}$  of the impacting particle, see figure 1.

In order to derive the sought-after constitutive equation, we have to understand the balance of the two species of mobile grains. If one considers the vertical fluxes  $\phi^{\text{sal}}$  and  $\phi^{\text{rep}}$  rather than the horizontal fluxes  $q^{\text{sal}}$  and  $q^{\text{rep}}$ , one has

$$\phi^{\text{rep}} = N\phi^{\text{sal}}, \quad (9)$$

with the average number  $N$  of reptating grains ejected by an impacting saltating grain. Together with the first relation in (8), we then have

$$\phi^{-1} = 1 + Nv_{z0}^{\text{rep}}/v_{z0}^{\text{sal}}. \quad (10)$$

Using also the second relation in (8) and remembering that we dismissed the horizontal component of the ejection velocity, we can thus write the overall density of mobile grains in



**Table 1.** Scaling functions  $f(U)$  for stationary aeolian sand transport relations of the form  $Q(U) = (1 - U^{-2})f(U)$ . Note that the coefficients of the various models cannot be identified even if represented by the same symbol. Explicit analytical expressions for the coefficients  $\alpha_0$ ,  $\beta_0$ ,  $\gamma_0$ ,  $a$  and  $b$  of the two-species model can be found in appendix D.

This work	$\frac{\alpha_0 U + \beta_0 - \gamma_0 U^{-1}}{aU - b}$
This work, one-species limit	$a - bU^{-1} \quad (b < 0)$
Sauermann <i>et al</i> [8]	$a\sqrt{1 + \alpha_0 U^{-2}} + bU^{-1}$
Sørensen [11]	$a + bU^{-1} + cU^{-2}$
Durán and Herrmann [12]	$a - bU^{-1} \quad (a, b < 0)$
Pächtz <i>et al</i> [33]	$-a + bU^{-1} + cU^{-2}$

the form

$$\rho = \frac{2Q_{\text{air}}}{g} \frac{u_*^2 - u_{*t}^2}{\varphi(v^{\text{sal}} - v_0^{\text{sal}})/v_{z0}^{\text{sal}} + (1 - \varphi)v^{\text{rep}}/v_{z0}^{\text{rep}}}. \quad (11)$$

As often found in the literature, we have employed the notion of the shear velocity or friction velocity  $u_*$ , defined by  $\tau \equiv Q_{\text{air}}u_*^2$ , as a more intuitive measure of the shear stress  $\tau$  here. The velocity ratios in the denominator of (11) are supposedly only very weakly dependent on the wind strength. The first one is recognized as an effective restitution coefficient

$$\alpha \equiv v_{z0}^{\text{sal}}/(v^{\text{sal}} - v_0^{\text{sal}}) \quad (12)$$

of the saltating grains [8]. Because of the complexity of the splash process, which makes first-principle quantitative estimates of  $\alpha$  forbiddingly complex, we suggest treating it as a phenomenological fit parameter. We do, however, provide a reasonable theoretical estimate of the ratio  $v^{\text{rep}}/v_{z0}^{\text{rep}}$ , based on the trajectory of a vertically ejected grain driven by the wind, in section 3.3 and appendix C. Anticipating the result  $v^{\text{rep}}/v_{z0}^{\text{rep}} = 0.7(\sigma v_{\text{air}}g)^{1/3}/u_{*t}$ , we can rewrite the density of the transported sand in the more explicit form

$$\rho = \frac{2Q_{\text{air}}}{g} \frac{u_*^2 - u_{*t}^2}{\varphi/\alpha + 0.7(1 - \varphi)(\sigma v_{\text{air}}g)^{1/3}/u_{*t}}. \quad (13)$$

Here  $\nu_{\text{air}}$  denotes the kinematic viscosity of air, and since the grain–air density ratio  $\sigma \gg 1$  under terrestrial conditions, we do not bother to distinguish between  $\sigma$  and  $\sigma - 1$  here and in the following. Note that on top of the explicit wind strength dependence of  $\rho$  via the numerator, there is an implicit, yet undetermined one via  $\varphi$ .

In the following, we develop the sought-after ‘second generation’ transport law  $q(u_*)$ , based on the grain-scale physics. Some empirical input is employed to fix certain phenomenological coefficients summarized in table D.1. Our result (see table 1) accounts for essential elements of the aeolian sand transport process beyond the single-trajectory approximation and turns out to be in remarkable agreement with wind tunnel measurements.



### 3. Implementing the two-species framework

The two-species framework is implemented in three steps. First, we deal with the mass balance between the species, then with their feedback onto the wind and their resulting transport velocities, before we finally arrive at an improved stationary transport law  $q(u_*)$ .

#### 3.1. Sand density: two-species mass balance

We first estimate the partition of the grain population into a saltating and a reptating fraction from several evident assumptions for the splash process, based on fundamental physical principles. In our formalism, a saltating grain always rebounds upon impact and ejects  $N$  reptating grains, while a certain fraction of its kinetic energy and momentum is dissipated in the sand bed. We further assume that every reptating grain performs only a single hop after which it remains trapped in the sand bed. These mild approximations for the stationary sand transport reduce the number of free parameters of our model compared with more elaborate descriptions [5].

As argued, e.g., by Kok and Renno [37], the relevant constraint limiting the number  $N$  of ejected grains per impact is given by the conservation of the grain-borne momentum rather than the energy. In writing the momentum balance, we make a physically plausible linear-response approximation, namely that all terms scale linearly in the velocity  $v^{\text{sal}}$  of the impacting grain. This amounts to assuming a wind-strength-independent scattering geometry, so that we can add  $z$ - and  $x$ -components up to constant geometric factors that are later absorbed in phenomenological coefficients. Including also the bed losses proportional to  $v_{\text{bed}}$  in this vein, we have

$$v^{\text{sal}} = v_0^{\text{sal}} + v_{z0}^{\text{sal}} + N v_{z0}^{\text{rep}} + v_{\text{bed}}. \quad (14)$$

For the first two terms on the right-hand side of (14), the proportionality to  $v^{\text{sal}}$  is already implicit in the definition (12) of the restitution coefficient  $\alpha$ . There is an important subtlety concerning the last two terms, however. Namely, the ejected grains have to gain enough momentum to jump over neighbouring grains in the bed in order to be counted as mobile grains. But they also should not themselves eject other grains upon impact; otherwise we would have to count them among the saltating fraction. Hence, the impact velocity  $v^{\text{rep}}$  and the ejection velocity  $v_{z0}^{\text{rep}}$  of the reptating grains are tightly constrained and cannot, by definition, be strongly dependent on the impact velocity of the saltating grain or the wind strength. Within experimental errors, observations of the collision process of saltating grains by Rice *et al* [49] are indeed in reasonable agreement with a constant  $v_{z0}^{\text{rep}}$  of the order of  $u_{*t}$ . In fact, they found the horizontal component of the ejection velocity to be independent of  $v^{\text{sal}}$ , and only a slight increase of the vertical component with  $v^{\text{sal}}$ . A compelling confirmation of this observation was recently obtained by better controlled laboratory experiments, in which PVC beads were injected at an impact angle of  $10^\circ$  onto a quiescent bed of such beads [34, 35]. There are two important consequences of the constraints on  $v_{z0}^{\text{rep}}$ . Firstly,  $N$  should grow linearly with  $v^{\text{sal}}$ . Secondly, since the momentum of the impacting grain is only partially transferred to the ejected grains, a critical impact velocity  $v^{\text{sal}} = v_c^{\text{sal}} \gg v_{z0}^{\text{rep}}$  has to be overcome to mobilize any grains at all. It can be interpreted as a constant offset in  $v_{\text{bed}}$ , which does not scale with  $v^{\text{sal}}$ . According to the collision experiments [34, 35], one can take  $v_c^{\text{sal}} \approx 40\sqrt{gd} \approx 9u_{*t}$ , where we used Bagnold's estimate  $u_{*t}^2 \approx 0.01\sigma gd$  [1]. A concise summary of the empirical input entering our model is provided in table D.1.

Summarizing the above discussion, we can rewrite the momentum balance (14) as

$$N v_{z0}^{\text{rep}} \propto v^{\text{sal}} - v_c^{\text{sal}}, \quad (15)$$

where  $v^{\text{sal}} > v_c^{\text{sal}}$  is tacitly assumed to hold throughout our discussion, and the omitted factor of proportionality should be insensitive to the wind strength. Observations of saltating grains [49], model collision experiments [34, 35, 47, 48], particle dynamics simulations [6, 50] and reduced numerical models, such as the binary collision scheme proposed by Valance and Crassous [36], all support this affine relation of the number of ejected grains, which is the cornerstone of our two-species mass balance. To fix the omitted factor in (15) and make contact with (10), we write

$$N v_{z0}^{\text{rep}} = (\eta/\alpha)(1 - v_c^{\text{sal}}/v^{\text{sal}})v_{z0}^{\text{sal}}. \quad (16)$$

The constant  $\eta$ , which serves as the second free fit parameter of our model, determines together with  $v_c^{\text{sal}}$  how the momentum lost by a rebounding grain is distributed between the bed and the ejected particles. (Details of the phenomenological values of  $\alpha$  and  $\eta$  obtained by fitting the complete model to the experimental flux data are given below.) Comparison with (10) now yields an explicit expression of the mass fraction

$$\varphi^{-1} = 1 + (1 - v_c^{\text{sal}}/v^{\text{sal}})\eta/\alpha \quad (17)$$

in terms of  $v^{\text{sal}}$  alone. Thereby, the problem of specifying the stationary mass balance between saltating and reptating grains has been completely reduced to the task of finding the stationary transport velocity  $v^{\text{sal}}$  of the saltating particles as a function of the wind strength.

### 3.2. Wind velocity field: two-species turbulent closure

Before we can work out the transport velocities of the two species of grains, we need to know the height-dependent wind speed  $u(z)$  and how it is affected by the presence of the airborne grains. Unfortunately, this leads us back to the question of the grain densities that we just delegated to the calculation of the grain velocities. In the past, an elaborate self-consistent calculation has been avoided by anticipating the resulting form of the wind profile on the basis of empirical observations. In the Sauermann model, for instance, an exponential vertical decay of the grain-borne shear stress is imposed,

$$\tau_g(z) = \tau_g(0) \exp(-z/z_m), \quad (18)$$

in good agreement with grain-scale simulations [6, 37, 38, 46]. Since the airborne stress  $\tau_a(z)$  follows from this via (4), it reduces the task to the problem of finding the mean saltation height  $z_m$ . In appendix B, we present a refined version of this approach, adapted to the two-species approach. It accounts for the contributions of the different species to the grain-borne shear stress, separately, and also for their considerably different trajectories. However, as we detail in the appendix, the whole exercise yields essentially identical results as (18), which can in fact be interpreted as the pre-averaged two-species expression. This lends further support to the general form of (18), recommending it as a suitable basis for our further discussion of the two-species model.

From (18), we obtain, via (4), the wind speed profile  $u(z)$  by integrating Prandtl's turbulence closure

$$\tau_a(z) = \varrho_{\text{air}} \kappa^2 z^2 [\partial_z u(z)]^2. \quad (19)$$

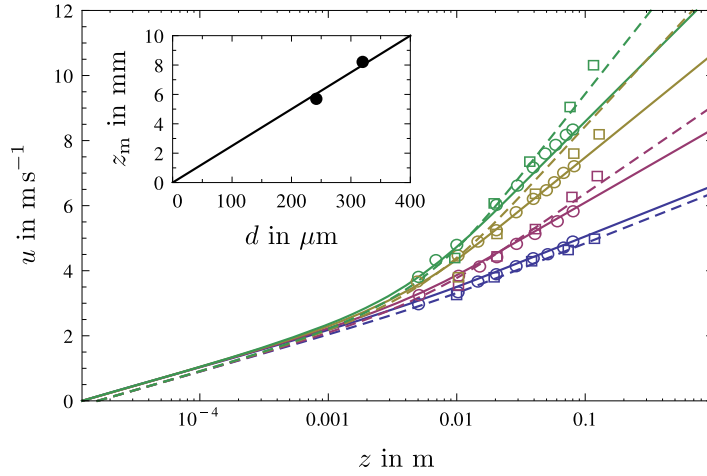


**Figure 2.** The wind speed  $u$  at height  $z$ . Theory, equation (21) (curves), compared with the measured data (symbols) for grains of diameter  $d = 242 \mu\text{m}$  (solid curves, circles) and  $d = 320 \mu\text{m}$  (dashed curves, boxes) and various shear velocities ( $u_* = 0.27, 0.39, 0.56, 0.69 \text{ m s}^{-1}$  and  $u_* = 0.27, 0.47, 0.74, 0.87 \text{ m s}^{-1}$  from bottom to top for  $d = 242 \mu\text{m}$  [42] and  $d = 320 \mu\text{m}$  [41], respectively); as global fit parameters we used the roughness length ( $z_0 = d/20$ ), the threshold shear velocity ( $u_{*t} = 0.19 \text{ m s}^{-1}, 0.20 \text{ m s}^{-1}$  for the finer/coarser sand) and the mean saltation height  $z_m$ , which is compared with (23) in the inset.

To proceed analytically, we use a modified secant approximation similar to what was proposed by Sørensen [11]. As shown in appendix A, the closure equation then becomes

$$\partial_z u \approx \frac{u_*}{\kappa z} \left[ 1 - (1 - u_{*t}/u_*) e^{-z/z_m} \right]. \quad (20)$$

Upon integration from the roughness length  $z_0 \ll z_m$ , defined by  $u(z_0) = 0$ , this yields the explicit result [11, 12]

$$u(z) = \frac{u_*}{\kappa} \ln(z/z_0) - \frac{u_* - u_{*t}}{\kappa} [E_1(z_0/z_m) - E_1(z/z_m)], \quad (21)$$

with the integral exponential  $E_1(z) \equiv \int_z^\infty dx e^{-x}/x$ . For small wind speeds  $u_* \rightarrow u_{*t}$  ( $u_* \geq u_{*t}$ ), the usual logarithmic velocity profile is recovered. Inside the saltation layer, a universal asymptotic wind velocity field

$$u(z) \sim \frac{u_{*t}}{\kappa} \ln(z/z_0) \quad (z_0 \lesssim z \ll z_m) \quad (22)$$

emerges, which is independent of the wind strength outside the saltation layer. This rationalizes the convergence of the wind profiles for different wind strengths, found in wind tunnel measurements, without the *ad hoc* assumption [12] of a debatable focal point [51], which resulted in the prediction of an unphysical negative flux  $q(u_*)$  at high wind speeds [12]. A direct comparison of our above prediction for  $u(z)$  with wind tunnel data from [41, 42] can be found in figure 2. From these data (available for two grain sizes  $d$ ) we determine the mean saltation height  $z_m$ . Past attempts to relate  $z_m$  to  $d$  invoked a new undetermined length scale

depending solely on atmospheric properties [52]. However, the results of our fit rather support the simpler (and more natural) linear relation

$$z_m \approx 25d \quad (23)$$

(right panel of figure 2). This is in line with recent analytical and numerical work [33], albeit possibly with a somewhat different numerical factor dependent on specific model assumptions.

### 3.3. Transport kinetics: two-species transport velocities

With the wind speed profile  $u(z)$  at hand, we can now determine the characteristic stationary transport velocity  $v^{\text{sal}}$  of the saltating sand fraction from a standard force-balance argument. We evaluate the wind speed at a characteristic height  $z^{\text{sal}}$ , at which the fluid drag on the grains is then balanced with the effective bed friction, in the usual way (for a detailed derivation and discussion, see [8, 12]). Namely, the drag force on a volume element of the saltation cloud (the force per mass acting on a single saltating grain times the density  $\rho^{\text{sal}}$  of the saltation cloud) is balanced with  $\tau_g^{\text{sal}}(0)$ . This yields the transport velocity of the saltating sand fraction

$$v^{\text{sal}} = u(z^{\text{sal}}) - v_\infty^{\text{sal}}, \quad (24)$$

with the estimate [12, 53]

$$v_\infty^{\text{sal}} \approx \frac{\sqrt{\sigma dg/\alpha}}{1.3 + 41 v_{\text{air}}/\sqrt{\sigma d^3 g/\alpha}} \quad (25)$$

for the terminal steady-state relative velocity  $u - v^{\text{sal}}$ . Formally,  $v_\infty^{\text{sal}}$  is equal to the settling velocity asymptotically reached by a grain freely falling in air (of kinematic viscosity  $\nu_{\text{air}}$  and with grain–air density ratio  $\sigma$ ), with a rescaled gravitational acceleration  $g \mapsto g/(2\alpha)$ .

We fix the  $u_*$ -independent parameter  $z^{\text{sal}}$  by the plausible assumption that the splash at the (impact) threshold wind speed  $u_{*t}$  dies out, corresponding to  $v^{\text{sal}}(u_* = u_{*t}) = v_c^{\text{sal}}$ . The underlying physical picture is that it is the splash that keeps the saltation process going, even below the aerodynamic entrainment threshold, because the reptating particles compensate for rebound failures [5]. Accordingly, using (24) with the logarithmic wind field, equation (22), we find that

$$z^{\text{sal}} = z_0 \exp\left(\kappa \frac{v_c^{\text{sal}} + v_\infty^{\text{sal}}}{u_{*t}}\right). \quad (26)$$

In appendix C, we use a similar argument to derive the mean reptation velocity, which turns out to be almost independent of the grain size  $d$ . It can thus be approximated by the constant

$$v^{\text{rep}} \approx 0.7(\sigma \nu_{\text{air}} g)^{1/3}, \quad (27)$$

for most practical purposes. This relation corresponds to a  $u_*$ -independent reptation length  $2v^{\text{rep}}v_{z_0}^{\text{rep}}/g = 0.14[\sigma^5 \nu_{\text{air}}^2 d^3/g]^{1/6}$  in the centimetre range, while the saltation length  $2v^{\text{sal}}v_{z_0}^{\text{sal}}/g \propto u_*^2/g$  is quadratic in the shear velocity  $u_*$  (see figure 3) and of the order of decimetres [1, 54, 55].

In figure 3, the transport velocities  $v^{\text{sal}}$  and  $v^{\text{rep}}$  for the two species and the mean velocity  $v = \varphi v^{\text{sal}} + (1 - \varphi)v^{\text{rep}}$  are plotted over the shear velocity  $u_*$ . An important result is that the species-averaged transport velocity  $v$  is nearly constant over a broad range of wind strengths. This is consistent with the fundamental assumption on which the model is based, namely that the number of mobilized grains is sensitive to the wind strength, but their overall transport kinetics is not.

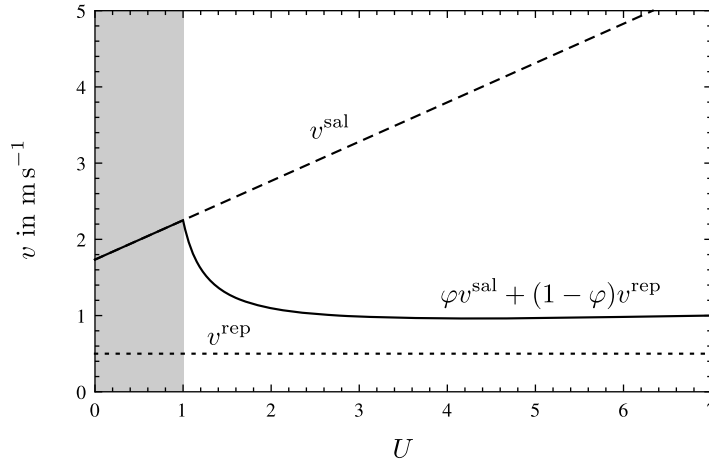


**Figure 3.** The transport velocities of the saltating (dashed) and reptating (dotted) sand fraction versus the rescaled shear velocity  $U \equiv u_*/u_{*t}$ , as predicted by (24) and (27), respectively. The solid line represents the average transport velocity in a reduced effective single-trajectory description.

### 3.4. Stationary sand flux: the two-species transport law

The stationary flux law is now obtained by collecting the above results for the saturated density  $\rho$  from (11), the saltation fraction  $\varphi$  from (10), the transport velocities (24) with the wind velocity (21), and inserting them into (3). We introduce reduced variables, measuring the shear velocity  $u_*$  in terms of the impact threshold  $u_{*t}$  and the saturated flux  $q$  in units of  $Q_{\text{air}}u_*^3/g$ ,

$$U \equiv u_*/u_{*t}, \quad Q \equiv qg/(Q_{\text{air}}u_*^3). \quad (28)$$

The result for our two-species stationary flux relation then takes the form

$$Q = (1 - U^{-2}) \frac{\alpha_0 U + \beta_0 - \gamma_0 U^{-1}}{aU - b}, \quad (29)$$

with the coefficients  $\alpha_0$ ,  $\beta_0$ ,  $\gamma_0$ ,  $a$  and  $b$  depending on the two free parameters  $\alpha$  and  $\eta$ , as summarized in appendix D. It goes without saying that this result pertains to  $U > 1$  and that  $Q(U < 1) \equiv 0$ . Except for  $b$ , which becomes negative for small  $\eta$ , and in particular for  $\eta = 0$ , all coefficients are positive. But since  $\gamma_0 < \alpha_0 + \beta_0$  and  $b < a$ , the flux always remains positive.

The positivity of the flux in (29) guarantees physically reasonable results, even under transient wind conditions, as occurring, for example, in sand dune simulations. The extension of the present discussion to non-stationary conditions is a major task for future investigations, in particular with regard to the saturation length, i.e. the characteristic length scale over which the system relaxes towards the steady state [8]. Its derivation within our two-species approach is of conceptual interest, since the wind strength dependence of the saturation length has recently been the subject of debates (see, e.g., [20]).

## 4. Discussion

Before we determine the free parameters  $\alpha$  and  $\eta$  by comparing (29) with experimental data, we first discuss the effect of our two-species parametrization on the two related transport

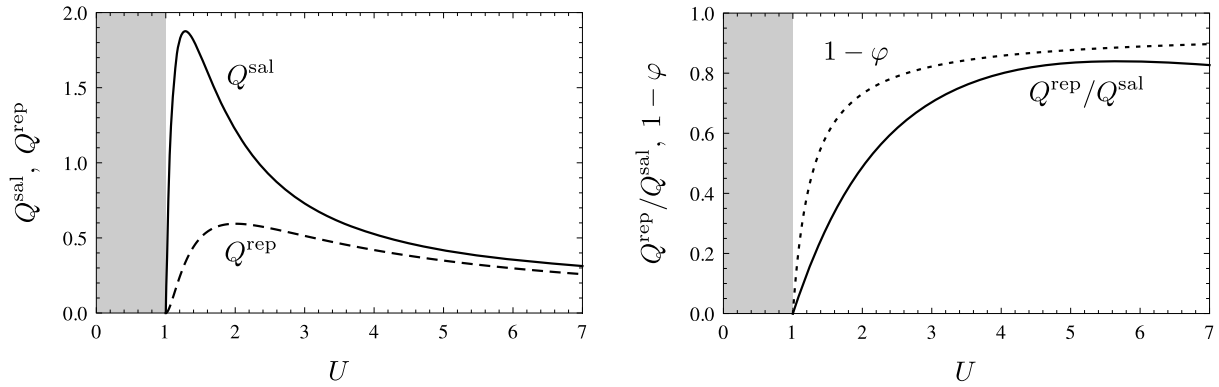


**Figure 4.** The rescaled fluxes  $Q^{\text{sal}} \equiv q^{\text{sal}} g / (\rho_{\text{air}} u_*^3)$  and  $Q^{\text{rep}} \equiv q^{\text{rep}} g / (\rho_{\text{air}} u_*^3)$  of the saltating and reptating grains, respectively, versus the rescaled shear velocity  $U \equiv u_* / u_{*t}$  (parameters:  $\alpha = 0.65$ ,  $\eta = 9$ , as determined in section 4.3; grain size  $d = 250 \mu\text{m}$ ). Left: direct comparison of  $Q^{\text{sal}}$  (solid line) and  $Q^{\text{rep}}$  (dashed line). Right: the flux ratio  $Q^{\text{rep}}/Q^{\text{sal}} = q^{\text{rep}}/q^{\text{sal}}$  (solid line) compared with the mass fraction  $1 - \varphi$  of reptating grains (dashed line).

modes—saltation and reptation—and present two different single trajectory reductions of the two-species model. Subsequently, we compare these reduced schemes to single-species transport laws that have previously been proposed in the literature.

#### 4.1. The two-species flux balance

Our derivation of the overall sand flux  $Q$ , given in (29), also yields the partial fluxes  $Q^{\text{sal}} \equiv q^{\text{sal}} g / (\rho_{\text{air}} u_*^3)$  and  $Q^{\text{rep}} \equiv q^{\text{rep}} g / (\rho_{\text{air}} u_*^3)$  of the saltating and reptating species, respectively. Their dependence on the wind velocity is illustrated in figure 4. It is frequently argued in the literature that the saltating grains dominate the sand transport, for they perform large jumps, while the reptating sand fraction might be negligible in terms of mass transport. Our model basically confirms this view for moderate winds, not too far above the impact threshold. However, it predicts that both species contribute almost equally to the total flux, under strong winds. The shift in the mass balance  $\varphi$  towards reptation (figure 4, right plot) reflects the dependence of the number of ejected grains on the wind strength, which follows from the splash-impact relation (15) if one inserts the transport velocities of the individual species, as given in figure 3. The variable contribution of the two species to the overall sand flux is a result that cannot be obtained from the conventional single-species models, but should be of interest for some of the more advanced applications mentioned in the introduction.

#### 4.2. One-species limits

It is interesting to see how the conventional one-species descriptions emerge from the two-species model upon contraction to a single effective grain species. This contraction is clearly not unique but may be performed in different ways. On the basis of the two-species flux balance, discussed in the preceding section, two natural contractions suggest themselves: one for moderate wind speeds where the flux is dominated by saltation, and one for strong winds,

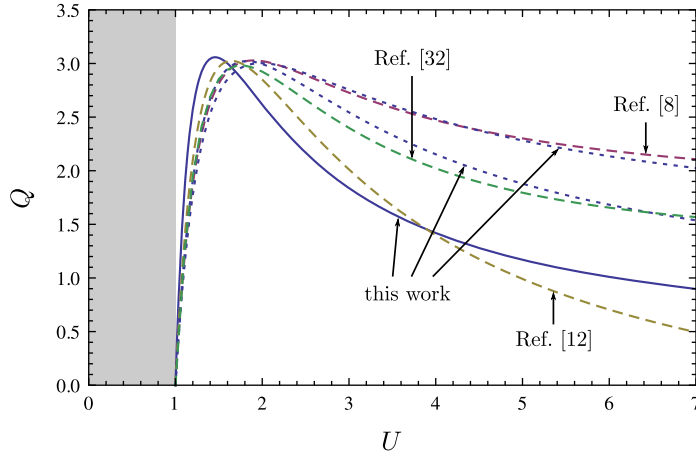


**Figure 5.** The stationary sand-flux laws. Predictions from the two-species model, equation (29) (solid line) with its natural one-species limits (30) and (31) (lower and upper dotted lines), are compared with transport laws from conventional one-species models: Sauermann *et al* [8] (upper dashed), Durán and Herrmann [12] (lower dashed) and Pächtz *et al* [33] (middle dashed). All curves have been obtained for a grain size of  $d = 250 \mu\text{m}$ . The values of the free parameters  $\alpha$  and  $\eta$  in (29) were determined by comparison with experiments as described in section 4.3. The predictions of the single-trajectory limits of the two-species model, (30) and (31), were adjusted by the parameter rescaling  $z^{\text{sal}} \rightarrow 0.18z^{\text{sal}}$  and  $\eta \rightarrow 0.138\eta$ .

where the ratio of the contributions from reptating and saltating grains was found to be roughly constant.

The first single trajectory reduction, where the reptating species is dismissed, is obtained by setting  $\varphi = 1$  or  $\eta = 0$ , which corresponds to the flux relation

$$Q = (1 - U^{-2})(a - b U^{-1}), \quad (30)$$

with a negative coefficient  $b < 0$  (appendix D). Since this equation accounts only for high-energy saltating grains, the resulting absolute flux is too large compared with the original two-species description. This can be corrected by reducing the effective trajectory height or, in our formalism, by rescaling the effective height  $z^{\text{sal}}$  at which the fluid drag is balanced with the effective bed friction. The lower dotted line in figure 5 was obtained in this way.

The second single trajectory reduction is motivated by the weak dependence of the mass fraction  $\varphi$  on  $u_*$  for strong winds  $u_* \gg u_{*t}$ , which suggests replacing  $\varphi$  by its  $u_*$ -independent limit  $1/(1 + \eta/\alpha)$ . This yields

$$Q = (1 - U^{-2})(\tilde{\alpha}_0 + \tilde{\beta}_0 U^{-1}), \quad (31)$$

with

$$\tilde{\alpha}_0 = \frac{\alpha_0}{a} \quad \text{and} \quad \tilde{\beta}_0 = \frac{\beta_0}{2a} + \frac{\tilde{\eta}}{1 + \tilde{\eta}} \frac{v_{z0}^{\text{rep}}}{u_{*t}}, \quad (32)$$

and the abbreviation  $\tilde{\eta} \equiv \eta v^{\text{rep}}/v_{z0}^{\text{rep}}$ . If one interprets the (now constant) species mass balance as a free phenomenological parameter, it may be adjusted by fine-tuning  $\eta$ , so that the absolute



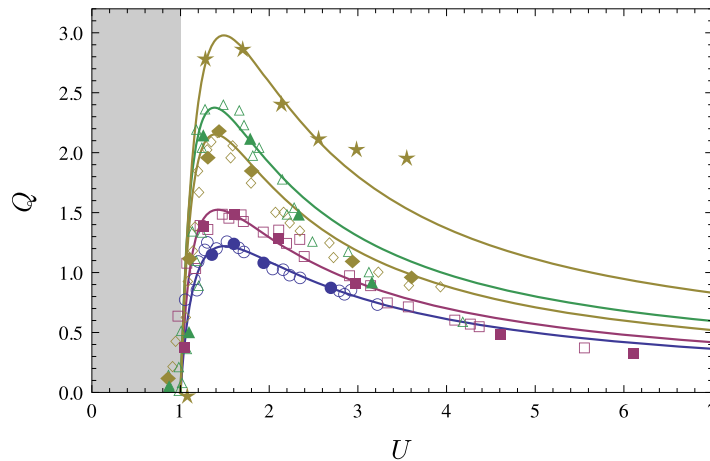


**Figure 6.** The rescaled saturated flux  $Q = qg/(\rho_{\text{air}}u_*^3)$  for various grain sizes ( $d = 125, 170, 242, 320$  and  $242 \mu\text{m}$  from bottom to top): data from wind tunnel measurements using particle tracking methods [43] (stars) and sand traps [40] (other symbols) are compared with the prediction by the two-species model, equation (29) (solid curves). The restitution coefficient  $\alpha$  served as a global but grain-size-dependent fit parameter (see figure 7), while  $\eta = 9$  and  $\eta = 3.8$  was fixed for the sand trap and the particle tracking data, respectively. (The open symbols represent several rescaled data sets, obtained for a variety of bed slopes.)

value of the sand flux predicted by this formula agrees better with experimental observations. This is how we obtained the upper dotted line in figure 5.

Both (30) and (31) have the functional form of the transport law proposed by Durán and Herrmann [12] based on the focal point assumption. Note that the effective height  $z^{\text{sal}}$  is small compared with the saltation height, where the wind speed obtained from the focal point assumption is very weak. As a consequence, the mean drag force is reduced, which results in a negative parameter  $a < 0$  in (30) and a negative sand transport rate  $Q < 0$  for large shear velocities  $U > |a/b|$ . Table 1 and figure 5 provide a summary of various stationary aeolian sand transport laws that have been proposed in the literature, in comparison with the prediction of our two-species model and its above single-trajectory contractions.

#### 4.3. Comparison with experiments

We now fit our two-species flux relation  $Q(U)$  from (29) to the empirical data from various wind tunnel measurements [40, 43], using  $\eta$  and  $\alpha$  as free fit parameters. As demonstrated in figure 6, we obtain excellent agreement with the experimental data for a grain-size-independent splash efficiency  $\eta$  and an effective coefficient of restitution  $\alpha$  that increases with increasing grain size  $d$ . The transport rates for four different grain sizes collected in [40] were obtained using sand traps; the data in [43] were obtained by particle tracking techniques for a single grain size only. The different methods yield different absolute values for the sand flux, which might be due to systematic differences in the detection efficiency. In the model, these differences are reflected in the (apparently) different efficiencies with which saltating grains generate reptating



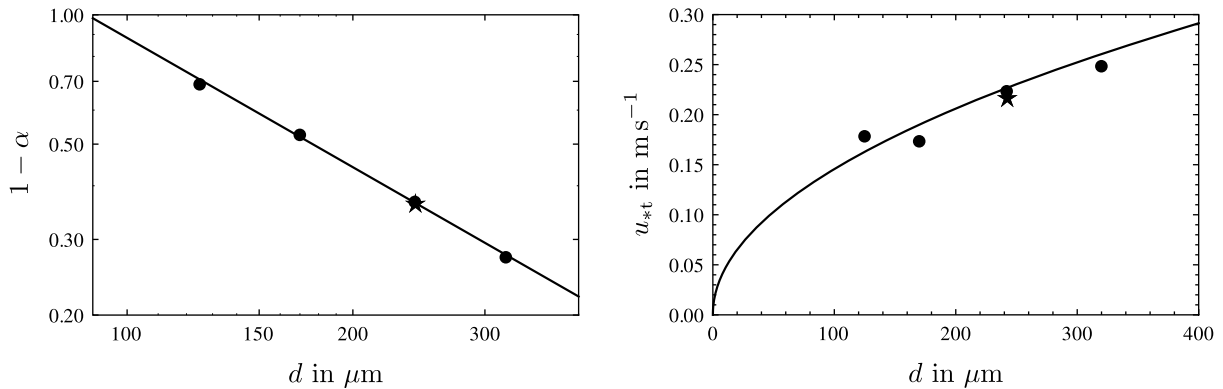


**Figure 7.** The restitution coefficient  $\alpha$  (left) and the threshold shear velocity  $u_{*t}$  (right) versus the grain size  $d$ . Parameter values deduced from model fits to flux data in figure 6. The solid lines represent the scaling  $(d/d_0)^{-1}$  according to (33) for  $1 - \alpha$  and the classical estimate  $u_{*t} = 0.1\sqrt{\sigma g d}$ , respectively.

grains, i.e. different values of the parameter  $\eta$ . We find that  $\eta = 3.8$  for the data obtained by particle tracking and  $\eta = 9$  for the sand trap data, independently of the grain size. But both data sets were consistent with the same formula for the bed restitution coefficient

$$\alpha = 1 - d_0/d, \quad (33)$$

with  $d > d_0 = 88 \mu\text{m}$  (left panel of figure 7). The rebound becomes increasingly elastic for larger grains, while  $\alpha$  vanishes for smaller grains at a critical grain diameter  $d = d_0$ , which is in accord with the observation that saltation only occurs for sand grains larger than about  $70 \mu\text{m}$  [56]. The dependence of the restitution coefficient  $\alpha$  on the grain size is physically plausible, for the collision of smaller grains is increasingly influenced by hydrodynamic interactions (and also by cohesive and electrostatic forces). In other words,  $d_0$  is a characteristic grain size marking the transition from a phenomenology typical of sand to one typical of dust.

Moreover, while we also fine-tune the threshold  $u_{*t}$  for each grain size by hand when fitting the experimental data, the values used turn out to be in very good agreement with the expectation  $u_{*t} \approx 0.1\sqrt{\sigma g d}$ , as demonstrated by the inset of figure 6. Altogether, the stationary sand transport rate observed in experiments is thus convincingly reproduced by the two-species result, equation (29), over a wide parameter range, with very plausible and physically meaningful values for the model parameters.

The observed value of  $d_0$  can be rationalized by a hydrodynamic order of magnitude estimate. Commonly, one relates the crossover from sand-like to dust-like behaviour to the difference in transport modes of these two classes of grains. While sand is transported by grain hopping dust remains suspended in the air for a while. Balancing the settling velocity of the grains by the typical (upward) eddy currents, which are of the order of  $u_{*t}$ , one obtains a minimal sand grain size of about  $1.5(v^2/\sigma g)^{1/3} \approx 30 \mu\text{m}$  [1]. To match  $d_0 = 88 \mu\text{m}$ , the eddy velocity would have to be  $4.5u_{*t}$ . Two further estimates of  $d_0$  may be obtained as follows. The first assumes that the crossover marked by  $d_0$  is concomitant with the crossover from a more elastic to a more viscous collision between individual grains. In this case, the relevant quantity is the Stokes number, which characterizes the particle inertia relative to the viscous forces.

Using the observations of the collision experiments by Gondret *et al* [57] for the critical Stokes number  $St$ , below which the impacting particles do not rebound from a rigid wall, one gets a critical grain size of about  $20 St^{2/3} v^{2/3} / \sigma / g^{1/3} \approx 20 \mu\text{m}$ . To match  $d_0 = 88 \mu\text{m}$ , the critical Stokes number would have to be of the order of 190, i.e. ten times larger than the value obtained in [57], for which experimental differences might possibly be blamed. Note, however, that the most pertinent argument should be the one that gives the largest value of  $d_0$ , as it provides a lower bound for the grain size contributing to saltation. A larger estimate of  $d_0$  is indeed obtained by observing that sand grains collide with the bed, and they are lifted from the bed by turbulent fluctuations in the wind velocity. In contrast, suspended and resting dust particles are protected from bed collisions and turbulent lift, respectively, by the laminar boundary layer that coats any solid (no slip) boundary. The characteristic length scale of this laminar coating is related to the so-called Kolmogorov dissipation scale  $(v_{\text{air}}^3 / \varepsilon)^{1/4}$  [58], where  $\varepsilon$  is the dissipation per unit mass of the driving medium (in our case air under normal conditions). For the logarithmic wind profile near the ground, equation (22), the scale-dependent dissipation takes the form  $\varepsilon(z) = u_{*t}^3 / \kappa z$  [59]. A self-consistency argument requiring that the Kolmogorov dissipation scale at height  $z$  above the ground equals  $z$  (if no externally imposed roughness scale is available) yields  $z \simeq [v_{\text{air}}^3 / \varepsilon(d_0)]^{1/4}$ . Extrapolating the logarithmic profile with  $u_{*t} = 0.1 \sqrt{\sigma g d}$  down to the scale  $z$ , we obtain  $z = 4.6 (v_{\text{air}}^2 / \sigma g)^{1/3} \approx 10^2 \mu\text{m}$ . We find this estimate to be in excellent agreement with the data in the left panel of figure 7, which suggests

$$d_0 \approx 4 (v_{\text{air}}^2 / \sigma g)^{1/3}. \quad (34)$$

## 5. Conclusions

We have developed a ‘second generation’ continuum description of aeolian sand transport, relaxing the strong mean-field approximation inherent in the classical single-trajectory models such as [8] and introducing a two-species framework, as advocated in [5]. We started from the physics on the grain scale and corroborated our explicit analytical expressions by a comprehensive comparison with empirical data for the splash, the wind velocity field and the sand flux, covering a broad range of ambient conditions and grain sizes. While the usefulness of our general approach of contracting the complicated splash and saltation process into a drastically reduced two-species picture was strongly suggested by empirical and theoretical work, it necessarily involved some free phenomenological coefficients. For our two-species model, these are, apart from a few minor numerical coefficients listed in table D.1, the effective bed restitution coefficient  $\alpha(d)$  for the saltating grains of diameter  $d$  and the parameter  $\eta$  that fixes the number of reptating grains ejected by the average impacting saltating grain. Both parameters were found to take consistent and plausible values if used as free parameters when fitting the empirical flux data obtained in wind tunnel experiments. In particular, the size dependence of the restitution coefficient fits perfectly to the phenomenological criteria commonly used to distinguish dust from sand. The predicted two-species stationary flux law (29) was found to be in excellent agreement with comprehensive data from different sources. It should provide an excellent analytical starting point for a variety of advanced applications calling for a more faithful description of the saltation process so far available—from wind-driven structure formation in the desert to saltation-driven dust production and emission.

## Acknowledgments

We thank Thomas Pätz and Jasper Kok for inspiring discussions and for making the manuscript of [33] available to us prior to its publication.

## Appendix A. Solving the Prandtl turbulent closure

With (4) and the assumption of an exponential decay of the grain-borne shear stress with height, equation (18), the modified Prandtl turbulence closure (19) reads as

$$\partial_z u = \frac{u_*}{\kappa z} \sqrt{1 - \frac{\tau_g(0)}{\tau} e^{-z/z_m}}. \quad (\text{A.1})$$

To make analytical progress, we follow Sørensen [11] in approximating the square root by a secant. The right-hand side of (A.1) has the functional form  $\sqrt{1 - \epsilon x}$ , with  $x \equiv \exp(-z/z_m)$  and  $\epsilon \equiv \tau_g(0)/\tau$ , which we approximate by a secant of the form  $ax + b(1 - x)$ . Matching the points  $\{0, 1\}$  and  $\{1, \sqrt{1 - \epsilon}\}$  yields  $b = 1$  and  $a = \sqrt{1 - \epsilon}$ , hence

$$\sqrt{1 - \epsilon x} \approx 1 - (1 - \sqrt{1 - \epsilon})x. \quad (\text{A.2})$$

Under stationary conditions, using (7), we have  $\sqrt{1 - \epsilon} = \sqrt{(\tau - \tau_g(0))/\tau} = u_{*t}/u_*$ , which leads to (20). This avoids an artefact of Sørensen's original approximation [11],  $\sqrt{1 - \epsilon x} \approx 1 - \epsilon x$ , which implies  $\sqrt{\tau_a(0)/\tau} = 1 - \tau_g(0)/\tau$  for the shear stress at the ground, as already criticized by Durán and Herrmann [12].

## Appendix B. The two-species approach for the wind profile

In (5) of section 2, the grain-borne shear stress was split into the contributions from saltating and reptating particles, respectively. The ratio of the grain-borne shear stresses at the ground,

$$\frac{\tau_g^{\text{rep}}(0)}{\tau_g^{\text{sal}}(0)} = \alpha \frac{v^{\text{rep}}}{v_{z0}^{\text{rep}}} \frac{1 - \varphi}{\varphi} \equiv \tilde{\alpha} \frac{1 - \varphi}{\varphi}, \quad (\text{B.1})$$

immediately follows from (8) and (12), and from our simplifying assumption that the reptating grains are ejected vertically. Assuming the exponential decay of the grain-borne shear stress  $\tau_g$  with height to hold for both components, the Prandtl turbulent closure reads as

$$\rho_{\text{air}} \kappa^2 z^2 (\partial_z u)^2 = \tau - \tau_g^{\text{rep}}(0) e^{-z/z_m^{\text{rep}}} - \tau_g^{\text{sal}}(0) e^{-z/z_m^{\text{sal}}}. \quad (\text{B.2})$$

We exploit the strong scale separation  $z_m^{\text{sal}}/z_m^{\text{rep}} \simeq 10^2$  between the characteristic jump heights of saltating and reptating grains [1, 60], on which the two-species model is based. (The precise value turns out to be irrelevant to our discussion.) It allows the closure to be solved for two separate height ranges: (i)  $z < z_m^{\text{rep}} \ll z_m^{\text{sal}}$  associated with reptation, where we may set  $\exp(-z/z_m^{\text{sal}}) \rightarrow 1$ , and (ii)  $z \gg z_m^{\text{rep}}$ , associated with saltation, where we may set  $\exp(-z/z_m^{\text{rep}}) \rightarrow 0$ . Applying the secant approximation for the square root as described in appendix A, we can perform the integrations within both ranges and match the asymptotic

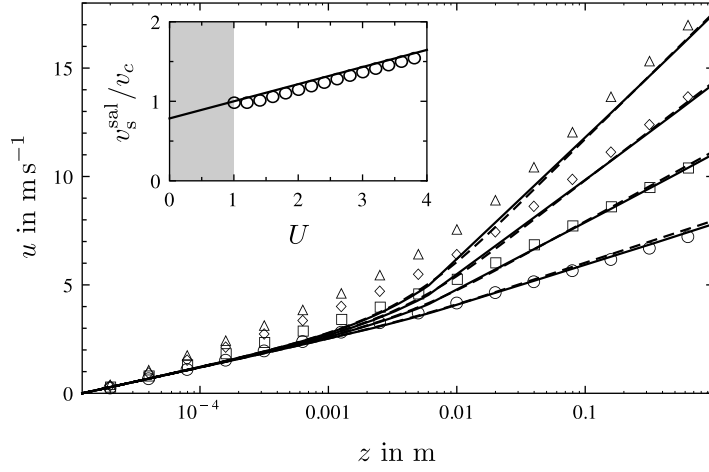


**Figure B.1.** Comparison of the wind velocity profile (B.3) obtained from the self-consistent numerical solution of (B.5) (solid lines) with the pre-averaged profile (21) (dashed lines) for grains of diameter  $d = 242 \mu\text{m}$  and for various shear velocities ( $U = 1.5, 2.5, 3.5$  and  $4.5$  from bottom to top). As explained in the main text, both approaches coincide for  $z_m = z_m^{\text{rep}}$ . In addition, we show the results of numerical solutions of the turbulence closure (B.2) (open symbols) to support the approximate expression (B.3). Inset: the saltation velocity  $v^{\text{sal}}$ , rescaled by the minimum saltation velocity  $v_c^{\text{sal}}$  needed to eject any grains, over the shear velocity: self-consistent numerical solution of (B.5) (symbols) and its analytical prediction in the limit  $(1 - \tau_t/\tau)\varphi \rightarrow 0$ , for which  $u(z)$  is given by (B.6) (line).

solutions at  $z = z_m^{\text{rep}}$ . Using (7) and (B.1) to eliminate  $\tau_g^{\text{sal}}(0)$  and  $\tau_g^{\text{rep}}(0)$ , this yields

$$u(z) = \begin{cases} \frac{Su_*}{\kappa} \ln \frac{z}{z_0} - \frac{Su_* - u_{*t}}{\kappa} [E_1(z_0/z_m^{\text{rep}}) - E_1(z/z_m^{\text{rep}})], & z \leq z_m^{\text{rep}}, \\ u(z_m^{\text{rep}}) + \frac{u_*}{\kappa} \ln \frac{z}{z_m^{\text{rep}}} - \frac{u_*(1-S)}{\kappa} [E_1(z_m^{\text{rep}}/z_m^{\text{sal}}) - E_1(z/z_m^{\text{sal}})], & z > z_m^{\text{rep}}, \end{cases} \quad (\text{B.3})$$

where we abbreviated

$$S = \sqrt{1 - \frac{(1 - \tau_t/\tau)\varphi}{\varphi + (1 - \varphi)\tilde{\alpha}}}. \quad (\text{B.4})$$

Using this in the force balance, (24), we gain the implicit equation

$$v^{\text{sal}} = u(z^{\text{sal}}, v^{\text{sal}}) - v_\infty^{\text{sal}}, \quad (\text{B.5})$$

where the fraction  $\varphi$  of saltating grains itself depends on the velocity  $v^{\text{sal}}$  of the saltating grains via (10). To solve it, we note that the fraction  $\varphi$  of saltating particles is a decreasing function of the shear stress  $\tau$ , bracketed by 1 and 0 (figure 4, right panel). Hence, the product  $(1 - \tau_t/\tau)\varphi$  is a small number for all  $\tau \geq \tau_t$ . Setting it to zero in (B.3), we obtain

$$u(z) \sim \frac{u_*}{\kappa} \ln \left( \frac{z}{z_0} \right) - \frac{u_* - u_{*t}}{\kappa} \times \begin{cases} [E_1(z_0/z_m^{\text{rep}}) - E_1(z/z_m^{\text{rep}})], & z \leq z_m^{\text{rep}}, \\ [E_1(z_0/z_m^{\text{rep}}) - E_1(1)], & z > z_m^{\text{rep}}. \end{cases} \quad (\text{B.6})$$

Since the exponential integral  $E_1(z/z_m)$  vanishes rapidly for increasing  $z > z_m$ , we recover the wind speed profile (21) successfully employed in the one-species models, with the characteristic decay height given by  $z_m \equiv z_m^{\text{rep}}$ . Inserting (B.6) into (B.5) yields an affine increase of  $v^{\text{sal}}$  with  $u_*$ , in good accord with the exact numerical solution of (B.5) (figure B.1, right panel).

For the numerical solution, one has to deal with the two free parameters  $z_m^{\text{rep}}$  and  $\alpha$ . While the former is directly related to the wind profile, the latter is a fit parameter of the model, determined from a comparison of the predicted sand transport rate with empirical data (figure 6). To make progress, we vary  $z_m^{\text{rep}}$  and take the value of  $\alpha$  from section 3.4, where the sand flux is estimated by means of the pre-averaged approach for the wind profile. For a grain diameter  $d = 242 \mu\text{m}$ , we obtained  $\alpha \approx 0.63$  (i.e.  $\tilde{\alpha} = 1.4$ ), which is consistent with collision experiments, as argued in [12]. From the numerical solution of (B.5), we find good agreement between the self-consistently gained  $u(z)$  and wind tunnel measurements [42] for  $z_m^{\text{rep}} = 25d$ , which is exactly the same value as obtained in section 3.2 within the pre-averaged approach. This supports our observation that (B.3) can be approximated by taking the limit  $\varphi \rightarrow 0$  in (B.6), which yields the pre-averaged wind profile for  $z_m \equiv z_m^{\text{rep}}$ . This result is almost independent of the ratio  $z_m^{\text{sal}}/z_m^{\text{rep}}$ , for (B.6) is independent of  $z_m^{\text{sal}}$ . Thereby, we formally confirm the intuitive expectation that the feedback of the grains on the wind profile is predominantly due to the many reptating particles and hardly affected by the saltating particles.

### Appendix C. Reptation velocity

As to the saltating grain fraction in section 3.3, we estimate the transport velocity of the reptating grains from the grain scale physics, i.e. from the hop-averaged horizontal velocity of an individual grain. (Note that we do not introduce a new variable to distinguish the grain-scale velocity from the mean transport velocity, because the context prevents confusion.) The time-dependent velocity of a reptating grain obeys the drag relation

$$\partial_t v^{\text{rep}} = \frac{g}{(v_\infty^{\text{rep}})^2} |u - v^{\text{rep}}| (u - v^{\text{rep}}), \quad (\text{C.1})$$

similar to that for saltating grains [8, 12]. For saltating grains, an additional friction force (besides the drag force) would appear on the right-hand side of the equation of motion, representing the mean loss of momentum upon rebound. But, since the reptating grains perform only a single hop, such a friction term does not enter (C.1). We assume that the ejection is essentially vertical with the initial velocity  $v_{z0}^{\text{rep}}$  of the order of  $u_{*t}$ . A more accurate discussion would not substantially change our findings, as confirmed by the numerical solution of (C.1). Note that the nonlinearity of the drag law entails a time-dependent ‘terminal settling velocity’  $v_\infty^{\text{rep}}$ , dependent on the actual relative grain velocity  $u - v^{\text{rep}}$  (e.g. [53]). However, for our purpose, and in view of the low reptation trajectories, we can safely approximate the reptation velocity from (C.1) by inserting the wind speed  $u(z^{\text{rep}})$  at a given reptation height and the steady-state terminal velocity

$$v_\infty^{\text{rep}} = \sqrt{\sigma g d [0.95 + 20 v_{\text{air}} / \sqrt{\sigma g d^3}]^{-1}} \quad (\text{C.2})$$

derived from the effective drag law proposed in [53], similar to (25) (see also [8, 12]). Neglecting moreover vertical drag forces, the maximum height of the reptation trajectory is  $(v_{z0}^{\text{rep}})^2 / (2g) \approx 10d < z_m$ . Consequently, we may insert the ground-level wind field (22) and

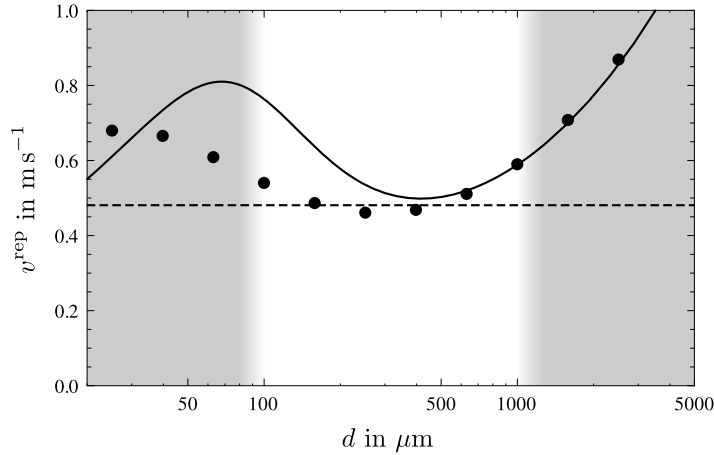


**Figure C.1.** The reptation velocity  $v^{\text{rep}}$  against the grain diameter  $d$ . The dots correspond to the numerical solution of (C.1) averaged over one trajectory, while the solid and dashed lines represent the approximate solution (C.3) and the representative value  $v^{\text{rep}} = 0.7(\sigma v_{\text{air}}g)^{1/3} \approx 0.5 \text{ m s}^{-1}$  proposed in (27), respectively. The latter can be understood as an average over the relevant grain sizes (white background).

obtain the mean reptation velocity

$$v^{\text{rep}} \approx \frac{u_{*t} \ln(z^{\text{rep}}/z_0)}{\kappa \left[ 1 + \kappa (v_{\infty}^{\text{rep}})^2 / (2v_{z_0}^{\text{rep}} u_{*t} \ln(z^{\text{rep}}/z_0)) \right]}, \quad (\text{C.3})$$

where we approximated the time of flight by that for a parabolic trajectory,  $2v_{z_0}^{\text{rep}}/g$ , as usual. Inserting the empirical observation  $v_{z_0}^{\text{rep}} \approx u_{*t}$  as well as  $u_{*t}^2 = 0.01\sigma g d$  and  $z_0 = d/20$ , see table D.1, results in an estimate for the reptation velocity  $v^{\text{rep}}$  as a function of the grain diameter  $d$ , illustrated by a solid line in figure C.1, which we may identify with the (mean field) transport velocity of the reptating grain fraction.

The yet undetermined value of the effective reptation height  $z^{\text{rep}}$  is expected to be of the order of the maximum height  $(v_{z_0}^{\text{rep}})^2/(2g)$  of the trajectory. Indeed, if we compare the approximate result given by (C.3) with the numerical solution  $v^{\text{rep}}(t)$  of (C.1) averaged over the whole trajectory,

$$\overline{v^{\text{rep}}} = \frac{g}{2v_{z_0}^{\text{rep}}} \int_0^{2v_{z_0}^{\text{rep}}/g} dt v^{\text{rep}}(t), \quad (\text{C.4})$$

we obtain a good match for large grain diameters  $d > 800 \mu\text{m}$  for  $z^{\text{rep}} = 0.14u_{*t}^2/(2g)$ . Note, however, that the numerical solution yields an almost  $d$ -independent reptation velocity  $\overline{v^{\text{rep}}} \approx 0.5 \text{ m s}^{-1}$  for the relevant grain sizes  $d \approx 100 \mu\text{m} \dots 1 \text{ mm}$ , as illustrated in figure C.1. To find an estimate for  $\overline{v^{\text{rep}}}$ , which still captures the dependence on other parameters appearing in (C.3), we evaluate this equation for a representative grain diameter within the relevant range. A closer look at (C.3) reveals that the reptation velocity at the inflection point  $d \approx 6.7v_{\text{air}}^{2/3}(\sigma g)^{-1/3} \approx 150 \mu\text{m}$  can be approximated by  $v^{\text{rep}} \approx (v_{\text{air}}\sigma g)^{1/3} = 0.68 \text{ m s}^{-1}$ , which provides the wanted parameter dependence. To better match the absolute values found from the numerical solution, we insert a factor of 0.7 by hand, thus arriving at the analytical estimate given in (27).

**Table D.1.** The parameters occurring in equations (D.1)–(D.5), which are either numerical constants or dependent on the grain diameter  $d$ , the gravitational acceleration  $g = 9.81 \text{ m s}^{-1}$ , the sand–air density ratio  $\sigma = 2163$  or the kinematic viscosity of air,  $\nu_{\text{air}} = 1.5 \times 10^{-5} \text{ m}^2 \text{ s}^{-1}$ .

Parameter	Value or formula
$u_{*t}$	$0.1\sqrt{\sigma g d}$
$\kappa$	0.4
$\eta$	9 [40], 3.8 [43]
$v_c^{\text{sal}}$	$10u_{*t}$
$v_{z0}^{\text{rep}}$	$u_{*t}$
$z_0$	$d/20$
$z_m$	$25d$
$\alpha$	$1 - d_0/d$ , $d_0 = 4(\nu_{\text{air}}^2/\sigma g)^{1/3}$
$v_\infty^{\text{sal}}$	$\sqrt{\sigma g d/\alpha}[1.3 + 41\sqrt{\alpha} \nu_{\text{air}}/\sqrt{\sigma g d^3}]^{-1}$
$v^{\text{rep}}$	$0.7(\sigma \nu_{\text{air}} g)^{1/3}$

#### Appendix D. The coefficients of the transport law

Here we give explicit expressions for the coefficients occurring in the saturated sand flux (29):

$$a = 2\alpha(1 + \tilde{\eta}) \frac{v_c^{\text{sal}} + v_\infty^{\text{sal}}}{u_{*t}} - 2\alpha \frac{1 + \tilde{\eta}}{\kappa} \mathcal{E} \left[ z_0 \exp \left( \kappa \frac{v_c^{\text{sal}} + v_\infty^{\text{sal}}}{u_{*t}} \right) \right], \quad (\text{D.1})$$

$$b = a - 2\alpha \frac{v_c^{\text{sal}}}{u_{*t}} \quad (\text{D.2})$$

$$\alpha_0 = \frac{a^2}{(1 + \tilde{\eta})^2}, \quad (\text{D.3})$$

$$\beta_0 = \frac{2\tilde{\eta}a}{1 + \tilde{\eta}} \left( \frac{v_{z0}^{\text{rep}}}{u_{*t}} + \frac{a}{1 + \tilde{\eta}} - \frac{b}{\tilde{\eta}} \right), \quad (\text{D.4})$$

$$\gamma_0 = \frac{\tilde{\eta}v_{z0}^{\text{rep}}}{u_{*t}} \left[ \frac{\tilde{\eta}v_{z0}^{\text{rep}}}{u_{*t}} + 2(a - b) \right] - \left( \frac{1 + \tilde{\eta}}{2a} \beta_0 \right)^2 \quad (\text{D.5})$$

with the abbreviations

$$\mathcal{E}(z) = E_1(z_0/z_m) - E_1(z/z_m) \quad (\text{D.6})$$

and

$$\tilde{\eta} \equiv \eta v^{\text{rep}}/v_{z0}^{\text{rep}}. \quad (\text{D.7})$$

All parameters occurring in these equations are listed in table D.1. As explained in the main text, these quantities are determined as follows. From collision experiments, we obtain the numerical values of the critical impact velocity  $v_c^{\text{sal}}$  and the vertical ejection speed  $v_{z0}^{\text{rep}}$ . The roughness length  $z_0$  and the height  $z_m$  (the characteristic decay height of the air-borne sand density) are estimated by fitting experimentally observed wind velocity profiles above the saltation layer. Finally, the parameters  $\eta$ ,  $\alpha$  and the threshold shear velocity  $u_{*t}$  are determined by fitting the sand transport rate to wind tunnel measurements.



## References

- [1] Bagnold R 1954 *The Physics of Blown Sand and Desert Dunes* (London: Methuen)
- [2] Anderson R S, Sørensen M and Willets B B 1991 *Acta Mech.* **1** (Suppl.) 1–19
- [3] Ungar J E and Haff P K 1987 *Sedimentology* **34** 289–99
- [4] Anderson R S 1987 *Sedimentology* **34** 943–56
- [5] Andreotti B 2004 *J. Fluid Mech.* **510** 47–70
- [6] Anderson R S and Haff P K 1991 *Acta Mech.* **1** (Suppl.) 21–51
- [7] Kroy K, Sauermann G and Herrmann H J 2002 *Phys. Rev. Lett.* **88** 054301
- [8] Sauermann G, Kroy K and Herrmann H J 2001 *Phys. Rev. E* **64** 031305
- [9] Andreotti B, Claudin P and Douady S 2002 *Eur. Phys. J. B* **28** 321–39
- [10] Andreotti B, Claudin P and Douady S 2002 *Eur. Phys. J. B* **28** 341–52
- [11] Sørensen M 2004 *Geomorphology* **59** 53–62
- [12] Durán O and Herrmann H J 2006 *J. Stat. Mech. Theory Exp.* **2006** P07011
- [13] Fischer S, Cates M E and Kroy K 2008 *Phys. Rev. E* **77** 031302
- [14] Jenkins J T, Cantat I and Valance A 2010 *Phys. Rev. E* **82** 020301
- [15] Schwämmle V and Herrmann H J 2005 *Eur. Phys. J. E* **16** 57–65
- [16] Durán O and Herrmann H J 2006 *Phys. Rev. Lett.* **97** 188001
- [17] Parteli E J R and Herrmann H J 2007 *Phys. Rev. E* **76** 041307
- [18] Parteli E J R, Durán O and Herrmann H J 2007 *Phys. Rev. E* **75** 011301
- [19] Durán O, Parteli E J and Herrmann H J 2010 *Earth Surf. Process* **35** 1591–600
- [20] Andreotti B and Claudin P 2007 *Phys. Rev. E* **76** 063301
- [21] Cahill T A, Gill T E, Reid J S, Gearhart E A and Gilette D A 1996 *Earth Surf. Process* **21** 621–39
- [22] Kok J F 2010 *Proc. Natl Acad. Sci. USA* **108** 1016–21
- [23] Anderson R S 1990 *Earth-Sci. Rev.* **29** 77–96
- [24] Prigozhin L 1999 *Phys. Rev. E* **60** 729–33
- [25] Hoyle R B and Mehta A 1999 *Phys. Rev. Lett.* **83** 5170–3
- [26] Valance A and Rioual F 1999 *Eur. Phys. J. B* **10** 543–8
- [27] Yizhaq H, Balmforth N J and Provenzale A 2004 *Physica D* **195** 207–28
- [28] Andreotti B, Claudin P and Pouliquen O 2006 *Phys. Rev. Lett.* **96** 028001
- [29] Manukyan E and Prigozhin L 2009 *Phys. Rev. E* **79** 031303
- [30] Yizhaq H 2008 *J. Coast. Res.* **24** 1369–78
- [31] Milana J P 2009 *Geology* **37** 343–6
- [32] Yizhaq H, Katra I, Kok J F and Isenberg O 2012 *Geology* **40** 459–62
- [33] Pähz T, Kok J F and Herrmann H J 2012 *New J. Phys.* **14** 043035
- [34] Beladjine D, Ammi M, Oger L and Valance A 2007 *Phys. Rev. E* **75** 061305
- [35] Ammi M, Oger L, Beladjine D and Valance A 2009 *Phys. Rev. E* **79** 021305
- [36] Valance A and Crassous J 2009 *Eur. Phys. J. E* **30** 43–54
- [37] Kok J F and Renno N O 2009 *J. Geophys. Res.* **114** D17204
- [38] Kang L and Zou X 2011 *Geomorphology* **125** 361–73
- [39] Duran O, Andreotti B and Claudin P 2011 arXiv:1111.6898
- [40] Iversen J D and Rasmussen K R 1999 *Sedimentology* **46**, 4 723–31
- [41] Rasmussen K R and Sørensen M 2005 Dynamics of particles in aeolian saltation *Proc. Powders and Grains* ed R Garcia-Rojo, H Herrmann and S McNamara (Rotterdam: Taylor and Francis) pp 967–72
- [42] Rasmussen K R and Sørensen M 2008 *J. Geophys. Res.* **113** F02S12
- [43] Creyssels M, Dupont P, el Moctar A O, Valance A, Cantat I, Jenkins J T, Pasini J M and Rasmussen K R 2009 *J. Fluid Mech.* **625** 47–74
- [44] Owen P R 1964 *J. Fluid Mech.* **20** 225–42
- [45] Raupach M R 1991 *Acta Mech.* **1** (Suppl.) 83–96



- [46] McEwan I K and Willets B B 1991 *Acta Mech.* **1** (Suppl.) 53–66
- [47] Rioual F, Valance A and Bideau D 2000 *Phys. Rev. E* **62** 2450–9
- [48] Rioual F, Valance A and Bideau D 2003 *Europhys. Lett.* **61** 194
- [49] Rice M A, Willets B B and McEwan I K 1995 *Sedimentology* **42** 695–706
- [50] Anderson R S and Haff P K 1988 *Science* **241** 820–3
- [51] Li Z S, Ni J R and Mendoza C 2004 *Geomorphology* **60** 359–69
- [52] Andreotti B 2008 *Proc. Natl Acad. Sci. USA* **105** E60
- [53] Jimenez J A and Madsen O S 2003 *J. Waterw. Port Coast. Ocean Eng.* **129** 70–8
- [54] Nalpanis P, Hunt J C R and Barrett C F 1993 *J. Fluid Mech.* **251** 661–85
- [55] Almeida M P, Parteli E J R, Andrade J S and Herrmann H J 2008 *Proc. Natl Acad. Sci. USA* **105** 6222–6
- [56] Shao Y 2000 *Physics and Modelling of Wind Erosion* (New York: Kluwer Academic)
- [57] Gondret P, Hallouin E, Lance M and Petit L 1999 *Phys. Fluids* **11** 2803–5
- [58] Frisch U 1995 *Turbulence: The Legacy of A N Kolmogorov* (Cambridge: Cambridge University Press)
- [59] Landau L D and Lifshitz E M 1987 *A Course in Theoretical Physics—Fluid Mechanics* vol 6 (Oxford: Elsevier Science)
- [60] Andreotti B, Claudin P and Pouliquen O 2010 *Geomorphology* **123** 343–8

**Analytical mesoscale modeling of aeolian sand transport**

Marc Lämmel and Klaus Kroy\*

*Institut für Theoretische Physik, Universität Leipzig, Postfach 100920, 04009 Leipzig, Germany*

(Received 5 September 2017; published 27 November 2017)

The mesoscale structure of aeolian sand transport determines a variety of natural phenomena studied in planetary and Earth science. We analyze it theoretically beyond the mean-field level, based on the grain-scale transport kinetics and splash statistics. A coarse-grained analytical model is proposed and verified by numerical simulations resolving individual grain trajectories. The predicted height-resolved sand flux and other important characteristics of the aeolian transport layer agree remarkably well with a comprehensive compilation of field and wind-tunnel data, suggesting that the model robustly captures the essential mesoscale physics. By comparing the predicted saturation length with field data for the minimum sand-dune size, we elucidate the importance of intermittent turbulent wind fluctuations for field measurements and reconcile conflicting previous models for this most enigmatic emergent aeolian scale.

DOI: [10.1103/PhysRevE.96.052906](https://doi.org/10.1103/PhysRevE.96.052906)**I. INTRODUCTION**

Aeolian sand transport is the process of erratic grain hopping occasionally observed on a windy day at the beach. It remains perplexing how the wide variety of distinctive aeolian sand patterns, from tiny ripples to huge dunes, emerges from such seemingly chaotic dynamics. The current knowledge about the grain-scale structure of aeolian transport largely rests on laboratory and field experiments [1]. Attempts to derive coarse-grained mathematical models that can rationalize the observations started with Bagnold's seminal work in the 1930s [2] and are still the subject of ongoing research [3–11], for good conceptual and practical reasons. With average grain trajectories exceeding the submillimeter grain scale by orders of magnitude, aeolian transport is a typical mesoscale phenomenon that should be amenable to such coarse-grained modeling. Moreover, despite growing computational resources, faithful grain-scale simulations remain forbiddingly expensive, so that also numerical approaches cannot avoid fairly drastic idealizations [12–16]. And even a perfect simulation of aeolian transport would *per se*, without a theory, not make the emergence of the various mesoscales and ensuing sand structures less mysterious.

A radically coarse-grained mean-field model [17] that maps the whole mobilized grain population onto a single effective grain trajectory has been successful in explaining desert dune formation [18–21]. Such mean-field approaches roughly account for the more energetic saltating grains but fail to resolve the heterogeneity of the transport layer, which contains a majority of grains that only perform very small hops and do not eject other grains from the bed [22]. Their less spectacular transport mode, conventionally referred to as bed load, reptation, or creep, is however thought to be largely responsible for ripple and megaripple formation [2,23–27], which therefore eludes the mean-field approaches. Also ecologically important processes, such as dust emission, rock abrasion, and vegetation invasion, are sensitive to the detailed mesostructure of aeolian transport [4,28]. Finally, an improved

theoretical model of the aeolian transport layer could help to infer more information about extraterrestrial conditions from the limited data obtained by remote sensing [29–32].

In the following, we propose a way to transcend the usual mean-field approximations and to account, with good precision, not only for the mean transport characteristics but also for the substantial heterogeneity and the fluctuations within the transport layer and in the turbulent wind. Similarly as in earlier contributions [12,22,33–35], the ballistic kinetics of an ensemble of wind-blown grains is coupled to the local wind strength and to the dissipative collisions with the sand bed. However, as one crucial novel key ingredient, we utilize a recently proposed analytical model for the grain-bed collisions [36] that was extensively tested against grain-scale computer simulations and laboratory experiments. It enables us to develop a neat analytical description for the whole distribution of grain trajectories (Sec. II), from which explicit formulas for various height-resolved observables, such as the grain concentration and flux, readily follow (Sec. III). In line with results from earlier numerical work [4,37], the wind strength is found to affect the transport-layer physics only weakly, as corroborated by various wind-tunnel studies [1,38–41]. It enters primarily via “global,” height-integrated quantities and the total height of the transport layer, which are amenable to conventional mean-field transport models [17,42–46]. To validate key ingredients of the analytical modeling, we put forward dedicated coarse-grained computer simulations that explicitly resolve the broad distribution of grain trajectories. The latter turns out to be crucial for a proper analysis of a large amount of field and laboratory data, as shown in Sec. IV, where the model predictions are thoroughly tested against literature data. The field and wind-tunnel data confirm that the mesoscale structure of the aeolian transport layer is well captured by the analytical model. On this basis, we can make a strong case for a proportionality of the minimum sand-dune size reported in field measurements to the so-called saturation length for flux transients in heterogeneous wind. As we show, the relation is somewhat masked by the renormalizing effect of intermittent turbulent-wind-strength fluctuations that therefore must explicitly be included in the data analysis. Throughout the main text, we emphasize conceptual aspects and defer technical details to six appendices.

\*Corresponding author: klaus.kroy@uni-leipzig.de

## II. ANALYTICAL MODEL

The crux of our approach is to condense the height-resolved “mesoscale” information about the heterogeneities in the stationary aeolian transport layer into a simple analytical form of the hop-height distribution:

$$P_H(h) \propto T(h)h^{-\nu}e^{-h/H}. \quad (1)$$

Here,  $T(h)$  denotes the hop time for the trajectory of height  $h$ ,  $H$  is the (wind-dependent) characteristic height of the transport layer, and the power-law exponent  $\nu$  quantifies the energy distribution of ejected bed grains. The combination  $h^{-\nu}e^{-h/H}$  refers to the probability to find a trajectory of height  $h$ ; weighting it with the flight time  $T(h)$  then yields the probability that a randomly selected grain in the transport layer follows such a trajectory. Approximating

$$T(h) \approx 2\sqrt{2h/g} \quad (2)$$

by the free flight time (neglecting vertical drag), with  $g$  being the gravitational acceleration, yields

$$P_H(h) = [H\Gamma(3/2 - \nu)]^{-1}(h/H)^{1/2-\nu}e^{-h/H}. \quad (3)$$

The Euler gamma function  $\Gamma$  arises upon normalization.

We now provide physical arguments for the proposed form of  $P_H(h)$ . Near the bed, the transport statistics is dominated by the large number of ejected grains, whose energies are log-normally distributed and very small compared to the energy of the saltating grain ejecting them [36,47]. Their hop-height distribution is therefore well captured by the asymptotic power-law relation  $P_H(h \ll H) \propto h^{-\nu}$  with

$$\nu = 1 - 2/\ln(4)^2 + 1/\ln(2) \approx 1.4, \quad (4)$$

as shown in Appendix E. In contrast, large hop heights ( $h > H$ ) are only reached by the few particles that survive many bed collisions, and are therefore expected to die out exponentially. More precisely, the identity of the particles need not to be conserved in the sequence of jumps, which may comprise Newton-cradle-type collisions. What matters is that the grain’s energy and momentum are not dispersed to many grains and thus increase with the number of bed collisions. We may then characterize the hop sequence by the fixed rebound probability  $P_{\text{reb}} \approx P_{\text{rep}}(h \gg a) \approx 0.86$  (for trajectories much higher than the grain diameter  $a$ —typically a few 100  $\mu\text{m}$ ) and the mean ejection height  $\bar{h}_{\text{ej}} \approx 11a$ , both computed from our splash model [36] in Appendix E, yielding  $P_H(h \gg \bar{h}_{\text{ej}}) \propto T(h)e^{-h/H}$  with

$$H \approx -\bar{h}_{\text{ej}}/\ln P_{\text{reb}} \approx 72a. \quad (5)$$

We also note that an alternative explanation for the exponential tail of  $P_H(h)$  in Eq. (1) invokes an analogy with the barometer formula for the concentration of a thermalized gas [48].

To further back up Eq. (3), we performed coarse-grained computer simulations, as described in Appendix C. The comparison between analytical theory and simulations in Fig. 1 shows excellent agreement if the transport layer height  $H$  is employed as a free fit parameter that slightly increases with increasing wind shear stress  $\tau$ . Figure 1(b) compares the extracted  $H(\tau)$  with the functional form computed in Sec. III C. But even a simpler version of the model, which disregards this weak wind dependence and fixes  $H$  to its

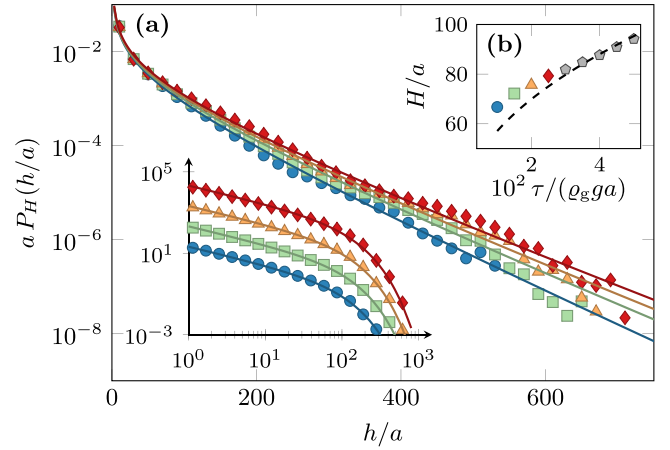


FIG. 1. (a) Coarse-grained numerical simulations (symbols) of the hop-height distribution  $P_H(h)$  compared to the analytical model, Eq. (3) (solid lines), for various wind shear stresses  $\tau$  [ $10^2 \tau / (\rho_g g a) = 1, 1.5, 2, 2.5$  from bottom to top]. The simulation computes the statistics of the ejected bed grains from the analytical model of Ref. [36], which yields a power-law distribution for low hop heights with exponent  $\nu = 1.4$ . The left inset is a log-log representation of the same data, with logarithmic binning widths (data shifted vertically for better readability). (b) Trajectories reaching beyond the characteristic height  $H$  of the transport layer die out exponentially. While  $H$  was, for each data point, used as a free fit parameter to match the simulation data, its  $\tau$  dependence is well reproduced by the more refined calculation in Sec. III C (dashed line).

characteristic value according to Eq. (5), will suffice for many practical purposes.

The model proposed in Eq. (3) has manifold consequences and applications. First, note that the hop-height distribution  $P_H(h)$  together with the purely ballistic conditional probability  $P(z|h)$  for grains on a trajectory of height  $h$  to be found at height  $z$  make up the joint probability  $P_H(z, h) = P(z|h)P_H(h)$  for grains to be at height  $z$  on a trajectory of height  $h$ . Using Eq. (2) for the free flight time and writing  $\Theta$  for the Heaviside step function,  $P(z|h)dz = [2/T(h)]dt$  yields

$$2hP(z|h) = \Theta(h - z)/\sqrt{1 - z/h}. \quad (6)$$

The ensuing joint probability  $P_H(z, h)$  then provides us with the height-dependent profiles

$$\varrho_H(z) = \rho_H \int dh P_H(z, h), \quad (7a)$$

$$j_H(z) = \rho_H \int dh P_H(z, h)v_x(z, h), \quad (7b)$$

$$\phi_H(z, \ell) = \frac{\rho_H}{2} \int_{l(h) > \ell} dh P_H(z, h)|v_z(z, h)|, \quad (7c)$$

$$\tau_{g, H}(z) = \rho_H \int_z^\infty d\tilde{z} \int dh P_H(\tilde{z}, h)f_x(\tilde{z}, h) \quad (7d)$$

of the mass concentration, the horizontal and vertical fluxes, and the stress contribution of the sand grains, respectively. Taken together, these functions allow for a comprehensive characterization of the height-resolved mesoscale structure of

the transport layer, so that the underlying model assumptions can be tested with unprecedented scrutiny. For brevity, we have introduced some additional notation in Eqs. (7), namely the horizontal and vertical components  $v_x(z, h)$ ,  $v_z(z, h)$  of the mean velocity, and the horizontal component  $f_x(z, h)$  of the force (per grain mass) contributed by a trajectory of height  $h$  to the grain-borne shear stress [22]. The common overall scale factor  $\rho_H = \int dz \rho_H(z)$  is the height-integrated mass concentration in the saltation layer (in units of mass/area). The factor  $1/2$  in Eq. (7c) arises because each trajectory contributes twice to the grain density  $P_H(z, h)$ , namely during ascent and descent, whereas it contributes only once to the local vertical flux  $\phi_H(z, \ell)$ , either when ascending or descending. Also note that we restricted the ensemble of trajectories in Eq. (7c) to those with total length  $l(h) > \ell$ , in order to make contact with experiments that use horizontal sand traps to measure the vertical flux  $\phi_H(z = 0, \ell)$  through the sand bed at a downwind distance  $\ell$  from the end of the bed [1, 41, 49].

The general form

$$\int dh K(z, h) P_H(z, h) = \int_z^\infty dh K(z, h) \frac{h^{-1/2-v} e^{-h/H}}{2\sqrt{1-z/h}} \quad (8)$$

of the integrals in Eqs. (7) already allows some general conclusions to be drawn as to how much the distribution and shape of the grain trajectories matter for a given mesoscale observable. Namely, the singularity of the denominator for  $h \rightarrow z$  gives large weight to the corresponding value of the rest of the integrand. The latter can then be taken out of the integral, and only the characteristic height  $H$  of the transport layer matters, unless one is specifically interested in the conditions very near the ground ( $z/H \ll 1$ ). The argument breaks down if the singularity is accidentally canceled by  $K(z, h)$ , which actually happens in Eqs. (7c), (7d); the vertical flux  $\phi_H(z, \ell)$  and the grain-borne stress  $\tau_{g,H}(z)$  are thus sensitive to the precise  $h$ -dependent shape of the short trajectories with  $h \ll H$ , while mass concentration and horizontal flux are not.

To explicitly evaluate the expressions in Eqs. (7), it is useful to make a few relatively uncritical simplifications concerning the shape and kinematics of the grain trajectories. First, as in Eq. (2), we again neglect the vertical drag for the individual trajectory, using the free-flight estimate for the vertical velocity for ascent and descent. The mean horizontal velocity then follows if the trajectories are approximated as parabolas of aspect ratio  $\epsilon(h) = h/l(h)$ :

$$v_z^2(z, h) \approx 2g(h - z), \quad (9a)$$

$$v_x(z, h) \approx v_x(h) \approx l(h)/T(h) \approx \sqrt{2gh}/[4\epsilon(h)]. \quad (9b)$$

Marked deviations only occur for the few very long trajectories with  $h \gg H$ . These “flyers” are exposed to the unscreened wind speed that increases approximately logarithmically with  $h$ . They therefore acquire exceptionally high forward speeds  $v_x(z, h)$  and strongly asymmetric trajectories, but have little effect on typical observables, due to their rare occurrence.

Disregarding them for now, each hopping grain can be said to be accelerated by the wind drag during most of its flight time. Since it passes each height  $z$  twice, its mean horizontal

velocity  $v_x(z, h)$  should thus, to a fair approximation, be  $z$ -independent, as indeed confirmed by numerically solving the equations of motion of a representative hopping grain (see, e.g., Ref. [7]). The forward speed during descent and ascent can then be written as  $v_x(h) \pm \Delta v_x(z, h)/2$ , with the net wind-induced speedup (to first order in  $z$ ) given by

$$\Delta v_x(z, h) \approx \alpha v_x(h)(1 - z/h). \quad (10)$$

Here, the momentum loss incurred upon rebound is represented by a constant ( $h$ -independent) effective restitution coefficient  $\alpha = \Delta v_x(z = 0, h)/v_x(h)$ . The velocity increment  $\Delta v_x(z, h)$  directly determines the force

$$f_x(z, h) = -\frac{dv_x(z, h)}{dt} = -|v_z(z, h)| \frac{\partial \Delta v_x(z, h)}{2\partial z} \quad (11)$$

entering the grain-borne shear stress via Eq. (7d). With Eqs. (9b), (10), the outer integral in Eq. (7d) thus reads

$$\int_z^\infty d\tilde{z} P(\tilde{z}, h) f_x(\tilde{z}, h) = P(0, h) v_z(0, h) \Delta v_x(z, h)/2. \quad (12)$$

In the above expressions for the forward velocity and derived quantities, the aspect ratio  $\epsilon(h) = h/l(h)$  of the trajectories remains to be specified. In cases where only the shape of the typical trajectory matters, it suffices to approximate  $\epsilon(h) \approx \epsilon(H)$ . Neglecting its weak wind-speed dependence, we consider conditions near the transport threshold, where few particles are mobilized and the bare logarithmic wind-speed profile prevails. Combining it with the prediction of our splash model for the typical rebound geometry of the hopping grains, we then find

$$\epsilon(H) \approx 0.1 \quad (13)$$

in Appendix E. While this estimate suffices for many practical purposes, the aspect ratios of the shortest and longest trajectories, corresponding to so-called reptating particles and flyers, respectively, deviate from  $\epsilon(H)$  according to

$$\frac{\epsilon(h)}{\epsilon(H)} \approx \begin{cases} (h/H)^{-1/2} & (h \ll H), \\ 1 & (h \simeq H), \\ 0 & (h \gg H). \end{cases} \quad (14)$$

The three regimes, which are clearly discernible in the simulations (see Fig. 9 of Appendix C), can be interpreted in terms of three asymptotically dominant transport modes, namely almost vertically splashed grains near the ground, saltating grains that attain a limiting speed near the top of the transport layer, and a few flyers above it. The power-law stretching for the shortest trajectories follows from the typical hop length of wind-blown ejected bed grains, as detailed in Appendix E. With increasing height, the flight time  $T(h)$  approaches the typical response time (“drag time”) for relaxation to the stationary velocity, so that one might expect the aspect ratio to evolve roughly as  $h/[T(H)u(h)] \propto \sqrt{h}/\ln(h/z_0)$ , using the logarithmic law of the wall for the wind speed  $u(h)$  at height  $h$  with surface roughness scale  $z_0$ . However, such an argument neglects the vertical drag that becomes increasingly important as  $h$  increases. It limits the vertical velocity (essentially to the terminal velocity) and thus effectively caps the hop height of the fastest ejecta.



The highest trajectories, beyond an intermittent regime of approximately shape-invariant trajectories for  $h \simeq H$ , will therefore ultimately become increasingly stretched.

An exception is provided by the rare Newton-cradle-type collisions already mentioned below Eq. (4), in which a bed grain can gain exceptionally high vertical momentum from a fast impactor. According to Eq. (3), all these highly energetic trajectories are so rare that they are buried in the far exponential tail of the hop-height distribution. They therefore have so little impact on typical mesoscale observables that the first two regimes in Eq. (1) suffice to derive a wealth of accurate analytical predictions. Nevertheless, an improved scheme that relaxes the shape invariance of the grain trajectories to also estimate the height dependence of flyer-sensitive observables for  $h > H$  is proposed below, in Secs. III B and III C. With all the ingredients in place, we can finally estimate the average value of the characteristic transport layer  $H$  from a flux-balance argument. Under stationary transport conditions, the vertical grain flux  $\phi_H(z=0, \ell=0)$  into the bed must compensate for the outgoing (rebounding and ejected) grains, yielding zero net erosion [37,50]. With the above notation, this criterion reads

$$\int_a^\infty dh [1 - P_{\text{reb}}(h) - N(h)] v_z(0, h) |P_H(0, h) = 0, \quad (15)$$

where the grain size  $a$  is used as minimum hop height to regularize the otherwise unbounded integral. Precise relations for the rebound probability  $P_{\text{reb}}$  and the number  $N$  of ejected grains per impact can be taken from our splash model [36]. It provides them as functions of the impact energy, approximately  $mgh[1 + 1/(4\epsilon)^2]$ , which in turn depends on the tangent of the impact angle, here rephrased as  $4\epsilon$ , according to Eq. (9). Together with  $\epsilon = 0.1$  from Eq. (13), the implicit equation (15) for the average transport layer height is readily solved and yields  $H \approx 70a$ . The quantitative agreement of this result with Eq. (5), which only relies on the rebound characteristics of the splash model [36], is no surprise, since it is dominated by the high-hopping and therefore frequently rebounding grains (rather than by the ejecta). If desired, the neglected weak wind-strength dependence of  $H$  through  $N$  and  $\epsilon$  can be included in the analysis using again the extended approach of Sec. III C.

At this point, we would like to emphasize that all system parameters introduced above were computed from our splash model, which was independently calibrated in Ref. [36] by comparison with collision experiments using plastic beads. However, to compare the various predictions derived in the following section with laboratory and field data in Sec. IV, below, the characteristic height  $H$  is better used as a free fit parameter, to compensate for the differences between the actual sand grains and said plastic beads, as well as for some poorly controlled environmental conditions such as humidity and temperature. Our comparison with field data also reveals that the value of the power-law exponent  $\nu$  characterizing the splash efficiency should be adapted to the actual experimental setup, whereas no adjustment is required for the values of both the aspect ratio  $\epsilon(H) \approx 0.1$  of the typical trajectories and the effective restitution coefficient  $\alpha \approx 0.6$ , computed in Appendix E.

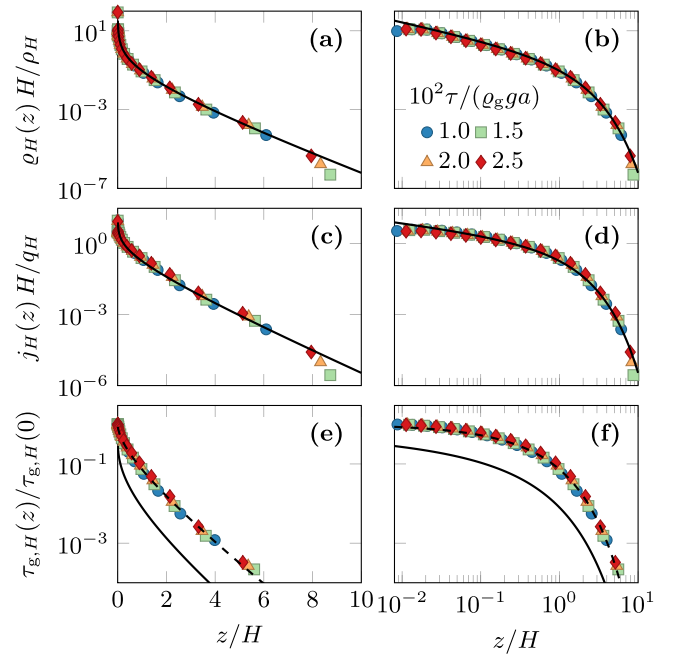


FIG. 2. Simulation data (symbols) and analytical predictions obtained from Eqs. (3)–(10) (lines) for the (a), (b) height-resolved mass concentration  $\rho_H(z)$ , (c), (d) flux  $j_H(z)$ , and (e), (f) grain-borne shear stress  $\tau_{g,H}(z)$ . Normalizing the data by the height-integrated concentration  $\rho_H$  and flux  $q_H$ , the grain stress at the ground  $\tau_{g,H}(0)$ , and the characteristic transport-layer height  $H$ , a good collapse is achieved for various wind shear stresses  $\tau$  (legend), as theoretically predicted. The solid lines correspond to the model approximation of shape-invariant trajectories with  $\epsilon(h) = \epsilon(H)$  independent of  $h$ ; the dashed lines represent Eq. (18), which invokes  $\epsilon(h) \propto h^{-1/2}$ , as appropriate for the majority of (low) trajectories, which collectively carry most of the momentum and therefore dominate the stress (see the inset of Fig. 9).

### III. RESULTS

#### A. Height-resolved transport characteristics

We now come back to the height-resolved observables introduced in Eqs. (7). Explicit analytical expressions for the height-resolved grain concentration and flux are given in Appendix A. They take the asymptotic forms

$$\frac{\rho_H(z)}{\rho_H/H} \propto \begin{cases} (z/H)^{1/2-\nu} & (z \ll H), \\ (z/H)^{-\nu} e^{-z/H} & (z \gg H), \end{cases} \quad (16)$$

and

$$\frac{j_H(z)}{q_H/H} \propto \begin{cases} (z/H)^{1-\nu} & (z \ll H), \\ (z/H)^{1/2-\nu} e^{-z/H} & (z \gg H), \end{cases} \quad (17)$$

with the height-integrated flux  $q_H \propto \rho_H v_x(H)$ . Here and for the plots in Fig. 2, we inserted Eq. (9b) for  $v_x(h, z)$  and assumed shape-invariant trajectories with  $\epsilon(h) = \epsilon(H)$ . The very good agreement, for all  $z$ , between model and numerical data in the upper and middle panels of Fig. 2 supports our simplifying assumptions.

Similarly, the height-resolved grain-borne shear stress  $\tau_{g,H}(z)$  is estimated by inserting Eqs. (9) and (10) into Eq. (7d). As anticipated above, one here needs to account for the shape

of the short trajectories  $\epsilon(h \ll H) \propto (h/H)^{1/2}$ , corresponding to the first regime of Eq. (14),

$$\frac{\tau_{g,H}(z)}{\tau_{g,H}(0)} \approx \frac{\Gamma(2 - \nu, z/H) - (z/H)\Gamma(1 - \nu, z/H)}{\Gamma(2 - \nu)}, \quad (18)$$

where  $\tau_{g,H}(0) = \alpha g \rho_H / [8\epsilon(H)]$ . Although this result rests on the assumption  $h \ll H$ , it provides a very good estimate for arbitrary values of  $z$ , because the exponential decay of the gamma functions for  $z \gg H$  dominates over any polynomial  $h$  dependence originating from  $\epsilon(h)$ . Physically speaking, the condition  $h \ll H$  comprises the majority of the grain trajectories, which account for almost the whole grain-borne shear stress. The quality of this prediction is illustrated in the lower two panels of Fig. 2.

Given any general relation  $h(\ell)$  between trajectory height and length, the vertical grain flux at arbitrary height  $z$  reads

$$\frac{\phi_H(z, \ell)}{q_H/L} = \frac{\Gamma(1 - \nu, \max\{z/H, h(\ell)/H\})}{\Gamma(3/2 - \nu)}, \quad (19)$$

with  $L = H/\epsilon(H)$  being the length of trajectories of height  $H$ . For  $h \gg H$ , the incomplete gamma function decays exponentially, so that  $\phi_H(z, \ell) \propto [h(\ell)/H]^{-\nu} e^{-\ell(h)/H}$  (tacitly assuming  $z < h$ ). Taking the derivative of Eq. (19) with respect to  $\ell$  at  $z = 0$  yields the hop-length distribution

$$-\frac{\partial}{\partial \ell} \frac{\phi_H(0, \ell)}{\phi_H(0, 0)} \propto \frac{1}{H} \frac{dh(\ell)}{d\ell} [h(\ell)/H]^{-\nu} e^{-h(\ell)/H}. \quad (20)$$

It is usually measured in experiments with sand traps [1,41] or in simulations by counting every trajectory once, independently of its length and hop time. It can also be directly inferred from the hop-height distribution in Eq. (1), after dropping the hop time  $T(h)$ . Inserting the asymptotic scaling  $\epsilon(h \ll H) \propto (h/H)^{-1/2}$  from Eq. (14) into Eq. (20), we find  $h(\ell)/H \approx (\ell/L)^{2/3}$ . From this, the power-law exponent of the hop-length distribution follows as  $1/3 + 2\nu/3 \approx 1.27$ . A slightly smaller exponent 1.2 was indeed observed by Durán *et al.* [27] in full-fledged grain-scale computer simulations of the saltation process.

The model predictions in Eqs. (16)–(20) can now be used to derive explicit expressions for further height-dependent transport properties. Combining Eqs. (16) and (17), for instance, immediately yields the height dependence of the mean grain velocity

$$V_H(z) = j_H(z)/Q_H(z) \propto v_x(H) \sqrt{z/H}. \quad (21)$$

Note, however, that the division makes the result sensitive to the precise functional form of the singular growth and the small tails of  $j_H(z)$  and  $\rho_H(z)$  for very small and large  $z$ , respectively. Therefore, it can only be trusted for intermediate heights  $z$ , as suggested by its square-root growth consistent with the regime of approximately shape-invariant saltation trajectories (see Fig. 3; the next section shows how this limitation can be overcome). In this regime, our model moreover provides an explicit prediction for the full height-resolved velocity distribution

$$P_H(v_x|z) = P_H[z, h(z, v_x)] \left| \frac{\partial}{\partial v_x} h(z, v_x) \right| \rho_H/Q_H(z), \quad (22)$$

which follows from the variable transformation  $h = h(z, v_x)$  together with the general relation  $P_H(z, v_x) =$

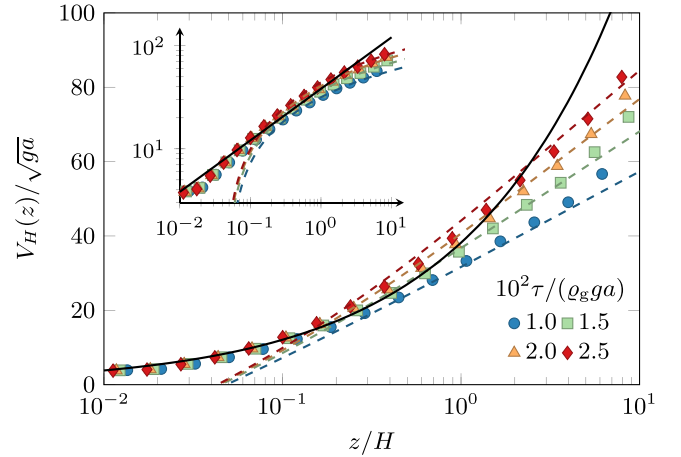


FIG. 3. Simulation data (symbols) and analytical predictions obtained from Eqs. (3)–(10) (lines) for the height-resolved grain velocity  $V_H(z)$  for various wind shear stresses  $\tau$  (legend). Solid lines represent Eq. (21), which corresponds to the model approximation of shape-invariant trajectories with  $\epsilon(h) = \epsilon(H)$  independent of  $h$ . Dashed lines show the long-trajectory estimate in Eq. (30) predicted from the wind-speed profile given in Eq. (26).

$P_H(v_x|z)Q_H(z)/\rho_H$  between joint and conditional distribution. Exploiting the shape invariance of the trajectories that dominate the statistics at intermediate  $z$ , we have  $v_x(h)^2 = (h/H)v_x(H)^2$  and thus

$$P_H(v_x|z) = \frac{\rho_H [v_x/v_x(H)]^{-2\nu} e^{-v_x^2/v_x(H)^2}}{\Gamma(3/2 - \nu) H Q_H(z) \sqrt{v_x^2 - v_x(H)^2} z/H}. \quad (23)$$

A similar calculation yields the distribution of the vertical grain velocity

$$P_H(v_z|z) = \frac{\rho_H [z/H + v_z^2/(2gH)]^{-\nu} e^{z/H + v_z^2/(2gH)}}{\Gamma(3/2 - \nu) H Q_H(z) v_z(0, H)}. \quad (24)$$

Our model also allows for a reliable analytical estimate of the wind-speed profile  $u_H(z)$  within and above the transport layer, by considering the feedback of the grain-borne momentum on the logarithmic law of the wall [42]. Inserting Eq. (18) into the modified Prandtl turbulence closure  $\tau - \tau_{g,H}(z) = \rho_a \kappa^2 z^2 [du_H(z)/dz]^2$ , where  $\rho_a$  is the air density and  $\kappa \approx 0.4$  the von Kármán constant, and approximating [45]

$$\sqrt{1 - \tau_{g,H}(z)/\tau} \approx 1 - [1 - \sqrt{1 - \tau_{g,H}(0)/\tau}] \frac{\tau_{g,H}(z)}{\tau_{g,H}(0)}, \quad (25)$$

we obtain the height-dependent wind velocity

$$u_H(z) = \frac{u_*}{\kappa} \ln(z/z_0) - \frac{u_* - u_{*t}}{\kappa} \omega(z_0/H, z/H) \sim \begin{cases} \frac{u_{*t}}{\kappa} \ln(z/z_0) & (z \ll H), \\ \frac{u_{*t}}{\kappa} \ln(z_f/z_0) + \frac{u_*}{\kappa} \ln(z/z_f) & (z \gg H), \end{cases} \quad (26)$$

with  $\omega(\zeta_0, \zeta_1) \equiv \int_{\zeta_0}^{\zeta_1} d\zeta \tau_{g,H}(\zeta H) / [\zeta \tau_{g,H}(0)]$ , the roughness height  $z_0 \approx a/10$  of the (quiescent) sand bed, and the shear velocity  $u_* \equiv \sqrt{\tau/\rho_a}$ . Following Ref. [42], we here approximated the air shear stress at the ground as a wind-strength-

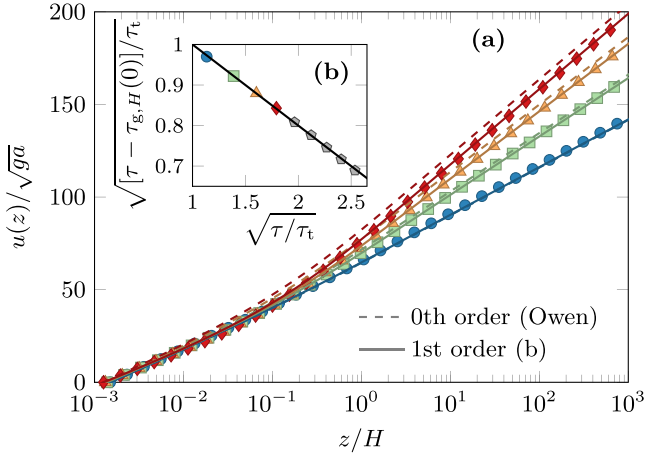


FIG. 4. (a) Height-resolved wind speed for various wind shear stresses  $\tau$  [ $10^2 \tau / (\rho_g g a) = 1, 1.5, 2, 2.5$  from bottom to top] from numerical simulations (symbols) and our model, Eq. (26), with (dashed lines) and without [solid lines, with first-order corrections shown in (b)] invoking the simplifying Owen hypothesis that the airborne shear stress at the bed is screened precisely to the threshold value  $\tau_t$  for grain entrainment [42].

independent constant  $\tau - \tau_{g,H}(0) \approx \tau_t \equiv \rho_a u_{*t}^2$ , which is justified near the transport threshold. As illustrated in Fig. 4, this (“zeroth-order”) approximation is already in good qualitative agreement with the numerical simulations, while they can be perfectly matched when small first-order corrections in  $\sqrt{\tau/\tau_t} - 1$  [45,51] are taken into account.

The asymptotic relations in Eq. (26) follow from  $\tau_{g,H}(z \ll H) \approx \tau_{g,H}(0)$  and  $\tau_{g,H}(z \gg H) \approx 0$ , according to Eq. (18). They correspond to the two limits of the screened logarithmic wind-speed profile near the ground [45] and the “shifted” logarithmic profile above the transport layer, which can also be rewritten as  $u_H(z) \sim (u_*/\kappa) \ln(z/z_0^{\text{eff}})$  with the wind-strength-dependent effective roughness length  $z_0^{\text{eff}} = z_0(z_f/z_0)^{1-u_*/u_*}$ . The crossover height

$$z_f \equiv z_0 e^{\omega(z_0/H, \infty)} \approx H e^{\Gamma(2-\nu)/\Gamma(2-\nu)-1} \approx 0.1H \quad (27)$$

between the two is comparable to the average hop height

$$\int dh h P_H(h) = (3/2 - \nu)H \approx 0.1H \quad (28)$$

of a randomly chosen grain in a transport layer of height  $H$ , and also to the median height  $z_m \approx 0.2H$  of its flux profile, indirectly defined through  $q_H/2 = \int_0^{z_m} dz j_H(z)$  (Appendix B). Recalling that  $H$  depends only weakly on the wind strength (Fig. 1), we may interpret  $z_f \approx 0.1H$  as the so-called “focus height” [2,50,51].

Altogether, our results corroborate theoretically that the mesoscale structure of aeolian transport is characterized by a very dense layer of hopping particles at the ground, which is only a few grain diameters high ( $\approx 0.1H \approx 7a$ ). The layer is predominantly populated by so-called reptating grains, which have hardly gained momentum from the wind, but collectively absorbed its excess power beyond the threshold shear stress  $\tau_t$ . This is a direct consequence of the power-law decay of the hop-height distribution in Eq. (3), which in turn is strictly tied

to the splash statistics of the bed collisions [36]. In contrast, the grains on typical saltation trajectories are accelerated by the wind, giving them an essentially length-independent shape. This symmetry is only broken by the longest trajectories of rare flyers that reach heights  $h \gg H$  far beyond the characteristic height  $H$  of the transport layer. It is this drastic change between the transport modes of the hopping particles as a function of their jump height and their unequal role in the momentum balance with the wind which limits most severely the application of mean-field models based on a single effective trajectory and has motivated the development of two-species approaches [45,50].

## B. Broken shape invariance: Height-dependent grain velocity

In the previous section, we noted that the power-law increase of the average grain velocity  $V_x(z)$  with height  $z$ , as obtained in Eq. (21), is restricted to intermediate  $z$ , where the shape-invariant trajectories contribute most. As we show now, this limitation can be overcome by an alternative approach that relates  $V_x(z)$  to the height-dependent wind speed  $u_H(z)$  from Eq. (26). We first note that the height-dependent average grain speed  $V_H(z) = j_H(z)/\rho_H(z)$  is well approximated by the velocity  $v_x(z, h = z) \equiv v_x(z)$  at the apex of a representative trajectory of overall height  $z$ . Technically, this is seen by applying Laplace’s method to the integrals for  $j_H(z)$  and  $\rho_H(z)$  (see Appendix A). The actual form of  $v_x(h)$  can then be estimated from the velocity gain  $\Delta v_x(z = 0, h) = \int_0^{T(h)} dt \dot{v}_x(t)$  of a grain during one hop of height  $h$ :

$$\Delta v_x(0, h) = \frac{\sqrt{2gh}}{v_\infty^2} \int d\tilde{z} P_H(\tilde{z}|h) [u_H(\tilde{z}) - v_x(\tilde{z}, h)]^2. \quad (29)$$

Here, the conditional probability  $P_H(\tilde{z}|h) \propto 1/v_z(\tilde{z}, h)$  results from the transformation  $d\tilde{z} = v_z dt$  of the integration variable, as in Eq. (6), and we used a single integral as a shorthand representation of both the ascending and descending part of the trajectory. The remaining terms on the right-hand side represent the drag force on the grain—see Eq. (C1) of Appendix C. We exploited the stretched shape of high trajectories, which implies  $v_z \ll v_x, u$ , to drop the vertical velocity components, and expressed the drag coefficient in terms of the turbulent settling velocity  $v_\infty$ . For typical dune sand with an average grain diameter  $a \approx 200 \mu\text{m}$ ,  $v_\infty \approx 27\sqrt{ga}$  [52]. The integral in Eq. (29) can roughly be approximated using the fact that  $P_H(\tilde{z}|h)$  diverges for  $\tilde{z} \rightarrow h$ ; again, only the value  $v_x(h, h)$  of the grain speed at the apex ( $z = h$ ) matters, while the shape of the whole trajectory is found to be irrelevant (and can thus not be determined within this approach). Inserting  $P_H(\tilde{z}|h) \approx 2\delta(\tilde{z} - h)\Theta(h - \tilde{z})$  in Eq. (29) and making contact with Eqs. (10) and (9b), which yield  $\Delta v_x(0, h) \propto \sqrt{h}$ , we eventually obtain

$$V_H(z) \approx u_H(z) - \sqrt{\alpha/[4\epsilon(z)]}v_\infty \quad (z \gg H). \quad (30)$$

This is of the same form as the force-balance estimate obtained by Sauermann *et al.* [17] for a representative grain that is exposed to turbulent drag and an additional (constant) bed friction. With the typical values for  $\alpha \approx 0.6$  and  $\epsilon(z \approx H) \approx 0.1$  derived in Appendix E, the ensuing prediction for the height-dependent grain velocity, Eq. (30), is found to be in

very good agreement with our simulations for the whole range  $z > z_f$ , above the focus height (see Fig. 3).

### C. Wind-dependent transport layer height

In Eq. (5) of Sec. II, we combined the splash-model predictions for the rebound probability and the average ejection height to estimate the overall value of the characteristic height  $H \approx 72a$  of the transport layer. This estimate was supported by our simulations, shown in Fig. 1(b), which, however, also revealed that  $H$  increases weakly the wind strength. And, based on the accurate prediction for the grain velocity  $V_x(z)$  in Eq. (30), we indeed expect such a wind-strength dependence of  $H$ . To calculate it quantitatively, it seems tempting to follow the relation between  $h$  and  $v_x$  given in Eq. (9b), namely  $H \approx 8[\epsilon(H_0)V_{H_0}(H_0)]^2/g$ , with  $H_0 = 72a$  and  $\epsilon(H_0) \approx 0.1$  being the wind-independent predictions of Eqs. (5) and (13), respectively. Our simulations show that the wind dependence of  $\epsilon(H)$  partly compensates for the one of  $V_H(H)$ , such that their product  $\epsilon(H)V_H(H)$  increases relatively weakly with the wind strength, but we could not obtain a good analytical estimate for the combined effect. Instead, a similar approach for the characteristic trajectory length,

$$L \approx \tilde{T}(H_0)V_{H_0}(H_0) \quad \text{and} \quad H \approx \epsilon(H_0)L, \quad (31)$$

turned out to work well if one allows for a slight phenomenological adjustment  $\tilde{T}(H_0) = 0.7T(H_0)$  of the hop time compared to Eq. (2), in order to match the theory quantitatively to our simulation data. Note that Eq. (31) leaves the characteristic aspect ratio  $H/L = \epsilon(H_0)$  independent of the wind strength, but the individual trajectories' shape invariance is broken, as expressed by the (yet unknown) dependence  $\epsilon(h)$ .

Alternatively, the wind-strength dependence of  $H$  may be taken from one of the mean-field transport models mentioned in Sec. I. In Appendix B, this is illustrated for the two-species model of Ref. [45], where the median height  $\approx 0.2H$  of the transport layer—calculated after Eq. (28)—is used to feed its prediction into our present discussion.

### D. Flux transients

Finally, we want to address what is probably the most enigmatic and most debated mesoscale property of aeolian sand transport, the so-called saturation length  $\ell_{\text{sat}}$ . This central notion was originally introduced by Sauermann *et al.* [17] to quantify how the aeolian sand transport adapts to changes in the wind over uneven topographies. Flux transients on the upwind slope of a sand dune and in the downwind wake region were discussed as two pertinent instances giving rise to quite diverse numerical values and parameter dependencies for  $\ell_{\text{sat}}$ . Later work has further elaborated on this point [5, 16, 50, 53, 54]. As an emergent mesoscale concept,  $\ell_{\text{sat}}$  is thus intrinsically context-dependent, and attempts to promote narrower definitions of the saturation length (such as the distance needed for a hopping grain to be accelerated to the fluid velocity [53] or the distance over which the sand flux saturates at the entrance of a sand bed [54]) seem counterproductive.

Arguably the most interesting saturation transients are those near the crest of a small dune, due to moderate local changes in the wind speed (rather than sand coverage). They are

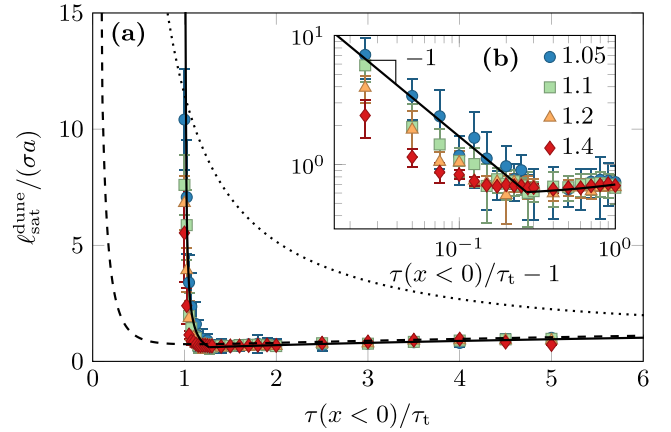


FIG. 5. “Bare” and “dressed” wind-strength-dependent saturation lengths (linear and logarithmic axes scaling). Simulation data for the bare saturation length  $\ell_{\text{sat}}$  (symbols) were obtained by fitting a linear relaxation process with decay length  $\ell_{\text{sat}}$  to the response of the height-integrated flux  $q(x)$  along the wind direction to a small step increase of the shear stress  $\tau(x)$  at  $x = 0$  (notice the improving agreement with the theoretical expectation upon approaching the ideal limit of an infinitesimal step height, given in the legend). Its power-law decay in  $\tau$  (b) close to the transport threshold  $\tau_t = 0.01\rho_g g a$  gives way to a weak growth at larger  $\tau$ , in good accord with Eqs. (31), (32), with a numerical factor  $\ell_{\text{sat}}/L = 2$  (solid lines). Under realistic field conditions, the sharp singularity at  $\tau = \tau_t$  is smeared out by intermittent wind-speed fluctuations, giving rise to the apparent “dressed” saturation length given by the right-hand side of Eq. (33), with a Weibull-distributed wind speed of variance  $0.1(u)^2$  [60] and the aerodynamic-impact threshold ratios  $\tau_{\text{ta}}/\tau_t = 1.27$  [obtained from our simulations; dashed line in panel (a)] and  $\tau_{\text{ta}}/\tau_t = 10$  (expected for wind-blown sand transport on Mars [53,62]; dotted line).

responsible for the emergence of the relevant mesoscale  $\ell_{\text{sat}}$  with respect to which aeolian dunes may be considered large or small, and which gives rise to a minimum dune length  $\mathcal{L}_{\text{min}}$  [18–20,55–57]. In Ref. [17], this particular length was predicted to decay with increasing wind strength  $\tau$ , whereas later studies argued that it might either be independent of  $\tau$  [54,58] or even grow monotonically in  $\tau$  [5,16]. To resolve the apparent conflict between these diverse proposals, we identify the saturation length in our simulations with the response length to a small wind-strength increment (to mimic the effect of the speed-up along the back of a dune within our stationary transport model).

Due to the scale separation between the minimum dune size  $\mathcal{L}_{\text{min}} \approx 10^5 a$  (see Fig. 8) and the characteristic hop length  $L = H/\epsilon(H) \approx 7.2 \times 10^2 a$ , as predicted by Eqs. (5), (13), the resulting flux gradients should not be sensitive to the heterogeneities inside the transport layer. As a consequence,  $\ell_{\text{sat}}$  can only depend on the overall transport characteristics and is thus expected to scale linearly in  $L$ . Indeed, our numerical data in Fig. 5 are consistent with

$$\ell_{\text{sat}}/L \propto 1 + \frac{\tau_{\text{ta}} - \tau}{\tau - \tau_t} \Theta(\tau_{\text{ta}} - \tau), \quad (32)$$

and conform with the expectation  $\ell_{\text{sat}} \simeq L$  above the direct aerodynamic entrainment threshold (for  $\tau > \tau_{\text{ta}}$ ). Physically, mobile grains are then abundant and their acceleration to the



stationary speed limits the adaptation to an increase in wind strength. Notice that  $L$  itself slightly increases with the wind speed, according to Eq. (31); see also Figs. 1 and 7. If the wind speed falls below the direct entrainment threshold  $\tau_{ta}$  and approaches the transport threshold  $\tau_t$ , grains not only need to be accelerated, but an increasing amount of energy and momentum has to be supplied to lift grains from the ground against gravity. The adaptation of the flux to an increase in wind speed is then limited by the number of grains gradually mobilized in successive bed collisions [17]. The lift force exerted by the wind on the bed still facilitates the splash by effectively reducing the heavy mass of the grains, which can be understood as a precursor of direct aerodynamic entrainment [59], as argued in Eq. (D5) of Appendix D. Accordingly, the net erosion rate scales with the excess shear stress  $\tau - \tau_t$ , which vanishes at the transport threshold  $\tau_t$ , causing a singular slowing-down of the adaptation of the flux to wind heterogeneities. This manifests itself in the divergence of the saturation length  $\ell_{sat}(\tau)$  at  $\tau_t$  [17]. A similar decomposition of the physics behind the saturation length according to two rate-limiting processes was previously proposed by Andreotti *et al.* [54] to interpret wind-tunnel measurements.

It is important to realize that a direct application of Eq. (32) to field data is problematic, though. Field data that do not conform with the intuitively expected scaling  $\mathcal{L}_{min} \propto \ell_{sat}$  for the minimum dune length  $\mathcal{L}_{min}$  do not necessarily indicate a failure of the theory. The reason is that the sharp peak of  $\ell_{sat}$  at  $\tau = \tau_t$ , with relative width  $(\tau_{ta} - \tau_t)/\tau_t \approx 0.27$ , is not resolved by typical field measurements, which inevitably average over some intermittent wind fluctuations. The importance of a given wind strength for the observed structure formation is determined by the erosion or deposition caused, which are proportional to the flux. We therefore propose that structural field data should be interpreted as flux-weighted averages of the corresponding “bare” theoretical predictions calculated for a fixed wind strength. In particular, the minimum dune length observed in the field should not scale in the bare saturation length but in its “dressed” version, according to

$$\mathcal{L}_{min} \propto \langle \phi \ell_{sat} \rangle_{\langle \tau \rangle} / \langle \phi \rangle_{\langle \tau \rangle}. \quad (33)$$

The average  $\langle \dots \rangle_{\langle \tau \rangle}$  is understood to extend over a range of wind-strength fluctuations around the measured average shear stress  $\langle \tau \rangle$ . The bare vertical flux

$$\phi \equiv \phi_H(0,0) \propto q_H/L \propto (\tau - \tau_t)\Theta(\tau - \tau_t)/L \quad (34)$$

vanishes at  $\tau < \tau_t$ , thereby effectively truncating the wind-strength distribution. The consequences of this are illustrated by the dashed line in Fig. 5 assuming a realistic Weibull distribution of variance  $0.05 \langle u \rangle^2$  ( $u \propto u_* \propto \sqrt{\tau}$ ) for the wind-speed fluctuations [60]. For  $\tau \gg \tau_t$ , the weakly wind-strength-dependent bare saturation length  $\ell_{sat}$  is hardly affected at all by the averaging: bare and dressed saturation length are indistinguishable in the plot. In contrast, close to the transport threshold  $\tau_t$ , the saturation length gets strongly renormalized by fluctuations. The flux-averaged or dressed saturation length as a function of the average shear stress  $\langle \tau \rangle$ —the right-hand side of Eq. (33)—has a strongly smeared-out shape compared to the bare prediction.

We incidentally find the dressed wind-strength dependence to be closely reminiscent of the form  $\ell_{sat} \propto L/(\tau/\tau_t - 1)$

originally proposed by Sauermann *et al.* [17]. This observation supports the interpretation of the measured (dressed) saturation length as an emergent hydrodynamic length scale and vindicates the use of Sauermann’s formula in past analytical and numerical studies that are at the core of our current understanding of the physics of sand dunes [61]. Similar but potentially more drastic renormalizations may be expected in applications to extraterrestrial dunes, in which the gap between the threshold shear stresses  $\tau_t$  and  $\tau_{ta}$  can be much larger than on Earth [53,62] (see Fig. 5).

#### IV. COMPARISON WITH LITERATURE DATA

After having established the accuracy of our analytical model by comparison with our simulation results, we now want to test it against a compilation of literature data. Experimental data for the height-resolved horizontal flux  $j_H(z)$  is usually approximated, with fair accuracy, by an exponential profile with a mean height on the order of a few centimeters that is almost independent of the wind strength [1]. This resonates well with our Eq. (17). However, there is apparently no clear consensus about possible deviations from the exponential form due to a possible deficit [39,63] or excess [1,49,64–67] of grains near the ground, probably because of difficulties in determining the exact number of mobile grains in the dense lower transport region. In particular, the particle tracking and laser scattering methods used in Refs. [39,63] seem prone to missing some of the mobile grains close to the bed (the ejected “reptating” grains), so that the flux in this region is most likely underestimated. In contrast, sand trap measurements in Refs. [49,64,66] reflect the pronounced near-bed excess contribution to  $j_H(z)$  that we expect from our model as a direct consequence of the splash statistics. They are indeed in remarkable agreement with the prediction of Eqs. (3)–(9a) if  $\nu$  and  $H$  are treated as free fit parameters, as illustrated in Fig. 6. The relatively small value deduced for the best-fitting power-law exponent  $\nu \approx 0.94$  could partly be a consequence of the above mentioned unavoidable systematic uncertainties in current flux measurements near the bed. More interestingly, it could also indicate that the splash for wind-blown sand grains is less efficient than for the plastic beads injected onto a quiescent bed in laboratory collision experiments [36,68], from which one infers  $\nu \approx 1.4$ . The transport layer heights  $H$  obtained from the wind-tunnel data are in very good agreement with the obtained average value and the weak wind dependence found in both our simulations and the analytical approach in Eq. (31) [Fig. 6(b)]. The field data, in contrast, yield an almost three times higher transport layer, which might be traced back to the nonequilibrium undersaturated transport conditions due to wind variations and/or due to moisture-induced stickiness of the used beach sand. This is also supported by the overall transport rates reported in Ref. [49] that are much smaller than those reported for wind-tunnel experiments.

Similar conclusions can be drawn from the comparison between literature data and the model prediction for the vertical flux  $\phi(z=0, \ell)$ , in Fig. 7. Again good agreement is obtained for  $\nu = 0.94$  and using the characteristic hop length  $L$  as a free fit parameter. The wind-tunnel data again agree well with the theoretical expectation  $L = H/\epsilon(H) \approx 10H$  based on Eq. (31), whereas field data suggest higher values.

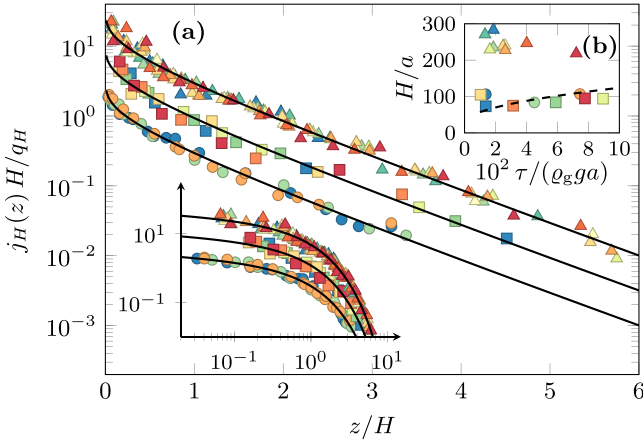


FIG. 6. (a) Theory and literature data for the height-resolved horizontal grain flux  $j_H(z)$  (linear/logarithmic height axis; data extracted from independent sources vertically shifted, for better visibility). The simple analytical model with shape-invariant grain trajectories, Eqs. (3)–(9a) (solid lines), is fitted to wind-tunnel measurements by Rasmussen and Mikkelsen [64] (dots), Rasmussen and Sørensen [66] (squares), and field data by Namikas [49] (triangles) for various wind strengths  $\tau$ , using  $\nu$  and  $H$  as free global fit parameters. This yields  $\nu = 0.94$  and the data for  $H$  shown in the inset (b) with the improved model prediction from Eq. (31) (dashed line). While laboratory data and theory agree well, field measurements (triangles) consistently find higher trajectories.

Besides such height-resolved characteristics for the stationary transport, our approach also gives access to its transient behavior, as shown in Sec. III D. There, we argued that

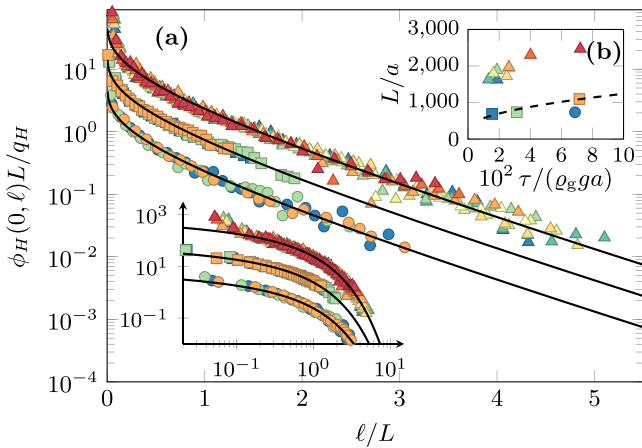


FIG. 7. (a) Theory and literature data for the vertical sand flux  $\phi_H(z=0, \ell)$  through the sand bed at a downwind distance  $\ell$  from the end of the sand bed (linear/logarithmic height axis; data extracted from independent sources vertically shifted, for better visibility). The simple analytical model with shape-invariant grain trajectories, Eq. (19), is fitted to wind-tunnel measurements by Ho *et al.* [41] (dots) and Rasmussen *et al.* [1] (squares), and to field data by Namikas [49] (triangles) for various wind strengths  $\tau$ , using the value  $\nu = 0.94$  obtained from Fig. 6. (b) The trajectory length  $L$  (the only free fit parameter) compared to the theoretical expectation  $H/\epsilon(H) \approx 10H$  [45] (dashed line). Again, laboratory data and theory agree well, while field measurements consistently find longer (and higher) trajectories.

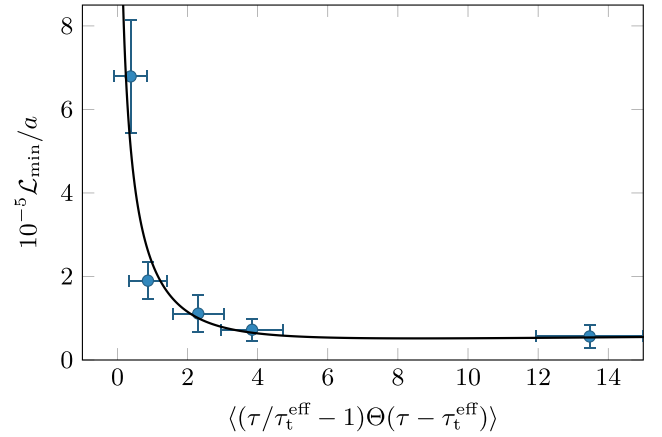


FIG. 8. Field data for the minimum dune length  $\mathcal{L}_{\min}$  reported by Andreotti *et al.* [54] (symbols) compared to the dressed saturation length  $\langle \phi \ell_{\text{sat}} \rangle / \langle \phi \rangle$  from Eqs. (32), (31) (line). The expected linear relation is recovered for Weibull-distributed intermittent wind-speed fluctuations of variance  $0.05 \langle u \rangle^2$  [60] and an effective threshold shear stress  $\tau_t^{\text{eff}} = 0.12 \tau_t$ , suggesting a factor of proportionality of about 35 in Eq. (33), reasonably close to previous theoretical estimates [55,56].

the minimum dune size measured in the field should be correlated with a “dressed” saturation length, averaged over some intermittent wind fluctuations. This hypothesis is tested against field data for the minimum dune length  $\mathcal{L}_{\min}$  [54] in Fig. 8. The authors quantify the wind strength by the average  $\langle (\tau / \tau_t^{\text{eff}} - 1) \Theta(\tau - \tau_t^{\text{eff}}) \rangle$ . Here  $\tau_t^{\text{eff}}$  is an effective transport threshold that is measured in the field under fluctuating wind conditions. Intriguingly, this procedure yields a relatively small value  $\tau_t^{\text{eff}}$  compared to theoretical expectations and laboratory values for  $\tau_t$  [53,69,70], in line with our finding of a substantially renormalized threshold in Fig. 5. Figure 8 moreover demonstrates good agreement of the field data with Eq. (33) for Weibull-distributed wind speeds  $u$  with variance  $0.1 \langle u \rangle^2$  [60],  $\tau_t^{\text{eff}} \approx 0.12 \tau_t$ . Even the ratio  $\mathcal{L}_{\min} \langle \phi \rangle / \langle \phi \ell_{\text{sat}} \rangle \approx 35$  between the minimum dune size and the dressed saturation length, which we used as a free fit parameter in the comparison, turns out to be reasonably close to (about 1.5 times larger than) the value predicted by numerical solutions of two- and three-dimensional versions of the minimal model for aeolian sand dunes [55,56]. This further supports our interpretation and underscores the importance of the distinction between bare and dressed mesoscale quantities in the analysis of field data.

For computational details and further theoretical and experimental support for an essentially constant value of  $\mathcal{L}_{\min} / \ell_{\text{sat}}$  (rather than a constant  $\ell_{\text{sat}}$  [54]), we refer the reader to Appendix F.

## V. SUMMARY AND CONCLUSIONS

We have developed an analytically tractable model for aeolian sand transport that resolves the whole distribution of grain trajectories. Our analytical approach was heavily based on a recently proposed model for grain hopping on a granular bed that admits an analytical parametrization of the splash [36], and guided and validated by coarse-grained computer

simulations. The core element of our model is the physically well grounded expression for the hop-height distribution in Eq. (3), which is complemented by the ballistic approximations in Eqs. (2)–(7a) for the grain trajectories. This combination allowed us to derive analytical predictions for various non-trivial mesoscale characteristics of the aeolian transport layer, among them the vertical and horizontal grain flux distributions and the saturation length, which we found to be in excellent agreement with an extensive compilation of independently generated field and wind-tunnel data using a consistent set of model parameters for the grain-scale physics. The comparison revealed that it is necessary to distinguish so-called “bare” mesoscale relations (corresponding to precisely controlled ambient conditions) from their “dressed” counterparts that involve an average over fluctuations. Altogether, we have thus provided solid evidence that our approach correctly captures the splash and transport statistics and provides a canonical theoretical formalism for various height-resolved mesoscale properties. It can be employed as a default in calculations when the actual profiles are not known, or as an alternative fit function (in place of the usual exponential) to extract parameters, such as the mean hop height, from experimental data. And it suggests itself as a sound and versatile starting point for a precise and highly efficient modeling of a wealth of applications, from aeolian structure formation over dust emission to desertification.

#### ACKNOWLEDGMENTS

We thank A. Meiwald for fruitful discussions during the early stages of this work, which was supported by a grant from the German-Israeli Foundation for Scientific Research and Development (GIF). We also acknowledge the KITP in Santa Barbara and the MPI-PKS in Dresden for their hospitality during our visits, which were financially supported by the National Science Foundation under Grant No. NSF PHY-1125915, the MPI-PKS Visitors Program, and the German Academic Exchange Service (DAAD) through a Kurztstipendium for M.L.

#### APPENDIX A: $q_H(z)$ AND $j_H(z)$ HEIGHT-DEPENDENT GRAIN CONCENTRATION AND FLUX FOR SHAPE-INVARIANT TRAJECTORIES

For shape-invariant trajectories, i.e.,  $\epsilon(h) = \epsilon(H)$  independent of the hop height  $h$ , Eqs. (3)–(9a) yield

$$\begin{aligned} \frac{q_H(z)}{\rho_H/H} &= \frac{\Gamma(1/2 - \nu)}{2\Gamma(3/2 - \nu)} M(1/2, 1/2 + \nu, -z/H) \\ &+ \frac{\sqrt{\pi}\Gamma(\nu - 1/2)}{2\Gamma(3/2 - \nu)\Gamma(\nu)} (z/H)^{1/2-\nu} \\ &\times M(1 - \nu, 3/2 - \nu, -z/H) \end{aligned} \quad (\text{A1})$$

and

$$\begin{aligned} \frac{j_H(z)}{q_H/H} &= \frac{\Gamma(1 - \nu)}{2\Gamma(2 - \nu)} M(1/2, \nu, -z/H) \\ &+ \frac{\sqrt{\pi}\Gamma(\nu - 1)}{2\Gamma(2 - \nu)\Gamma(\nu - 1/2)} (z/H)^{1-\nu} \\ &\times M(3/2 - \nu, 2 - \nu, -z/H) \end{aligned} \quad (\text{A2})$$

for the grain mass concentration and flux, respectively. Here,

$$M(a, b, z) = \frac{\Gamma(b)}{\Gamma(a)\Gamma(b-a)} \int_0^1 ds e^{zs} s^{a-1} (1-s)^{b-a-1} \quad (\text{A3})$$

denotes Kummer’s confluent hypergeometric function and  $q_H = \Gamma(2 - \nu)\Gamma(3/2 - \nu)^{-1} \rho_H v_x(H)$  is the height-integrated grain flux. The asymptotic forms in Eqs. (16) and (17) can be directly inferred from Eqs. (A1) and (A2), respectively. For  $z \gg H$ , we may estimate the dependence of  $j_H(z) \propto [\epsilon(H)/\epsilon(z)](z/H)^{1/2-\nu} e^{-z/H}$  on  $\epsilon(z)$  using Laplace’s method to approximate the integral of the form

$$\int_z^\infty dh f(h) \frac{e^{-h/H}}{\sqrt{h-z}} \sim \sqrt{\pi H} f(z) e^{-z/H} \quad (\text{A4})$$

after substituting  $h = z \cosh^2 \theta$ , expanding the exponent  $(h/H) \cosh^2 \theta$  around  $\theta = 0$ , and integrating over all  $\theta > 0$ .

#### APPENDIX B: MEDIAN TRANSPORT HEIGHT AND TWO-SPECIES PREDICTION FOR $H$

The median height  $z_m$  of the transport layer is implicitly defined through

$$\begin{aligned} 1/2 &= \int_0^{z_m} dz j_H(z)/q_H \\ &= 1/2 - M(-1/2, \nu - 1, -z_m/H)/2 \\ &+ \frac{\sqrt{\pi}\Gamma(\nu - 1)}{4\Gamma(\nu - 1/2)\Gamma(3 - \nu)} (z_m/H)^{2-\nu} \\ &\times M(3/2 - \nu, 3 - \nu, -z_m/H), \end{aligned} \quad (\text{B1})$$

where we inserted Eq. (A2) to evaluate the integral in the second line. For  $\nu = 1.4$ , as predicted from the splash model [36] underlying Eq. (3), this relation can be solved numerically, which yields  $H \approx 5.8z_m$ , i.e.,  $z_m \approx 0.17H$ . The smaller value  $\nu = 0.94$  that we used to fit the laboratory and field data in Figs. 6 and 7 corresponds to a larger median height of value  $z_m \approx 0.43H$ .

This relation can be used to make contact with the two-species model for aeolian sand transport proposed in Ref. [45]. We therefore obtain the two-species prediction for  $z_m$  assuming that it lies above the reptation layer, where the (saltation) grain flux decays exponentially. This yields

$$H \approx 0.76 \ln[2/(1 + q^{\text{rep}}/q^{\text{sal}})](v^{\text{sal}})^2/(2g), \quad (\text{B2})$$

where  $q^{\text{rep}}$  and  $q^{\text{sal}}$  are the reptation and saltation contributions to the height-integrated grain flux, respectively. The numerical prefactor that relates the saltation velocity  $v^{\text{sal}}$  (computed in Ref. [45]) to the vertical component  $v_z^{\text{sal}}(z=0)$  of the rebound velocity of a saltating grain (required here) is determined by fitting this relation to our simulation data for  $H$ , shown in Fig. 1(b). The so obtained value  $v_z^{\text{sal}}(z=0)/v^{\text{sal}} \approx 0.13$  of this effective restitution coefficient is in accord with what we expect from the splash model of Ref. [36].

### APPENDIX C: COMPUTER SIMULATIONS

In our computer simulations, the trajectory of each grain is obtained by solving the equations of motion

$$\dot{\mathbf{v}} = \frac{3C_D}{4\sigma a} |\mathbf{u} - \mathbf{v}|(\mathbf{u} - \mathbf{v}) + \mathbf{g}. \quad (\text{C1})$$

Here,  $\mathbf{v} \equiv \mathbf{v}(t) = \dot{\mathbf{r}}(t)$  is the velocity of the grain at time  $t$ ,  $\mathbf{r}(t)$  its position,  $\mathbf{u} \equiv \mathbf{u}[\mathbf{r}(t), t]$  the wind velocity field,  $\mathbf{g} \equiv -g\mathbf{e}_z$  the gravitational acceleration,  $\sigma \equiv \rho_g/\rho_a$  the grain-air mass-density ratio, and  $a$  the grain diameter. For the particle drag coefficient, we use the accurate expression [52]

$$C_D = \frac{1}{3} [A + \sqrt{A^2 + 16B\nu_{\text{air}}/(a|\mathbf{u} - \mathbf{v}|)}]^2 \quad (\text{C2})$$

( $A \approx 0.95$  and  $B \approx 5.12$  for natural sand), where the viscous contributions to the drag are quantified by the Reynolds number  $a|\mathbf{u} - \mathbf{v}|/\nu_{\text{air}}$ , with the kinematic viscosity  $\nu_{\text{air}} \approx 1.5 \times 10^{-5} \text{ m}^2 \text{ s}^{-1}$  for air. To compute the grain trajectories with sufficient accuracy to resolve the short hops of the low-energy ejecta, the equations of motion are solved using a standard Euler forward integration scheme with a discretization time of  $0.1\sqrt{a/g}$  (corresponding to about 0.45 ms for a grain diameter of 200  $\mu\text{m}$ ).

Assuming a horizontally uniform stationary air flow in the  $x$  direction, the only nonvanishing component of the air velocity  $\mathbf{u}$  is given by the height-dependent wind speed  $u(z) \equiv \mathbf{u} \cdot \mathbf{e}_x$ . For constant pressure, the Reynolds-averaged Navier-Stokes equations reduce to the relation

$$\partial_z \tau_a(z) = F_x(z) \quad (\text{C3})$$

between the  $xz$  component  $\tau_a$  of the Reynolds stress tensor for the air and the body force  $F_x(z)$  exerted by the grains on the air [22]. Without particles,  $F_x(z) = 0$ , this means that  $\tau_a = \tau$  is independent of  $z$  and given by the overall shear stress  $\tau$ . That this holds above the transport layer for  $z \rightarrow \infty$  provides us with the boundary condition for integrating Eq. (C3) for  $F_x(z) \neq 0$ ,

$$\tau - \tau_a(z) = \int_z^\infty d\tilde{z} F_x(\tilde{z}) \equiv \tau_{g,H}(z), \quad (\text{C4})$$

which defines the grain-borne shear stress  $\tau_{g,H}$  [42]. In the simulations, the contribution of each grain to  $F_x$  is obtained as the negative  $x$  component of the right-hand side of Eq. (C1) times the grain mass  $(\pi/6)\rho_g a^3$ . The grain stress  $\tau_{g,H}$  is pre-averaged over a short time interval  $\sqrt{a/g}$  (ten time steps), in order to obtain smooth profiles. With Eq. (C4), the Prandtl turbulence closure  $\kappa^2 \rho_a z^2 [u'(z)]^2 = \tau_a(z)$  yields the height-dependent wind speed

$$u(z) = \frac{1}{\kappa \sqrt{\rho_a}} \int_{z_0}^z d\zeta \frac{\sqrt{\tau - \tau_{g,H}(\zeta)}}{\zeta}. \quad (\text{C5})$$

The roughness height  $z_0$ , where the wind speed nominally vanishes, is set to  $a/10$  by convention.

Equations (C1)–(C5) have to be complemented by a set of boundary conditions describing the sand bed collisions. They are taken from an extended version of the coarse-grained splash model proposed in Ref. [36] that accounts for wind-induced lift forces acting on the bed grains, as briefly outlined in Appendix D. To keep the computation simple, we neglect midair collisions. They are most frequent in the dense reptation

layer close to the bed [27,71] and therefore probably well captured by appropriate effective bed parameters, except under extreme wind conditions [15].

### APPENDIX D: SPLASH MODEL

For convenience, we now outline the key properties of the splash model of Ref. [36] used to quantify the sand bed collisions in the numerical simulations (Appendix C) and in our analytical derivation of Eq. (3) for the hop-height distribution. Its original version was developed assuming vacuum conditions. For our present purpose, we extend it to effectively account for the drag and lift forces exerted on the bed grains by the wind.

The rebound of a hopping grain from a rough immobile bed is quantified in terms of the mean total restitution coefficient  $\bar{e}$  and rebound angle  $\theta'$  for a given impact angle  $\theta$ . Averaging over all possible collision geometries gives

$$\bar{e} \equiv |\mathbf{v}'|/|\mathbf{v}| = \beta_s - (1 - \alpha_s^2/\beta_s^2)\beta_s\theta/2, \quad (\text{D1})$$

where  $\alpha_s \approx 0.20$  and  $\beta_s \approx 0.63$  were calibrated [36] with collision experiments by Beladjine *et al.* [68]. The rebound angle  $\theta'$  is randomly drawn from the distribution

$$P(\theta'|\theta) = (2/\gamma_s)(1 + \theta'/\theta) \ln[\gamma_s\theta/(\theta + \theta')^2] \quad (\text{D2})$$

defined in the interval  $0 < \theta' + \theta < \sqrt{\gamma_s\theta}$  and set to zero outside. We multiplied the parameter  $\gamma_s = (9/2)(1 + \alpha_s/\beta_s)^2$  by an order-unity factor  $3\sqrt{3}/4 \approx 1.3$  for harmonization with the approach underlying Eq. (D1). Note that Eq. (D2) can yield negative rebound angles, corresponding to a grain that gets trapped in the bed. Rebounding grains with  $|\mathbf{v}'| \sin\theta' \geq \sqrt{2}$  fail to leap over the downwind bed neighbor grain and are thus not propagated further. To avoid discretization artifacts at the ground, which become apparent in height-resolved quantities like the grain concentration or the grain shear stress, we distribute the initial height of a grain ricocheted off the bed uniformly between  $z = 0$  and  $z = \delta t |\mathbf{v}'| \sin\theta'$ , where  $\delta t$  is the duration of one time step in the simulations.

To mimic the statistics of the ejecta close to the ground, we set the ejection angle to  $90^\circ$  and draw the kinetic energy of the ejected grains from the log-normal distribution [47]

$$P(E'_{\text{ej}}|E) = \frac{1}{\sqrt{2\pi}\sigma E'_{\text{ej}}} \exp\left[-\frac{(\ln E'_{\text{ej}} - \mu)^2}{2\sigma^2}\right] \quad (\text{D3})$$

with the energy  $E = m\mathbf{v}^2/2$  of the impacting grain of mass  $m = (\pi/6)\rho_g a^3$  and  $\sigma = \sqrt{\lambda \ln 2}$ ,  $\mu = \ln[(1 - \bar{e}^2)E] - \lambda \ln 2$ ,  $\lambda = 2 \ln[(1 - \bar{e}^2)E/E_a]$ , and  $E_a = mga$ . The number

$$N'_2 = 0.06[(1 - \bar{e}^2)E/E_a]^\kappa \int_{E_{\text{eff}}}^\infty dE'_2 P(E'_2|E) \quad (\text{D4})$$

of ejected bed grains again follows from the same energy balance approach underlying Eq. (D3), with the value  $\kappa = (2 - \ln 2) \ln 2 \approx 0.9$  of the exponent close to 1.

In Eq. (D4), we extended the original splash model of Ref. [36] to account for drag and lift forces exerted on the bed grains. We therefore introduced an effective minimum energy  $E_{\text{eff}} < E_a$  required for a bed grain to be mobilized during the collision. Rewriting it in terms of an effective mass  $m_{\text{eff}} \equiv E_{\text{eff}}/(ga)$  of a bed grain exposed to the turbulent



shear flow, we estimate its value following Bagnold's classic prediction of the shear stress value at the threshold of grain movement [2]. Balancing the net torque due to the horizontal drag force  $F_D$  and vertical gravitational force  $mg$  acting on a bed grain of mass  $m$  with the purely gravity-induced torque of a grain of same size but different mass  $m_{\text{eff}}$ , one obtains  $\sin(\beta_s)F_D - \cos(\beta_s)m = -\cos(\beta_s)m_{\text{eff}}$ , for an angle  $\beta_s$  between the horizontal and the axis crossing the point of support and the center of the lifted bed grain. This yields

$$E_{\text{eff}}/E_a = m_{\text{eff}}/m = 1 - \tau_a(z=0)/\tau_{\text{ta}}. \quad (\text{D5})$$

Here, we expressed the drag force  $F_D \propto \pi(a/2)^2 \tau_a(z=0)$  in terms of the air shear stress at the ground and identified its threshold value  $\tau_{\text{ta}} \propto (2/3)b/[\tan(\beta_s)]$ , above which bed grains are mobilized by the flowing air (corresponding to a vanishing effective weight,  $m_{\text{eff}} = 0$ ). We set  $\tau_{\text{at}} = 1.2 \times 10^{-2} \rho_g g a$ , yielding a minimum shear stress  $\tau_t \approx 0.9 \times 10^{-2} \rho_g g a$  required to maintain transport (once initialized), which is in agreement with typical values for the ratio  $\tau_{\text{at}}/\tau_t \approx 0.8$  observed in wind-tunnel experiments [2,72].

#### APPENDIX E: SPLASH PREDICTIONS FOR $\nu$ , $H$ , $\epsilon$ , $\alpha$

The quantitative description of the bed collisions outlined in Appendix D allows us to estimate typical values for the power-law exponent  $\nu$ , the trajectory aspect ratio  $\epsilon(H)$ , and the effective restitution coefficient  $\alpha$  introduced in Sec. II as model parameters.

Relating the ejection energy  $E'_{\text{ej}} = mgh$  to the hop height, Eq. (D3) provides us with the hop-height distribution per impacting grain of energy  $E$ . As  $E \gg mga$ , i.e.,  $\mu \gg \ln(mga)$ , it is expanded to  $\propto h^{-\nu}$ , with  $\nu$  given in Eq. (4). Multiplying it with the hop time  $T(h)$ , Eq. (2), it yields the hop-height distribution  $P_H(h \ll H) \propto h^{1/2-\nu}$  per time step.

Next, we estimate the characteristic height  $H$  of the transport layer at low-wind conditions close to the transport threshold employing the splash-model prediction for collisions between saltating grains and the bed grains. We start with the relation

$$H = -\overline{E_{\text{ej}}}(E)/(mg \ln P_{\text{reb}}) \quad (\text{E1})$$

between  $H$  and the rebound probability  $P_{\text{reb}}$  derived in the text below Eq. (3). Here, we expressed the mean ejection height  $\overline{h_{\text{ej}}}(E) = \overline{E_{\text{ej}}}(E)/(mg)$  for a given impact energy  $E$  in terms of the mean ejection energy  $\overline{E_{\text{ej}}}(E)$ . The latter is obtained from the distribution in Eq. (D3) as

$$\begin{aligned} \overline{E_{\text{ej}}}(E) &= \frac{\int dE'_{\text{ej}} P(E'_{\text{ej}}|E) \Theta(E'_{\text{ej}} - E_a) E'_{\text{ej}}}{\int dE'_{\text{ej}} P(E'_{\text{ej}}|E) \Theta(E'_{\text{ej}} - E_a)}, \\ &= \frac{\text{erfc}[(\ln E_a - \mu - \sigma^2)/(\sqrt{2}\sigma)]}{\text{erfc}[(\ln E_a - \mu)/(\sqrt{2}\sigma)]} e^{\mu + \sigma^2/2}, \end{aligned} \quad (\text{E2})$$

where the integrals extend over all energies  $E'_{\text{ej}} > E_a$  above the minimum ejection energy  $E_a = mga$ . As the impact energy  $E$  is determined by the difference  $u(H) - v_\infty$  between the wind speed at height  $H$  and the turbulent settling velocity  $v_\infty \approx 27\sqrt{ga}$ , we may approximate it as

$$E \approx (m/2)[u(H) - v_\infty]^2. \quad (\text{E3})$$

Making use of the low-transport conditions assumed here, the wind-speed profile in Eq. (26) simplifies to  $u(z) = (u_{*t}/\kappa) \ln(z/z_0)$ , with  $u_{*t}^2/(ga) \approx 0.01\sigma \approx 20$ ,  $\kappa = 0.4$ , and  $z_0 \approx a/10$ . We can now insert this relation, together with Eqs. (E2), (E3) and the rebound probability  $P_{\text{reb}} \approx P_{\text{reb}}(h \gg a) = \int_0^\infty d\theta' P(\theta'|\theta)$  as predicted by Eq. (D2), into Eq. (E1), which yields  $H(\theta)$  as a monotonically decreasing function of the impact angle  $\theta$ . For reasonable values  $\theta = 90^\circ \dots 90^\circ$ , it varies within the range  $H/a \approx 190 \dots 54$ . To determine its actual value, we use the relation  $\epsilon(H) \approx \tan(\theta)/4$  between trajectory aspect ratio and impact angle, as inferred from Eq. (9b), and combine it with

$$\epsilon(H) = H/L \approx H/\{T(H)[u(H) - v_\infty]\}, \quad (\text{E4})$$

where we approximated the hop length with the flight time  $T(H)$ , given in Eq. (2), times the typical grain speed. Putting all together, we obtain a transcendental equation for the impact angle  $\theta$ :

$$\cot(\theta)4H(\theta)/T[H(\theta)] \approx u[H(\theta)] - v_\infty. \quad (\text{E5})$$

With the parameters listed above, it is solved by  $\theta \approx 14.5^\circ$ , for which Eqs. (5) and (13) yield  $H = H(\theta) \approx 72a$  and  $\epsilon(H) \approx 0.1$ , respectively.

While trajectories of height on the order of  $H$  are crucially influenced by the impactor-bed rebound, the shape of small trajectories of height  $h \ll H$  is mainly dictated by the characteristics of the ejecta created during these bed collisions. To estimate the height dependence  $\epsilon(h)$  of their aspect ratio, we simplify the equations of motion, Eq. (C1), as follows. Since  $v_z \ll u$ , vertical and horizontal motion decouple, and thus

$$\dot{v}_x \approx L_D^{-1}[u(h) - v_x]^2, \quad (\text{E6})$$

with the constant drag length  $L_D = 4\sigma a/(3C_D^\infty)$ , where  $C_D^\infty \approx 1.2$  is the strong-turbulence limit of the drag coefficient computed from Eq. (C2) for vanishing air viscosity  $\nu_{\text{air}} = 0$ , i.e.,  $\text{Re}_g \rightarrow \infty$ . We further replaced the height-dependent wind speed  $u(z)$  in the drag relation by the constant value  $u(h)$  taken at the height of the trajectory. It is computed using the above relation for threshold conditions [which also holds for  $\tau > \tau_t$ , as  $u(z < H)$  exhibits the universal  $\tau$ -independent shape obtained in Eq. (26)]. For the initial condition  $v_x(t=0) = 0$  and the total flight time  $T(h)$ , the time integral of the solution  $v_x(t) = u(h)^2 t/[L_D + u(h)t]$  of Eq. (E6) readily yields the hop length

$$h/\epsilon(h) \approx T(h)u(h) - L_D \ln[1 + T(h)u(h)/L_D] \quad (\text{E7})$$

for  $h \ll H$ . While the overall value of  $\epsilon(h)$  obtained from this estimate is found to be a bit too large (by a factor of  $1/0.65 \approx 1.5$ ), its qualitative form is indeed in very good agreement with our simulations (even for intermediate heights  $h \approx H$ ), as illustrated in Fig. 9. Inserting Eq. (2) for  $T(h)$  together with the scaling relations  $u(h) \sim \sqrt{\sigma g a} \ln(h/z_0)$  and  $L_D \sim \sigma a$ , and expanding the right-hand side of Eq. (E7) for  $h \ll \sigma a$  [equivalent to  $T(h)u(h) \ll L_D$ ], it becomes  $\epsilon(h) \propto \ln(h/z_0)^{-2}$ . For  $h \gg z_0$ , the  $h$  dependence is (locally) very close to a power law with an exponent of value  $-2/\ln(h/z_0)$  that varies only weakly as  $h$  gets larger. Substituting the typical ejection height  $\langle h \rangle_H \approx 7a$  obtained in Eq. (28) [or  $h_{\text{ej}H} \approx 10a$  from (E2)] for  $h$ , this exponent takes the value  $0.47 \approx 1/2$ ,

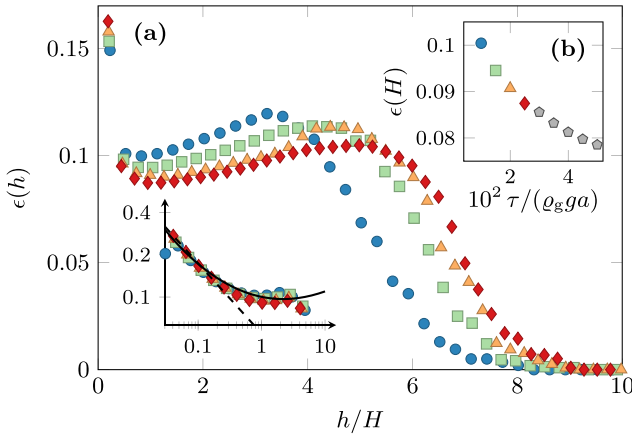


FIG. 9. Trajectory aspect ratio  $\epsilon \equiv h/l$  for various wind strengths, as obtained from our simulations. For most mesoscale measures, its dependence on the hop height  $h$  is negligible (a), as is the weak dependence on the wind shear stress  $\tau$ , as illustrated for the aspect ratio  $\epsilon(H)$  of the characteristic trajectory (b). However, the height-resolved grain stress, Eq. (18), crucially depends on the power-law decay for  $h \ll H$ , which is better resolved on the logarithmic scale in the left inset (same data logarithmically binned), solid and dashed lines representing Eq. (E7) (scaled by an empirical prefactor 0.65) and the power law  $\epsilon \propto h^{-1/2}$ , respectively.

which gives rise to the first line of Eq. (14). The applicability of this power-law approximation for  $h \ll H$  is supported by the comparison with our simulations in Fig. 9.

We eventually derive a splash-model prediction for the effective restitution coefficient  $\alpha$ , introduced in Eq. (10). Identifying  $v_x(h)$  with the average of the horizontal impact and rebound velocities, it is related to the total restitution  $\bar{e}$  and the impact and rebound angle  $\theta, \theta'$  via

$$\alpha = 2(\cos \theta - \bar{e} \cos \theta') / (\cos \theta + \bar{e} \cos \theta'). \quad (\text{E8})$$

With Eqs. (D1), (D2),  $\alpha$  takes values between 0.45 (for  $\theta = 0$ ) and 0.64 (at  $\theta \approx 90^\circ$ ). For the typical impact angle  $\theta \approx 90^\circ$  obtained from Eq. (E5), we get  $\alpha \approx 0.6$ .

## APPENDIX F: MINIMUM DUNE SIZE

We provide a theoretical estimate for the minimum dune length  $\mathcal{L}_{\min}$ , for which literature field data are shown in Fig. 5. To this end, we employ a slightly improved version of the linear stability analysis proposed in Refs. [20,57]. It identifies  $\mathcal{L}_{\min}$  with the wavelength of the (initially) fastest growing mode of a weakly perturbed flat sand bed. The starting point is the out-of-phase response of shear stress and sand transport to weak perturbations of a flat bed [18,19]. In Ref. [57], Andreotti and coworkers used the generic formula  $q_{\text{sat}} \propto \tau^\chi (\tau - \tau_t)$  for the saturated flux, which is *indirectly* slope-dependent via the variation of the local shear stress  $\tau$  and the threshold value  $\tau_t$ . However, they neglected the *direct* slope dependence, which obtains even for fixed wind parameters, and should be accounted for, to first order in  $h'$ , according to

$$q_{\text{sat}} \propto \tau^\chi (\tau - \tau_t) (1 - h' \cot \theta_f), \quad (\text{F1})$$

where  $\theta_f$  is the friction angle. This direct slope dependence of  $q_{\text{sat}}$  was first predicted by Bagnold and later validated by Iversen and Rasmussen [73], who obtained  $\theta_f \approx 40^\circ$  for typical dune sand (with grain diameter  $a \geq 170 \mu\text{m}$ ). Equation (F1) can also be derived from the continuum saltation model by Sauermaun *et al.* [17] if we extend its kinematics to sloped beds. Accounting for the gravitational force  $-gh'$  in the momentum balance, Eq. (33) in Ref. [17], we obtain

$$q_{\text{sat}} \propto (v_0/g)(\tau - \tau_t)(1 - h'\alpha v_\infty/v_0). \quad (\text{F2})$$

Here, the turbulent settling velocity  $v_\infty$  accounts for the bed friction and is equal to the difference between the wind speed and the steady-state transport velocity  $v_0$  over the unperturbed bed. For moderate wind strengths, i.e.,  $\tau \approx \tau_t$ ,  $v_0$  is independent of  $\tau$ , corresponding to  $\chi = 0$ , and the coefficient  $\alpha v_\infty/v_0$  takes values on the order of 0.5 for typical dune sand, which corresponds to  $\theta_f \approx 60^\circ$  in Eq. (F1), in reasonable agreement with the phenomenological law.

For the stability analysis, we follow Fourri re *et al.* [57] and expand the perturbation  $\delta q_{\text{sat}} = q_{\text{sat}} - q_{\text{sat}0}$  of the saturated flux from its flat bed value  $q_{\text{sat}0}$  to first order in the perturbation  $\delta h$  of the bed profile. From Eq. (F1), we obtain its Fourier transform  $\delta \hat{q}_{\text{sat}} = \int dx \delta q_{\text{sat}} e^{-ikx} \propto \tau_0^{1+\chi} (A_q + iB_q)k \delta \hat{h}$  with

$$\begin{aligned} A_q &= A_\tau + \chi A_\tau (1 - \tau_{t0}/\tau_0), \\ B_q &= B_\tau + \chi B_\tau (1 - \tau_{t0}/\tau_0) - \cot \theta_f, \end{aligned} \quad (\text{F3})$$

where we used the shear stress perturbation  $\delta \hat{\tau} = \tau_0(A_\tau + iB_\tau)k \delta \hat{h}$  (for  $k \geq 0$ ) and the slope-dependent threshold  $\delta \hat{\tau}_t = ik \delta \hat{h} \cot \theta_f$ . Following the convention, we denote the unperturbed shear stress over a flat ground far away from the obstacle by  $\tau_0$  (the subscript was suppressed in the main text). Only the  $\tau_0$ -independent term  $\cot \theta_f$  in the expression for  $B_q$  differs from the result  $(\tau_t/\tau_0) \cot \theta_f$  by Fourri re *et al.*, who neglected the direct slope dependence of  $q_{\text{sat}}$ . While this may seem to be a minor change of the original argument, it yields a qualitatively different result. Combining the linearized differential equation for the flux evolution with mass conservation  $\partial_t h \propto -\partial_x q$  for the sand bed profile  $h$ , the ratio  $\mathcal{L}_{\min}/\ell_{\text{sat}}$  of the wavelength of the fastest growing mode to the saturation length follows as a function of the ratio  $A_q/B_q$ . For  $\mathcal{L}_{\min}/\ell_{\text{sat}} \gg 1$ , it scales as

$$\mathcal{L}_{\min}/\ell_{\text{sat}} \sim 3\pi A_q/B_q. \quad (\text{F4})$$

Substituting  $A_q$  and  $B_q$  from Eq. (F3), we see that  $\mathcal{L}_{\min}/\ell_{\text{sat}}$  decreases with increasing  $\tau_0$  as long as  $\chi > 0$ . This is qualitatively similar to what was obtained by Fourri re *et al.* neglecting the experimentally well established and theoretically derived rightmost factor in Eq. (F1). However, for the theoretically expected and generally accepted value  $\chi = 0$ , the ratio  $A_q/B_q = A_\tau/(B_\tau - \cot \theta_f)$  becomes independent of  $\tau_0$ , and so does  $\mathcal{L}_{\min}/\ell_{\text{sat}}$ . Evidently, the direct slope dependence of the flux, represented by the friction angle  $\theta_f$ , can be understood as an effective renormalization of the symmetry-breaking part of the driving wind field perturbation, quantified by  $B_\tau$ . This correction crucially affects the absolute value of  $A_q/B_q$ , which diverges at  $B_\tau \rightarrow \cot \theta_f \approx 1.2$ . The numerical values of the coefficients  $A_\tau$  and  $B_\tau$  can be estimated as functions of the dimensionless hydrodynamic bed roughness  $\eta_0$ . Using for simplicity the analytical dependencies  $A_\tau(\eta_0)$  and  $B_\tau(\eta_0)$

calculated by Hunt and coworkers [74] (see Fig. 2 of Ref. [19]), the divergence of  $A_q/B_q$  is expected near  $\eta_0 \approx 1.7 \times 10^{-5}$ . We can match the fit result  $\mathcal{L}_{\min}/\ell_{\text{sat}} \approx 35$  obtained from Fig. 5 for  $\eta_0 \approx 4.0 \times 10^{-3}$ , which lies in the estimated range  $10^{-4}$  to  $10^{-2}$  [57] for  $\eta_0$  for typical sand dunes (corresponding to  $\mathcal{L}_{\min}/\ell_{\text{sat}} \approx 30 \dots 140$ ).

In summary, we showed that an improved version of the linear stability analysis proposed by Fourrière *et al.* yields a  $\tau_0$ -independent ratio  $\mathcal{L}_{\min}/\ell_{\text{sat}}$  if the experimentally and theoretically well established form of the wind-strength-

dependent sand flux given by Eq. (F1) with  $\chi = 0$  is employed. Together with the experimentally observed wind dependence of the minimum dune size  $\mathcal{L}_{\min}$  (see Fig. 5), this implicates that the saturation length  $\ell_{\text{sat}} \propto \mathcal{L}_{\min}$  must strongly decrease with increasing wind strength. It is argued in the main text that this can be rationalized by a strong renormalization of the effective saturation length by intermittent turbulent-wind-strength fluctuations near the threshold rather than by a rapid decay of  $\mathcal{L}_{\min}/\ell_{\text{sat}}$  with increasing  $\tau_0$  and a constant saturation length, as previously proposed [54,57].

- 
- [1] K. R. Rasmussen, A. Valance, and J. Merrison, *Geomorphology* **244**, 74 (2015).
- [2] R. A. Bagnold, *The Physics of Blown Sand and Desert Dunes* (Methuen, London, 1941).
- [3] O. Durán, P. Claudin, and B. Andreotti, *Aeolian Res.* **3**, 243 (2011).
- [4] J. F. Kok, E. J. R. Parteli, T. I. Michaels, and D. B. Karam, *Rep. Prog. Phys.* **75**, 106901 (2012).
- [5] T. Pähtz, J. F. Kok, E. J. R. Parteli, and H. J. Herrmann, *Phys. Rev. Lett.* **111**, 218002 (2013).
- [6] T. E. Barchyn, R. L. Martin, J. F. Kok, and C. H. Hugenholtz, *Aeolian Res.* **15**, 245 (2014).
- [7] J. T. Jenkins and A. Valance, *Phys. Fluids* **26**, 073301 (2014).
- [8] D. Berzi, J. T. Jenkins, and A. Valance, *J. Fluid Mech.* **786**, 190 (2016).
- [9] J. R. Mayaud, R. M. Bailey, G. F. Wiggs, and C. M. Weaver, *Geomorphology* **280**, 108 (2017).
- [10] R. L. Martin and J. F. Kok, *Sci. Adv.* **3**, e1602569 (2017).
- [11] D. Berzi, A. Valance, and J. T. Jenkins, *J. Geophys. Res. Earth Surf.* **122**, 1374 (2017).
- [12] R. S. Anderson and P. K. Haff, *Science* **241**, 820 (1988).
- [13] J. F. Kok and D. J. Lacks, *Phys. Rev. E* **79**, 051304 (2009).
- [14] O. Durán, B. Andreotti, and P. Claudin, *Phys. Fluids* **24**, 103306 (2012).
- [15] M. V. Carneiro, N. A. M. Araújo, T. Pähtz, and H. J. Herrmann, *Phys. Rev. Lett.* **111**, 058001 (2013).
- [16] T. Pähtz, A. Omeradžić, M. V. Carneiro, N. A. M. Araújo, and H. J. Herrmann, *Geophys. Res. Lett.* **42**, 2063 (2015).
- [17] G. Sauermann, K. Kroy, and H. J. Herrmann, *Phys. Rev. E* **64**, 031305 (2001).
- [18] K. Kroy, G. Sauermann, and H. J. Herrmann, *Phys. Rev. Lett.* **88**, 054301 (2002).
- [19] K. Kroy, G. Sauermann, and H. J. Herrmann, *Phys. Rev. E* **66**, 031302 (2002).
- [20] B. Andreotti, P. Claudin, and S. Douady, *Eur. Phys. J. B* **28**, 341 (2002).
- [21] O. Durán, E. J. Parteli, and H. J. Herrmann, *Earth Surf. Processes Landforms* **35**, 1591 (2010).
- [22] J. E. Ungar and P. K. Haff, *Sedimentology* **34**, 289 (1987).
- [23] R. S. Anderson, *Sedimentology* **34**, 943 (1987).
- [24] R. B. Hoyle and A. Mehta, *Phys. Rev. Lett.* **83**, 5170 (1999).
- [25] H. Yizhaq, *Physica A* **338**, 211 (2004).
- [26] E. Manukyan and L. Prigozhin, *Phys. Rev. E* **79**, 031303 (2009).
- [27] O. Durán, P. Claudin, and B. Andreotti, *Proc. Natl. Acad. Sci. USA* **111**, 15665 (2014).
- [28] H. Yizhaq, Y. Ashkenazy, and H. Tsoar, *Phys. Rev. Lett.* **98**, 188001 (2007).
- [29] R. Sullivan, D. Banfield, J. F. Bell, W. Calvin, D. Fike, M. Golombek, R. Greeley, J. Grotzinger, K. Herkenhoff, D. Jerolmack, M. Malin, D. Ming, L. A. Soderblom, S. W. Squyres, S. Thompson, W. A. Watters, C. M. Weitz, and A. Yen, *Nature (London)* **436**, 58 (2005).
- [30] N. T. Bridges, F. Ayoub, J.-P. Avouac, S. Leprince, A. Lucas, and S. Mattson, *Nature (London)* **485**, 339 (2012).
- [31] F. Ayoub, J.-P. Avouac, C. Newman, M. Richardson, A. Lucas, S. Leprince, and N. Bridges, *Nat. Commun.* **5**, 5096 (2014).
- [32] D. M. Burr, N. T. Bridges, J. R. Marshall, J. K. Smith, B. R. White, and J. P. Emery, *Nature (London)* **517**, 60 (2015).
- [33] B. T. Werner, *J. Geol.* **98**, 1 (1990).
- [34] R. S. Anderson, M. Sørensen, and B. B. Willetts, *Aeolian Grain Transport I: Mechanics* (Springer Vienna, Vienna, 1991), pp. 1–19.
- [35] J. F. Kok and N. O. Renno, *J. Geophys. Res.* **114**, D17204 (2009).
- [36] M. Lämmel, K. Dzikowski, K. Kroy, L. Oger, and A. Valance, *Phys. Rev. E* **95**, 022902 (2017).
- [37] J. F. Kok, *Geophys. Res. Lett.* **37**, L12202 (2010).
- [38] Z. Dong, X. Liu, H. Wang, A. Zhao, and X. Wang, *Geomorphology* **49**, 219 (2003).
- [39] M. Creyssels, P. Dupont, A. Ould el Moctar, A. Valance, I. Cantat, J. T. Jenkins, J. M. Pasini, and K. R. Rasmussen, *J. Fluid Mech.* **625**, 47 (2009).
- [40] T. D. Ho, A. Valance, P. Dupont, and A. Ould El Moctar, *Phys. Rev. Lett.* **106**, 094501 (2011).
- [41] T. Ho, A. Valance, P. Dupont, and A. Ould El Moctar, *Aeolian Res.* **12**, 65 (2014).
- [42] P. R. Owen, *J. Fluid Mech.* **20**, 225 (1964).
- [43] M. Sørensen, *Geomorphology* **59**, 53 (2004).
- [44] O. Durán and H. Herrmann, *J. Stat. Mech.: Theor. Exp.* (2006) P07011.
- [45] M. Lämmel, D. Rings, and K. Kroy, *New J. Phys.* **14**, 093037 (2012).
- [46] T. Pähtz, J. F. Kok, and H. J. Herrmann, *New J. Phys.* **14**, 043035 (2012).
- [47] T. D. Ho, P. Dupont, A. Ould El Moctar, and A. Valance, *Phys. Rev. E* **85**, 052301 (2012).
- [48] J. T. Jenkins, I. Cantat, and A. Valance, *Phys. Rev. E* **82**, 020301(R) (2010).
- [49] S. L. Namikas, *Sedimentology* **50**, 303 (2003).
- [50] B. Andreotti, *J. Fluid Mech.* **510**, 47 (2004).
- [51] O. Durán and H. J. Herrmann, *Phys. Rev. Lett.* **97**, 188001 (2006).

- [52] J. A. Jimenez and O. S. Madsen, *J. Waterw. Port Coast. Ocean Eng.* **129**, 70 (2003).
- [53] P. Claudin and B. Andreotti, *Earth Planet. Sci. Lett.* **252**, 30 (2006).
- [54] B. Andreotti, P. Claudin, and O. Pouliquen, *Geomorphology* **123**, 343 (2010).
- [55] K. Kroy, S. Fischer, and B. Obermayer, *J. Phys.: Condens. Matter* **17**, S1229 (2005).
- [56] E. J. R. Parteli, O. Durán, and H. J. Herrmann, *Phys. Rev. E* **75**, 011301 (2007).
- [57] A. Fourrière, P. Claudin, and B. Andreotti, *J. Fluid Mech.* **649**, 287 (2010).
- [58] B. Andreotti, P. Claudin, and S. Douady, *Eur. Phys. J. B* **28**, 321 (2002).
- [59] R. S. Anderson and P. K. Haff, *Acta Mech.* **1**, 21 (1991).
- [60] S. Pfeifer and H.-J. Schönfeldt, *Earth Surf. Processes Landforms* **37**, 1056 (2012).
- [61] E. Parteli, K. Kroy, H. Tsoar, J. Andrade, and T. Pöschel, *Eur. Phys. J.: Spec. Top.* **223**, 2269 (2014).
- [62] J. F. Kok, *Phys. Rev. Lett.* **104**, 074502 (2010).
- [63] Z. Dong, G. Qian, W. Luo, and H. Wang, *J. Geophys. Res.* **111**, D16111 (2006).
- [64] K. R. Rasmussen and H. E. Mikkelsen, *Sedimentology* **45**, 789 (1998).
- [65] K. Nishimura and J. C. R. Hunt, *J. Fluid Mech.* **417**, 77 (2000).
- [66] K. R. Rasmussen and M. Sørensen, *J. Geophys. Res.* **113**, F02S12 (2008).
- [67] H. Cheng, J. He, X. Zou, J. Li, C. Liu, B. Liu, C. Zhang, Y. Wu, and L. Kang, *Sedimentology* **62**, 1497 (2015).
- [68] D. Beladjine, M. Ammi, L. Oger, and A. Valance, *Phys. Rev. E* **75**, 061305 (2007).
- [69] R. Greeley and J. Iversen, *Wind as a Geological Process on Earth, Mars, Venus and Titan* (Cambridge University Press, Cambridge, 1985).
- [70] Y. Shao, *Physics and Modelling of Wind Erosion*, edited by R. Sadourny (Kluwer Academic Publishers, Dordrecht, 2000).
- [71] N. Huang, Y. Zhang, and R. D'Adamo, *J. Geophys. Res. Atmos.* **112**, D08206 (2007).
- [72] M. V. Carneiro, K. R. Rasmussen, and H. J. Herrmann, *Sci. Rep.* **5**, 11109 (2015).
- [73] J. D. Iversen and K. R. Rasmussen, *Sedimentology* **46**, 723 (1999).
- [74] J. C. R. Hunt, S. Leibovich, and J. K. Richards, *Q. J. R. Meteorol. Soc.* **144**, 1435 (1988).



## Structure formation

In the previous chapters, we reviewed the various processes and mechanisms contributing to the physics of aeolian sand transport. We are now in the position to use this insight to theoretically describe the spontaneous formation of the whole zoo of wind-created sand structures, ranging from decimeter-sized ripples to kilometer-long dunes. As already discussed in the previous chapter, the size scale of the considered sand structure dictates to what level the transport model has to resolve the transport process. While the grain-scale transport statistics can be safely integrated out in a dune model, it dominates the physics of the more delicate ripples.

Based on the physical mechanisms responsible for their formation, aeolian sand structures are usually categorized into ripples, megaripples, and dunes. Figure 4.1 shows all three bedforms collocated in close proximity. Chiefly, aeolian sand ripples are formed due to a screening instability that yields a slope-dependent impact intensity of fast saltating grains [26, 40, 89, 90] (enhanced/reduced reptation transport uphill/downhill), whereas the dune instability is of hydrodynamic origin, namely caused by the symmetry breaking of the turbulent flow field over a sand heap [83, 193]. Megaripples stand out from ripples and dunes, because their formation is accompanied by—and may even crucially require [67]—aeolian sand sorting that creates a stabilizing armoring layer of coarse grains. For typical wind conditions, these coarse surface grains are transported in terms of reptation only, which crucially determines the megaripples' morphology and dynamics. To further illuminate the physical and morphological differences between the aeolian structures we review them in more detail in the following three sections. A succinct comparison of the different structures can be found in Table 1 of Ref. [67] (attached at the end of this chapter). Since the most profound understanding has been accumulated over the last decades for the conceptually simpler sand dunes, we start with these large objects, before we come to the theoretically more challenging sand ripples and megaripples.

### 4.1 Dunes

Despite their intriguing morphological diversity, ranging from transverse dunes over crescentic barchans to elongated seif dunes [42, 258, 259], the formation and evolution of sand dunes can



Figure 4.1: Ripples, megaripples, and large sand dunes collocated in the same area. Monodisperse wind-blown sand creates centimeter-scale ripples (front) and decameter-scale dunes (back). Polydisperse wind-blown sand gets sorted, the heavier grains forming decimeter-scale megaripples (middle) in the otherwise forbidden wavelength gap. Closer to ripples in size, they share their morphology and migration dynamics with dunes. Photo taken at al-Fayyum ( $29^{\circ}9'56.17''\text{N}$ ,  $30^{\circ}11'8.55''\text{E}$ ), Egypt. (Image credit: Hezi Yizhaq)

in fact be traced back to very few key mechanisms. This insight and our today's understanding of the general physics of these wind-shaped objects has been established only relatively recently, notwithstanding the various past attempts reaching back to the first phenomenological discussions by Bagnold [40]. One important door opener was the formulation and analysis of a minimal mathematical model for aeolian sand dunes by Sauermann and coworkers in the early 2000s [82, 83, 193, 260]. It provided us with a clear understanding of the basic mechanisms that govern the formation, shape, and migration of dunes under ideal conditions. The existence of an unstable shape attractor, characterized by strong static and dynamic similarity rules and the shape transition from smooth domes (or heaps) to crescentic dunes with slip face, has been demonstrated on this basis [87, 261, 262]. A wealth of predictions could be systematically tested in precision measurements to scrutinize the theoretical picture [31, 32, 43, 84, 88, 212, 263–267].

#### 4.1.1 Minimum dune size

Structure formation of wind-blown sand is governed by two mechanisms that make a flat sand bed unstable against height fluctuations on a certain length scale [193, 268]. First, a spatial symmetry breaking leading to net deposition at the brink and thus growth of any spontaneous height fluctuation. For dunes, this symmetry breaking emerges spontaneously from the turbulent structure of the wind [269–271]. It is therefore scale invariant [193], and yields an infinite spectrum of unstable wavelengths, such that every perturbation of the bed profile would grow (the shorter their wavelength the faster their growth). This catastrophic behavior is tamed by a second counteracting mechanism, which stabilizes short-wavelength modes, thereby introducing a minimum length  $\mathcal{L}_{\min}$  of the structures. For dunes, this stabilization is due to saturation transients in the sand transport. The minimum size of a dune—which has actually a flat pancake shape—is thus determined by the saturation length [83, 193],

$$\mathcal{L}_{\min} \propto \ell_{\text{sat}} \quad (4.1)$$

with a numerical prefactor on the order of 20 [86, 142]. According to theory, any sand heap below this minimum size is simply eroded by the wind, any larger one will grow indefinitely.

Combining Eq. (4.1) with Eq. (3.1) of Chap. 3, we obtain the scaling  $\mathcal{L}_{\min} \propto (\sigma - 1)a$  for the minimum dune length, up to a wind-dependent prefactor, with the fluid–grain density ratio  $\sigma$  and the grain size  $a$ . As a consequence, fluvial sand dunes formed under water ( $\sigma \approx 3$ ) are much smaller than their aeolian cousins ( $\sigma \approx 2 \cdot 10^3$ ). With a minimum length on the order of a few centimeters, the subaqueous dunes thereby provide an ideal model system for laboratory studies. And indeed, many of the striking theoretical predictions of the aforementioned dune model by Sauermann *et al.* and of its later variants have not only been corroborated by field data for aeolian dunes [31, 32, 212, 263, 264] but also in systematic studies of dunes formed in water channels [43, 84, 88, 212, 265–267]. The dependence of the dune size on the atmospheric density captured by Eq. (4.1) can also be applied to extraterrestrial atmospheres, like on Mars, Venus, or Saturn's moon Titan (see, *e.g.*, Ref. [47, 48, 50] and references given there). Due to the more dilute atmosphere (and the lower gravity), dunes on Mars are expected to be much larger than on Earth [142], as confirmed by the extensive data gathered during orbiter and rover missions [49, 85, 272, 273].

### 4.1.2 Shape invariance

A direct consequence of the flux saturation underlying the dune formation, together with the scale-invariant perturbation of the turbulent flow over a heap, is the broken shape invariance [87, 142]. This can be understood as follows. A stationary dune shape requires net deposition at all locations downwind of the brink. So, the saturation transient along its windward slope has to end just at the brink. This means that the dune size dictates the length of this transient, which, in turn, depends on the wind speedup along the back of the dune, regulated by the aspect ratio of the dune. In other words, the steeper the dune the stronger the wind speedup and, thus, the longer the saturation transient. Hence, larger (quasi-stationary) dunes are steeper. As a direct consequence, large enough dome-shaped heaps transition into dunes with a slip face, when their lee slope becomes so steep that avalanches take place [32, 87, 142, 193]. The growth of the very large “megadunes” or draas (few kilometers long) is ultimately limited by the finite height of the atmosphere [35], while the size of desert dunes is often dictated by the limited sand availability and growth time [36]. Sand supply does not only influence the total size of the dunes, but, more interestingly, also their overall shape. For unlimited sand supply (*i.e.*, at saturated sand influx), transverse dunes are formed with relatively straight crest lines perpendicular to the wind direction and continuous asymmetric cross sections in wind direction. As the sand availability is reduced, their crests become separated in wind direction and are likely to break up into individual crescentic barchan dunes [262, 274].

### 4.1.3 Extensions and applications of the Sauermaun dune model

Over the years, various extensions of the minimal dune model introduced by Sauermaun and coworkers have been proposed and applied to manifold problems. Succinct overviews can, for example, be found in the recent review articles by Parteli and coworkers [57, 69, 72], Charru *et al.* [45], and Courrech du Pont [275]. To name just a few examples: the two-dimensional model was extended to three dimensions [260, 261, 276, 277] and to interacting dunes and whole dune fields [38, 39, 263, 276]; the influence of a reptation transport mode [261], varying wind strength [120] and direction [262, 278], vegetation [279, 280], and an exposed water table [281] on the dune morphology was investigated. Particularly fruitful was the extension of the dune model by Fourrière *et al.* [44] to finite flow depths, as needed to describe the aqueous structure formation in channels and rivers.<sup>1</sup> The additional length scale, together with the larger viscosity that allows for both turbulent [44, 283] and viscous [284–286] flow regimes, makes the phenomenology of subaqueous bedforms even richer than for the aeolian case [45]. Extended to three dimensions, the model allowed Andreotti and Claudin [283] to explain the emergence chevrons (inclined bedforms in shallow flow), alternate bars (diagonally repeating deposits in a shallow channel, see also

---

<sup>1</sup>In the literature on subaqueous structure formation, the under-water analog of aeolian desert dunes is usually called (subaqueous or current) ripples if their length is comparable to the grain size and their morphology independent of the flow depth, whereas subaqueous dunes commonly refer to bedforms of size comparable to the flow depth. While some authors delegate the emergence of these two structures to two different physical mechanisms related to a hydrodynamically either smooth or rough flow regime [282], Fourrière *et al.* [44] found from their analysis that large-scale dunes cannot appear due to a linear instability, because of their too slow growth rate compared to pervasive fast-growing instabilities at shorter wavelengths. These authors instead argued that small ripples should always appear first and then coarsen to form the mature dunes, whose growth ultimately stalls due to the finite flow depth.

Ref. [287]), and antidunes (propagating upstream in supercritical flow, characterized by a Froude number<sup>2</sup> greater than unity). A good starting point to acquaint oneself with this pretty diverse field is the review article by Charru *et al.* [45]. Notwithstanding the formidable progress achieved over the very recent years, mainly by the group around Bruno Andreotti and Philippe Claudin (see, *e.g.*, [www.pmmh.espci.fr/fr/morphodynamique](http://www.pmmh.espci.fr/fr/morphodynamique)), various questions regarding subaqueous structure formation are still unanswered or only partly solved. The fundamental flow properties in the transitional laminar–turbulent regime, which is crucial for the formation of subaqueous structures, and the role of (secondary) turbulent structures (*e.g.*, streaks) still remain poorly understood [45, 72]. A systematic study of the long-time evolution and dynamic scaling of the diverse subaqueous patterns is still lacking and requires a modeling framework that goes beyond the linear stability analysis—*e.g.*, along the lines of the work by Fischer *et al.* [87] for the aeolian case. In contrast to the aeolian dune formation, structure formation under water is expected to be crucially influenced by sand polydispersity and grain sorting, which is however still poorly understood despite numerous modeling attempts in the past [288].

Another hotly debated topic concerns the dynamic stability of aeolian sand dunes. All theoretical approaches strongly suggest that isolated dunes that are small compared to the flow depth (*i.e.*, the height of the atmosphere for desert dunes) are unstable [69, 263, 274], either shrinking or growing. In contrast, field observations reveal that dunes of similar size cover extended corridors in the desert [37–39], indicating that bedform interactions somehow stabilize the individual dunes. Several mechanisms that might be responsible for this size selection have been proposed in the past, from dune collisions [37, 39, 289, 290], over calving [37, 264, 291] to remote transfer through wind-driven sand transport [36, 292–295], but a satisfying explanation for the stationary dune-size distribution is still lacking. Tackling this large-scale problem with a computationally expensive three-dimensional version of the original Sauermann model seems illusive [72]. It instead calls for radically coarse-grained approaches that describe the dynamics of an individual dune by a reduced set of simple laws, particularly promising approaches being the “skeleton” or “migrating string” dune model developed by Nishimory and coworkers [274, 296, 297] or the reduced version of the Sauermann model proposed in the master’s thesis by Sven Auschra [293].

## 4.2 Ripples, aeolian sand sorting, and megaripples

Compared to dune formation, aeolian ripple formation is more complex, because it lacks the scale separation between the emerging structure and the underlying grain-scale processes; which, in return, should make studies more profitable to learn about the superficially mundane yet obstructively complex grain-scale physics, as argued in Chap. 3. Despite the considerable experimental [26–28, 40, 298–306] and theoretical [89, 90, 198, 222, 307–319] effort over the last decades, we do not yet have such a coherent set of systematic predictions on parameter dependencies for ripples as for dunes, *e.g.*, how their wavelength and amplitude change with environmental conditions, such as wind, sand supply, and grain size distribution. Neither is it straightforward to extract such information from existing field and wind-tunnel data, which seem to report conflicting evidence. The main reason for this unfortunate situation, as opposed

---

<sup>2</sup>The Froude number  $Fr$  is defined as  $Fr = U/\sqrt{gH}$ , with  $U$  being the free stream velocity,  $g$  the gravitational acceleration, and  $H$  the flow depth.

to, say, aeolian dune formation, is that the delicate ripples in the field are highly sensitive to intermittent turbulent wind fluctuations [79, 227], making them inherently transient. Since they are much shorter than the saturation length, the saturation transients that follow the pervasive wind-strength variations in the field can easily change the shape of these fragile bedforms and moderate gusts may even flatten them out completely [26, 30, 40, 147, 300, 320]. Their ubiquitous presence in windy arid regions on Earth (*e.g.*, as secondary structures on sand dunes) [25, 26, 28, 40, 41, 301, 302, 305, 321] and Mars [143, 144, 322], on the other hand, implies that a flat sand bed is highly unstable once subjected to turbulent flow. Further uncertainty and complication comes from the inevitable wind-driven sand sorting at the surface of the ripples [25, 26, 40, 299, 321], accumulating coarse grains at their crests, while fine sand prevails in the bulk and at their base [26, 40, 299–302, 323–327]. Contrary to the often aleatory conditions in the field, the much better controlled laboratory experiments [27, 28, 40, 298–300, 303, 304, 306] allow to extract functional dependencies with relatively high reliability and reproducibility, thereby paving the way to a more quantitative benchmarking for mathematical models.

#### 4.2.1 Screening instability and ripple wavelength

The topography–transport symmetry breaking that gives rise to the emergence of sand ripples is thought to be due to the slope-dependent impact intensity of the saltating grains that eject reptating bed grains: the ripple’s lee side is screened from the most energetic shallow impacts, which are, in turn, very efficient at the stoss slope.<sup>3</sup> As for the dune instability, such a screening instability leads to an unbounded spectrum of unstable modes, with shorter wavelengths growing faster. Anderson [89] therefore suggested that the disperse reptation transport, as characterized by a distribution of reptation lengths, stabilizes the short wavelengths, which yields an estimate for the wavelength of the fastest growing mode that is, however, much below the initial ripple wavelength measured in wind-tunnel experiments [28, 40] (see, *e.g.*, Ref. [315] for a review of Anderson’s model and related approaches). In fact, Bagnold [40] already argued that the initial ripple size is determined by the length of the characteristic (*i.e.*, average) path of the wind-blown grains, because such a representative grain should hop from crest to crest, thereby dictating the ripple wavelength via a phase-locking mechanism. From his wind tunnel observations he indeed found the average hop length to be on the same order as the ripple wavelength. Very recently, this picture was taken up by Durán *et al.* [90], who argued that the short-wavelength stabilization originates from the slope-dependent (overall) sand transport—carrying sand uphill is less efficient than downhill. From their grain-scale simulations, these authors identified the characteristic initial ripple length as the ratio between the height-integrated horizontal mass flux of the saltating grain fraction (defined by a minimum hop height of three grain diameters) and the vertical flux through the bed surface. This ratio may be interpreted as the mean hop length of the transported grains, which is the length of Bagnold’s characteristic path. It yields an affine relation between ripple wavelength and wind speed, in agreement with various wind-tunnel experiments [28, 40, 299, 300, 303]. Yet, Durán *et al.* did not provide a compelling explanation how the stabilizing slope-dependent transport is related to the phase locking due to crest-to-crest grain leaps. Without the phase locking, one would expect isolated ripples to exist similar to isolated dunes. Note, however, that isolated normal-sand ripples would be quickly eroded, as mentioned

---

<sup>3</sup>Aeolian sand ripples are often called impact or ballistic ripples, in order to discriminate them from subaqueous (current) ripples.

above. Only markedly polydisperse sand allows for long-lived isolated bedforms: when the coarse grain fraction is transported by reptation, megaripples can be formed, as suggested by our repton-dune model in Sec. 4.2.4. It seems tempting to speculate that the phase locking can instead be responsible for a finite asymptotic (long-time) ripple size. That a final ripple wavelength exists was argued by Andreotti *et al.* [28] based on their wind-tunnel experiments, where they manually prepared wavy sand bed profiles that rapidly adapted their amplitude once the wind was turned on, whereas the ripple wavelength apparently remained at its initial value, letting these authors conclude that the ripples “do not evolve at all and the pattern purely propagates”. However, a closer look at the profiles shown in Ref. [28] reveals that the average wavelength increases by about 5% (from 9.1 cm to 9.6 cm) within about twelve minutes. This slight growth might be due to experimental noise; but, one should be careful with interpreting the shown data as a proof for the existence of stable ripple states. Another poorly understood property is the nontrivial grain-size dependence of the affine law between wind speed and ripple length, namely that the size of fine-sand ripples significantly increases with increasing wind strength, whereas the length of coarse-sand ripples appears to be almost wind-speed independent. A possible explanation could be the gradually enhanced influence of turbulent suspension [57, 131, 201, 328] as the grains become smaller, making their trajectories longer. Alternatively, big-grain reptation, which is characterized by the wind-strength independent splash statistics, can become more and more dominant the coarser the sand is, corresponding to the repton-dune model described below.

#### 4.2.2 Sand polydispersity and megaripples

A concomitant phenomenon of the above described impact screening is that bigger (and/or denser and/or less spherical/round/smooth) grains that reptate or roll down the ripple’s lee face less efficiently, as characterized by a reduced reptation length [316, 319] compared to the finer grain fraction, always accumulate at the ripple crests [26, 40, 299–302, 323–327]. The analogy with normal sand dunes, where the drastic drop of the wind strength at the brink yields net deposition at its downwind side, is a major insight underlying the repton-dune approach in Sec. 4.2.4. For both polydisperse-sand ripples and normal-sand dunes, the deposition at the brink leads to a short steep slope around the angle of repose ( $\approx 30^\circ$ ) at the upper part of the lee side, which crosses over into a long, flatter lee slope (below  $20^\circ$ ) [26]. Reptating fine grains that are fast enough to leap down to this lower part of the ripples’ lee slope are typically trapped there, because energetic grain impacts are screened by the ripple crest as described in the previous section. Again, this shadow zone is very much reminiscent of the wake zone of the turbulent wind field behind the dune brink. It is responsible for the so-called nebka effect, referring to the fine-sand deposit at the lee side of an obstacle—here, the ripple crest itself.

The grain-size separation at the ripple crest becomes particularly evident under erosive conditions, *i.e.*, for limited fine-sand supply. Then, fine-grain ripples either quickly vanish—namely, if they are formed on plain rock or in a wind tunnel—or winnowing (*i.e.*, fine-grain erosion) makes the grain-size distribution at the ripple surface strongly nonuniform, typically bimodal. As a consequence, normal sand ripples quickly turn into megaripples, characterized by a coarse-grain armoring layer, when the sand availability is limited [1]. The big immobile grains can prevent the underlying fine material from being eroded, making the megaripples more resistant to wind-strength fluctuations and thus allowing them to become older and larger than the fragile normal fine-sand ripples. Very large wavy structures can also be formed from mixed

material where the grains differ not only in their size, but also in their density [148, 329–331], whereby the denser material plays the same role as the coarse grain fraction for polydisperse sand, *e.g.*, winnowing of the lighter grains, accumulation of the denser ones at the crests etc.

Only rare strong gusts can destroy the megaripples' armor layer and thereby flatten them [30, 147, 320]. This can also be rephrased in terms of the saturation transients: As the reptation of the coarse grains is characterized by a saturation length that is shorter (on the order of the grain size) than the megaripple length, the megaripples are not eroded by moderate wind gusts—contrary to the normal ripples made from fine sand, for which the saturation length is much larger than the ripple wavelength. Consequently, megaripples can become separated and more irregular, and can eventually form individual barchan-shaped objects [26, 29, 321, 323, 324, 332, 333], quite similar to what is observed for dunes, which evidently distinguishes the megaripples from the stripe-like normal-ripple patterns. For such separated bedforms, the crests-to-crest distance can vary a lot [79, 334] and a much better correlation is found between the base length of the megaripples and their length-to-height ratio (called ripple index) or their migration speed, as we demonstrated in Ref. [67] (attached at the end of this chapter).

The above characterization suggests that the discrimination between sand ripples and megaripples is of gradual nature, as it merely originates from the saturation degree of the fine-sand supply. An increasing sand polydispersity allows the megaripples to continuously expand into the wavelength gap that cannot be reached by ripples and dunes that are made from monodisperse normal sand. Indeed, from their large data set, ranging from about 2 cm to 8 m in terms of the bedforms' crest-to-crest distance, Wilson and coworkers [27, 41] showed that properties like ripple wavelength, height, aspect ratio, and grain sorting do not fall into two distinct groups, but form a single continuum region in the parameter space, which is clearly distinguished from a region representing aeolian sand dunes (see also Ref. [273]). Under ideal (fluctuation-free) conditions, the two regions representing unlimited and limited fine-sand supply may nevertheless become asymptotically separated in the long-time limit.

### 4.2.3 Martian ripple structures

The numerous field surveys and wind-tunnel studies on our own planet are complemented by orbiter and rover missions on Mars, which allow for detailed investigations of the abundant aeolian structures similar to terrestrial ripples and megaripples. Since the dilute atmosphere and low gravity on Mars leads to relatively long grain trajectories [141], these bedforms are generally larger than on Earth, as we already noticed for the sand dunes on these two planets, below Eq. (4.1). From the discussion in Secs. 1.2 and 3.5, we know that the large gap between the fluid and the impact threshold, together with intermittent turbulent wind fluctuations, might explain the current activity of various aeolian features observed on Mars, despite the fact that the average wind strength is below the fluid threshold.<sup>4</sup> [115–118, 128, 143–146] From landing missions we know that large coarse-grained ripples, apparently inactive today, are formed on Mars [143, 144], which seem to be analogs of our terrestrial megaripples. Although very likely, it is not yet clear if the very abundant light-toned so-called “transverse aeolian ridges” (TARs) with (nearly) symmetric profiles [48] are similar to the coarse-grained megaripples [144]. This hypothesis is however suggested by the observation that they obey the same morphometric

<sup>4</sup>Note that the idea of sustained transport initiated by a burst-like gust was recently challenged by Sullivan and Kok [150]. See Sec. 1.2.



scaling laws as the megaripples on Earth, as we demonstrated in Ref. [67] (attached to the present chapter).

#### 4.2.4 Megaripples as “reptation dunes”

Altogether, the above listed observations illustrate that the physics of such mesoscale structures is controlled by a complex interplay between intermittent turbulent wind fluctuations, sand transport, polydispersity, sorting, and structure formation. It gives rise to a wealth of phenomena, many of them still waiting for a satisfying explanation in terms of the underlying physical mechanisms. A first step towards a more comprehensive understanding of the intermingled processes responsible for aeolian structure formation was presented in the paper [67] appended below this section. To disentangle the various contributions to the formation and morphology of megaripples, we approach this problem in two steps: first, the erosive sand sorting is identified as the prerequisite for the megaripple formation, as it creates the characteristic bimodal grain-size distribution. Second, the dynamic reptation transport is described in terms of saturation transients, characterized by a saturation length that is given by the reptation length and thus comparable with the grain size, which gives rise to a “reptation dune” picture for the megaripples.

# Aeolian sand sorting and megaripple formation

Marc Lämmel<sup>1</sup>, Anne Meiwald<sup>1</sup>, Hezi Yizhaq<sup>2</sup>, Haim Tsoar<sup>3</sup>, Itzhak Katra<sup>3</sup> and Klaus Kroy<sup>1\*</sup>

**Sand is blown across beaches and deserts by turbulent winds. This seemingly chaotic process creates two dominant bedforms: decametre-scale dunes and centimetre-scale ripples, but hardly anything in between. By the very same process, grains are constantly sorted. Smaller grains advance faster, while heavier grains trail behind. Here, we argue that, under erosive conditions, sand sorting and structure formation can conspire to create distinct bedforms in the ‘forbidden wavelength gap’ between aeolian ripples and dunes. These so-called megaripples are shown to co-evolve with an unusual, predominantly bimodal grain-size distribution. Combining theory and field measurements, we develop a mechanistic understanding of their formation, shape and migration, as well as their cyclic ageing, renewal and sedimentary memory, in terms of the intermittent wind statistics. Our results demonstrate that megaripples exhibit close similarities to dunes and can indeed be mechanistically characterized as a special type of (‘reptation’) dune.**

Aeolian ripples and dunes are sand waves of vastly different size<sup>1–3</sup> (see Fig. 1a, Table 1 and Supplementary Figs. 1 and 2, for some photographs and data). Ripples are neatly periodic corrugations of a sand bed on a centimetre scale. They are thought to arise from a spontaneous synchronization of the ballistic (‘saltating’) grain trajectories with the wavy topography<sup>1,4</sup>. The synchronization is lost for wavelengths beyond the hop length of the grains, so that ripple growth stalls<sup>5,6</sup>. A similar feedback between transport and topography is mediated by the wind. The sensitivity of its speed and transport capacity to height modulations of the sand bed renders a flat bed unstable, which is the mechanism that creates sand dunes<sup>7,8</sup>. A spatial lag or ‘saturation transient’<sup>9</sup> between the wind shear stress and the sand flux breaks the scale invariance of the process and defines a minimum dune length of some ten metres for typical dune sand<sup>10,11</sup>. Bedforms of intermediate wavelengths, between the saltation length and the minimum dune length, are flattened out by the wind. They should thus not regularly be observed in the field and have indeed not generally been reported from natural observations<sup>2,12</sup>.

Here, we provide theoretical and empirical evidence for a notable exception. Erosive conditions can initiate a complex feedback between aeolian transport and structure formation, giving rise to the peculiar bedforms commonly characterized as (gravel or pebble) ridges<sup>1</sup>, granule ripples<sup>13</sup> or megaripples<sup>14,15</sup>. The key to their understanding is the sorting of the sand by aeolian transport. Natural sand is always (more or less) polydisperse, as it is formed by quite chaotic processes: breaking up crustal rock and crushing by weathering, erosion, abrasion, turbulent transport and so on<sup>16</sup>. However, since the aeolian transport efficiency depends on the grain size, finer grains are quickly carried away by the wind while coarser grains trail behind. As a consequence, aeolian sand becomes increasingly monodisperse further downwind (for example, in the middle of a large dune field<sup>17</sup>). In return, if not compensated by incoming sand, the winnowing of the finer grains may also cause rare coarse grains to accumulate at the bed surface. Below, we put forward a mathematical model to quantify how this process may gradually create a bimodal surface grain-size distribution (GSD) out of a unimodal bulk GSD. As a consequence, the aeolian transport process itself can develop a bimodal structure that further reinforces

the sand sorting. More precisely, a window of wind strengths can be identified, in which the coarse grains do not themselves saltate but merely creep or ‘reptate’<sup>1</sup> over the sand bed, slowly driven by the saltating fraction of fine grains. This wind range is delimited by the threshold wind shear stresses  $\tau_t^c$  and  $\tau_r^c$  for saltation and reptation of the coarse grains and thereby sensitive to the ratio  $a_c/a_f$  of the characteristic coarse and fine sand grain diameters  $a_c$  and  $a_f$ ,

$$\tau_t^c / \tau_r^c - 1 \propto (a_f / a_c)^6 \approx 10^{-4} \dots 10^{-2} \quad (1)$$

with the omitted factor of proportionality ranging from  $10^2$  to  $10^4$  (Methods). The ensuing strong scale separation between the hop lengths of fine and coarse grains has two important consequences. First, it reinforces the winnowing of fine grains and the accumulation of coarse grains at the bed surface. Second, the coarse surface grains respond very locally to wind variations, resulting in much shorter saturation transients than for the fine grains<sup>9,11</sup>. The associated minimum dune size is thus greatly diminished: from some ten metres for typical dune sand down to decimeters for grains of diameters in the millimetre range<sup>10,11</sup>. This allows the coarse grain fraction to form small dunes in the otherwise forbidden wavelength gap. We postulate that these dunes made from coarse reptating grains or ‘reptation dunes’ are the bedforms commonly known as megaripples (Supplementary Fig. 1). We also demonstrate the predictive potential of this interpretation. Namely, since dunes with low sand supply tend to evolve in loosely spaced ensembles, our model immediately explains why megaripples are much less regularly spaced and aligned than ordinary ripples<sup>13,14,18–21</sup> (Fig. 1a and Supplementary Figs. 2,3). Further, that the aeolian surface accumulation of coarse grains is predicted to take substantially longer for less polydisperse sands naturally explains the rare occurrence of megaripples in regions with narrowly sorted sand<sup>1,13,16</sup> and establishes the emergence of a strictly forbidden wavelength gap in the limit of monodisperse sand. Finally, the reptation-dune model quantitatively predicts key features of the morphology and migration of megaripples.

While a correlation between grain sorting and megaripple formation is suggested by much observational evidence (Fig. 1 and refs <sup>1,2,16,18,22–30</sup>), the responsible physical mechanism has so far eluded

<sup>1</sup>Institut für Theoretische Physik, Universität Leipzig, Leipzig, Germany. <sup>2</sup>Department of Solar Energy and Environmental Physics, Blaustein Institutes for Desert Research, Ben-Gurion University of the Negev, Sede Boqer Campus, Be'er Sheva, Israel. <sup>3</sup>Department of Geography and Environmental Development, Ben-Gurion University of the Negev, Be'er Sheva, Israel. \*e-mail: [klaus.kroy@itp.uni-leipzig.de](mailto:klaus.kroy@itp.uni-leipzig.de)

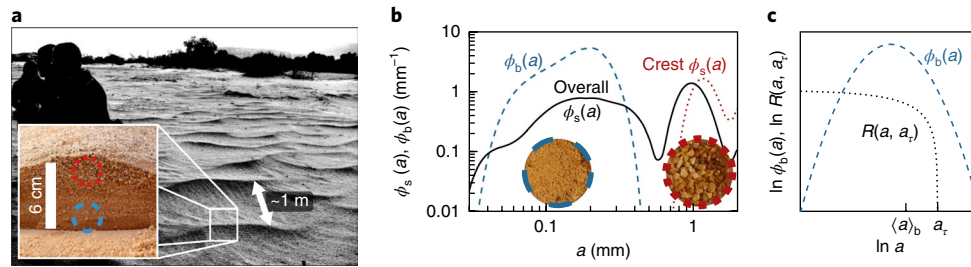


**Fig. 1 | Sand sorting and megaripples.** **a**, Megaripples in the southern Negev desert (Israel). Inset: cross-section of a typical megaripple, revealing vertical sand grading (coarser grains on top). **b**, Representative bulk and surface GSDs  $\phi_b(a)$  and  $\phi_s(a)$  (measured globally and at the crest). Inset: sand samples from the marked circular regions of panel **a**. (See Methods for further details.) **c**, Log-normal model bulk distribution  $\phi_b(a)$  with standard deviation of about half the mean bulk grain diameter  $\langle a \rangle_b$ , and model erosion rate  $R(a, a_t)$ , decaying with grain size  $a$  up to a maximum erodible  $a_t$  dependent on the wind shear stress  $\tau$  (here set to  $a_t = 3\langle a \rangle_b$ ). A monotonically decreasing form of  $R(a)$  accounts for the fact that more small grains than big ones are carried away, due to their easier mobilization by the wind and their longer hop lengths and higher transport speeds.

experimental and mathematical characterization. A main difficulty has been the wide scatter of field data for megaripples, which our analysis demonstrates is a natural consequence of the intricate interplay between the three processes involved in their formation: sand sorting, evolution of the topography and intermittent wind fluctuations. To elucidate their poorly understood interdependence, we propose a mesoscale minimal model of erosion-driven sand sorting. The key idea is to break down the complex evolution of the GSD in the sand bed to the volumetric (that is, volume-weighted) distributions  $\phi_b(a, t)$  and  $\phi_s(a, t)$  of the grain diameter  $a$  at time  $t$  in the bulk ‘b’ and surface ‘s’ of the sand bed, respectively (Fig. 1). The processes that create both GSDs in the field will typically not be fundamentally different. In particular, as the wind strength or direction changes, or new upwind sources become temporarily available, a developed surface layer can be covered by some sand deposit and thereby become part of the bulk. The crucial difference lies in the timescales over which they are generated. The bulk GSD  $\phi_b$  develops over geological timescales. The surface GSD  $\phi_s$  emerges from the bulk distribution over much shorter times, typically during an intermittent period of weaker winds between two storms, over which  $\phi_b$  can be taken to be stationary. In a first (mean-field type) approximation, we therefore model the sorting process in the overall surface distribution by

$$\frac{\partial}{\partial t} \phi_s(a, t) = -R(a)\phi_s(a, t) + [\langle R(a) \rangle_s + J(a)]\phi_b(a) \quad (2)$$

The erosion rate  $R(a)$  determines the net removal of surface grains of diameter  $a$  via the first term on the right-hand side, while the remainder continuously replenishes the (time-dependent) lost volume fraction  $\langle R(a) \rangle_s$  from the bulk, to maintain the normalization of  $\phi_s(a, t)$ . The optional effective deposition rate  $J(a)$  is included to allow some upwind sand supply to be portrayed, whereby  $J(a)\phi_b(a)$  is understood to vanish on integration over all  $a$ . Dynamic averages  $\langle \dots \rangle_{s,b}$  are defined by  $\int da \dots \phi_{s,b}(a, t)$ . At the present stage, our minimal description deliberately neglects some details, such as the feedback of the developing topography on the grain sorting and does not discern horizontal heterogeneities and vertical versus horizontal sorting<sup>5,31,32</sup>, which are not critical for our discussion.

We now show that these ingredients are sufficient to explain the observation that megaripples co-localize with accumulations of coarse grains and emerge as long-lived transient structures from a unimodal bulk distribution dominated by much finer sand. Consider first the illustrative example of a log-normal model bulk GSD (Fig. 1c), as thought to arise from weathering, grinding and abrasion<sup>3,33</sup>, and in reasonable agreement with our field data displayed in Fig. 1b. As a schematic model for the erosion rate, we assume (see Methods and Fig. 1c)

$$R(a, a_t) = \sqrt{ra_\tau} (1 - a/a_\tau) \Theta(a_t - a) \quad (3)$$

**Table 1 | Morphological and physical characteristics of ripples, megaripples and dunes**

	Ripples	Megaripples	Dunes
Length scale	<30 cm (refs <sup>1,5,13,36</sup> )	>30 cm (refs <sup>2,13,14,18,19,22,43</sup> )	>10 m (refs <sup>2,51,52</sup> )
Crest-line shape	Straight, continuous <sup>2,13</sup>	Sinuuous, irregular <sup>13,18–20,23</sup>	Transverse dunes: straight, continuous; isolated dunes: irregular, crescentic or linear <sup>1–3</sup>
Cross-section shape	Contiguous (sinusoidal) <sup>1</sup>	Smooth, rarely with slip face <sup>19,53</sup>	Smooth or with slip face <sup>1,3,52</sup>
Length-to-height ratio	>20 (refs <sup>1,5,13,15,24,36</sup> ) (size independent <sup>5,15,36</sup> )	>4 (refs <sup>13,43</sup> ) (size dependent, Fig. 4)	>8 (refs <sup>47,51,54–56</sup> ) (size dependent <sup>47</sup> )
Formation timescale	Minutes <sup>5,36,57</sup>	Hours to years <sup>18,34</sup>	Weeks to decades <sup>58</sup>
Long-time behaviour	Stationary size and shape <sup>5,6</sup>	Algebraic growth expected	Algebraic growth <sup>37,58,59</sup>
Grain-size distribution	Unimodal <sup>11,6</sup> ; mean: 0.1–0.3 mm	Bimodal <sup>13,16,18,20,22,53</sup> (or bidisperse density <sup>25–27,60</sup> ); coarse grains: 0.7–4 mm	Unimodal <sup>11,6</sup> ; typical mean: 0.1–0.3 mm
Physical mechanism	Mesoscale structure (reptation, saltation) matters; screening instability <sup>113,61</sup> , saltation phase locking <sup>1,4</sup>	(Erosive) sorting, coarsening, coarse-grain reptation <sup>1,13,16</sup>	Only overall properties of transport layer matter; air-stress phase lag, saturation transients <sup>8,41</sup>

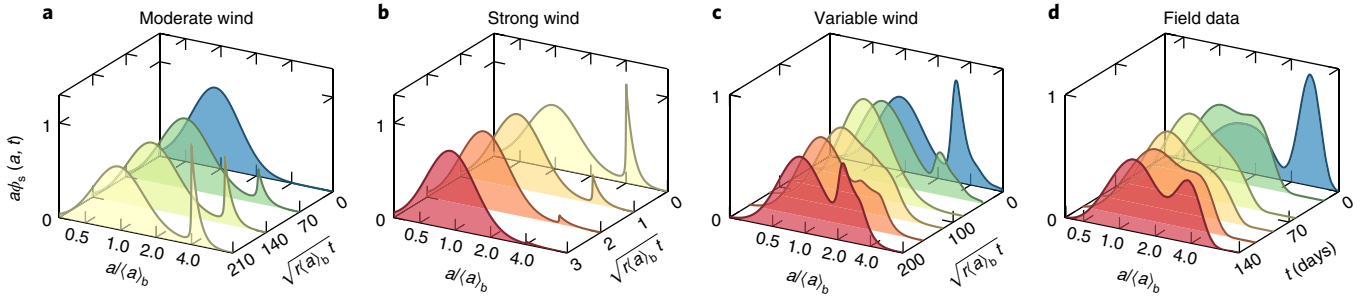


**Fig. 2 | Model and field data for wind-driven sand sorting.** **a, b** Evolving surface GSD  $\phi_s(a, t)$  obtained by numerical integration of the sorting equation (2) for constant wind speed. Erosion rate and log-normal bulk GSD  $\phi_b(a)$  of mean  $\langle a \rangle_b$  and variance  $\langle a \rangle_b^2/4$ , as in Fig. 1c. **a**, Constant moderate wind speeds ( $a_c = 4 \langle a \rangle_b$ ) create a bimodal distribution. **b**, The bimodality is quickly destroyed by a brief storm ( $a_c = 10 \langle a \rangle_b$ ). **c**, Simulating a fluctuating wind history by the coupled stochastic processes (16) with  $a_c(t)$  of long-time mean  $\langle a \rangle_b$  and variance  $0.038 \langle a \rangle_b^2$ , and an influx  $J \langle a \rangle_b \phi_b(a) = 0.7 [R(a, a_c) \phi_b(a) - \langle R(a, a_c) \rangle_b]$ , brings the model results visually closer to actual field data (**d**) taken from ref. 34 and collected from megaripple crests at Nahal Kasuy in the Negev, Israel, during a time period (2 October 2008–20 February 2009) with some intermittent autumn storms ( $\langle a \rangle_b \approx 120 \mu\text{m}$ ).

where  $\Theta$  denotes the Heaviside step function,  $r$  is a scale factor and  $a_c$  is the maximum diameter of grains that can be eroded by a given wind shear stress  $\tau$ . During moderately windy periods,  $a_c$  will considerably exceed the average bulk grain size  $\langle a \rangle_b$ . Figure 2a depicts a corresponding time series of the surface GSD obtained by direct integration of equation (2), for constant wind strength and vanishing influx ( $J \equiv 0$ ). As expected, the heavy grains from the tail of the bulk GSD  $\phi_b$  are seen to accumulate in  $\phi_s$ , so that an initially unimodal  $\phi_s(a, t=0) = \phi_b(a)$  gradually develops a second peak, much the same as the surface GSDs commonly found in field studies of megaripples<sup>14,22,23,34</sup>. The asymptotic surface GSD  $\phi_s(a, t \rightarrow \infty) \propto \phi_b(a) \Theta(a - a_c)$  takes the form of the truncated tail of the bulk distribution (see Methods), which physically amounts to an armouring layer of immobile coarse grains covering a more fine-grained sand bed.

This formal prediction hinges on the prescribed constant wind (and zero-influx) conditions, though, as they might be realized in dedicated wind-tunnel studies. In the field, variable ambient conditions can always (partly) revert the grain sorting: either via an intermittent deposition of a surplus of erodible grains picked up elsewhere (represented by the influx  $J$ , which will usually be hard to quantify); or, via mixing the upper bed layers during brief gusts that entrain also the grains of the armouring layer into saltation<sup>35</sup>. The latter mechanism is illustrated in Fig. 2b, which extends the time series from Fig. 2a, under more windy conditions. The result clearly looks very reminiscent of a time reversal, except for the much shorter timescale displayed. Indeed, evaluating equation (2) for a temporally varying synthetic wind history (fabricated as described in Methods) may incidentally yield transient results that visually compare well with field measurements (Fig. 2c,d).

The aeolian grain sorting and ensuing structure formation are thereby plainly revealed as transient phenomena. In contrast to the situation for ordinary ripples and dunes, which are expected to be much more tolerant to wind strength variations<sup>1,524,36–38</sup>, measurements of megaripples will thus always retain an anecdotal character, conditional on the actual wind history<sup>39,40</sup>—at best capturing some more or less typical (not necessarily average) behaviour. Moreover, waiting for an incipient structure formation process to saturate into a hypothetical stationary regime may be futile.

To make these qualitative conclusions more quantitative, we now establish the timescales governing the rapid relaxation of  $\phi_s$  towards the bulk distribution  $\phi_b$  during a storm, and the slow development of the armouring layer during periods of more gentle winds. During storms, the threshold grain size  $a_c$  of non-erodible grains lies far above the bulk mass of both distributions  $\phi_s$  and  $\phi_b$ , and the respective average grain sizes obey the inequality  $\langle a \rangle_b \leq \langle a \rangle_s \ll a_c$ . The

erosion rate may then be approximated by  $R(a, a_c) \sim \sqrt{ra_c}$ , and integrating the sorting equation (2) multiplied by  $a$  over all  $a$  gives (for  $J \equiv 0$ )

$$\frac{d}{dt} (\langle a \rangle_s - \langle a \rangle_b) = -\sqrt{ra_c} (\langle a \rangle_s - \langle a \rangle_b) \quad (4)$$

with the fast ‘mixing’ rate  $\sqrt{ra_c}$ . The slow ‘coarsening’ rate  $T_\tau^{-1} \equiv \langle R(a, a_c) \rangle_s \langle \Theta(a - a_c) \rangle_b / \langle \Theta(a - a_c) \rangle_s$  for the development of the armouring layer  $\langle \Theta(a - a_c) \rangle_s$  is instead obtained by integrating equation (2) over the declining fraction of erodible grains of diameters  $a < a_c$ . With  $\Theta(a_c - a) = 1 - \Theta(a - a_c)$ , this yields

$$\frac{d}{dt} \langle \Theta(a_c - a) \rangle_s = -T_\tau^{-1} \langle \Theta(a_c - a) \rangle_s \quad (5)$$

from  $\langle R(a, a_c) \rangle_s \leq \sqrt{ra_c} \langle \Theta(a_c - a) \rangle_s$ , we conclude that  $T_\tau^{-1}$  is diminished against  $\sqrt{ra_c}$  by a factor smaller than  $\langle \Theta(a - a_c) \rangle_b$ , which is itself small, by construction.

The deduced timescale separation between the formation and destruction of the armouring layer is corroborated by the numerical data displayed in Fig. 2. Accordingly, if we accept the notion of megaripples as dunes that self-assemble from reptating coarse grains by the conventional turbulent symmetry-breaking mechanism<sup>41,42</sup>, their formation requires long periods of erosion by moderate winds. First, an armouring surface layer of coarse grains needs to build up via winnowing, which must then be entrained into a considerable amount of reptation. Even brief interruptions by short storms can be detrimental. Namely, by entraining the coarse grains of the armouring layer into saltation, they quickly destroy the sorting and dramatically increase the coarse grains’ hop length and thus the minimum dune size (Methods), thereby rendering the evolved structures subcritical, hence unstable. Moreover, the erosion of dunes/heaps of subcritical length has been theoretically shown to be fast compared to dune growth<sup>37</sup>. Altogether, this suggests a slow formation and quick destruction of megaripples, in agreement with observations<sup>35,40,43</sup>. Importantly, the coarsening time  $T_\tau$  is predicted to be sensitive to the width of the bulk GSD (and to the influx  $J$ ), such that sorting and armouring are substantially slower for more homogeneous bulk sand (and more fine-grained influx). The effect is illustrated in Fig. 3 for unimodal bulk GSDs of diverse widths.

To further establish the pertinence of the notion of reptation dunes, we conducted a thorough quantitative morphological and dynamic comparison of dunes and megaripples. We first consider their shapes along the wind direction, namely the relation between

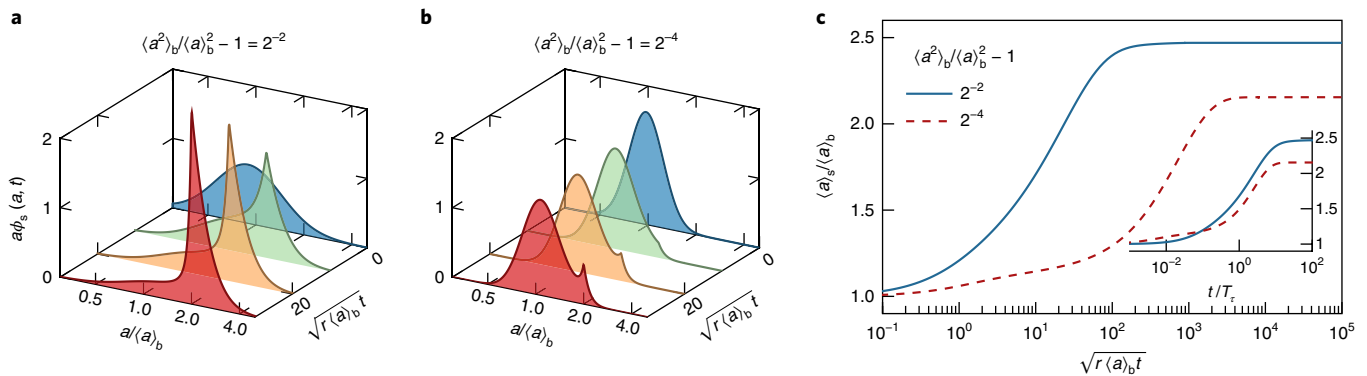


**Fig. 3 | Bulk sand polydispersity and coarsening rate.** **a, b**, The theoretical model predicts the accumulation of coarse grains at the surface of a wind-eroded sand bed to speed up with increasing bulk-grain-size polydispersity, here characterized by the variance  $2^{-2} \langle a \rangle_b^2$  (**a**) and  $2^{-4} \langle a \rangle_b^2$  (**b**) of the bulk GSD  $\phi_b(a, t)$ . The initial surface GSD (blue) is set equal to the bulk GSD,  $\phi_s(x, t=0) = \phi_b(x)$ , and acted on by a wind of constant strength  $\tau$ , which leads to the growth of the coarse-grain peak at  $a = a_c$  in the surface GSD. **c**, The diverse coarsening rates observed in **a** and **b** are also manifest in the evolution of the mean grain size  $\langle a \rangle_s$ . Rescaling time by the coarsening rate  $T_\tau^{-1} \approx \sqrt{r a_c} \langle \Theta(a - a_c) \rangle_b$  estimated below equation (5) yields the data collapse in the inset.

their slopes (estimated by their height-to-length ratio  $H/L$ ) and their size or mass (estimated by the geometric mean of  $H$  and  $L$ ). Treating megaripples as ordinary ripples, one identifies  $L$  with wavelength, often estimated by the distance between crests, and  $L/H$  with the ripple index<sup>13,22,23,44</sup>. A failed attempt to correlate ripple index and ripple size is shown in Fig. 4a, using data collected from Kelso Dunes<sup>13</sup> (cloud of triangles) and in Supplementary Fig. 4 for more recent data<sup>22</sup>. In contrast, treating individual megaripples as (more or less) isolated dunes requires one to identify  $L$  with their base length<sup>39,45</sup>. Plotting  $L/H$  against mass then unveils a striking correlation (squares and circles), extending over data sets from widely varied locations with different environmental conditions

(wind, sand supply and grain size). Furthermore, the field data then nicely match the theoretical prediction<sup>37</sup>

$$L / H - \epsilon_\infty^{-1} \propto (HL)^{-1/2} \quad (6)$$

for sand dunes. The fit in Fig. 4a directly employs the theoretical value for the asymptotic height-to-length ratio at low saturation,  $\epsilon_\infty = 0.46$ , as appropriate for erosive conditions. The only fit parameter is the omitted prefactor in equation (6), which is a characteristic dune length<sup>37</sup> that we find to be in good accord with the observations (Fig. 4c). Importantly, equation (6) attests the broken scale invariance of megaripples, which has to be contrasted with the

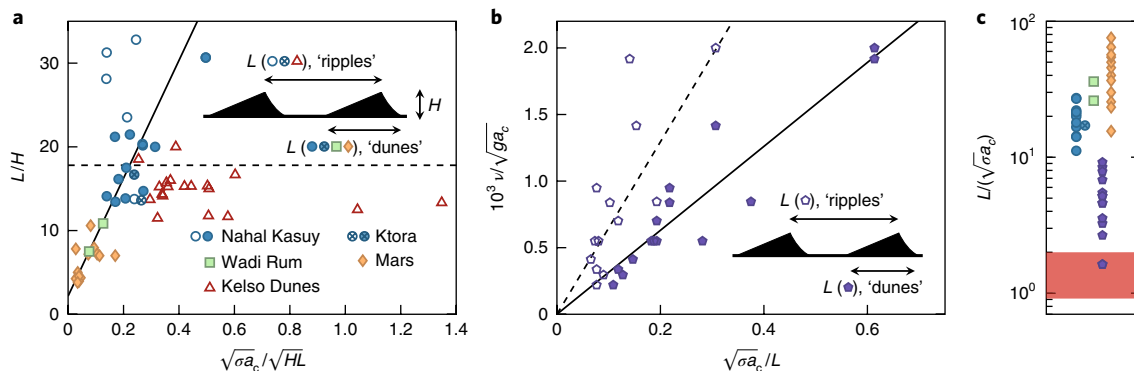


**Fig. 4 | Dune-type versus ripple-type analysis of megaripple morphology and migration.** Shape data (slope versus mass) and migration data (speed versus length) analysed as commonly done for ripples ( $L$  interpreted as wavelength, open symbols) and dunes ( $L$  interpreted as base length, filled symbols). **a**, Shape data: Megaripples at Kelso Dunes, California<sup>13</sup>,  $a_c \approx 2$  mm (triangles), at Nahal Kasuy, Israel<sup>14</sup>,  $a_c \approx 0.55$  mm, 0.78 mm (open circles), and at Ktora, Israel,  $a_c \approx 1.12$  mm (open crossed circles), all analysed as ripples and compared to the mean value 17.8 (dashed line, standard deviation 6.3) of the ripple index  $H/L$  that is expected to be independent of  $H$  and  $L$  for ripples. Contrast this with the Nahal-Kasuy (filled circles) and Ktora (filled crossed circles) data, data for megaripples at Wadi Rum, Jordan<sup>43</sup>,  $a_c \approx 1.85$  mm (squares), and so-called transverse aeolian ridges (TARs) on Mars (Ius Chasma)<sup>46</sup>,  $a_c \approx 1$  mm (diamonds), all analysed as dunes with grain-air density ratios  $\sigma \approx 2 \cdot 10^3$  (Earth),  $2 \times 10^5$  (Mars)<sup>62,63</sup> and fitted by the prediction (6) (line, with coefficient of determination  $R^2 = 0.81$ ) for dunes<sup>37,41</sup>, yielding the estimate  $70 \cdot \sqrt{\sigma a_c}$  for the characteristic 'reptation dune' base length, corresponding to 2.5 m (Kasuy Nahal), 3.5 m (Ktora), 5.8 m (Wadi Rum) and 32 m (Mars), in good agreement with the observations in **c, b**. **b**, Migration data from ref. <sup>39</sup>, measured at Great Sand Dunes National Park and Preserve, USA ( $a_c \approx 1.5$  mm) analysed as ripples (triangles) and dunes (pentagons): migration speed  $v$  also correlates better with base length than with wavelength and is well fitted by the prediction  $v \propto L^{-1}$  (line) for dunes<sup>37,41</sup>, with fit factor  $2.6 (\sigma a_c^3)^{1/2}$  ( $R^2 = 0.47$  and  $0.87$  for the ripples and dunes fit, respectively). **c**, Sizes of terrestrial megaripples and TARs on Mars are bounded from below. The red-shaded area represents the model prediction (7) for the minimum megaripple length in the appropriate range of wind strengths ( $\tau_r^c < \tau < \tau_t^c$ ), as delineated by equation (1). The larger base lengths reported for TARs on Mars could be indicative of their longer maturation, and/or of an increased wind-averaged saturation length<sup>11</sup> due to the larger gap between the threshold winds for impact and aerodynamic entrainment of bed grains on Mars<sup>64,65</sup>.



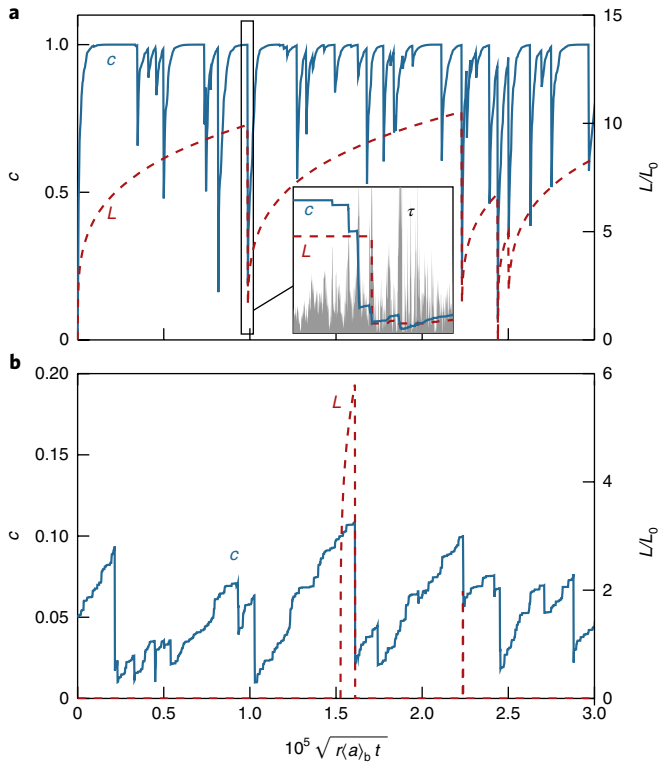


**Fig. 5 | Transient sand sorting and megaripple evolution under variable winds. a, b.** The combined schematic model (6)–(9) predicts the relative surface accumulation  $c_s(t)$  (solid line) of coarse grains and the megaripple length  $L(t)$  (dashed line), depicted here for the same influx as assumed in Fig. 2c. The fluctuating synthetic wind protocol (16) with rare intermittent gusts was simulated in a time window corresponding to some decade of real time in the field. The chance of megaripple formation is much higher with more heterogeneous (a, with  $a_c = 3a_r$ ,  $\bar{c}_b = 10^{-2}$ ) than with more homogeneous (b, with  $a_c = 2a_r$ ,  $\bar{c}_b = 10^{-3}$ ) bulk sand. It is determined by the characteristic coarsening rate  $T_\tau^{-1} = \bar{c}_b R(a_r, a_c)$  relative to the typical time period during which the wind strength remains in the range given in equation (1). The inset in a zooms in on a narrow time slice of width  $90/\sqrt{r(a)_b}$  containing some brief storms (that is, high peaks in the wind shear stress  $\tau(t)$ ; grey histogram).

size-independent aspect ratio observed for normal sand ripples<sup>5</sup>. A related natural implication of the reptation-dune interpretation is the intriguing prediction of a minimum megaripple size

$$L_0 \approx 2\sqrt{\sigma\tau / \tau_c^c} a_c \quad (7)$$

as a function of the grain–air density ratio  $\sigma$ , the wind shear strength  $\tau$  and the characteristic coarse grain diameter  $a_c$  (see Methods). This, too, is borne out qualitatively and quantitatively by the data in Fig. 4c for terrestrial megaripples and for a Martian bedform called transverse aeolian ridges (TARs)<sup>46</sup>. Finally, the model predicts a reciprocal correlation between dune migration speed and dune length. This has successfully been tested for aeolian sand dunes and their subaqueous counterparts<sup>47–49</sup>, and Fig. 4b demonstrates good agreement with available megaripple data. In contrast, a conventional interpretation, identifying  $L$  with the distance between crests, fails to yield convincing correlations (let alone a mechanistic explanation). However, given the lack of data in the full range of megaripple lengths and the natural scatter in the data, more measurements would clearly be highly desirable to substantiate the statistical significance of this conclusion.

Taken together, the above results provide strong support for the mechanistic interpretation of megaripples as reptation dunes. Moreover, the close similarity of rescaled data for terrestrial megaripples and TARs suggests that both might represent different realizations of the same type of bedform. To exemplify how this new understanding might be employed in the interpretation of future field studies, we generated extensive time series from the combined model of sand sorting and ‘reptation-dune’ formation (Fig. 5). This requires suitable synthetic wind protocols that must reproduce realistic distributions of intermittent storms and wakes covering the whole hierarchy of relevant timescales from minutes (grain mixing) to years (megaripple growth). To fabricate them efficiently, we utilize a piggyback (or ‘superstatistics’<sup>50</sup>) model coupling two stationary Gaussian Markov processes (Methods). The sand sorting effected by such wind protocols has, for a relatively short time series, already been illustrated in Fig. 2c. To make the connection with structure formation, note that the reptation dune ‘volume’  $HL$  grows proportionally to the horizontal reptation flux of the coarse grains, which itself is proportional to  $\sqrt{\tau}(\tau - \tau_c^c)$ . Inserting this into equation (6), we predict a slow algebraic megaripple coarsening. For  $L/H \gg \epsilon_\infty^{-1}$ , it takes the simple form  $dL/dt \propto \sqrt{\tau}(\tau - \tau_c^c) / L^3$ . By virtue of the strong timescale separations between grain sorting and mixing and megaripple growth and decay, respectively, an equally simple criterion for megaripple destruction, such as resetting  $L$  to the minimum reptation-dune size whenever the fraction of coarse grains falls below 0.1, should suffice for our present purpose. In the same vein, we can simplify the sorting model and idealize the transient bimodal form of  $\phi_s(a, t)$  by a weighted bidisperse function

$$\phi_s(a, t) \approx (1 - c_s)\delta(a - a_f) + c_s\delta(a - a_c) \quad (8)$$

with  $c_s(t)$  being the fraction of the coarse subpopulation of mean size  $a_c$  (the position of the right peak in Fig. 2c) and  $a_f \approx a_r$  being the size of the relevant saltating grains under the prevalent wind conditions of mean wind shear stress  $\tau$ . Thereby, the grain sorting equation (2) simplifies to

$$T_\tau \frac{d}{dt} c_s(t) = \bar{c}_s - c_s(t) \quad (9)$$

with favourable consequences for the computational efficiency and visualization of long-time predictions. Here,  $\bar{c}_s \equiv \bar{c}_b [R(a_f, a_r) + J(a_c)] T_\tau$  and  $\bar{c}_b$  are the (wind-dependent) stationary surface and bulk fractions of coarse grains, respectively, and  $T_\tau^{-1} \equiv \bar{c}_b R(a_f, a_r) + (1 - \bar{c}_b) R(a_c, a_r)$  is the bidisperse version of the wind-dependent sorting rate introduced in equation (5). For  $\bar{c}_b \ll 0.1$ , corresponding to fine bulk sand with a low amount of coarse grains, the time needed to develop some armouring is about  $0.1 T_\tau \approx 0.1 / [\bar{c}_b R(a_f, a_r)]$ , which is sensitive to the size of the armouring grains. Megaripples can grow only if this time is shorter than the typical waiting time between two gusts of strength  $\tau \geq \tau_c^c \propto a_c$ , as illustrated in Fig. 5.

In summary, we have proposed a quantitative modelling framework that elucidates how megaripples form through an intricate coupling of sand sorting, structure formation and the intermittent statistics of the wind. The mechanistic interpretation of megaripples as reptation dunes provides a unified explanation for their evolution and morphology. The theory will allow one to quantitatively address the wind-driven sand sorting and the complicated dependence of megaripple growth on the prevailing sand and wind characteristics, and hence to estimate the likelihood of megaripple formation under various environmental conditions. It may also serve as a starting point for dealing with finer details of the sorting and structure formation process, such as the mutual feedback between the evolution of the topography and the lateral grain sorting. So far, we have merely provided a first glimpse of the potential of the model for

interpreting long-term field and laboratory studies, using a representative synthetic time series. The outcome already exhibits important qualitative features that are likely to survive in more elaborate models: chiefly, the slow algebraic growth and fast decay of megariipples, the imperfect but vital correlation of sorting and growth, and the encoding of a long-term memory of wind and sand-supply conditions in the emerging transient bedforms and GSDs. All of these properties set megariipples clearly apart from their smaller and larger cousins, ordinary ripples and dunes (Table 1), thereby establishing an important independent self-organized aeolian bedform, with a unique potential for inferring past climatic and environmental conditions from morphological data.

## Methods

Methods, including statements of data availability and any associated accession codes and references, are available at <https://doi.org/10.1038/s41567-018-0106-z>.

Received: 10 May 2017; Accepted: 8 March 2018;

Published online: 30 April 2018

## References

- Bagnold, R. A. *The Physics of Blown Sand and Desert Dunes* (Methuen, London, 1941).
- Wilson, I. G. Aeolian bedforms—their development and origins. *Sedimentology* **19**, 173–210 (1972).
- Pye, K. & Tsoar, H. *Aeolian Sand and Sand Dunes* (Springer, Berlin, 2009).
- Durán, O., Claudin, P. & Andreotti, B. Direct numerical simulations of aeolian sand ripples. *Proc. Natl Acad. Sci. USA* **111**, 15665 (2014).
- Andreotti, B., Claudin, P. & Pouliquen, O. Aeolian sand ripples: Experimental study of fully developed states. *Phys. Rev. Lett.* **96**, 028001 (2006).
- Manukyan, E. & Prigozhin, L. Formation of aeolian ripples and sand sorting. *Phys. Rev. E* **79**, 031303 (2009).
- Kroy, K., Sauermann, G. & Herrmann, H. J. Minimal model for sand dunes. *Phys. Rev. Lett.* **88**, 054301 (2002).
- Andreotti, B., Claudin, P. & Douady, S. Selection of dune shapes and velocities part 1: Dynamics of sand, wind and barchans. *Eur. Phys. J. B* **28**, 321–339 (2002).
- Sauermann, G., Kroy, K. & Herrmann, H. J. Continuum saltation model for sand dunes. *Phys. Rev. E* **64**, 031305 (2001).
- Andreotti, B., Claudin, P. & Pouliquen, O. Measurements of the aeolian sand transport saturation length. *Geomorphology* **123**, 343–348 (2010).
- Lämmel, M. & Kroy, K. Analytical mesoscale modeling of aeolian sand transport. *Phys. Rev. E* **96**, 052906 (2017).
- Lapotre, M. G. A. et al. Large wind ripples on Mars: A record of atmospheric evolution. *Science* **353**, 55–58 (2016).
- Sharp, R. P. Wind ripples. *J. Geol.* **71**, 617–636 (1963).
- Yizhaq, H., Isenberg, O., Wenkart, R., Tsoar, H. & Karnieli, A. Morphology and dynamics of aeolian mega-ripples in Nahal Kasuy, southern Israel. *Isr. J. Earth Sci.* **57**, 149–165 (2009).
- Ellwood, J. M., Evans, P. D. & Wilson, I. G. Small scale aeolian bedforms. *J. Sediment. Res.* **45**, 554–561 (1975).
- Tsoar, H. Grain-size characteristics of wind ripples on a desert seif dune. *Geogr. Res. Forum* **10**, 37–50 (1990).
- Sørensen, M. in *The Fascination of Probability, Statistics and their Applications: In Honour of Ole E. Barndorff-Nielsen* (eds Podolskij, M. et al.) 1–13 (Springer International, Cham, 2016).
- Sakamoto-Arnold, C. M. Eolian features produced by the December 1977 windstorm, southern San Joaquin Valley, California. *J. Geol.* **89**, 129–137 (1981).
- Ackert, R. The origin of isolated gravel ripples in the western Asgard Range, Antarctica. *Antarct. J.* **24**, 60–62 (1989).
- Selby, M. J., Rains, R. B. & Palmer, R. W. P. Eolian deposits of the ice-free Victoria Valley, Southern Victoria Land, Antarctica. *New Zeal. J. Geol. Geophys.* **17**, 543–562 (1974).
- Yizhaq, H., Katra, I., Kok, J. F. & Isenberg, O. Transverse instability of megariipples. *Geology* **40**, 459–462 (2012).
- Qian, G., Dong, Z., Zhang, Z., Luo, W. & Lu, J. Granule ripples in the Kumtagh Desert, China: Morphology, grain size and influencing factors. *Sedimentology* **59**, 1888–1901 (2012).
- Gillies, J. A., Nickling, W. G., Tilton, M. & Furtak-Cole, E. Wind-formed gravel bed forms, wright valley, Antarctica. *J. Geophys. Res. Earth Surf.* **117**, F04017 (2012).
- Brugmans, F. Wind ripples in an active drift sand area in the Netherlands: A preliminary report. *Earth Surf. Proc. Land.* **8**, 527–534 (1983).
- Milana, J. P. Largest wind ripples on Earth? *Geology* **37**, 343–346 (2009).
- de Silva, S., Spagnuolo, M., Bridges, N. & Zimbelman, J. Gravel-mantled megariipples of the Argentinean Puna: A model for their origin and growth with implications for Mars. *Geol. Soc. Am. Bull.* **125**, 1912–1929 (2013).
- Bridges, N., Spagnuolo, M., de Silva, S., Zimbelman, J. & Neely, E. Formation of gravel-mantled megariipples on Earth and Mars: Insights from the Argentinean Puna and wind tunnel experiments. *Aeolian Res.* **17**, 49–60 (2015).
- Blom, A. & Parker, G. Vertical sorting and the morphodynamics of bed form-dominated rivers: A modeling framework. *J. Geophys. Res. Earth Surf.* **109**, F02007 (2004).
- Jerolmack, D. J., Mohrig, D., Grotzinger, J. P., Fike, D. A. & Watters, W. A. Spatial grain size sorting in eolian ripples and estimation of wind conditions on planetary surfaces: Application to meridiani planum, Mars. *J. Geophys. Res.* **111**, E12S02 (2006).
- McKenna Neuman, C. & Bédard, O. A wind tunnel investigation of particle segregation, ripple formation and armouring within sand beds of systematically varied texture. *Earth Surf. Proc. Land.* **42**, 749–762 (2017).
- Anderson, R. S. & Bunas, K. L. Grain size segregation and stratigraphy in aeolian ripples modelled with a cellular automaton. *Nature* **365**, 740–743 (1993).
- Makse, H. A. Grain segregation mechanism in aeolian sand ripples. *Eur. Phys. J. E* **1**, 127–135 (2000).
- Shiryayev, A. N. in *Selected Works of A. N. Kolmogorov: Volume II Probability Theory and Mathematical Statistics* (ed. Shiryayev, A. N.) 281–284 (Springer Netherlands, Dordrecht, 1992).
- Yizhaq, H., Katra, I., Isenberg, O. & Tsoar, H. Evolution of megariipples from a flat bed. *Aeolian Res.* **6**, 1–12 (2012).
- Katra, I., Yizhaq, H. & Kok, J. F. Mechanisms limiting the growth of aeolian megariipples. *Geophys. Res. Lett.* **41**, 858–865 (2014).
- Seppälä, M. & Lindé, K. Wind tunnel studies of ripple formation. *Geogr. Ann. A* **60**, 29–42 (1978).
- Fischer, S., Cates, M. E. & Kroy, K. Dynamic scaling of desert dunes. *Phys. Rev. E* **77**, 031302 (2008).
- Goossens, D. Aeolian dust ripples: Their occurrence, morphometrical characteristics, dynamics and origin. *CATENA* **18**, 379–407 (1991).
- Lorenz, R. D. & Valdez, A. Variable wind ripple migration at Great Sand Dunes National Park and Preserve, observed by timelapse imaging. *Geomorphology* **133**, 1–10 (2011).
- Yizhaq, H. & Katra, I. Longevity of aeolian megariipples. *Earth. Planet. Sci. Lett.* **422**, 28–32 (2015).
- Kroy, K., Sauermann, G. & Herrmann, H. J. Minimal model for aeolian sand dunes. *Phys. Rev. E* **66**, 031302 (2002).
- Musa, R. A., Takarrouht, S., Louge, M. Y., Xu, J. & Berberich, M. E. Pore pressure in a wind-swept rippled bed below the suspension threshold. *J. Geophys. Res. Earth Surf.* **119**, 2574–2590 (2014).
- Isenberg, O. et al. Megaripple flattening due to strong winds. *Geomorphology* **131**, 69–84 (2011).
- Williams, S. H., Zimbelman, J. R. & Ward, A. Large ripples on Earth and Mars. In *Proc. 33rd Annual Lunar and Planetary Science Conference 1508* (NASA, 2002).
- Zimbelman, J. R., Williams, S. H. & Johnston, A. K. Cross-sectional profiles of sand ripples, megariipples, and dunes: a method for discriminating between formational mechanisms. *Earth Surf. Proc. Land* **37**, 1120–1125 (2012).
- Zimbelman, J. R. Transverse aeolian ridges on Mars: First results from hirise images. *Geomorphology* **121**, 22–29 (2010).
- Groh, C., Wierschem, A., Aksel, N., Rehberg, I. & Kruehle, C. A. Barchan dunes in two dimensions: Experimental tests for minimal models. *Phys. Rev. E* **78**, 021304 (2008).
- Kroy, K. & Guo, X. Comment on “relevant length scale of barchan dunes”. *Phys. Rev. Lett.* **93**, 039401 (2004).
- Franklin, E. M. & Charru, F. Subaqueous barchan dunes in turbulent shear flow. Part 1. Dune motion. *J. Fluid. Mech.* **675**, 199–222 (2011).
- Beck, C. Statistics of three-dimensional lagrangian turbulence. *Phys. Rev. Lett.* **98**, 064502 (2007).
- Finkel, H. J. The barchans of southern Peru. *J. Geol.* **67**, 614–647 (1959).
- Sauermann, G. The shape of the barchan dunes of Southern Morocco. *Geomorphology* **36**, 47–62 (2000).
- Fryberger, S., Hesp, P. & Hastings, K. Aeolian granule ripple deposits, Namibia. *Sedimentology* **39**, 319–331 (1992).
- Hesp, P. A. & Hastings, K. Width, height and slope relationships and aerodynamic maintenance of barchans. *Geomorphology* **22**, 193–204 (1998).
- Hersen, P., Douady, S. & Andreotti, B. Relevant length scale of barchan dunes. *Phys. Rev. Lett.* **89**, 264301 (2002).
- Andreotti, B., Fourrière, A., Ould-Kaddour, F., Murray, B. & Claudin, P. Giant aeolian dune size determined by the average depth of the atmospheric boundary layer. *Nature* **457**, 1120–1123 (2009).
- Rasmussen, K. R., Valance, A. & Merrison, J. Laboratory studies of aeolian sediment transport processes on planetary surfaces. *Geomorphology* **244**, 74–94 (2015).

58. Ping, L., Narteau, C., Dong, Z., Zhang, Z. & Courrech du Pont, S. Emergence of oblique dunes in a landscape-scale experiment. *Nat. Geosci.* **7**, 99–103 (2014).
59. Hersen, P., Andersen, K. H., Elbelrhiti, H., Andreotti, B., Claudin, P. & Douady, S. Corridors of barchan dunes: Stability and size selection. *Phys. Rev. E* **69**, 011304 (2004).
60. Hugenholtz, C. H., Barchyn, T. E. & Favaro, E. A. Formation of periodic bedrock ridges on Earth. *Aeolian Res.* **18**, 135–144 (2015).
61. Anderson, R. S. A theoretical model for aeolian impact ripples. *Sedimentology* **34**, 943–956 (1987).
62. Larsen, S. E., Jørgensen, H. E., Landberg, L. & Tillman, J. E. Aspects of the atmospheric surface layers on Mars and Earth. *Boundary Layer Meteorol.* **105**, 451–470 (2002).
63. Sullivan, R. et al. Aeolian processes at the Mars Exploration Rover Meridiani Planum landing site. *Nature* **436**, 58–61 (2005).
64. Claudin, P. & Andreotti, B. A scaling law for aeolian dunes on Mars, Venus, Earth, and for subaqueous ripples. *Earth. Planet. Sci. Lett.* **252**, 30–44 (2006).
65. Kok, J. F. An improved parameterization of wind-blown sand flux on mars that includes the effect of hysteresis. *Geophys. Res. Lett.* **37**, L12202 (2010).

### Acknowledgements

We thank E. Schmerler for his kind help with the sand sample preparation and analysis. This research was supported by a grant from the GIF, the German-Israeli Foundation for Scientific Research and Development (no. 1143-60.8/2011). We also acknowledge

the hospitality of the KITP in Santa Barbara and the MPI-PKS in Dresden, where this work was started, and financial support by the National Science Foundation under grant no. NSF PHY-1125915, the MPI-PKS Visitors Program, and the German Academic Exchange Service (DAAD) through a Kurzzstipendium (for M.L.).

### Author contributions

M.L. and K.K. developed the theory; M.L., A.M., H.Y., H.T. and I.K. designed and conducted the experiments and field surveys; M.L., A.M., I.K. and H.Y. analysed the data; M.L. and K.K. wrote the paper. All authors discussed the results and implications and commented on the manuscript at all stages.

### Competing interests

The authors declare no competing interests.

### Additional information

**Supplementary information** is available for this paper at <https://doi.org/10.1038/s41567-018-0106-z>.

**Reprints and permissions information** is available at [www.nature.com/reprints](http://www.nature.com/reprints).

**Correspondence and requests for materials** should be addressed to K.K.

**Publisher's note:** Springer Nature remains neutral with regard to jurisdictional claims in published maps and institutional affiliations.



## Methods

**Reptation regime.** The range of wind strengths and grain-size ratios for which we expect megaripples to form corresponds to the pure reptation regime for the coarse-grain fraction (wind shear stresses  $\tau$  between the reptation and saltation threshold of the coarse grains):  $\tau_r^c < \tau < \tau_c^c$ . Bagnold's classical estimate is  $\tau_r^c \propto \sigma \rho a_c g$ , with the grain–air density ratio  $\sigma$ , the mass density  $\rho$  of the atmosphere and the gravitational acceleration  $g$  (ref.<sup>1</sup>). Assuming reptation to be driven by kicks from hopping fine grains, we may roughly estimate  $\tau_r^c$  from binary collisions that transfer enough energy to the bed grain to be lifted up to a height on the order of its own diameter  $a_c$ . Following ref.<sup>66</sup>, we use momentum and energy conservation for head-on collisions between fine and coarse grains of mass  $m_{fc} = (\pi/6)\rho\sigma a_{fc}^3$ , which yields

$$m_c g a_c \approx 2e^2 m_c m_f^2 v_f^2 / (m_f + m_c)^2 \quad (10)$$

for the minimum required impact speed  $v_f$  of the fine saltating grains. The effective restitution coefficient  $\epsilon < 1$  quantifies the energy dissipation during collisions. To account for additional drag and lift forces exerted by the unsaturated turbulent air flow on the bed grains, the gravitational mass  $m_c$  on the left-hand side of equation (10) is replaced by a reduced effective mass  $m_c^{\text{eff}} < m_c$ . It is estimated by requiring the net torque due to drag and gravity forces exerted on a coarse bed particle of mass  $m_c$  to balance the purely gravity-induced torque on a grain with mass  $m_c^{\text{eff}}$  (ref.<sup>1</sup>). For an absolute value  $F_D$  of the drag force (pointing into the wind direction) and an effective friction coefficient  $\mu$  that relates  $F_D$  to the grain weight<sup>64</sup>, this balance reads  $\mu F_D - m_c g = -m_c^{\text{eff}} g$ , or

$$m_c^{\text{eff}} / m_c = 1 - \tau / \tau_r^c \quad (11)$$

Here, we expressed the drag force  $F_D \propto \pi(a_c/2)^2 \tau$  in terms of the fluid shear stress acting on the bed grains and identified the threshold value  $\tau_r^c \propto (2\pi/3)\sigma \rho g a_c / \mu$ , above which bed grains are mobilized by the flow (corresponding to a vanishing effective weight  $m_c^{\text{eff}} = 0$ ). Replacing  $m_c$  on the left-hand side of equation (10) by  $m_c^{\text{eff}}$  and inserting equation (11) gives

$$2e^2 v_f^2 / (g a_c) \approx (1 - \tau / \tau_r^c) (m_c / m_f)^2 \quad (m_f \ll m_c) \quad (12)$$

For undersaturated transport, the impact speed  $v_f$  can be taken to be the characteristic wind velocity (at a certain height), which itself is proportional to  $\sqrt{\tau}$ ; that is,  $v_f \approx v_{ft} \sqrt{\tau / \tau_r^c}$ , where  $v_{ft}$  is the impact speed at the transport threshold  $\tau_r^c$ . At  $\tau = \tau_r^c$ , this yields equation (1) with a factor of proportionality  $2e^2 v_{ft}^2 / (g a_c)$  (using again  $\tau_r^c / \tau_r^f = a_c / a_f$ ). Inserting typical values of  $v_{ft}$  yields a plausible range  $e v_{ft} (g a_c / 2)^{-1/2} \approx 10 \dots 10^2$ .

For a continuum GSD, the characteristic size  $a_f$  of the saltating fine grains is given by the biggest grains transported by saltation at the actual wind strength  $\tau$ , hence  $\tau = \tau_r^f$ ; that is,  $\tau / \tau_r^f = a_c / a_f$ . The maximum grain-size ratio

$$a_c / a_f = \tau_r^c / \tau_r^f \approx 2.1 \dots 3.9 \quad (13)$$

consistent with megaripple formation is attained for wind strengths  $\tau = \tau_r^c$  at the reptation threshold for the coarse particles; that is, it follows by inserting  $\tau_r^c = \tau_r^f$  into equation (1). Note that, according to the foregoing discussion,  $a_f$  pertains to the fine grains that are most relevant for the reptation of the coarse grains. For typical bimodal GSDs as those in Fig. 2, it thus corresponds to grain sizes in the gap between the coarse and fine subpopulations, not to the fine-grain peak position. Accordingly, the maximum grain-size ratio refers to the width of the coarse-grain peak rather than to the peak separation.

**Minimum length of a reptation dune.** The response (or 'saturation') length  $\ell$  of the flux of reptating coarse grains is approximately estimated by their hop length, which follows from a reasoning along the lines of the previous paragraph. As the energy of a splashed grain depends only weakly on the impact energy<sup>66</sup>, the hop height of a reptating grain is approximately independent of the actual wind strength and, as argued above equation (10), on the order of its diameter  $a_c$ . We thus estimate  $\ell$  by the product of the hop time  $\approx 2\sqrt{2a_c/g}$  and the typical wind speed near the ground,  $\ell \propto \sqrt{a_c \tau / (\rho g)} \approx 0.1 \sqrt{\sigma \tau / \tau_r^c} a_c$ , with the grain–air mass density ratio  $\sigma$  and the threshold shear stress  $\tau_r^c \approx 0.01 \sigma \rho g a_c$  (ref.<sup>1</sup>). The omitted numerical prefactor is expected to be on the order of unity. With  $\sigma \approx 2 \times 10^3$  for sand on Earth, we thus get  $\ell \approx 5a_c$  at the reptation threshold, which is almost two orders of magnitude below the typical saltation length  $\approx 20\tau/(\rho g) \approx 400a$  at the transport threshold<sup>9,11</sup>. The minimum length  $L_0$  of a (reptation) dune is approximately  $L_0 \approx 20\ell$  (refs.<sup>11,67–69</sup>) (that is,  $L_0 \approx 100a_c$  at the reptation threshold), which yields equation (7).

**Erosion rate.** The grain-size dependence of the erosion rate  $R(a, a_c)$  given in equation (3) follows from the approximate scaling

$$R(a, a_c) \propto q / l \propto (\tau - \tau_r) / \sqrt{\tau} \quad (14)$$

of the vertical mass flux  $q/l$  through the sand bed, where  $q \propto \sqrt{\tau/\rho} (\tau - \tau_r) / g$  is the height-integrated horizontal mass flux and  $l \propto \tau / (\sigma \rho g)$  is the characteristic hop length of the grains<sup>9</sup> expected for under-saturated transport<sup>70,71</sup>. As above,  $\rho$  and  $\sigma$  denote the mass density of the atmosphere and the grains, respectively,  $g$  is the gravitational acceleration,  $\tau$  is the wind shear stress and  $\tau_r$  is the threshold shear stress below which grains of diameter  $a$  cannot be transported by the wind; that is,  $q(\tau < \tau_r) = 0$ . Inserting the scaling<sup>1</sup>  $\tau_r \propto \sigma \rho g a$  into equation (14), we obtain equation (3).

**Stationary limit of grain sorting.** The right-hand side of the sorting equation (2) vanishes for any surface GSD of the form  $\phi_s(a) = \varphi(a)\Theta(a - a_c)$ , which is thus a stationary solution. Integrating equation (2) over  $t$ , for a given  $a > a_c$ , yields

$$\begin{aligned} \varphi(a) &= \phi_s(a, 0) + \phi_b(a) \int_0^\infty dt \langle R(a, a_c) \rangle_s \\ &= \phi_s(a, 0) + \frac{\langle \Theta(a_c - a) \rangle_{s0}}{\langle \Theta(a - a_c) \rangle_b} \phi_b(a) \end{aligned} \quad (15)$$

In the second step, we used  $\int_0^\infty da \varphi(a) = 1$  and that  $\langle R(a, a_c) \rangle_s$  does not depend on  $a$ . The subscript  $s0$  refers to an average over the initial surface distribution  $\phi_s(a, 0) = \phi_b(a)$ , we get  $\varphi(a) = \phi_b(a) / \langle \Theta(a - a_c) \rangle_b$ , which is quoted in the main text after equation (3).

**Fluctuating wind.** The wind protocols used in Figs. 2c and 5 are obtained from coupled stochastic processes for the wind speed  $u$ , fluctuating around its mean  $U$ , and the logarithm  $\theta \equiv \ln(\sigma_u^2 / U^2)$  of its variance<sup>50</sup>,

$$\begin{aligned} \frac{d}{dt} u &= -\gamma_u (u - U) + \xi_u \\ \frac{d}{dt} \theta &= -\gamma_\theta (\theta - \theta_0) + \xi_\theta \end{aligned} \quad (16)$$

with  $\langle \xi_i(t) \xi_j(0) \rangle = 2\gamma_i \sigma_i^2 \delta(t)$  and  $\gamma_u = 10^2 \gamma_\theta$ . Within our reduced units, the minimum size  $a_c$  of the eroded grains at wind velocity  $u$  is given by  $a_c = u^2$ . To fix the overall timescale and wind strength, we set  $\gamma_u = \sqrt{r(a_c)_b}$ ,  $U^2 = 2 \langle a \rangle_b$  (Fig. 2) and  $\gamma_u = \sqrt{ra_c}$ ,  $U^2 = a_c$  (Fig. 5). We chose  $\theta_0 = -6$  and  $\sigma_\theta = 1.5$ , so that the velocity increments  $u(t + \Delta t) - u(t)$  per time step  $\Delta t$  are log-normal distributed, in accord with empirical observations<sup>72,73</sup>.

**Field data.** The data for the bulk and crest GSD shown in Fig. 2b were obtained from samples taken locally from a megaripple near Ktora (Arabah valley, southern Negev), Israel. We first drained the sand with water to stabilize the ripple, cut it as shown in the inset of Fig. 2a, and took the samples using a plastic tube (about 5 mm and 6 cm below the ripple apex for the crest and bulk sample, respectively). The surface GSD in Fig. 2b represents a thin surface layer (about 5 mm thick) taken from a square of area 1 m<sup>2</sup> in the flat area between the megaripples at Nahal Kasuy (southern Negev), Israel. All GSDs were obtained using a laser diffraction technique (Fritsch GmbH). The two sampling methods, depth-resolved and surface-averaged, reflect the vertical and horizontal segregation of the GSDs, respectively. Crest, slope and trough GSDs contribute to the horizontally averaged surface GSD, which effectively corresponds to a superposition of the local bulk and crest GSDs.

The field data from Nahal Kasuy, Israel, and Wadi Rum, Jordan, in Fig. 4a were extracted from megaripple profiles shown in refs.<sup>14,43</sup>. The numerical values are listed in Supplementary Table 2. The data from Kelso Dunes were taken from Table 2 of ref.<sup>13</sup>, and the approximate mean diameters  $a_c = 2$  mm of the coarse grain fraction were estimated from Table 3 and from the section entitled Granule Ripples in Kelso Dunes. The morphological data from Ius Chasma and Terra Sirenum on Mars were taken from Table 1 of ref.<sup>46</sup>; the coarse grains' diameter  $a_c \approx 1$  mm that gives the best match with the terrestrial data in Fig. 4a lies indeed in the range 0.7...1.8 mm observed at El Dorado<sup>74</sup>.

The size  $a_c \approx 1.5$  mm of the coarse grain fraction used to rescale the migration data in Fig. 4b is obtained as the mean of the range 1...2 mm given in Fig. 3 of ref.<sup>39</sup>.

**Data availability.** The data that support the plots within this paper and other findings of this study are available from the corresponding author upon request.

## References

- Lämmel, M., Dzikowski, K., Kroy, K., Oger, L. & Valance, A. Grain-scale modeling and splash parametrization for aeolian sand transport. *Phys. Rev. E* **95**, 022902 (2017).
- Andreotti, B., Claudin, P. & Douady, S. Selection of dune shapes and velocities part 2: A two-dimensional modelling. *Eur. Phys. J. B* **28**, 341–352 (2002).
- Kroy, K., Fischer, S. & Obermayer, B. The shape of barchan dunes. *J. Phys. Condens. Matter* **17**, S1229–S1235 (2005).

69. Parteli, E. J. R., Durán, O. & Herrmann, H. J. Minimal size of a barchan dune. *Phys. Rev. E* **75**, 011301 (2007).
70. Ho, T. D., Valance, A., Dupont, P. & Ould El Moctar, A. Scaling laws in aeolian sand transport. *Phys. Rev. Lett.* **106**, 094501 (2011).
71. Jenkins, J. T. & Valance, A. Periodic trajectories in aeolian sand transport. *Phys. Fluids* **26**, 073301 (2014).
72. Castaing, B., Gagne, Y. & Hopfinger, E. Velocity probability density functions of high Reynolds number turbulence. *Phys. D* **46**, 177–200 (1990).
73. Bohr, T., Jensen, M. H., Paladin, G. & Vulpiani, A. *Dynamical Systems Approach to Turbulence* (Cambridge Univ. Press, Cambridge, 2005).
74. Sullivan, R. et al. Wind-driven particle mobility on mars: Insights from Mars Exploration Rover observations at “El Dorado” and surroundings at Gusev Crater. *J. Geophys. Res. Planets* **113**, E06S07 (2008).

## Outlook

Following the bottom-up approach proposed in Sec. 1.1, we discussed the grain-scale splash process, the mesoscale structure of the aeolian transport, and the ensuing structure formation in this first part of the thesis. At various occasions, I commented on some tasks that I found particularly promising for future studies. The following concise list summarizes such open questions that might be answered on the basis of my own work.

**Criticality, turbulence, intermittency.** The influence of the intermittent turbulent wind strength fluctuations on the transport initiation/cessation has been addressed in the past by numerous authors [114, 124, 125, 131, 132, 250–254, 256, 257, 335–339]. An analysis in the spirit of a classical phase transition, with a critical region, diverging length/time scales, (universal?) critical exponents, etc., has not been proposed, so far. With its two thresholds, the transport transition exhibits a similarity with the rigidity transition of crosslinked fiber networks (see Sec. 8.5 of Part II of the thesis). These networks become solid-like at densities above the isostatic point; however, as soon as bending contributions (or other weak interactions or perturbations) are switched on, this transition is (discontinuously) shifted to lower densities [340]. A different, yet closely related, perspective, becomes apparent from the insight that the critical transport is characterized by almost balanced rebound (survival), ejection (birth), and trapping (death) rates of the mobilized grains. This is very much reminiscent of a predator–prey mechanism or, (asymptotically equivalently), a directed-percolation phase transition (see, *e.g.*, Ref. [341] for recent experimental and computational evidence that the laminar–turbulence transition is of second-order and falls into the directed percolation universality class). One might, for instance, analyze the intermittent transport along the lines of the recent discussion of laminar–turbulent transition by Shih, Hsieh, and Goldenfeld [342]. Finally, the self-sustained sand transport near the threshold conditions might also be discussed in the context of self-organized criticality [228].

**Saturation length.** The above concept of a phase transition for the transport initiation/cessation implies the existence of “macroscopic” fluctuations and a critical slowing down near the transport threshold, as reflected by the singularity of the saturation length. Recent systematic wind-tunnel measurements by Selmani *et al.* [197] show a qualitatively similar behavior as we obtained from

our coarse-grained computer simulations [52]. These data might serve as a benchmark for the above proposal.

**Transport regimes for poly-/bidisperse sand.** Sand polydispersity plays an undoubtedly important role for various phenomena, as we illustrated for the megaripple formation [67]. There, our discussion however merely scratched the surface of the complex transport process and therefore calls for a more detailed study. One starting point might be Fig. 3.1, which shows the various transport regimes for bidisperse sand as a function of the grain-size ratio and the wind strength. This could be solidified by computational data obtained from our coarse-grained simulations [52], which can be readily extended to a bidisperse sand bed via our splash model [140].

**Saturation transients, turbulent fluctuations, polydispersity.** Since the saturation length and the associated saturation time increase with the grain size, the intermittent turbulent wind gusts might be too short to transport big grains efficiently (even though the average wind strength might exceed the threshold value for their transport). Instead of performing high jumps, these big grains will undergo reptation during the short gusts [105], thereby widening the wind-strength (and grain-size) window within which megaripples can be formed (see Fig. 3.1). Finer grains, in contrast, are easier promoted into saltation, thus helping to sustain the transport at relatively low wind speeds (as particularly relevant on Mars [150]).

**Space-resolved sand sorting.** Our mean-fieldish sorting model [67] should be extended to allow for spatial heterogeneities of the grain-size distribution. In particular, it should resolve the depth-dependent evolution<sup>1</sup>[319] and the influence of spatial saturation transients on the erosion rate. Since the erosion becomes less effective further downwind of a sand bed, megaripples are expected to be predominantly formed at its upwind end. Based on this argument, one might also predict the spatial gradient of the megaripple age, size, shape, etc. Accounting for spatial transients further allows to quantitatively discuss the influence of the grain-size distribution of the sand source (located at the upwind end of the sand bed) on the megaripple formation.

**Sand sorting and selected value statistics.** To describe a general selection process, Smerlak and Youssef [343] defined a selected value as a transformation  $S_t W$  of a non-negative random variable  $W$  via the relation  $P(S_t W = w) \propto w^t P(W = w)$  between the distributions  $P$  after and before the transformation. They showed that, for somewhat tame initial distributions (no power-law tails),  $W$  approaches a universal family of limiting distributions (as  $t \rightarrow \infty$ ) that generalize

<sup>1</sup> Following Ref. [67], the evolution of the distribution  $\phi(a, z, t)$  of the grain size  $a$  at depth  $z$  and time  $t$  is given by

$$[\partial_t + \langle R(a) \rangle_0 \delta z \partial_z - D \partial_z^2] \phi(a, z, t) = 0 \quad (5.1)$$

The (fixed) thickness  $\delta z$  of the considered layer should be on the order of the diameter of the biggest grains. Equation (5.1) relates the distribution  $\phi(d, z - \delta z, t)$  in the next layer to  $\phi(d, z, t)$  by expanding  $\phi(d, z - \delta z, t) \simeq \phi(d, z, t) - \delta z \partial_z \phi(d, z, t)$ . As the eroded sand volume  $\langle R(d) \rangle_0$  at each layer has to be filled up by material from the next lower layer, the net sand exchange at each layer is  $-\langle R(d) \rangle_0 \phi(d, z, t) + \langle R(d) \rangle_0 \phi(d, z + \delta z, t) = -\langle R(d) \rangle_0 \delta z \partial_z \phi(d, z, t)$ , which is the second term in the brackets. The third diffusive term accounts for additional inter-layer mixing, its strength being characterized by the diffusion constant  $D$  that might be taken to be grain-size independent, for simplicity.

the log-normal distribution, with the “tail thickness” of  $W$  determining the universality class. Very recently, Smerlak [344] showed that selection exhibits close similarities to coarsening, with equivalent features, like dynamic scaling and self-similarity.

Introducing a time-dependent distribution  $p(w, t)$  of  $w$ , the above selection dynamics may be rewritten as  $\partial_t p(w, t) = (\ln w - \langle \ln w \rangle_t) p(w, t)$  with the average  $\langle \dots \rangle_t \equiv \int dw \dots p(w, t)$ . Its general form is thus similar to the dynamics we derived for our sorting model [67], which suggests to interpret sand sorting as a (special kind of a) selection and/or coarsening process—as one might immediately expect due to the closely related notions of sorting and selection. It raises the question if the asymptotic distributions and the universality classes identified by Smerlak and Youssef should also be observed for the grain-size distributions in the field and if concepts like dynamic scaling and self-similarity can be applied to sand sorting. In Ref. [344] Smerlak already speculated that selection and coarsening may be unified to a general extreme values theory; sorting would then be just another variation of it.

**Dynamic scaling analysis for sand ripples.** Manukyan and Prigozhin [319] proposed a computational model for sand sorting and (mega)ripple formation. It seems promising to analyze it along the lines of the work by Fischer *et al.* [87] in order to investigate the long-time dynamics of these bedforms.

**Dynamic scaling analysis for subaqueous bedforms.** Over the last years, linear stability analysis has been successfully used to gain a deep understanding of the creation of the various three-dimensional subaqueous bedforms [45]. However, a systematic study also their long-time evolution and their dynamic scaling, requires a different approach. Again, one may analyze these models along the lines of Ref. [87].



# Bibliography

- [1] R. Greeley and J. D. Iversen, *Wind as a geologic process*, edited by W. I. Axford, G. E. Hunt, and R. Greeley, Vol. 4, Cambridge Planetary Science Series (Cambridge University Press, 1985).
- [2] Y. Jiang and M. Liu, “Why granular media are thermal, and quite normal, after all”, *Eur. Phys. J. E* **40**, 10 (2017).
- [3] H. M. Jaeger, S. R. Nagel, and R. P. Behringer, “Granular solids, liquids, and gases”, *Rev. Mod. Phys.* **68**, 1259–1273 (1996).
- [4] E. DeGiuli, J. N. McElwaine, and M. Wyart, “Phase diagram for inertial granular flows”, *Phys. Rev. E* **94**, 012904 (2016).
- [5] DeGiuli, Eric and Wyart, Matthieu, “Unifying suspension and granular flows near jamming”, *EPJ Web Conf.* **140**, 01003 (2017).
- [6] Schröter, Matthias, “A local view on the role of friction and shape”, *EPJ Web Conf.* **140**, 01008 (2017).
- [7] C.-H. Liu, S. R. Nagel, D. A. Schecter, S. N. Coppersmith, S. Majumdar, O. Narayan, and T. A. Witten, “Force fluctuations in bead packs”, *Science* **269**, 513–515 (1995).
- [8] T. S. Majmudar and R. P. Behringer, “Contact force measurements and stress-induced anisotropy in granular materials”, *Nature* **435**, 1079–1082 (2005).
- [9] P. G. de Gennes, “Granular matter: a tentative view”, *Rev. Mod. Phys.* **71**, S374–S382 (1999).
- [10] Q. Zheng and A. Yu, “Why have continuum theories previously failed to describe sandpile formation?”, *Phys. Rev. Lett.* **113**, 068001 (2014).
- [11] A. J. Liu and S. R. Nagel, “The jamming transition and the marginally jammed solid”, *Annu. Rev. Condens. Matter Phys.* **1**, 347–369 (2010).
- [12] S. Torquato and F. H. Stillinger, “Jammed hard-particle packings: from kepler to bernal and beyond”, *Rev. Mod. Phys.* **82**, 2633–2672 (2010).
- [13] M. van Hecke, “Jamming of soft particles: geometry, mechanics, scaling and isostaticity”, *J. Phys.: Condens. Matter* **22**, 033101 (2010).
- [14] A. Baule, F. Morone, H. J. Herrmann, and H. A. Makse, “Edwards statistical mechanics for jammed granular matter”, *Rev. Mod. Phys.*, (2017).
- [15] I. S. Aranson and L. S. Tsimring, “Patterns and collective behavior in granular media: Theoretical concepts”, *Rev. Mod. Phys.* **78**, 641–652 (2006).

- [16] GDR MiDi, “On dense granular flows”, *Eur. Phys. J. E* **14**, 341–365 (2004).
- [17] C. Song, P. Wang, and H. A. Makse, “A phase diagram for jammed matter”, *Nature* **453**, 629–632 (2008).
- [18] F. Boyer, É. Guazzelli, and O. Pouliquen, “Unifying suspension and granular rheology”, *Phys. Rev. Lett.* **107**, 188301 (2011).
- [19] C. P. Goodrich, A. J. Liu, and J. P. Sethna, “Scaling ansatz for the jamming transition”, *Proc. Natl. Acad. Sci. U.S.A.* **113**, 9745–9750 (2016).
- [20] H. A. Vinutha and S. Sastry, “Disentangling the role of structure and friction in shear jamming”, *Nat. Phys.* **12**, 578–583 (2016).
- [21] E. DeGiuli and M. Wyart, “Friction law and hysteresis in granular materials”, *Proc. Natl. Acad. Sci. U.S.A.* **114**, 9284–9289 (2017).
- [22] P. Charbonneau, J. Kurchan, G. Parisi, P. Urbani, and F. Zamponi, “Glass and jamming transitions: from exact results to finite-dimensional descriptions”, *Annu. Rev. Condens. Matter Phys.* **8**, 265–288 (2017).
- [23] M. Creyssels, P. Dupont, A. Ould el Moctar, A. Valance, I. Cantat, J. T. Jenkins, J. M. Pasini, and K. R. Rasmussen, “Saltating particles in a turbulent boundary layer: experiment and theory”, *J. Fluid Mech.* **625**, 47–74 (2009).
- [24] O. Durán, B. Andreotti, and P. Claudin, “Numerical simulation of turbulent sediment transport, from bed load to saltation”, *Phys. Fluids* **24**, 103306 (2012).
- [25] V. Cornish, *Waves of sand and snow and the eddies which make them* (Open Court Publishing Co., 1913).
- [26] R. P. Sharp, “Wind ripples”, *J. Geol.* **71**, 617–636 (1963).
- [27] J. M. Ellwood, P. D. Evans, and I. G. Wilson, “Small scale aeolian bedforms”, *J. Sediment. Res.* **45**, 554–561 (1975).
- [28] B. Andreotti, P. Claudin, and O. Pouliquen, “Aeolian sand ripples: experimental study of fully developed states”, *Phys. Rev. Lett.* **96**, 028001 (2006).
- [29] H. Yizhaq, O. Isenberg, R. Wenkart, H. Tsoar, and A. Karnieli, “Morphology and dynamics of aeolian mega-ripples in Nahal Kasuy, southern Israel”, *Israel J. Earth Sci.* **57**, 149–165 (2009).
- [30] H. Yizhaq and I. Katra, “Longevity of aeolian megaripples”, *Earth Planet. Sci. Lett.* **422**, 28–32 (2015).
- [31] G. Sauermann, “The shape of the barchan dunes of Southern Morocco”, *Geomorphology* **36**, 47–62 (2000).
- [32] B. Andreotti, P. Claudin, and S. Douady, “Selection of dune shapes and velocities part 1: dynamics of sand, wind and barchans”, *EPJ B* **28**, 321–339 (2002).
- [33] C. S. Breed, “Terrestrial analogs of the hellespontus dunes, mars”, *Icarus* **30**, 326–340 (1977).
- [34] Z. Dong, G. Qian, W. Luo, Z. Zhang, S. Xiao, and A. Zhao, “Geomorphological hierarchies for complex mega-dunes and their implications for mega-dune evolution in the Badain Jaran Desert”, *Geomorphology* **106**, 180–185 (2009).



- [35] B. Andreotti, A. Fourrière, F. Ould-Kaddour, B. Murray, and P. Claudin, “Giant aeolian dune size determined by the average depth of the atmospheric boundary layer.”, *Nature* **457**, 1120–3 (2009).
- [36] G. Kocurek, R. C. Ewing, and D. Mohrig, “How do bedform patterns arise? new views on the role of bedform interactions within a set of boundary conditions”, *ESPL* **35**, 51–63 (2010).
- [37] H. Elbelrhiti, B. Andreotti, and P. Claudin, “Barchan dune corridors: field characterization and investigation of control parameters”, *J. Geophys. Res.* **113**, F02S15 (2008).
- [38] O. Durán, V. Schwämmle, P. G. Lind, and H. J. Herrmann, “The dune size distribution and scaling relations of barchan dune fields”, *Granular Matter* **11**, 7–11 (2009).
- [39] O. Durán, V. Schwämmle, P. G. Lind, and H. J. Herrmann, “Size distribution and structure of barchan dune fields”, *Nonlinear Processes Geophys.* **18**, 455–467 (2011).
- [40] R. A. Bagnold, *The physics of blown sand and desert dunes*. (Methuen, London, 1941).
- [41] G. Wilson, “Aeolian bedforms—their development and origins”, *Sedimentology* **19**, 173–210 (1972).
- [42] K. Pye and H. Tsoar, *Aeolian sand and sand dunes* (Springer, 2009).
- [43] C. Groh, A. Wierschem, N. Aksel, I. Rehberg, and C. A. Kruelle, “Barchan dunes in two dimensions: experimental tests for minimal models”, *Phys. Rev. E* **78**, 021304 (2008).
- [44] A. Fourrière, P. Claudin, and B. Andreotti, “Bedforms in a turbulent stream: formation of ripples by primary linear instability and of dunes by nonlinear pattern coarsening”, *J. Fluid Mech.* **649**, 287–328 (2010).
- [45] F. Charru, B. Andreotti, and P. Claudin, “Sand ripples and dunes”, *Annu. Rev. Fluid Mech.* **45**, 469–493 (2013).
- [46] B. Andreotti and P. Claudin, “Aeolian and subaqueous bedforms in shear flows”, *Philos. Trans. Royal Soc. A* **371**, (2013).
- [47] M. C. Bourke, N. Lancaster, L. K. Fenton, E. J. Parteli, J. R. Zimbelman, and J. Radebaugh, “Extraterrestrial dunes: an introduction to the special issue on planetary dune systems”, *Geomorphology* **121**, 1–14 (2010).
- [48] J. R. Zimbelman, M. C. Bourke, and R. D. Lorenz, “Recent developments in planetary Aeolian studies and their terrestrial analogs”, *Aeolian Res.* **11**, 109–126 (2013).
- [49] N. Bridges, P. Geissler, S. Silvestro, and M. Banks, “Bedform migration on Mars: Current results and future plans”, *Aeolian Res.* **9**, 133–151 (2013).
- [50] L. Fenton, R. Ewing, N. Bridges, and R. Lorenz, in *Treatise on geomorphology* (Academic Press, San Diego, 2013), pp. 287–312.

- [51] N. Thomas, H. Sierks, C. Barbieri, P. L. Lamy, R. Rodrigo, H. Rickman, D. Koschny, H. U. Keller, J. Agarwal, M. F. A'Hearn, F. Angrilli, A.-T. Auger, M. A. Barucci, J.-L. Bertaux, I. Bertini, S. Besse, D. Bodewits, G. Cremonese, V. Da Deppo, B. Davidsson, M. De Cecco, S. Debei, M. R. El-Maarry, F. Ferri, S. Fornasier, M. Fulle, L. Giacomini, O. Groussin, P. J. Gutierrez, C. Güttler, S. F. Hviid, W.-H. Ip, L. Jorda, J. Knollenberg, J.-R. Kramm, E. Kührt, M. Küppers, F. La Forgia, L. M. Lara, M. Lazzarin, J. J. L. Moreno, S. Magrin, S. Marchi, F. Marzari, M. Massironi, H. Michalik, R. Moissl, S. Mottola, G. Naletto, N. Oklay, M. Pajola, A. Pommerol, F. Preusker, L. Sabau, F. Scholten, C. Snodgrass, C. Tubiana, J.-B. Vincent, and K.-P. Wenzel, "The morphological diversity of comet 67p/churyumov-gerasimenko", *Science* **347**, (2015).
- [52] M. Lämmel and K. Kroy, "Analytical mesoscale modeling of aeolian sand transport", *Phys. Rev. E* **96**, 052906 (2017).
- [53] S. L. Namikas, "Field measurement and numerical modelling of aeolian mass flux distributions on a sandy beach", *Sedimentology* **50**, 303–326 (2003).
- [54] L. Gomes, J. L. Arrue, M. V. Lopez, G. Sterk, D. Richard, R. Gracia, M. Sabre, A. Gaudichet, and J. P. Frangi, "Wind erosion in a semiarid agricultural area of spain: the welsons project", *CATENA* **52**, 235–256 (2003).
- [55] H. Du, X. Xue, and T. Wang, "Estimation of saltation emission in the kubuqi desert, north china", *Sci. Total Environ.* **479**, 77–92 (2014).
- [56] Y. Shao, *Physics and modelling of wind erosion*, edited by R. Sadourny, Vol. 23, Atmospheric and Oceanographic Science Library (Kluwer Academic Publishers, 2000).
- [57] J. F. Kok, E. J. R. Parteli, T. I. Michaels, and D. B. Karam, "The physics of wind-blown sand and dust", *Rep. Progr. Phys.* **75**, 106901 (2012).
- [58] S. Ravi, P. D'Odorico, D. D. Breshears, J. P. Field, A. S. Goudie, T. E. Huxman, J. Li, G. S. Okin, R. J. Swap, A. D. Thomas, S. Van Pelt, J. J. Whicker, and T. M. Zobeck, "Aeolian processes and the biosphere", *Rev. Geophys.* **49**, (2011).
- [59] J. J. Whicker, D. D. Breshears, and J. P. Field, "Progress on relationships between horizontal and vertical dust flux: mathematical, empirical and risk-based perspectives", *Aeolian Res.* **14**, 105–111 (2014).
- [60] W. Zhang, T. Wang, W. Wang, J. Qu, X. Xue, and Z. Yao, "The gobi sand stream and its control over the top surface of the mogao grottoes, china", *Bull. Eng. Geol. Environ.* **63**, 261–269 (2004).
- [61] W. Wang, Z. Dong, T. Wang, and G. Zhang, "The equilibrium gravel coverage of the deflated gobi above the mogao grottoes of dunhuang, china", *Environ. Geol.* **50**, 1077–1083 (2006).
- [62] B. Liu, W. Zhang, J. Qu, K. Zhang, and Q. Han, "Controlling windblown sand problems by an artificial gravel surface: a case study over the gobi surface of the mogao grottoes", *Geomorphology* **134**, 461–469 (2011).
- [63] J. Allen, "Transverse erosional marks of mud and rock: their physical basis and geological significance", *Sediment. Geol.* **5**, 167–385 (1971).

- [64] M. Day and G. Kocurek, “Aeolian dune interactions preserved in the ancient rock record”, *Sediment. Geol.* **358**, 187–196 (2017).
- [65] J. E. Ungar and P. K. Haff, “Steady state saltation in air”, *Sedimentology* **34**, 289–299 (1987).
- [66] R. S. Anderson, M. Sørensen, and B. B. Willetts, in *Aeolian grain transport 1: mechanics* (Springer Vienna, Vienna, 1991), pp. 1–19.
- [67] M. Lämmel, A. Meiwald, H. Yizhaq, H. Tsoar, I. Katra, and K. Kroy, “Aeolian sand sorting and megaripple formation”, 2018.
- [68] K. Pye, *Aeolian dust and dust deposits* (Academic Press Inc. (London) Ltd., 1987).
- [69] O. Durán, E. J. Parteli, and H. J. Herrmann, “A continuous model for sand dunes: review, new developments and application to barchan dunes and barchan dune fields”, *ESPL* **35**, 1591–1600 (2010).
- [70] O. Durán, P. Claudin, and B. Andreotti, “On aeolian transport: grain-scale interactions, dynamical mechanisms and scaling laws”, *Aeolian Res.* **3**, 243–270 (2011).
- [71] J. Merrison, “Sand transport, erosion and granular electrification”, *Aeolian Res.* **4**, 1–16 (2012).
- [72] E. Parteli, K. Kroy, H. Tsoar, J. Andrade, and T. Pöschel, “Morphodynamic modeling of aeolian dunes: review and future plans”, *The European Physical Journal Special Topics* **223**, 2269–2283 (2014).
- [73] K. R. Rasmussen, A. Valance, and J. Merrison, “Laboratory studies of aeolian sediment transport processes on planetary surfaces”, *Geomorphology* **244**, 74–94 (2015).
- [74] P. Yang, Z. Dong, G. Qian, W. Luo, and H. Wang, “Height profile of the mean velocity of an aeolian saltating cloud: Wind tunnel measurements by Particle Image Velocimetry”, *Geomorphology* **89**, 320–334 (2007).
- [75] W. Zhang, Y. Wang, and S. J. Lee, “Simultaneous piv and ptv measurements of wind and sand particle velocities”, *Exp. Fluids* **45**, 241–256 (2008).
- [76] K. R. Rasmussen and M. Sørensen, “Vertical variation of particle speed and flux density in aeolian saltation: measurement and modeling”, *J. Geophys. Res.* **113**, F02S12 (2008).
- [77] K. R. Rasmussen, J. F. Kok, and J. P. Merrison, “Enhancement in wind-driven sand transport by electric fields”, *Planet. Space Sci.* **57**, 804–808 (2009).
- [78] D. M. Burr, N. T. Bridges, J. K. Smith, J. R. Marshall, B. R. White, and D. A. Williams, “The titan wind tunnel: a new tool for investigating extraterrestrial aeolian environments”, *Aeolian Res.* **18**, 205–214 (2015).
- [79] R. D. Lorenz and A. Valdez, “Variable wind ripple migration at great sand dunes national park and preserve, observed by timelapse imaging”, *Geomorphology* **133**, 1–10 (2011).
- [80] H. Yizhaq, I. Katra, O. Isenberg, and H. Tsoar, “Evolution of megaripples from a flat bed”, *Aeolian Res.* **6**, 1–12 (2012).
- [81] L. Ping, C. Narteau, Z. Dong, Z. Zhang, and S. Courrech du Pont, “Emergence of oblique dunes in a landscape-scale experiment”, *Nat. Geosc.* **7**, 99–103 (2014).

- [82] G. Sauermann, K. Kroy, and H. J. Herrmann, “Continuum saltation model for sand dunes”, *Phys. Rev. E* **64**, 031305 (2001).
- [83] K. Kroy, G. Sauermann, and H. J. Herrmann, “Minimal model for sand dunes”, *Phys. Rev. Lett.* **88**, 054301 (2002).
- [84] P. Hersen, S. Douady, and B. Andreotti, “Relevant length scale of barchan dunes”, *Phys. Rev. Lett.* **89**, 264301– (2002).
- [85] P. Claudin and B. Andreotti, “A scaling law for aeolian dunes on mars, venus, earth, and for subaqueous ripples”, *Earth Planet. Sci. Lett.* **252**, 30–44 (2006).
- [86] E. J. R. Parteli, O. Durán, and H. J. Herrmann, “Minimal size of a barchan dune”, *Phys. Rev. E* **75**, 011301 (2007).
- [87] S. Fischer, M. E. Cates, and K. Kroy, “Dynamic scaling of desert dunes”, *Phys. Rev. E* **77**, 031302 (2008).
- [88] C. Groh, I. Rehberg, and C. a. Kruehle, “How attractive is a barchan dune?”, *New J. Phys.* **11**, 023014 (2009).
- [89] R. S. Anderson, “A theoretical model for aeolian impact ripples”, *Sedimentology* **34**, 943–956 (1987).
- [90] O. Durán, P. Claudin, and B. Andreotti, “Direct numerical simulations of aeolian sand ripples”, *Proc. Natl. Acad. Sci. U.S.A.* **111**, 15665–15668 (2014).
- [91] B. Andreotti, “A two-species model of aeolian sand transport”, *J. Fluid Mech.* **510**, 47–70 (2004).
- [92] M. Lämmel, D. Rings, and K. Kroy, “A two-species continuum model for aeolian sand transport”, *New J. Phys.* **14**, 093037 (2012).
- [93] X. J. Zheng, N. Huang, and Y.-H. Zhou, “Laboratory measurement of electrification of wind-blown sands and simulation of its effect on sand saltation movement”, *J. Geophys. Res.* **108**, (2003).
- [94] D. S. Schmidt, R. A. Schmidt, and J. D. Dent, “Electrostatic force on saltating sand”, *J. Geophys. Res.* **103**, 8997–9001 (1998).
- [95] D. S. Schmidt, R. A. Schmidt, and J. D. Dent, “Electrostatic force in blowing snow”, *Bound.-Layer Meteor.* **93**, 29–45 (1999).
- [96] T.-L. Bo, H. Zhang, and X.-J. Zheng, “Charge-to-mass ratio of saltating particles in wind-blown sand”, *Sci. Rep.* **4**, 5590 (2014).
- [97] J. Kolehmainen, A. Ozel, C. M. Boyce, and S. Sundaresan, “Triboelectric charging of monodisperse particles in fluidized beds”, *AIChE J.* **63**, 1872–1891 (2017).
- [98] J. F. Kok and D. J. Lacks, “Electrification of granular systems of identical insulators”, *Phys. Rev. E* **79**, 051304 (2009).
- [99] G. Williams, “Some aspects of the eolian saltation load”, *Sedimentology* **3**, 257–287 (1964).
- [100] J. F. Leys and G. H. McTainsh, “Sediment fluxes and particle grain-size characteristics of wind-eroded sediments in southeastern australia”, *ESPL* **21**, 661–671 (1996).

- [101] Y. Shao and M. Mikami, “Heterogeneous saltation: theory, observation and comparison”, *Bound.-Layer Meteor.* **115**, 359–379 (2005).
- [102] L. Tan, W. Zhang, J. Qu, J. Du, D. Yin, and Z. An, “Variation with height of aeolian mass flux density and grain size distribution over natural surface covered with coarse grains: a mobile wind tunnel study”, *Aeolian Res.* **15**, 345–352 (2014).
- [103] H. Cheng, J. He, X. Zou, J. Li, C. Liu, B. Liu, C. Zhang, Y. Wu, and L. Kang, “Characteristics of particle size for creeping and saltating sand grains in aeolian transport”, *Sedimentology* **62**, 1497–1511 (2015).
- [104] C. McKenna Neuman and O. Bédard, “A wind tunnel investigation of particle segregation, ripple formation and armouring within sand beds of systematically varied texture”, *ESPL* **42**, 749–762 (2017).
- [105] R. L. Martin and J. F. Kok, “Equal susceptibility and size-selective mobility in aeolian saltation”, arXiv:1707.09964, (2017).
- [106] T. Pächt, H. J. Herrmann, and T. Shinbrot, “Why do particle clouds generate electric charges?”, *Nat. Phys.* **6** (5), (2010).
- [107] T. Siu, J. Cotton, G. Mattson, and T. Shinbrot, “Self-sustaining charging of identical colliding particles”, *Phys. Rev. E* **89**, 052208 (2014).
- [108] R. Yoshimatsu, N. A. M. Araujo, T. Shinbrot, and H. J. Herrmann, “Field driven charging dynamics of a fluidized granular bed”, *Soft Matter* **12**, 6261–6267 (2016).
- [109] R. Yoshimatsu, N. A. M. Araujo, G. Wurm, H. J. Herrmann, and T. Shinbrot, “Self-charging of identical grains in the absence of an external field”, *Sci. Rep.* **7**, 39996 (2017).
- [110] T. Shinbrot, M. Rutala, and H. Herrmann, “Surface contact charging”, *Phys. Rev. E* **96**, 032912 (2017).
- [111] J. F. Kok and N. O. Renno, “Electrostatics in wind-blown sand”, *Phys. Rev. Lett.* **100**, 014501 (2008).
- [112] T. Bo, H. Zhang, W. Zhu, and X. Zheng, “Theoretical prediction of electric fields in wind-blown sand”, *J. Geophys. Res.* **118**, 4494–4502 (2013).
- [113] J. S. Mendez Harper, G. D. McDonald, J. Dufek, M. J. Malaska, D. M. Burr, A. G. Hayes, J. McAdams, and J. J. Wray, “Electrification of sand on titan and its influence on sediment transport”, *Nat. Geosc.* **10**, 260–265 (2017).
- [114] H.-J. Schönfeldt, “Remarks on the definition and estimation of the aeolian erosion threshold friction velocity”, *Meteor. Z.* **12**, 137–142(6) (2003).
- [115] R. Sullivan, R. Greeley, M. Kraft, G. Wilson, M. Golombek, K. Herkenhoff, J. Murphy, and P. Smith, “Results of the imager for mars pathfinder windsock experiment”, *J. Geophys. Res.* **105(E10)**, 24, 547–24, 562 (2000).
- [116] J. F. Kok, “Difference in the wind speeds required for initiation versus continuation of sand transport on mars: implications for dunes and dust storms”, *Phys. Rev. Lett.* **104**, 074502 (2010).
- [117] N. T. Bridges, F. Ayoub, J.-P. Avouac, S. Leprince, A. Lucas, and S. Mattson, “Earth-like sand fluxes on mars”, *Nature* **485**, 339–342 (2012).

- [118] H. Yizhaq, J. Kok, and I. Katra, “Basaltic sand ripples at Eagle Crater as indirect evidence for the hysteresis effect in Martian saltation”, *Icarus*, (2013).
- [119] M. Lämmel, “Aeolian Sand Transport”, Diplomarbeit (Universität Leipzig, 2011).
- [120] S. Fischer and K. Kroy, “Dynamics of aeolian sand heaps and dunes: the influence of the wind strength”, *Traffic and Granular Flow '05*, 79–98 (2007).
- [121] T. E. Barchyn, R. L. Martin, J. F. Kok, and C. H. Hugenholtz, “Fundamental mismatches between measurements and models in aeolian sediment transport prediction: the role of small-scale variability”, *Aeolian Res.* **15**, 245–251 (2014).
- [122] G. R. Butterfield, “Transitional behaviour of saltation: wind tunnel observations of unsteady winds”, *J. Arid. Environ.* **39**, 377–394 (1998).
- [123] B. Li and C. McKenna Neuman, “A wind tunnel study of aeolian sediment transport response to unsteady winds”, *Geomorphology* **214**, 261–269 (2014).
- [124] J. E. Stout and T. M. Zobeck, “Intermittent saltation”, *Sedimentology* **44**, 959–970 (1997).
- [125] C. M. Neuman, N. Lancaster, and W. G. Nickling, “The effect of unsteady winds on sediment transport on the stoss slope of a transverse dune, silver peak, nv, usa”, *Sedimentology* **47**, 211–226 (2000).
- [126] S. Pfeifer and H.-J. Schönfeldt, “The response of saltation to wind speed fluctuations”, *ESPL* **37**, 1056–1064 (2012).
- [127] M. Sørensen, “On the effect of time variability of the wind on rates of aeolian sand transport.”, *Aarhus Geoscience* **7**, 73–77 (1997).
- [128] J. F. Kok, “An improved parameterization of wind-blown sand flux on mars that includes the effect of hysteresis”, *Geophys. Res. Lett.* **37**, (2010).
- [129] P. Wang and X. Zheng, “Saltation transport rate in unsteady wind variations”, *Eur. Phys. J. E* **37**, 40 (2014).
- [130] H. Zhang, X.-J. Zheng, and T.-L. Bo, “Electric fields in unsteady wind-blown sand”, *Eur. Phys. J. E* **37**, 13 (2014).
- [131] S. Dupont, G. Bergametti, B. Marticorena, and S. Simoëns, “Modeling saltation intermittency”, *J. Geophys. Res.* **118**, 7109–7128 (2013).
- [132] M. V. Carneiro, K. R. Rasmussen, and H. J. Herrmann, “Bursts in discontinuous aeolian saltation”, *Sci. Rep.* **5**, 11109– (2015).
- [133] A. N. Shiriyayev, “On the logarithmic normal distribution of particle sizes under grinding”, in *Selected works of a. n. kolmogorov: volume ii probability theory and mathematical statistics*, edited by A. N. Shiriyayev (Springer Netherlands, Dordrecht, 1992), pp. 281–284.
- [134] M. Sørensen, “On the size distribution of sand”, in *The fascination of probability, statistics and their applications: in honour of ole e. barndorff-nielsen*, edited by M. Podolskij, R. Stelzer, S. Thorbjørnsen, and A. E. D. Veraart (Springer International Publishing, Cham, 2016), pp. 1–13.
- [135] R. A. Bagnold and O. Barndorff-Nielsen, “The pattern of natural size distributions”, *Sedimentology* **27**, 199–207 (1980).

- [136] M. A. Rice, B. B. Willetts, and I. K. McEwan, “An experimental study of multiple grain-size ejecta produced by collisions of saltating grains with a flat bed”, *Sedimentology* **42**, 695–706 (1995).
- [137] R. S. Anderson and B. Hallet, “Sediment transport by wind: toward a general model”, *GSA Bulletin* **97**, 523–535 (1986).
- [138] J. L. Jensen and M. Sørensen, “Estimation of some aeolian saltation transport parameters: a re-analysis of williams’ data”, *Sedimentology* **33**, 547–558 (1986).
- [139] J. F. Kok and N. O. Renno, “A comprehensive numerical model of steady state saltation (comsalt)”, *J. Geophys. Res.* **114**, D17204 (2009).
- [140] M. Lämmel, K. Dzikowski, K. Kroy, L. Oger, and A. Valance, “Grain-scale modeling and splash parametrization for aeolian sand transport”, *Phys. Rev. E* **95**, 022902 (2017).
- [141] M. P. Almeida, E. J. R. Parteli, J. S. Andrade, and H. J. Herrmann, “Giant saltation on mars”, *Proc. Natl. Acad. Sci. U.S.A.* **105**, 6222–6226 (2008).
- [142] K. Kroy, S. Fischer, and B. Obermayer, “The shape of barchan dunes”, *J. Phys.: Condens. Matter* **17**, S1229–S1235 (2005).
- [143] R. Sullivan, D. Banfield, J. F. Bell, W. Calvin, D. Fike, M. Golombek, R. Greeley, J. Grotzinger, K. Herkenhoff, D. Jerolmack, M. Malin, D. Ming, L. A. Soderblom, S. W. Squyres, S. Thompson, W. A. Watters, C. M. Weitz, and A. Yen, “Aeolian processes at the mars exploration rover meridiani planum landing site”, *Nature* **436**, 58–61 (2005).
- [144] R. Sullivan, R. Arvidson, I. F. Bell, R. Gellert, M. Golombek, R. Greeley, K. Herkenhoff, J. Johnson, S. Thompson, P. Whelley, and J. Wray, “Wind-driven particle mobility on Mars: Insights from Mars Exploration Rover observations at "El Dorado" and surroundings at Gusev Crater”, *J. Geophys. Res.* **113**, 1–70 (2008).
- [145] M. Chojnacki, D. M. Burr, J. E. Moersch, and T. I. Michaels, “Orbital observations of contemporary dune activity in endeavor crater, meridiani planum, mars”, *J. Geophys. Res.* **116** (2011).
- [146] F. Ayoub, J.-P. Avouac, C. Newman, M. Richardson, A. Lucas, S. Leprince, and N. Bridges, “Threshold for sand mobility on mars calibrated from seasonal variations of sand flux”, *Nat. Comm.* **5**, 5096– (2014).
- [147] O. Isenberg, H. Yizhaq, H. Tsoar, R. Wenkart, A. Karnieli, J. F. Kok, and I. Katra, “Megaripple flattening due to strong winds”, *Geomorphology* **131**, 69–84 (2011).
- [148] N. Bridges, M. Spagnuolo, S. de Silva, J. Zimbelman, and E. Neely, “Formation of gravel-mantled megaripples on earth and mars: insights from the argentinean puna and wind tunnel experiments”, *Aeolian Res.* **17**, 49–60 (2015).
- [149] M. Foroutan and J. Zimbelman, “Mega-ripples in iran: a new analog for transverse aeolian ridges on mars”, *Icarus* **274**, 99–105 (2016).
- [150] R. Sullivan and J. F. Kok, “Aeolian saltation on mars at low wind speeds”, *J. Geophys. Res.* **122**, 2111–2143 (2017).
- [151] A. C. W. Baas and D. J. Sherman, “Formation and behavior of aeolian streamers”, *J. Geophys. Res.* **110**, (2005).



- [152] B. B. Willetts and M. A. Rice, "Collisions in aeolian saltation", *Acta Mech.* **63**, 255–265 (1986).
- [153] B. B. Willetts and M. a. Rice, "Collisions of quartz grains with a sand bed: The influence of incident angle", *Earth Surf. Proc. Land.* **14**, 719–730 (1989).
- [154] P. Nalpanis, J. C. R. Hunt, and C. F. Barrett, "Saltating particles over flat beds", *J. Fluid Mech.* **251**, 661–685 (1993).
- [155] Z. Dong, X. Liu, F. Li, H. Wang, and A. Zhao, "Impact-entrainment relationship in a saltating cloud", *Earth Surf. Proc. Land.* **27**, 641–658 (2002).
- [156] D. Wang, Y. Wang, B. Yang, and W. Zhang, "Statistical analysis of sand grain/bed collision process recorded by high-speed digital camera", *Sedimentology* **55**, 461–470 (2008).
- [157] M. Gordon and C. M. Neuman, "A study of particle splash on developing ripple forms for two bed materials", *Geomorphology* **129**, 79–91 (2011).
- [158] K. Nishimura and J. C. R. Hunt, "Saltation and incipient suspension above a flat particle bed below a turbulent boundary layer", *J. Fluid Mech.* **417**, 77–102 (2000).
- [159] K. Sugiura and N. Maeno, "Wind-tunnel measurements of restitution coefficients and ejection number of snow particles in drifting snow: determination of splash functions", *Bound.-Layer Meteor.* **95**, 123–143 (2000).
- [160] J. N. McElwaine, N. Maeno, and K. Sugiura, "The splash function for snow from wind-tunnel measurements", *Ann. Glaciol.* **38**, 71–78 (2004).
- [161] B. T. Werner, "A steady-state model of wind-blown sand transport", *J. Geol.* **98**, 1–17 (1990).
- [162] B. R. White and J. C. Schulz, "Magnus effect in saltation", *J. Fluid Mech.* **81**, 497–512 (1977).
- [163] S. Mitha, M. Tran, B. Werner, and P. Haff, "The grain-bed impact process in aeolian saltation", *Acta Mech.* **63**, 267–278 (1986).
- [164] F. Rioual, A. Valance, and D. Bideau, "Experimental study of the collision process of a grain on a two-dimensional granular bed", *Phys. Rev. E* **62**, 2450–2459 (2000).
- [165] F. Rioual, A. Valance, and D. Bideau, "Collision process of a bead on a two-dimensional bead packing: importance of the inter-granular contacts", *Europhys. Lett.* **61**, 194 (2003).
- [166] D. Beladjine, M. Ammi, L. Oger, and A. Valance, "Collision process between an incident bead and a three-dimensional granular packing", *Phys. Rev. E* **75**, 061305 (2007).
- [167] M. Ammi, L. Oger, D. Beladjine, and A. Valance, "Three-dimensional analysis of the collision process of a bead on a granular packing", *Phys. Rev. E* **79**, 021305 (2009).
- [168] M. Nishida, M. Okumura, and K. Tanaka, "Effects of density ratio and diameter ratio on critical incident angles of projectiles impacting granular media", *Granular Matter* **12**, 337–344 (2010).
- [169] R. S. Anderson and P. K. Haff, "Simulation of Eolian Saltation", *Science* **241**, 820–823 (1988).

- [170] B. T. Werner and P. K. Haff, “The impact process in aeolian saltation: two-dimensional simulations”, *Sedimentology* **35**, 2, 189–196 (1988).
- [171] R. S. Anderson and P. K. Haff, “Wind modification and bed response during saltation of sand in air”, *Acta Mech.* **1 (Suppl.)** 21–51 (1991).
- [172] I. K. McEwan and B. B. Willets, “Numerical model of the saltation cloud”, *Acta Mech.* **1 (Suppl.)** 53–66 (1991).
- [173] P. Haff and R. Anderson, “Grain scale simulations of loose sedimentary beds: The example of grain–bed impacts in aeolian saltation”, *Sedimentology*, 175–198 (1993).
- [174] L. Oger, M. Ammi, a. Valance, and D. Beladjine, “Discrete Element Method studies of the collision of one rapid sphere on 2D and 3D packings.”, *Eur. Phys. J. E* **17**, 467–76 (2005).
- [175] X. Yin, N. Huang, and Z. Wang, “A numerical investigation into sand grain/slope bed collision”, *Powder Technol.* **314**, Special Issue on Simulation and Modelling of Particulate Systems, 28–38 (2017).
- [176] L. Oger, M. Ammi, a. Valance, and D. Beladjine, “Study of the collision of one rapid sphere on 3D packings: Experimental and numerical results”, *Comput. Math. Appl.* **55**, 132–148 (2008).
- [177] M. Nishida and Y. Tanaka, “DEM simulations and experiments for projectile impacting two-dimensional particle packings including dissimilar material layers”, *Granular Matter* **12**, 357–368 (2010).
- [178] M. Nishida, J. Nagamatsu, and K. Tanaka, “Discrete element method analysis of ejection and penetration of projectile impacting granular media:” *J. Mech. Mater. Struct.* **5**, 164–178 (2011).
- [179] L. Oger, *How discrete element method code can model dynamical phenomena such as saltation transport, multiple collision process and granular avalanches*, KITP Program: Fluid-Mediated Particle Transport in Geophysical Flows, (2013) <http://online.kitp.ucsb.edu/online/geoflows13/oger/> (visited on 08/23/2017).
- [180] M. Xing and C. He, “3D ejection behavior of different sized particles in the grain-bed collision process”, *Geomorphology* **187**, 94–100 (2013).
- [181] T. Tanabe, T. Shimada, N. Ito, and H. Nishimori, “Splash detail due to a single grain incident on a granular bed”, *Phys. Rev. E* **95**, 022906 (2017).
- [182] D. a. Rumpel, “Successive aeolian saltation: studies of idealized collisions”, *Sedimentology* **32**, 267–280 (1985).
- [183] I. K. McEwan, B. B. Willets, and M. A. Rice, “The grain/bed collision in sand transport by wind”, *Sedimentology* **39**, 971–981 (1992).
- [184] J. Crassous, D. Beladjine, and A. Valance, “Impact of a projectile on a granular medium described by a collision model”, *Phys. Rev. Lett.* **99**, 248001 (2007).
- [185] A. Valance and J. Crassous, “Granular medium impacted by a projectile: experiment and model.”, *Eur. Phys. J. E* **30**, 43–54 (2009).
- [186] T. D. Ho, P. Dupont, A. Ould El Moctar, and A. Valance, “Particle velocity distribution in saltation transport”, *Phys. Rev. E* **85**, 052301 (2012).

- [187] F. Comola and M. Lehning, “Energy- and momentum-conserving model of splash entrainment in sand and snow saltation”, *Geophys. Res. Lett.* **44**, 1601–1609 (2017).
- [188] S. F. Foerster, M. Y. Louge, H. Chang, and K. Allia, “Measurements of the collision properties of small spheres”, *Phys. Fluids* **6**, 1108–1115 (1994).
- [189] N. V. Brilliantov, F. Spahn, J.-M. Hertzsch, and T. Pöschel, “Model for collisions in granular gases”, *Phys. Rev. E* **53**, 5382 (1996).
- [190] L. Oger and A. Valance, *Collision of one rapid sphere on 3d sphere packings: effect of size difference*, private communication, 2013.
- [191] T. D. Ho, A. Valance, P. Dupont, and A. Ould El Moctar, “Scaling laws in aeolian sand transport”, *Phys. Rev. Lett.* **106**, 094501 (2011).
- [192] T. D. Ho, A. Valance, P. Dupont, and A. Ould El Moctar, “Aeolian sand transport: Length and height distributions of saltation trajectories”, *Aeolian Res.*, (2014).
- [193] K. Kroy, G. Sauermann, and H. J. Herrmann, “Minimal model for aeolian sand dunes”, *Phys. Rev. E* **66**, 031302 (2002).
- [194] B. Andreotti, P. Claudin, and O. Pouliquen, “Measurements of the aeolian sand transport saturation length”, *Geomorphology* **123**, 343–348 (2010).
- [195] T. Pähtz, J. F. Kok, E. J. R. Parteli, and H. J. Herrmann, “Flux saturation length of sediment transport”, *Phys. Rev. Lett.* **111**, 218002 (2013).
- [196] T. Pähtz, A. Omeradžić, M. V. Carneiro, N. A. M. Araújo, and H. J. Herrmann, “Discrete element method simulations of the saturation of aeolian sand transport”, *Geophys. Res. Lett.* **42**, 2063–2070 (2015).
- [197] H. Selmani, A. Valance, A. Ould El Moctar, P. Dupont, and R. Zegadi, “Aeolian sand transport in out-of-equilibrium regimes”, *Geophys. Res. Lett.*, (2018).
- [198] R. B. Hoyle and A. Mehta, “Two-species continuum model for aeolian sand ripples”, *Phys. Rev. Lett.* **83**, 5170–5173 (1999).
- [199] M. Sørensen, in *Aeolian grain transport 1: mechanics* (Springer Vienna, Vienna, 1991), pp. 67–81.
- [200] M. Sørensen, “On the rate of aeolian sand transport”, *Geomorphology* **59**, 53–62 (2004).
- [201] J. T. Jenkins, I. Cantat, and A. Valance, “Continuum model for steady, fully developed saltation above a horizontal particle bed”, *Phys. Rev. E* **82**, 020301 (2010).
- [202] T. Pähtz, J. F. Kok, and H. J. Herrmann, “The apparent surface roughness of moving sand transported by wind”, *ArXiv e-prints*, (2011).
- [203] T. Pähtz, O. Durán, T.-D. Ho, A. Valance, and J. F. Kok, “The fluctuation energy balance in non-suspended fluid-mediated particle transport”, *Phys. Fluids* **27**, 013303– (2015).
- [204] R. Kawamura, “Study on sand movement by wind”, *Rep. Phys. Sci. Res. Inst. Tokyo Univ.* **5**, 95–112 (1951).
- [205] P. R. Owen, “Saltation of uniform grains in air”, *J. Fluid Mech.* **20**, 225–242 (1964).

- [206] R. Kind, “A critical examination of the requirements for model simulation of wind-induced erosion/deposition phenomena such as snow drifting”, *Atmospheric Environment* (1967) **10**, 219–227 (1976).
- [207] B. R. White, “Soil transport by winds on mars”, *J. Geophys. Res.* **84**, 4643–4651 (1979).
- [208] J. M. Pasini and J. T. Jenkins, “Aeolian transport with collisional suspension”, *Philosophical Transactions of the Royal Society A: Mathematical, Physical and Engineering Sciences* **363**, 1625–1646 (2005).
- [209] O. Durán and H. Herrmann, “Modelling of saturated sand flux”, *J. Stat. Mech: Theory Exp.* **2006**, P07011 (2006).
- [210] J. T. Jenkins and A. Valance, “Periodic trajectories in aeolian sand transport”, *Phys. Fluids* **26**, 073301 (2014).
- [211] T. Pähtz, J. F. Kok, and H. J. Herrmann, “The apparent roughness of a sand surface blown by wind from an analytical model of saltation”, *New J. Phys.* **14**, 043035 (2012).
- [212] K. Kroy and X. Guo, “Comment on “relevant length scale of barchan dunes””, *Phys. Rev. Lett.* **93**, 039401 (2004).
- [213] D. Berzi, J. T. Jenkins, and A. Valance, “Periodic saltation over hydrodynamically rough beds: aeolian to aquatic”, *J. Fluid Mech.* **786**, 190–209 (2016).
- [214] C. Ji, A. Munjiza, E. Avital, D. Xu, and J. Williams, “Saltation of particles in turbulent channel flow”, *Phys. Rev. E* **89**, 052202 (2014).
- [215] M. V. Carneiro, N. A. M. Araújo, T. Pähtz, and H. J. Herrmann, “Midair collisions enhance saltation”, *Phys. Rev. Lett.* **111**, 058001 (2013).
- [216] T. Pähtz and O. Durán, “Fluid forces or impacts: what governs the entrainment of soil particles in sediment transport mediated by a newtonian fluid?”, *Phys. Rev. Fluids* **2**, 074303 (2017).
- [217] M. P. Almeida, J. S. Andrade, and H. J. Herrmann, “Aeolian transport layer”, *Phys. Rev. Lett.* **96**, 018001 (2006).
- [218] M. P. Almeida, J. S. Andrade, and H. J. Herrmann, “Aeolian transport of sand”, *Eur. Phys. J. E* **22**, 195 (2007).
- [219] Y. Shao and A. Li, “Numerical modelling of saltation in the atmospheric surface layer”, *Bound.-Layer Meteor.* **91**, 199–225 (1999).
- [220] G. S. Ma and X. J. Zheng, “The fluctuation property of blown sand particles and the wind-sand flow evolution studied by numerical method”, *Eur. Phys. J. E* **34**, 54 (2011).
- [221] D. Berzi, A. Valance, and J. T. Jenkins, “The threshold for continuing saltation on earth and other solar system bodies”, *J. Geophys. Res.*, (2017).
- [222] L. Prigozhin, “Nonlinear dynamics of aeolian sand ripples”, *Phys. Rev. E* **60**, 729–733 (1999).
- [223] T. Pähtz, E. J. R. Parteli, J. F. Kok, and H. J. Herrmann, “Analytical model for flux saturation in sediment transport”, *Phys. Rev. E* **89**, 052213 (2014).

- [224] *Beaufort scale for land areas*, Royal Meteorological Society, <https://www.rmets.org/weather-and-climate/observing/beaufort-scale> (visited on 08/16/2017).
- [225] U. Frisch, *Turbulence: The Legacy of A. N. Kolmogorov* (Cambridge University Press, 1995).
- [226] V. Carbone, R. Cavazzana, V. Antoni, L. Sorriso-Valvo, E. Spada, G. Regnoli, P. Giuliani, N. Vianello, F. Lepreti, R. Bruno, E. Martines, and P. Veltri, "To what extent can dynamical models describe statistical features of turbulent flows?", *EPL (Europhysics Letters)* **58**, 349 (2002).
- [227] F. Boettcher, C. Renner, H.-P. Waldl, and J. Peinke, "On the statistics of wind gusts", *Bound.-Layer Meteor.* **108**, 163–173 (2003).
- [228] P. Bak, *How nature works: the science of self-organized criticality* (Springer-Verlag New York, Inc., 1996).
- [229] M. Paczuski, S. Boettcher, and M. Baiesi, "Interoccurrence times in the bak-tang-wiesenfeld sandpile model: a comparison with the observed statistics of solar flares", *Phys. Rev. Lett.* **95**, 181102 (2005).
- [230] T. Bohr, M. H. Jensen, G. Paladin, and A. Vulpiani, *Dynamical systems approach to turbulence* (Cambridge University Press, 2005).
- [231] C. Beck and E. Cohen, "Superstatistics", *Physica A* **322**, 267–275 (2003).
- [232] C. Beck, "Statistics of three-dimensional lagrangian turbulence", *Phys. Rev. Lett.* **98**, 064502 (2007).
- [233] E. Van der Straeten and C. Beck, "Superstatistical fluctuations in time series: applications to share-price dynamics and turbulence", *Phys. Rev. E* **80**, 036108 (2009).
- [234] F. Böttcher, S. Barth, and J. Peinke, "Small and large scale fluctuations in atmospheric wind speeds", *Stochastic Environmental Research and Risk Assessment* **21**, 299–308 (2007).
- [235] S. E. Tuller and A. C. Brett, "The goodness of fit of the weibull and rayleigh distributions to the distributions of observed wind speeds in a topographically diverse area", *J. Climatol.* **5**, 79–94 (1985).
- [236] R. D. Lorenz, "Martian surface wind speeds described by the weibull distribution", *J. Spacecraft Rockets* **33**, 754–756 (1996).
- [237] G. K. Batchelor, *An introduction to fluid dynamics* (Cambridge university press, 2000).
- [238] J. M. Dallavalle, *Micromeritics*. Vol. 56, 2 (LWW, 1943).
- [239] N.-S. Cheng, "Simplified settling velocity formula for sediment particle", *J. Hydraul. Eng.* **123**, 149–152 (1997).
- [240] R. Ferguson and M. Church, "A simple universal equation for grain settling velocity", *J. Sediment. Res.* **74**, 933–937 (2004).
- [241] J. A. Jimenez and O. S. Madsen, "A simple formula to estimate settling velocity of natural sediments", *J. Waterw. Port Coast. Ocean Eng.* **129**, 70–78 (2003).
- [242] X.-Y. Zou, H. Cheng, C.-L. Zhang, and Y.-Z. Zhao, "Effects of the magnus and saffman forces on the saltation trajectories of sand grain", *Geomorphology* **90**, 11–22 (2007).

- [243] Z.-T. Wang, C.-L. Zhang, and H.-T. Wang, “Forces on a saltating grain in air”, *Eur. Phys. J. E* **36**, 112 (2013).
- [244] J. C. R. Hunt and A. H. Weber, “A Lagrangian statistical analysis of diffusion from a ground-level source in a turbulent boundary layer”, *Quart. J. Roy. Meteor. Soc.* **105**, 423–443 (1979).
- [245] A. Shields, *Anwendung der Ähnlichkeitsmechanik und der Turbulenzforschung auf die Geschiebebewegung*, Preussische Versuchsanstalt für Wasserbau und Schiffbau (Berlin, 1936).
- [246] J. D. Iversen, J. B. Pollack, R. Greeley, and B. R. White, “Saltation threshold on mars: the effect of interparticle force, surface roughness, and low atmospheric density”, *Icarus* **29**, 381–393 (1976).
- [247] J. D. Iversen and B. R. White, “Saltation threshold on earth, mars and venus”, *Sedimentology* **29 (1)**, 111–119 (1982).
- [248] Y. Shao and H. Lu, “A simple expression for wind erosion threshold friction velocity”, *J. Geophys. Res.* **105(D17)**, 22437–22443 (2000).
- [249] D. M. Burr, N. T. Bridges, J. R. Marshall, J. K. Smith, B. R. White, and J. P. Emery, “Higher-than-predicted saltation threshold wind speeds on titan”, *Nature* **517**, 60–63 (2015).
- [250] P. Diplas, C. L. Dancey, A. O. Celik, M. Valyrakis, K. Greer, and T. Akar, “The role of impulse on the initiation of particle movement under turbulent flow conditions”, *Science* **322**, 717–720 (2008).
- [251] M. Valyrakis, P. Diplas, C. L. Dancey, K. Greer, and A. O. Celik, “Role of instantaneous force magnitude and duration on particle entrainment”, *J. Geophys. Res.* **115**, (2010).
- [252] M. Valyrakis, P. Diplas, and C. L. Dancey, “Entrainment of coarse grains in turbulent flows: an extreme value theory approach”, *Water Resour. Res.* **47**, (2011).
- [253] M. Valyrakis, P. Diplas, and C. L. Dancey, “Entrainment of coarse particles in turbulent flows: an energy approach”, *J. Geophys. Res.* **118**, 42–53 (2013).
- [254] A. Singh, K. Fienberg, D. J. Jerolmack, J. Marr, and E. Foufoula-Georgiou, “Experimental evidence for statistical scaling and intermittency in sediment transport rates”, *J. Geophys. Res.* **114**, (2009).
- [255] R. L. Martin and J. F. Kok, “Field measurements demonstrate distinct initiation and cessation thresholds governing aeolian sediment transport flux”, *arXiv:1610.10059*, (2017).
- [256] A. H. Clark, M. D. Shattuck, N. T. Ouellette, and C. S. O’Hern, “Onset and cessation of motion in hydrodynamically sheared granular beds”, *Phys. Rev. E* **92**, 042202 (2015).
- [257] A. H. Clark, M. D. Shattuck, N. T. Ouellette, and C. S. O’Hern, “Role of grain dynamics in determining the onset of sediment transport”, *Phys. Rev. Fluids* **2**, 034305 (2017).
- [258] H. Tsoar, in *Geomorphological fluid mechanics* (Springer Berlin Heidelberg, Berlin, Heidelberg, 2001), pp. 403–429.
- [259] I. Livingstone, G. F. Wiggs, and C. M. Weaver, “Geomorphology of desert sand dunes: a review of recent progress”, *Earth-Sci. Rev.* **80**, 239–257 (2007).

- [260] G. Sauermann, “Modeling of wind blown sand and desert dunes”, PhD thesis (Universität Stuttgart, 2001).
- [261] P. Hersen, “On the crescentic shape of barchan dunes”, *EPJ B* **37**, 507–514 (2004).
- [262] E. J. R. Parteli, O. Durán, H. Tsoar, V. Schwämmle, and H. J. Herrmann, “Dune formation under bimodal winds”, *Proc. Natl. Acad. Sci. U.S.A.* **106**, 22085–22089 (2009).
- [263] P. Hersen, K. H. Andersen, H. Elbelrhiti, B. Andreotti, P. Claudin, and S. Douady, “Corridors of barchan dunes: stability and size selection”, *Phys. Rev. E* **69**, 011304 (2004).
- [264] H. Elbelrhiti, P. Claudin, and B. Andreotti, “Field evidence for surface-wave-induced instability of sand dunes”, *Nature* **437**, 720–723 (2005).
- [265] C. Groh, N. Aksel, I. Rehberg, and C. Kruelle, “Grain size dependence of barchan dune dynamics”, *AIP Conference Proceedings* **1145**, 955–958 (2009).
- [266] C. Groh, I. Rehberg, and C. A. Kruelle, “Observation of density segregation inside migrating dunes”, *Phys. Rev. E* **84**, 050301 (2011).
- [267] E. M. Franklin and F. Charru, “Subaqueous barchan dunes in turbulent shear flow. part 1. dune motion”, *J. Fluid Mech.* **675**, 199–222 (2011).
- [268] B. Andreotti, P. Claudin, and S. Douady, “Selection of dune shapes and velocities part 2: a two-dimensional modelling”, *EPJ B* **28**, 341–352 (2002).
- [269] P. S. Jackson and J. C. R. Hunt, “Turbulent wind flow over a low hill”, *Quart. J. Roy. Meteor. Soc.* **101**, 929–955 (1975).
- [270] W. S. Weng, J. C. R. Hunt, D. J. Carruthers, A. Warren, G. F. S. Wiggs, I. Livingstone, and I. Castro, in *Aeolian grain transport: the erosional environment* (Springer Vienna, Vienna, 1991), pp. 1–22.
- [271] S. E. Belcher and J. C. R. Hunt, “Turbulent flow over hills and waves”, *Annu. Rev. Fluid Mech.* **30**, 507–538 (1998).
- [272] E. J. R. Parteli and H. J. Herrmann, “Dune formation on the present mars”, *Phys. Rev. E* **76**, 041307, 041307 (2007).
- [273] M. G. A. Lapotre, R. C. Ewing, M. P. Lamb, W. W. Fischer, J. P. Grotzinger, D. M. Rubin, K. W. Lewis, M. J. Ballard, M. Day, S. Gupta, S. G. Banham, N. T. Bridges, D. J. Des Marais, A. A. Fraeman, J. A. Grant, K. E. Herkenhoff, D. W. Ming, M. A. Mischna, M. S. Rice, D. Y. Sumner, A. R. Vasavada, and R. A. Yingst, “Large wind ripples on mars: a record of atmospheric evolution”, *Science* **353**, 55–58 (2016).
- [274] L. Guignier, H. Niiya, H. Nishimori, D. Lague, and a. Valance, “Sand dunes as migrating strings”, *Phys. Rev. E* **87**, 052206 (2013).
- [275] S. Courrech du Pont, “Dune morphodynamics”, *C. R. Phys.* **16**, 118–138 (2015).
- [276] V. Schwämmle and H. J. Herrmann, “Geomorphology: solitary wave behaviour of sand dunes”, *Nature* **426**, 619–620 (2003).
- [277] V. Schwämmle and H. J. Herrmann, “A model of barchan dunes including lateral shear stress”, *Eur. Phys. J. E* **16**, 57–65 (2005).



- [278] H. Tsoar and E. J. R. Parteli, “Bidirectional winds, barchan dune asymmetry and formation of seif dunes from barchans: a discussion”, *Environmental Earth Sciences* **75**, 1237– (2016).
- [279] O. Durán and H. J. Herrmann, “Vegetation against dune mobility”, *Phys. Rev. Lett.* **97**, 188001 (2006).
- [280] O. Durán and L. J. Moore, “Vegetation controls on the maximum size of coastal dunes”, *Proc. Natl. Acad. Sci. U.S.A.* **110**, 17217–17222 (2013).
- [281] M. C. d. M. Luna, E. J. Parteli, and H. J. Herrmann, “Model for a dune field with an exposed water table”, *Geomorphology* **159**, 169–177 (2012).
- [282] M. Colombini and A. Stocchino, “Three-dimensional river bed forms”, *J. Fluid Mech.* **695**, 63–80 (2012).
- [283] B. Andreotti, P. Claudin, O. Devauchelle, O. Durán, and A. Fourrière, “Bedforms in a turbulent stream: ripples, chevrons and antidunes”, *J. Fluid Mech.* **690**, 94–128 (2012).
- [284] V. Langlois and A. Valance, “Formation of two-dimensional sand ripples under laminar shear flow”, *Phys. Rev. Lett.* **94**, 248001 (2005).
- [285] A. Valance, “Nonlinear sand bedform dynamics in a viscous flow”, *Phys. Rev. E* **83**, 1–6 (2011).
- [286] F. Charru, J. Bouteloup, T. Bonometti, and L. Lacaze, “Sediment transport and bedforms: a numerical study of two-phase viscous shear flow”, *Meccanica* **51**, 3055–3065 (2016).
- [287] F. Chiodi, B. Andreotti, and P. Claudin, “The bar instability revisited”, arXiv:1210.3223, (2012).
- [288] G. Parker, “Transport of gravel and sediment mixtures”, *Sedimentation engineering : processes, management, modeling, and practice* **110**, 165–252 (2008).
- [289] P. Hersen and S. Douady, “Collision of barchan dunes as a mechanism of size regulation”, *Geophys. Res. Lett.* **32**, (2005).
- [290] M. Génois, S. C. du Pont, P. Hersen, and G. Grégoire, “An agent-based model of dune interactions produces the emergence of patterns in deserts”, *Geophys. Res. Lett.* **40**, 3909–3914 (2013).
- [291] S. L. Worman, A. B. Murray, R. Littlewood, B. Andreotti, and P. Claudin, “Modeling emergent large-scale structures of barchan dune fields”, *Geology* **41**, 1059–1062 (2013).
- [292] A. Lima, G. Sauermann, H. Herrmann, and K. Kroy, “Modelling a dune field”, *Physica A* **310**, 487–500 (2002).
- [293] S. Auschra, “Gegenseitige stabilisierung von sicheldünen”, MA thesis (Universität Leipzig, 2014).
- [294] M. Will, “Computersimulation zur dynamik von dünenfeldern”, BA thesis (Universität Leipzig, 2014).
- [295] M. Guthardt, “Mutual stabilization of barchan dunes”, MA thesis (Universität Leipzig, 2016).
- [296] H. Niiya, A. Awazu, and H. Nishimori, “Three-Dimensional Dune Skeleton Model as a Coupled Dynamical System of Two-Dimensional Cross Sections”, *J. Phys. Soc. Jpn.* **79**, 063002 (2010).

- [297] H. Niiya, A. Awazu, and H. Nishimori, “Bifurcation analysis of the transition of dune shapes under a unidirectional wind”, *Phys. Rev. Lett.* **108**, 158001 (2012).
- [298] R. Bagnold, “The transport of sand by wind”, *The Geographical Journal* **89**, 409–438 (1937).
- [299] M. Seppälä and K. Lindé, “Wind tunnel studies of ripple formation”, *Geogr. Ann. A* **60**, 29–42 (1978).
- [300] J. D. Walker, “An experimental study of wind ripples”, MA thesis (Massachusetts Institute of Technology. Dept. of Earth and Planetary Sciences., 1981).
- [301] F. Brugmans, “Wind ripples in an active drift sand area in the netherlands: a preliminary report”, *ESPL* **8**, 527–534 (1983).
- [302] H. Tsoar, “Grain-size characteristics of wind ripples on a desert seif dune”, in *Geography research forum*, Vol. 10 (1990), pp. 37–50.
- [303] D. Goossens, “Aeolian dust ripples: their occurrence, morphometrical characteristics, dynamics and origin”, *CATENA* **18**, 379–407 (1991).
- [304] M. Y. Louge, A. Valance, A. Ould el-Moctar, and P. Dupont, “Packing variations on a ripple of nearly monodisperse dry sand”, *J. Geophys. Res.* **115**, 1–12 (2010).
- [305] R. D. Lorenz, “Observations of wind ripple migration on an Egyptian seif dune using an inexpensive digital timelapse camera”, *Aeolian Res.* **3**, 229–234 (2011).
- [306] E. Schmerler, I. Katra, J. F. Kok, H. Tsoar, and H. Yizhaq, “Experimental and numerical study of sharp’s shadow zone hypothesis on sand ripple wavelength”, *Aeolian Res.* **22**, 37–46 (2016).
- [307] S. Forrest and P. Haff, “Mechanics of Wind Ripple Stratigraphy”, *Science* **255**, 1240–1243 (1992).
- [308] R. S. Anderson and K. L. Bunas, “Grain size segregation and stratigraphy in aeolian ripples modelled with a cellular automaton”, *Nature* **365**, 740–743 (1993).
- [309] H. Nishimori and N. Ouchi, “Formation of ripple patterns and dunes by wind-blown sand”, *Phys. Rev. Lett.* **71**, 197–200 (1993).
- [310] B. T. Werner and D. T. Gillespie, “Fundamentally discrete stochastic model for wind ripple dynamics”, *Phys. Rev. Lett.* **71**, 3230–3233 (1993).
- [311] W. Landry and B. Werner, “Computer simulations of self-organized wind ripple patterns”, *Physica D* **77**, 238–260 (1994).
- [312] R. Hoyle and a. Woods, “Analytical model of propagating sand ripples”, *Phys. Rev. E* **56**, 6861–6868 (1997).
- [313] O. Terzidis, P. Claudin, and J.-P. Bouchaud, “A model for ripple instabilities in granular media”, *Eur. Phys. J. B* **5**, 245–249 (1998).
- [314] A. Valance and F. Rioual, “A nonlinear model for aeolian sand ripples”, *Eur. Phys. J. B* **10**, 543–548 (1999).
- [315] Z. Csahók, C. Misbah, F. Rioual, and A. Valance, “Dynamics of aeolian sand ripples”, *English, Eur. Phys. J. E* **3**, 71–86 (2000).

- [316] H. A. Makse, “Grain segregation mechanism in aeolian sand ripples”, *Eur. Phys. J. E* **1**, 127–135 (2000).
- [317] H. Yizhaq, N. J. Balmforth, and A. Provenzale, “Blown by wind: nonlinear dynamics of aeolian sand ripples”, *Physica D* **195**, 207–228 (2004).
- [318] a. Valance, “Formation of ripples over a sand bed submitted to a turbulent shear flow”, *Eur. Phys. J. B* **45**, 433–442 (2005).
- [319] E. Manukyan and L. Prigozhin, “Formation of aeolian ripples and sand sorting”, *Phys. Rev. E* **79**, 031303 (2009).
- [320] I. Katra, H. Yizhaq, and J. F. Kok, “Mechanisms limiting the growth of aeolian megaripples”, *Geophys. Res. Lett.* **41**, 858–865 (2014).
- [321] E. Kindle, “Recent and fossile ripple-mark”, *Canada Geol. Survey Mus. Bull.* **25**, 121 (1917).
- [322] N. T. Bridges, P. E. Geissler, A. S. McEwen, B. J. Thomson, F. C. Chuang, K. E. Herkenhoff, L. P. Keszthelyi, and S. Martínez-Alonso, “Windy Mars: A dynamic planet as seen by the HiRISE camera”, *Geophys. Res. Lett.* **34**, (2007).
- [323] C. M. Sakamoto-Arnold, “Eolian features produced by the december 1977 windstorm, southern san joaquin valley, california”, *J. Geol.* **89**, 129–137 (1981).
- [324] R. Ackert, “The origin of isolated gravel ripples in the western asgard range, antarctica”, *Antarct. J.* **24**, 60–62 (1989).
- [325] S. Williams, “Large ripples on earth and mars”, *Lunar and Planetary*, (2002).
- [326] J. A. Gillies, W. G. Nickling, M. Tilson, and E. Furtak-Cole, “Wind-formed gravel bed forms, wright valley, antarctica”, *J. Geophys. Res.* **117**, F04017 (2012).
- [327] G. Qian, Z. Dong, W. Zhang Z. adn Luo, and J. Lu, “Granule ripples in the kumtagh desert, china: morphology, grain size and influencing factors”, *Sedimentology* **59**, 1888–1901 (2012).
- [328] T.-J. Hsu, J. T. Jenkins, and P. L.-F. Liu, “On two-phase sediment transport: dilute flow”, *J. Geophys. Res.* **108**, (2003).
- [329] J. P. Milana, “Largest wind ripples on earth?”, *Geology* **37**, 343–346 (2009).
- [330] S. de Silva, M. Spagnuolo, N. Bridges, and J. Zimbelman, “Gravel-mantled megaripples of the argentinean puna: a model for their origin and growth with implications for mars”, *Geol. Soc. Am. Bull.* **125**, 1912–1929 (2013).
- [331] C. H. Hugenholtz, T. E. Barchyn, and E. a. Favaro, “Formation of periodic bedrock ridges on Earth”, *Aeolian Res.* **18**, 135–144 (2015).
- [332] M. J. Selby, R. B. Rains, and R. W. P. Palmer, “Eolian deposits of the ice-free victoria valley, southern victoria land, antarctica”, *N.Z. J. Geol. Geophys.* **17**, 543–562 (1974).
- [333] H. Yizhaq, I. Katra, J. F. Kok, and O. Isenberg, “Transverse instability of megaripples”, *Geology* **40**, 459–462 (2012).
- [334] J. R. Zimbelman, S. H. Williams, and A. K. Johnston, “Cross-sectional profiles of sand ripples, megaripples, and dunes: a method for discriminating between formational mechanisms”, *Earth Surf. Proc. Land.* **37**, 1120–1125 (2012).

- [335] T. G. Drake, R. L. Shreve, W. E. Dietrich, P. J. Whiting, and L. B. Leopold, “Bedload transport of fine gravel observed by motion-picture photography”, *J. Fluid Mech.* **192**, 193–217 (1988).
- [336] H. Lu, M. R. Raupach, and K. S. Richards, “Modeling entrainment of sedimentary particles by wind and water: a generalized approach”, *J. Geophys. Res.* **110**, (2005).
- [337] R. Davidson-Arnott and B. Bauer, “Aeolian sediment transport on a beach: thresholds, intermittency, and high frequency variability”, *Geomorphology* **105**, Contemporary research in aeolian geomorphology, 117–126 (2009).
- [338] E. Lajeunesse, L. Malverti, and F. Charru, “Bed load transport in turbulent flow at the grain scale: experiments and modeling”, *J. Geophys. Res.* **115**, (2010).
- [339] R. L. Martin, J. F. Kok, C. H. Hugenholtz, T. E. Barchyn, M. Chamecki, and J. T. Ellis, “High-frequency measurements of aeolian saltation flux: field-based methodology and applications”, *Aeolian Res.* **30**, 97–114 (2018).
- [340] C. P. Broedersz, X. Mao, T. C. Lubensky, and F. C. MacKintosh, “Criticality and isostaticity in fibre networks”, *Nat. Phys.* **7**, 983–988 (2011).
- [341] G. Lemoult, L. Shi, K. Avila, S. V. Jalikop, M. Avila, and B. Hof, “Directed percolation phase transition to sustained turbulence in couette flow”, *Nat. Phys.* **12**, 254 (2016).
- [342] H.-Y. Shih, T.-L. Hsieh, and N. Goldenfeld, “Ecological collapse and the emergence of travelling waves at the onset of shear turbulence”, *Nat. Phys.* **12**, 245 (2015).
- [343] M. Smerlak and A. Youssef, “Universal statistics of selected values”, *Europhys. Lett.* **117**, 50003 (2017).
- [344] M. Smerlak, “Natural selection as coarsening”, *J. Stat. Phys.*, (2017).

## **Part II**

# **Solutions of stiff biopolymers**



## Introduction

Stiff polymers are the fundamental structural and functional building blocks of biological matter [1–5]. They are integral constituents of the highly organized meshworks and bioscaffolds that form both the intracellular cytoskeleton and the extracellular matrices. Since the typical energies required to bend these stiff biopolymers are comparable to the thermal energy scale, they constitute an intermediate class between the highly flexible synthetic polymers and perfectly rigid rod-shaped molecules. Their intermediate rigidity gives rise to a very rich and distinct phenomenology and makes their study interesting from a fundamental physics perspective. This explains why they are highly attractive for both experimental and theoretical studies [6, 7].

The cytoskeleton of eukaryotic cells comprises three main types of biopolymers: quite rigid microtubules, stiff filamentous actin (F-actin), and a whole class of more easily bendable intermediate filaments. Together with a multitude of crosslinker, motor, and regulatory proteins, they control the cells' shape, mechanical stability, integrity, and mobility [4, 7]. More precisely, the biopolymers spatially organize the cell contents, coordinate intracellular transport and physical and biochemical connections of cells to their external environment [5]. Understanding the rich behavior of living organisms on the basis of the microscopic machinery of these building blocks is a long-standing interdisciplinary program that combines biology, chemistry, physics, and materials science [8]. Over the last decades, great progress has been made by studying reduced *in vitro* model systems that mimic various macroscopic features of the far more complex natural systems [3, 9, 10]. Comprising only a few integral parts, such reconstituted cytoskeletal model systems range from pure (entangled) solutions of identical polymers [11–19], over composites of stiff and soft filaments [20–22], crosslinked polymers [9, 23–26], and polymer-bundle networks [9, 27–32] to active dynamic networks made from filaments and molecular motors [22, 33–38]. Elaborate experiments that combine bulk and microrheology measurements with optical microscopy [39], electron microscopy, light scattering, and fluorescence-marking and particle-tracking techniques have illuminated the interplay between the mechanical properties of these systems and their transient architecture. Despite their apparent simplicity, the reduced model systems indeed show various striking analogies with cells or living tissue. Most prominently, ubiquitous rheological features, like intermittent power-law regimes for the linear mechanical spectra and nonlinear strain softening/stiffening, are widely found for these systems (see, *e.g.*, Refs. [7, 10, 40]).

This second part of the thesis focuses on entangled solutions of stiff polymers. Their statistics and microstructure are discussed in Chap. 7, their dynamics and viscoelastic rheology in Chap. 8. Here, the term entangled refers to the fact that the polymers cannot pass through each other. The interaction between polymers is of markedly short-range character, because the repulsive electrostatic repulsion between the (usually) negatively charged biopolymers dissolved in a (near to) physiological aqueous buffer is strongly screened by positively charged salt ions. This is utilized in many models that approximate the polymer–polymer interactions by pure contact interactions. In the absence of any chemical crosslinks, the physics of the semidilute polymer solutions (*i.e.*, up to concentrations well below the isotropic–nematic transition) is dominated by the topological entanglements and their impact on the polymers’ bending fluctuations. This insight gives rise to the tube model for semiflexible polymers, where the entanglement effects on a test polymer are delegated to a mean-field tube-like cage that is formed by the neighboring polymers [6, 41–43]. However, as we will discuss in Chap. 8, fast enough deformations may cause frictional sliding between contacting filaments, letting the pure solutions respond much like a chemically crosslinked gel [44–46]. Before we turn to entangled polymer solutions, I first outline the fundamental physical properties of a single stiff polymer (corresponding to the dilute limit of a solution) and the basic statistical-physics tools that are employed to analyze them theoretically.

## 6.1 Single-polymer physics

From a physics perspective, the notion of a polymer refers to a chain-like mesoscale object, whose microscopic chemical details are represented on an abstract coarse-grained level. Its mechanics is then determined by the bending rigidity that we conveniently quantify in terms of the persistence length  $L_p$ , which is the characteristic length scale over which the polymer direction is randomized along its contour at ambient temperature. Since the polymer is a chain of many (identical) monomers, the value of  $L_p$  depends on how strong the relative motion of adjacent monomers is constrained. The persistence length  $L_p$  is thus a mesoscopic length scale that reflects the microscopic chemical binding strength on a coarse-grained level. We denote the total length of a polymer by  $L$  and the typical monomer diameter by  $a$ , the latter being on the order of a few nanometers. These three length scales suggest the following classification [42, 47]:

$$\begin{aligned}
 a \approx L_p \ll L & \quad (\text{flexible}) \\
 a \ll L_p, L & \quad (\text{semiflexible}) \\
 a \ll L \ll L_p & \quad (\text{stiff})
 \end{aligned} \tag{6.1}$$

For flexible polymers, the (rotational) motion of adjacent monomers is weakly constrained. Monomers of semiflexible and stiff polymers, in contrast, are more rigidly connected, so that the enthalpic bending contribution to the overall free energy of the chain outcompetes its entropic tendency to crumble up. The conformation of a stiff polymer thus features small thermally driven fluctuations around a straight ground-state contour, which is the zero-temperature or rigid-rod limit. Weak deviations from the ground state allow for systematic expansions in the small parameter  $L/L_p$  [48, 49]. Here,  $L$  can also denote the length of a relevant subsegment of a long polymer, in which case the calculations apply to local properties. Alternatively, one may identify  $L$  as the wavelength of a fluctuation mode of the polymer; the broad spectrum of modes of a long semiflexible chain ( $L \gg L_p$ ) exhibits a crossover between a range of short-wavelength



Biopolymer	diameter $a$	persistence length $L_p$	contour length $L$
Microtubule	25 nm	$\approx 1-5$ mm	10s of $\mu\text{m}$
F-actin	7 nm	17 $\mu\text{m}$	$\lesssim 20$ $\mu\text{m}$
Intermediate filaments	9 nm	0.2–1 $\mu\text{m}$	2–10 $\mu\text{m}$
DNA	2 nm	50 nm	$\lesssim 1$ m
DNA tubes	$\approx 9-60$ nm	$\approx 1-26$ $\mu\text{m}$	$\lesssim 20$ $\mu\text{m}$
Carbon nanotubes	$<1$ nm	$\approx 10$ $\mu\text{m}$	$\gtrsim 1$ $\mu\text{m}$

Table 6.1: Typical dimensions and persistence lengths for various biopolymers under physiological conditions, ( $n$ -helix) DNA tubes, and carbon nanotubes. Taken from Ref. [7], data for DNA tubes from Refs. [52, 53].

stiff modes and a range of long-wavelength soft modes resembling modes of a flexible chain [6, 50]. (The latter can be mapped to the modes of a freely-jointed chain of “Kuhn” length  $2L_p$  [51]). Typical values for  $a$ ,  $L_p$ , and  $L$  for various biopolymers and synthetic carbon nanotubes are listed in Table 6.1.

### 6.1.1 The wormlike chain

The standard model for a semiflexible polymer is the wormlike-chain (WLC) model [54], with an effective free energy  $\mathcal{H}_{\text{WLC}}$  given by the bending energy of an elastic rod [55] of bending rigidity  $\kappa$ :

$$\mathcal{H}_{\text{WLC}} \equiv \mathcal{H}_{\text{WLC}}[\mathbf{r}(s)] = \frac{\kappa}{2} \int_0^L ds [\mathbf{r}''(s)]^2 \quad (6.2)$$

In this continuum version of the WLC model,  $\mathbf{r}(s)$  denotes the contour of the chain with arclength  $s \in [0, L]$  if the tangent vector  $\mathbf{r}'(s) \equiv d\mathbf{r}(s)/ds$  is constrained to  $|\mathbf{r}'(s)| = 1$ ;  $|\mathbf{r}''(s)| \equiv |d^2\mathbf{r}(s)/ds^2|$  is the curvature. Thermal averages are formally computed from the path integral

$$\langle \dots \rangle = \int \mathcal{D}\mathbf{r}(s) \dots e^{-\mathcal{H}_{\text{WLC}}[\mathbf{r}(s)]/k_B T} \quad (6.3)$$

over possible contours  $\mathbf{r}(s)$ . From the discrete version of the WLC model, which corresponds to the classic Heisenberg chain, one conveniently computes the tangent autocorrelation function,

$$\langle \mathbf{r}'(s_1) \cdot \mathbf{r}'(s_2) \rangle = e^{-|s_1 - s_2|/L_p}, \quad L_p = \kappa/k_B T, \quad (6.4)$$

in the continuum limit [56]. Equation (6.4) gives the formal definition of the above introduced persistence length  $L_p$  as the correlation length of the chain direction. It relates  $L_p$  to the bending rigidity  $\kappa$  via the Boltzmann constant  $k_B$  and the temperature  $T$ . The WLC model, defined in Eq. (6.2), already gives rise to various interesting physical properties, like a non-trivial distribution of the end-to-end vector  $\mathbf{r}(L) - \mathbf{r}(0)$  [57, 58] or the (static) force-extension relation [59, 60]

$$f(x) = (6k_B T L_p / L^3) x + \mathcal{O}(x^2), \quad x \equiv |\mathbf{r}(L) - \mathbf{r}(0)|. \quad (6.5)$$

Here, the non-linear contributions are not given explicitly. They, however, become large when the chain undulations are pulled taut (*i.e.*, as  $x \rightarrow L$ ), yielding a pronounced stiffening. This is

of particular relevance for interpreting real-world phenomena of biological matter, like pulling on DNA strands or understanding the resistance of crosslinked polymeric meshworks, like the cytoskeleton, to mechanical load. As a side remark, it should be noted that polymers that are straightened under tension have conformations belonging to the stiff-polymer class [48], although the persistence length of their free conformation might be relatively small.

### 6.1.2 The weakly-bending rod limit

The above description of stiff polymers suggests to decompose  $\mathbf{r}(s)$  into a longitudinal component  $r_{\parallel}(s) \equiv \hat{\mathbf{u}} \cdot \mathbf{r}(s)$  and small transverse deviations  $\mathbf{r}_{\perp}(s) \equiv (\mathbb{1} - \hat{\mathbf{u}}\hat{\mathbf{u}})\mathbf{r}(s)$ . The mean direction  $\hat{\mathbf{u}} = \mathbf{u}/|\mathbf{u}|$  of the chain is given by the mean end-to-end vector  $\mathbf{u} = \langle \mathbf{r}(L) - \mathbf{r}(0) \rangle$ . In the stiff-polymer limit, the transverse deviations vary only weakly along the contour,  $[\mathbf{r}'_{\perp}(s)]^2 \ll 1$ , which is known as the weakly-bending rod (WBR) limit. One may integrate the correlation function in Eq. (6.4) over  $s_1$  and  $s_2$  to obtain the mean-square end-to-end distance

$$\frac{1}{L^2} \langle [\mathbf{r}(L) - \mathbf{r}(0)]^2 \rangle = 1 - L/3L_p + \mathcal{O}[(L/L_p)^2], \quad (6.6)$$

from which one infers that  $[\mathbf{r}'_{\perp}(s)]^2$  is on the order of  $L/L_p$ , while the longitudinal contributions  $[r'_{\parallel}(s)]^2$  are of order  $(L/L_p)^2$ . For stiff polymers,  $\mathcal{H}_{\text{WLC}}$  can thus be approximated (to zeroth order in  $L/L_p$ ) by the WBR hamiltonian

$$\mathcal{H}_{\text{WBR}} = \frac{\kappa}{2} \int_0^L ds [\mathbf{r}'_{\perp}(s)]^2. \quad (6.7)$$

Since the WBR approximation guarantees, per construction, the inextensibility  $|\mathbf{r}'(s)| = 1$  to hold (to given order), the fluctuations  $\mathbf{r}_{\perp}(s) \in \mathbb{R}^2$  are unconstrained and calculating, say, the distribution of the end-to-end vector and its moments [61] or the static force-extension relation [59, 62] from  $\mathcal{H}_{\text{WBR}}$  is much easier than for the full WLC model (see, e.g., [56]).

A quantity that will be repeatedly used in the following is the average amplitude

$$\frac{1}{L} \int_0^L ds \langle [\mathbf{r}_{\perp}(s)]^2 \rangle \propto L^3/L_p \quad (6.8)$$

of the transverse fluctuations, which readily follows from equipartition or can easily be computed from the sliced path integral (in Fourier space). Equation (6.8) is a direct consequence of the diffusive variation of the tangent vector along  $s$  with characteristic diffusion length (or step size)  $L_p$  according to the WLC hamiltonian in Eq. (6.2).

### 6.1.3 WBR dynamics

Neglecting excluded volume-effects and hydrodynamic interactions between the monomers (*i.e.*, approximating the transverse viscous friction between polymer and solvent to be constant), Eq. (6.7) yields the Langevin equation [48]

$$\zeta_{\perp} \partial_t \mathbf{r}_{\perp}(s, t) = -\kappa \partial_s^4 \mathbf{r}_{\perp}(s, t) + \xi_{\perp}(s, t) \quad (6.9)$$

for the contour fluctuations. Here,  $\zeta_{\perp}$  is the friction coefficient per contour length and the Gaussian white noise  $\xi_{\perp}(s, t)$  obeys the fluctuations-dissipation theorem  $\langle \xi_{\perp}(s_1, t_1) \cdot \xi_{\perp}(s_2, t_2) \rangle =$

$2k_B T \zeta_{\perp} \delta(s_1 - s_2) \delta(t_1 - t_2)$ . For a rigid rod of length  $L$ , the friction coefficient is of the form  $\zeta_{\perp} = 4\pi\eta_s/\ln(L/a)$  [50]. To account for the hydrodynamic interactions among neighboring chains in semidilute solutions, the polymer length  $L$  in the logarithm is often replaced by a screening length  $\xi_{\perp}$  that is expected to be on the order of the mesh size (*i.e.*, the average polymer distance) [63, 64].

Equation (6.9) describes the dynamics of a stiff polymer at low Reynolds numbers, which exhibits the characteristic frequency  $\omega_L \sim \kappa/(\zeta_{\perp} L^4)$ , as obtained from dimensional analysis with  $\partial_t \sim \omega$ ,  $\partial_s \sim L^{-1}$ . An explicit calculation for a long chain (neglecting boundary effects or using, say, hinged ends [65]), yields the subdiffusive growth

$$\text{MSD}_{\perp}(t) \equiv \frac{1}{L} \int_0^L ds \langle [\mathbf{r}_{\perp}(s, t) - \mathbf{r}_{\perp}(s, 0)]^2 \rangle \propto (L^3/L_p)(\omega_L t)^{3/4}, \quad \omega_L = \pi^4 \kappa / (\zeta_{\perp} L^4), \quad (6.10)$$

for the transverse mean square displacement (MSD) of the monomers averaged along the contour [64, 66, 67]. The power-law exponent 3/4 is a plain manifestation of the bending rigidity of semiflexible polymers, which has to be contrasted with that obtained for flexible polymers (subdiffusive behavior with an exponent 1/2 for the Rouse model<sup>1</sup>). It has been widely observed in experiments of F-actin using passive tracer beads [68, 69], dynamic light scattering techniques [70, 71], or fluorescence correlation spectroscopy [72]; and it gives rise to the  $\omega^{3/4}$  scaling of the storage and loss moduli at high frequencies  $\omega$  commonly encountered in biological materials, like entangled solutions [18, 73–75] and crosslinked F-actin networks [76] and even cells [77]. For affine shear flow, where tension propagation along the filament can be neglected<sup>2</sup>, one obtains a similar scaling  $\text{MSD}_{\parallel}(t) \propto t^{3/4}$  for the longitudinal fluctuations of the end-to-end distance at short enough times, before it saturates at its equilibrium value [83], such that both the bending- and stretch-dominated regimes exhibit the  $\omega^{3/4}$  signature [84, 85], making it a robust hallmark for semiflexibility at high frequencies.

<sup>1</sup>Flexible polymers are usually described by random flight models like the freely-jointed-chain model with fixed bond length  $a$  or a Gaussian-chain model with normally distributed bond lengths around  $a$  [50]. The latter, which naturally emerges from the former via coarse graining, corresponds to a chain of harmonic springs of stiffness  $\approx k_B T/a^2$  and is described by  $\mathcal{H}/k_B T = (3/2a^2) \sum_j (\mathbf{r}_{j+1} - \mathbf{r}_j)^2 \sim (3/2a) \int ds [\mathbf{r}'(s)]^2$ , corresponding to diffusive motion for a contour point  $\mathbf{r}(s)$ . In the Rouse model for the dynamics of such a spring chain one neglects excluded volume-effects and hydrodynamic interactions between the bead-like monomers, as in Eq. (6.9), yielding the Langevin equation  $\zeta \partial_t \mathbf{r} = (3k_B T/a) \partial_s^2 \mathbf{r} + \xi$ . It follows that  $\text{MSD}(t) \propto aL(\omega_L t)^{1/2}$  with  $\omega_L = 3\pi^2 k_B T / (\zeta a L^2)$ , which gives rise to a  $\omega^{1/2}$  scaling for the linear shear modulus.

<sup>2</sup>Due to the longitudinal friction, stretching-mode relaxation in a quiescent solvent is only possible on a local scale and elongational deformations cannot equilibrate globally before the tension variations have propagated along the filament [48, 78]. This leads to a quite complex response, whose exact long-time form depends on the particular deformation protocol [49]. At very short times ( $t \ll \zeta \kappa f^{-2}$  for a tension  $f$ ), the response is dominated by the fast relaxing bending modes, whereas the built-up tension does not yet contribute, yielding the power-law scaling  $\text{MSD}_{\parallel}(t) \propto t^{7/8}$  for the longitudinal fluctuations [79, 80] (corresponding to the high-frequency scaling  $\omega^{7/8}$  of the linear shear modulus [81]) that differs only slightly from the  $t^{3/4}$  scaling without friction. In the nonlinear regime, the transverse bending modes nonaffinely couple to longitudinal stretching modes, giving rise to a nontrivial stiffening at intermediate times, namely long enough that the tension can be built up, but short enough that the straightened part of the polymer does not yet extend to its ends [82]. For typical actin filaments ( $L \approx 20 \mu\text{m}$ ,  $L_p \approx 17 \mu\text{m}$ , with  $f = 1 \text{ pN}$ ,  $\eta = 1 \text{ mPa s}$ ,  $T = 300 \text{ K}$ ), this time window is roughly estimated as  $10^{-5} \dots 1 \text{ s}$ . The upper bound scales as  $t_L \sim (L/L_p)^{5/2} \zeta L^2 / f_{\perp}$ , the transverse force as  $f_{\perp} \sim (r_{\perp}/L_p)^{9/5} \zeta L_p^2 / t$ .



# Microstructure of entangled semiflexible-polymer solutions

The physics of semidilute solutions of stiff polymers is dominated by their entanglements [6]. They constrain the thermal motion of each constituent filament, effectively confining it to a tube-like cage collectively formed by surrounding filaments. The packing structure and the mechanical properties of such pure solutions of semiflexible polymers is crucially controlled by three length scales: the polymers' persistence length  $L_p$ , their (average) length  $L$ , and the mesh size  $\xi$ . The latter gives the average distance between the polymers (up to some numerical factor of order unity) and is a measure for the polymer number concentration  $c$ , namely as  $\xi \approx \rho^{-1/2}$  with the contour length density  $\rho \equiv Lc$ . In the following, I give a concise overview of the concept of the tube for semiflexible-polymer solution and its main predictions for the solutions' packing structure and the typical free-energy scales. First developed in the 1980s by Odijk [41], Doi [42], and Semenov [43], the tube model for semiflexible polymers has been systematically established in the late 1990s by of Morse [6, 84, 86–88]. His seminal papers served as a major source for various parts of this chapter, while some newer extensions and alternative approaches are outlined in Sec. 7.2. The present chapter focuses on the statistics of the entangled solutions, the associated dynamics and the underlying relaxation processes are considered in Chap. 8.

## 7.1 Tube model. Scaling arguments

For dense enough solutions, the transverse fluctuations of each polymer are confined to a tube-like cage formed by neighboring polymers. Then, only fluctuation modes of wavelengths shorter than a characteristic interaction length scale  $L_e$  can be expected to follow the statistics of an unconfined WLC, while longer modes are impeded. The crossover wavelength  $L_e$  between effectively free and perturbed modes is called the entanglement length. Within in the classical tube model, it is argued that, on length scales larger than  $L_e$  (and at correspondingly long times), each polymer can diffuse only in longitudinal direction, *i.e.*, along its backbone contour, a mechanism called reptation. Below and in Sec. 8.2, we will briefly discuss the limitations of this simplification and

outline theoretical approaches that account for collective relaxation processes that allow for tube renewal and thereby for slowed-down transverse long-time diffusion of the polymers.

Traditionally, the tube model has been used to describe the dynamics of the entangled polymer solutions. The entanglements may however also skew their statistics, as they divide the system's phase space into topologically separated regions. A single measurement thus corresponds to a quenched average over fluctuations within a particular topological realization of the polymer solution, many measurements can average over many such realizations. Although one may eventually end up with the same ensemble as without any geometrical constraints (*i.e.*, for “phantom” polymers), the entanglements affect the result when the quenched average does not commute with the one over topological realizations. The most prominent example for an observable that emerges only in the quenched state, while its full-ensemble average evaluates to zero, is the effective tube potential [89], introduced below. This is in qualitative analogy to a ferromagnet in the thermodynamic limit, where boundary contributions to the total energy become irrelevant. Then, a vanishing magnetization is energetically equal to the true ground state (all spins up or all spins down). To obtain the latter from the theory (e.g., the Ising model), one manually breaks the system's symmetry by an external field  $h$  and defines the ferromagnet's ground-state magnetization through the limit  $h \rightarrow 0$ .

Both  $L_e$  and the characteristic width  $D_e$  of the confinement tube are functions of  $L_p$  and  $\rho$  (or  $\xi$ ). They provide important mesoscale measures to describe the dominant contributions to the solution's mechanical properties—in particular, its rheological response. They can be used to discriminate between semiflexible-polymer, flexible-polymer, and rigid-rod solutions [6]. A solution of long semiflexible polymers with  $L \gg L_p$ , for instance, qualitatively differs from one of flexible polymers only if  $L_p > L_e$ , because only then the bending modes are impeded by the topological entanglements while otherwise self-avoidance plays the dominant role. For stiffer (shorter) polymers with  $L < L_p$ , in contrast, the size of the transverse contour fluctuations has to be on the order of  $D_e$ , such that the transverse confinement provides a constraint on the bending deformations, in order to qualitatively differ from a solution of rigid rods. This criterion for the transverse fluctuations is equivalent to  $L > L_e$ . It is important to notice that the whole concept of topological entanglements and the ensuing confinement tube should break down on (arguably long) time scales, for which the tube itself becomes a transient object due to global collective relaxation processes. Identifying this time scale is, however, anything but trivial and the transition from a well-defined static to a dynamic tube is rather given by a broad crossover region that crucially depends on the entanglement density—thereby challenging the concept of the static confinement tube [90]. In Chap. 8, we will take a closer look at the underlying relaxation processes and the associated time scales.

### 7.1.1 Tube geometry

The two conditions  $L, L_p \gg L_e$  characterize the “tightly entangled” concentration regime, where bending modes of the polymers are impeded [6]. Rough estimates for both  $L_e$  and  $D_e$  then follow from the concept of the tube as follows [41, 43]. The contour fluctuations of a WLC that is confined to a cylindrical tube of width  $D_e$  are assumed to follow the statistics of a free WLC over only a relatively short contour length  $L_e$ , namely before it collides with the tube wall. Thus, one identifies  $L_e$  with the so-called deflection length [41], which yields  $D_e^2 \propto L_e^3/L_p$ , according to Eq. (6.10). In order to form such tubes at all, each cylinder of width  $D_e$  and length  $L_e$  should be

crossed by about one polymer, on average, which yields  $\rho D_e L_e \approx 1$ . Combing the two scaling estimates, one obtains

$$L_e \propto \rho^{-2/5} L_p^{1/5}, \quad D_e \propto \rho^{-3/5} L_p^{-1/5}, \quad (\text{tightly entangled}) \quad (7.1)$$

with numerical prefactors on the order of one [19, 88]. Inserting the relation for  $L_e$  into the length-scale separations  $L_p, L \gg L_e$ , they become  $\rho L_p^2 \gg 1, (L_p/L)^{5/2}$ , where the omitted numerical coefficients, and thus the minimum concentration for the tightly entangled regime, could be quite large (e.g., ten entanglements per polymer of length  $L \approx L_p$  requires  $\rho L_p^2 \approx 10^{2.5}$ )

The (mean-field) scaling relations in Eq. (7.1), predicted from the tube model for tightly entangled semiflexible-polymer solutions, were indeed found to be in good agreement with fluorescence-microscopy experiments of F-actin [12, 13, 19, 91, 92] and computer simulations of entangled WLCs [93]. However, the concentration dependence of the average tube width  $D_e$  obtained from similar experiments by Lauter *et al.* [94] and, later on, by Jaschinski [95] was found to be weaker than what is expected from the tube model in Eq. (7.1) (approximately  $D_e \propto \rho^{-(0.35 \dots 0.25)}$  [95] as opposed to the expected  $D_e \propto \rho^{-0.6}$ ). So, maybe the polymers have not yet “traversed the whole tube” during the measurement time or this deviation indicates that the concept of a *static* tube is not valid (at such concentrations), suggesting the *dynamic*-tube approach instead that will be reviewed in Sec. 8.2. Alternatively, the deviations might hint at strong heterogeneities of the polymeric meshwork or at increasingly pronounced filament alignment at higher concentrations. In Ref. [96] (attached at the end of this chapter), we showed that the degree of nematic order depends on the preparation protocol and can in fact be quite high for semidilute F-actin solutions (*i.e.*, below the biphasic isotropic–nematic concentration regime,  $\rho < \rho_{\text{nem}}$ , which is expected to start at  $\rho_{\text{nem}} \approx 4.3/(La)$  for rigid rods [97] and  $\rho_{\text{nem}} \approx 6.7/(L_p a)$  for semiflexible polymers [98]). Although the alignment itself turned out to be long-lived, the alignment-induced tube dilation was found to relax quickly after the preparation, making it a rather unlikely candidate for the observed deviations from the tube-model predictions.

### 7.1.2 Energy scales

Based on the tube model, one can predict the typical free-energy scales corresponding to the different response and relaxation processes at work when the solution is mechanically driven. The corresponding free-energy densities provide the rough estimates [6, 85, 99]

$$G/k_B T \approx \begin{cases} \rho/L & (\text{rotation}) \\ \rho/L_e \propto \rho^{7/5} L_p^{-1/5} & (\text{bending}) \\ \rho L_p^2/L_e^3 \propto \rho^{11/5} L_p^{7/5} & (\text{affine stretching}) \end{cases} \quad (7.2)$$

for the magnitudes of the linear shear modulus  $G$ , where Eq. (7.1) was used to replace  $L_e$  in the second and third line. The first line describes the rotation of a polymer as a whole, which is associated with an energy contribution of  $k_B T$  per chain. The contribution in the second line follows from the excess free energy due to bending fluctuations that are impeded by the topological entanglements. All modes of wavelength larger than  $L_e$  are “frozen” or effectively “caged”, their number being given by  $L/L_e$ , and the excess free energy that is stored in the tube of length  $L$  evaluates to  $k_B T(L/L_e)$ . The third line gives the characteristic energy scale of longitudinal stretch modes of wavelength  $\approx L_e$ . For stiff-polymer segments of length  $L_e$ , the modulus for the

stretch response exceeds the one for bending by  $(L_p/L_e)^2$ , which is on the order of  $10^2$  to  $10^3$  for entangled F-actin solution. One thus concludes that the longitudinal stretching should not contribute to the linear response, which is instead dominated by the bending contributions. Note that this implies that the polymer does not follow the applied strain affinely (see also Sec. 8.5.2, where nonaffinity is discussed for crosslinked polymer networks).

Over a broad range of low frequencies—slow enough that all unconstrained bending modes are allowed to relax, but fast enough that the meshwork’s topology remains unchanged (Sec. 8.1)—entangled semiflexible-polymer solutions exhibit an approximately constant shear modulus, called the plateau modulus  $G_0$ . While the concentration dependence  $G_0 \propto \rho^{7/5}$  in the second line of Eq. (7.2) has been confirmed in various micro- and macrorheology experiments [14, 52, 74, 75, 100], the expected persistence-length scaling  $G_0 \propto L_p^{-1/5}$  was recently found to be in conflict with data obtained for solutions of DNA-helix tubes [52] and F-actin [53], which instead indicate that  $G_0$  increases with increasing  $L_p$  (with an exponent on the order of one [52], or even larger [53]). A comparison of the latter with Eq. (7.2) suggests that stretch modes are excited, which, in turn, would require that somewhat sticky contacts prevent the polymers from freely sliding past each other. Alternatively, stretch contributions might be traced back to long-lived topologically constrained hairpin configurations that are often created during sample preparation [96]. Since such strongly bent filaments exhibit a large prestrain/-stress, transverse deformations can couple to longitudinal stretching modes via hydrodynamic friction [82], even in the linear regime (see, e.g., Ref. [81] for an analysis of the linear response of a WLC under prestress). A complete picture that would explain the experimentally observed scaling laws of  $G_0$  is however lacking (see the recent article by Tassieri [53] for a concise overview and discussion).

## 7.2 Microscopic approaches

In the previous section, simple scaling arguments were employed to describe the packing structure and the mechanical properties of entangled stiff-polymer solutions as a function of the concentration  $\rho$  and persistence length  $L_p$  of the polymers. Despite its impressive success on a qualitative level, this approach cannot provide us with the numerical values of the omitted coefficients. Moreover, its purely static mean-field character implies that it neglects any spatial variations and correlations of the tube geometry and that it does not capture the dynamical nature of the polymers’ thermal fluctuations. Addressing such questions instead requires a microscopic approach that explicitly captures the single-chain physics as well as the confinement effects of the topological entanglements. To proceed analytically, the central idea is to tackle the complicated many-body problem by a mean-field approximation, where the entanglement effects are represented at a drastically coarse-grained level. An estimate for the strength (and form) of this mean field may then be derived using theoretical-physics tools known from liquid-state theory or continuum mechanics, say.

In Sec. 8.1, we discuss how polymer reptation (*i.e.*, longitudinal diffusion) triggers collective relaxation processes that render the topological entanglements—and thus the tube—transient on time scales beyond the typical reptation time. This means that the concept of the static tube is valid only at intermediate time scales, long enough that unconfined bending modes have equilibrated in the tube, but short enough that the topology of the polymer network remains invariant. In the remainder of the present chapter, I summarize the mean-field attempts proposed



by Morse [88] and their recent extension to the tube-size statistics.

The usual starting point for a microscopic description of entangled solutions of stiff polymers is the Hamiltonian

$$\mathcal{H} = \mathcal{H}_{\text{WBR}} + \mathcal{H}_{\text{tube}} = \frac{\kappa}{2} \int_0^L ds [\mathbf{r}'_{\perp}(s)]^2 + \frac{\phi}{2} \int_0^L ds [\mathbf{r}_{\perp}(s)]^2 \quad (7.3)$$

for a test filament that is confined to a homogeneous harmonic tube potential of strength  $\phi$ . In this form, the confinement contribution  $\mathcal{H}_{\text{tube}}$  represents a static mean-field approximation to the full dynamic heterogeneous tube. Possible extensions might allow for heterogeneities via a tube strength  $\phi(s)$  that varies along the tube backbone [19, 88, 89]. The tube width  $D_e$  and the entanglement length  $L_e$  are defined via

$$\frac{1}{4} D_e^2 \equiv R_e^2 \equiv \frac{1}{2L} \int_0^L ds \langle [\mathbf{r}_{\perp}(s)]^2 \rangle, \quad \frac{L}{L_e} \equiv \frac{1}{k_B T} \langle \mathcal{H} - \mathcal{H}_{\text{tube}} \rangle = \frac{1}{k_B T} \langle \mathcal{H}_{\text{WBR}} \rangle, \quad (7.4)$$

respectively, with the averages  $\langle \dots \rangle \equiv \int \mathcal{D}\mathbf{r} \dots e^{-\mathcal{H}/k_B T}$  performed over all polymer conformations. The tube radius  $R_e$  thus gives the mean amplitude of one component of the transverse fluctuations. The definition for  $L_e$  follows from an equipartition argument, namely that the free energy  $\langle \mathcal{H} - \mathcal{H}_{\text{tube}} \rangle$  of the impeded bending modes corresponds to  $k_B T$  times the number  $L/L_e$  of these modes. Employing equipartition (now, for all modes), Eq. (7.3) yields  $D_e = 2^{1/4} L_p^{-1/8} (\phi/k_B T)^{-3/8}$  and  $L_e = 2^{3/2} L_p^{1/4} (\phi/k_B T)^{-1/4}$ .

As written above, the central task is now to relate the mean tube strength  $\phi$  to the properties of the solution ( $\rho$  and  $L_p$ ). To this end, Morse [88] proposed three approaches: (i) a binary collision approximation (BCA), (ii) an effective medium approximation (EMA), and (iii) an elastic network approximation (ENA). While the BCA explicitly accounts for topological entanglements on the level of (“dressed”) pair collisions, the EMA considers a test chain that is tightly embedded in a linear elastic medium. Synthesizing these two approaches, the chain displacement is estimated within the ENA as the sum of a BCA and an EMA contribution, aiming at a combination of local entanglement and collective network effects.

In the BCA,  $\phi$  is derived from a potential  $V(x)$  of mean force for two topologically entangled WLCs of center-of-mass distance  $x$ , which is obtained by tracing out the chains’ transverse fluctuations. Each chain is thereby confined to the harmonic mean-field tube potential of strength  $\phi$ . After averaging over all possible orientations and topological configurations for such a “dressed” pair collision, the tube strength is basically obtained as the second-order Taylor coefficient of the entanglement potential,  $\phi = -d^2V/dx^2$ . Averaging over all tube-backbone distances  $x$ , this yields [89]

$$D_e \approx 1.3 \rho^{-3/5} L_p^{-1/5}, \quad L_e \approx 3.0 \rho^{-2/5} L_p^{1/5}, \quad G_0/k_B T \approx 0.3 \rho^{7/5} L_p^{-1/5}, \quad (\text{BCA}) \quad (7.5)$$

which agree with the scaling laws<sup>1</sup> obtained from the deflection-length arguments in Eq. (7.1). Since the BCA provides the tube strength  $\phi(x)$  as a function of the (uniformly distributed) tube-backbone distance  $x$ , it actually gives access to the whole distribution of  $\phi$  and thus to the

<sup>1</sup>Based on the idea of the BCA, one can derive the scaling laws for  $D_e$  and  $L_e$  by balancing the typical harmonic confinement free energy  $\phi D_e^2 L$  of a tube of length  $L$  with  $k_B T$  times the number of chains crossing this tube, which is on the order of  $\rho D_e L$ , hence  $\phi \propto k_B T \rho / D_e$ . Together with the scaling  $\phi \propto D_e^{-8/3} L_p^{1/3}$  obtained from Eqs. (7.3), (7.4), one arrives at  $\phi \propto k_B T \rho^{8/5} L_p^{1/5}$ .

tube-width distribution [19, 89]. Glaser *et al.* [19] showed that the BCA prediction for the shape of this distribution is in excellent agreement with the statistics of the tube-size variations along the tube backbone observed from fluorescence-microscopy experiments of entangled F-actin solutions. However, the theoretically predicted numerical magnitudes of both the mean tube width, Eq. (7.5), and the relative tube-width fluctuations were found to generally underestimate the measurements by a factor on the order of 1.5 to 2 [88, 89]. A possible reason for this widely seen discrepancy might be the approximation of a straight tube backbone that is employed in the BCA calculation. Bending the tube, instead, goes along with tube dilation, thereby lowering the confinement free energy and impeding less bending modes. Indeed, following the lines of the unit-cell model by Fernández *et al.* [101], which yields the tube conformation from a tradeoff between bending and confinement contributions to the overall free energy, we estimated a relative tube dilation on the order of 1.4, and even larger values for a (quasi-statically) sheared solution [96] (appended to this chapter). As another reason for the too small tube-width prediction the absence of collective deformation modes in the BCA has been identified, which leads to the EMA and ENA approaches that account for such global effects on a coarse-grained level.

In the EMA, the test polymer is assumed to affinely follow the displacement of a linear elastic medium of shear modulus  $G \approx \rho k_B T / L_e$ . Matching  $G$  with the tube spring constant  $\phi \approx L_p L_e^{-4}$  yields

$$D_e \approx 0.84 \rho^{-1/2}, \quad L_e \approx 2.2 \rho^{-1/3} L_p^{1/3}, \quad G_0 / k_B T \approx 0.82 \rho^{4/3} L_p^{-1/3}, \quad (\text{EMA}) \quad (7.6)$$

where the numerical coefficients depend on technical details of the underlying calculation. The ENA combines both the BCA and the EMA results by adding up the transverse polymer displacements as  $\langle r_{\perp} \rangle_{\text{ENA}} \equiv \langle r_{\perp} \rangle_{\text{BCA}} + \langle r_{\perp} \rangle_{\text{EMA}}$ , which yields the relation  $1/\phi_{\text{ENA}} = 1/\phi_{\text{BCA}} + 1/\phi_{\text{EMA}}$  for the overall tube strength  $\phi_{\text{ENA}}$ . As a sum of the two comparable BCA and EMA estimates, the ENA prediction for the tube width is found to be in better agreement with (but still slightly below) the F-actin data [88].

Article

# Microstructure of Sheared Entangled Solutions of Semiflexible Polymers

Marc Lämmel <sup>1</sup>, Evelin Jaschinski <sup>2</sup>, Rudolf Merkel <sup>2,\*</sup> and Klaus Kroy <sup>1,\*</sup>

<sup>1</sup> Institut für theoretische Physik, Universität Leipzig, Postfach 100920, 04009 Leipzig, Germany; marc.laemmel@itp.uni-leipzig.de

<sup>2</sup> Institute of Complex Systems 7: Biomechanics, Forschungszentrum Jülich, 52425 Jülich, Germany; evelin.jaschinski@gmail.com

\* Correspondence: r.merkel@fz-juelich.de (R.M.); klaus.kroy@uni-leipzig.de (K.K.); Tel.: +49-246-161-3080 (R.M.); +49-341-973-2436 (K.K.)

Academic Editor: Martin Kröger

Received: 25 July 2016; Accepted: 16 September 2016; Published: 28 September 2016

**Abstract:** We study the influence of finite shear deformations on the microstructure and rheology of solutions of entangled semiflexible polymers theoretically and by numerical simulations and experiments with filamentous actin. Based on the tube model of semiflexible polymers, we predict that large finite shear deformations strongly affect the average tube width and curvature, thereby exciting considerable restoring stresses. In contrast, the associated shear alignment is moderate, with little impact on the average tube parameters, and thus expected to be long-lived and detectable after cessation of shear. Similarly, topologically preserved hairpin configurations are predicted to leave a long-lived fingerprint in the shape of the distributions of tube widths and curvatures. Our numerical and experimental data support the theory.

**Keywords:** shear alignment; F-actin; tube model

## 1. Introduction

Semiflexible polymers are fundamental structural and functional building blocks of biological matter. They are the main constituents of the dynamic cytoskeletal networks and extracellular matrices that maintain the cell's mechanical stability and integrity. By controlling the mesoscale architecture of these scaffolds, cells regulate their response to mechanical load, and living organisms realize a wide range of mechanical properties and functions using only relatively few polymeric constituents [1,2]. Networks of semiflexible polymers are therefore at the core of many attempts to understand the rich mesoscopic and macroscopic mechanical response of biological matter in terms of its molecular machinery [3]. Over the last decades, great progress has been made by studying reduced in vitro model systems that share many macroscopically observed features of the far more complex natural systems [3–6]. Their mesoscale architecture is commonly characterized by a small set of mesoscopic parameters such as mesh size, polymer bundle thickness, and crosslinker concentration [7–9].

The classical rheological model for entangled solutions of flexible polymers is the so-called tube model [10,11]. It reduces the complex many-body problem to a simple mean-field picture featuring a test polymer in a long-lived tube-shaped confining cage, and thereby light-handedly accounts for some gross features of the linear rheology. Additional considerations are required to address the more intricate nonlinear rheology. For example, finite-chain stretching due to intermolecular friction [12] and tube contraction [13] were proposed to cause shear-stiffening and a rate-dependent stress overshoot during shear startup; (convective) constraint release [14] and similar concepts [15] were proposed to account for shear-softening.

One may expect similar ideas to apply to the much stiffer biopolymers that govern the mechanics of biological cells and tissues. Indeed, biopolymer solutions are generally reported to exhibit strain-softening and shear-thinning [16–19] under slow or stationary shearing, in accordance with predictions [20,21] based on a version of the tube model adapted to semiflexible polymers [22]. Again additional concepts, such as transient entropic filament stretching excited by some interchain friction due to transient filament crosslinking [1,23], were invoked to account for observations of transient shear-stiffening in response to large finite shear strains at higher rates [18,19,23–25]. Alternatively, fiber-lattice or “mikado” models for crosslinked networks relate the macroscopic stiffening not to the response of the individual constituents (modeled as linear elements) but to the collective behavior of a sparse sub-isostatic network [26]. An imposed strain is first taken up by so-called floppy modes [27,28], before the network becomes rigid at a critical strain [29,30]. Brownian-dynamics simulations [31] support the notion that stiffening at intermediate timescales (when the individual fibers have locally equilibrated) is due to slower collective modes.

Recent experiments combining bulk and microrheology measurements with confocal fluorescence microscopy and particle tracking techniques were able to record the conformation and orientation of individual filaments under shear [17,32–35], and found them to be very sensitive to the polymer concentration. In very dilute solutions, actin filaments perform a tumbling motion, switching between an advective and a diffusive phase, corresponding to strongly buckled (U-shaped) and stretched polymer conformations, respectively [34]. In the semi-dilute regime, tumbling is modified by filament–filament collisions, increasing both filament alignment [35] and bending [17], as evidenced by broad tails in the distribution of the local filament curvature. Such observations challenge mesoscopic theories and computer simulations [26,36–39] to extend the simple network models and also consider densification [33], ordering and alignment [17,40], and even lengthening [41] of fibers.

In the present paper, we address two major effects of shear onto the constituent polymers, namely alignment and bending, on the basis of the tube model of semiflexible polymers. In the following section, we derive theoretical predictions for the affine and non-affine shear alignment and the tube-width and curvature distributions in a sheared semiflexible polymer solution. They are then tested by dedicated computer simulations and experiments with semidilute F-actin solutions. Technical details are deferred to Section 4.

## 2. Results and Discussion

As pointed out in the introduction, shearing a semidilute polymer solution will generally deform and align the individual polymers and their long-lived tube-shaped confinement cages. In the following, we study these two effects separately. We first concentrate on the effect of an externally imposed nematic tube alignment on the local packing structure, quantified in terms of the tube width, in Section 2.1. We then ask how much alignment is actually caused by shearing. Following Morse [20] and Fernández et al. [21], we moreover estimate the tube deformation due to large finite shear strains by minimizing a model free energy and analyze the consequences for the tube-width and curvature distributions, in Section 2.2. Finally, we corroborate our key theoretical predictions by computer simulations and experiments with F-actin solutions, in Sections 2.3 and 2.4.

### 2.1. Tube Alignment

In the absence of crosslinking molecules, the structure and mechanics of the transient polymer network that dominates the mechanical response of a semidilute biopolymer solution is governed by long-lived topological entanglements. They constrain the thermal motion of each constituent filament so that it remains effectively confined to a tube-like cage formed by surrounding filaments [42]. Shear is expected to cause some alignment of the polymers and their confining tubes, which is otherwise not entropically favorable below the nematic transition, and thereby to widen the tubes.

In the following, we extend the so-called binary-collision approximation (BCA) developed in the classical tube model of semiflexible polymers [43] to quantify the effect theoretically.

As usual, the polymer solution is characterized by its chain length concentration  $\rho$ , the persistence length  $L_p$  of the constituting polymers, and the nematic order parameter

$$S = (3/2) \int d\mathbf{u} (\mathbf{u} \cdot \mathbf{d})^2 f_S(\mathbf{u}) - 1/2. \tag{1}$$

Here,  $f_S(\mathbf{u})$  denotes the distribution of the normalized tangent vector  $\mathbf{u}$  of the filaments or tubes, respectively, and  $\mathbf{d}$  their mean direction. Extending standard procedures [43,44], as detailed in Section 4.3, we arrive at the following BCA predictions for the mean tube radius and entanglement length for a solution of prealigned polymers:

$$\begin{aligned} \bar{R}(S) &= [4\alpha_0 I(S)\rho]^{-3/5} L_p^{-1/5} \sim \bar{R}(0)(1 + 3S^2/8), \\ \bar{L}_e(S) &= [\alpha_0 I(S)\rho/8]^{-2/5} L_p^{1/5} \sim \bar{L}_e(0)(1 + S^2/4). \end{aligned} \tag{2}$$

Here,  $I(S)$  is the normalized packing entropy of the solution, which we estimate by Onsager’s rigid-rod prediction [45] to derive the final asymptotic expressions, valid for weak alignment (small  $S$ ). A numerical solution of the full theory corroborates what the asymptotic expressions suggest, namely that strong alignment ( $S \rightarrow 1$ ) is required to induce any sizeable tube widening. This is in line with the prediction  $\bar{R}(S)/\bar{R}(0) \propto I(S)^{-1/2}$  for rigid rod solutions, as derived by Doi and Edwards from geometrical arguments based on pair collisions [11] and by Sussman and Schweizer [46] building on the binary-collision approach to rigid-rod solutions by Szamel [47]. The caging of rigid rods and the entropic repulsion and attraction induced by the conformational fluctuations of semiflexible polymers, encoded in Equation (2), thus yield quantitatively similar predictions. Our quantitative result is compared to our experiments and simulations in Section 2.3, below.

In References [44,48], the BCA scheme was generalized to the so-called segment-fluid approximation that gives access to the tube fluctuations as encoded in the distributions  $P(R)$  and  $P(L_e)$  of both the tube width and the entanglement length. The predictions were found to be in good agreement with experimental data obtained from partially fluorescently labeled F-actin solutions, allowing for a decent global fit for various actin concentrations. Within our extended version of the BCA with preferential filament alignment (detailed in Section 4), the distribution functions for the reduced variables  $r \equiv R/\bar{R}$  and  $l_e \equiv L_e/\bar{L}_e$  take the form of universal scaling functions that are not only independent of concentration but also of the nematic order parameter  $S$ . Moreover, the distribution of the entanglement length, which is the characteristic correlation length (of the local tangent orientations, tube widths, curvatures, etc.) along the tube backbone, is predicted to be strongly peaked around the its mean:  $\bar{l}_e^2 - 1 \approx 0.01$ . As a consequence, our above discussion of the effect of alignment onto the solution rheology on the level of the mean values  $\bar{R}$  and  $\bar{L}_e$  should suffice.

To get a rough idea, how much alignment is actually caused by shearing an initially isotropic solution, we estimate the alignment of short, relatively straight tube segments from the affine response of a solution of rigid phantom rods [45],

$$S(\gamma) \sim 3\gamma/10 \quad (S < 1). \tag{3}$$

The linear increase with applied strain is dictated by symmetry [38] and thus more general than its derivation, which is detailed in Section 4.4, where we additionally derive the corresponding angular distribution of the tube-segment directions. Beyond the linear asymptotic regime, we find a considerable flattening of  $S(\gamma)$  at about  $\gamma \gtrsim 3$ , as illustrated in Figure 1. Shear alignment beyond  $S \approx 0.7$  is thus very hard to achieve. Now, using the result for  $S(\gamma)$  in Equation (2), we obtain the

following prediction for the strain-dependence of the tube radius and entanglement length due to shear alignment,

$$\begin{aligned}\bar{R}(\gamma)/\bar{R}(0) &\sim 1 + 0.034\gamma^2, \\ \bar{L}_e(\gamma)/\bar{L}_e(0) &\sim 1 + 0.023\gamma^2.\end{aligned}\quad (4)$$

The small numerical coefficients show that both quantities are weakly affected even by quite substantial shearing, as far as shear alignment is considered. This is indeed also borne out by our computer simulations and experiments discussed in Section 2.3, below. As a consequence, also the restoring forces associated with shear alignment should be weak. For this reason we expect it to persist long after a large finite shear deformation has been applied. However, shearing affects the packing structure of the polymer solution not only through shear alignment, but also through (non-affine) tube deformations, for which more sizeable rheological consequences were indeed predicted by Morse [20] and Fernández et al. [21]. These are analyzed in the next paragraph.

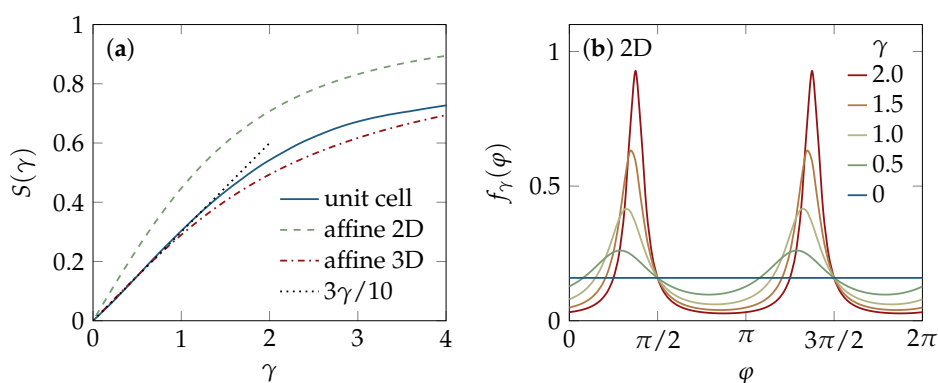


**Figure 1.** Shear alignment of tube segments. (a) Strain-dependence of the nematic order parameter  $S(\gamma)$ : affine scaling, as obtained for two- and three-dimensional solutions of phantom rods (Section 4.4), and the numerical estimate from the unit-cell model [21] (see Section 4.5). Up to strains of order one, the results are well captured by the linear asymptotic scaling of Equation (3), while  $S(\gamma)$  flattens out for larger strains, implying that perfect shear alignment is hard to achieve, even if quite substantial strains are imposed; (b) The angular distribution of the two-dimensional phantom-rod solution, according to Equation (19). With increasing strain the bimodal structure becomes more pronounced.

## 2.2. Tube Deformation

The extended BCA theory used in the above calculation is an effective two-body theory and thus blind to the complicated many-body effects involved in shearing. The unit-cell approach by Fernández et al. [21] considers a test polymer together with two collision partners located on opposite sides, instead (see Section 4.5), and can thereby capture some geometric aspects inaccessible to the BCA. In particular, it predicts non-affine deformations of the microstructure, because only the tube–tube collision points (or, alternatively, the centers of the confining tubes) are slaved to the affine deformation field, whereas the backbone contour of the considered test tube relaxes to a (non-affine) conformation that minimizes the unit-cell free energy. As a consequence, the strain-dependent order parameter  $S(\gamma)$  may generally be expected to differ from the affine estimate in Equation (3). But we find good agreement between both predictions for moderate strains  $\gamma < 1$ , and even for the saturation at large strains (beyond  $\gamma \approx 3$ ), as detailed in Section 4.5 and illustrated in Figure 1. The non-affine contributions merely slightly enhance the alignment at intermediate strains. Altogether, the unit-cell model thus confirms the above phantom-rod prediction that shear alignment is effectively bound to remain relatively moderate ( $S \lesssim 0.7$ ), even up to quite substantial strains of several hundred percent.

Importantly, though, the unit cell model predicts sizable non-affine deformations of the local packing structure, beyond the pure shear-alignment effect. For example, we find for the strain dependence of the tube radius:

$$\overline{\mathcal{R}}(\gamma)/\overline{\mathcal{R}}(0) \sim 1 + b_{\mathcal{R}}\gamma^2. \quad (5)$$

Here and in the following, we use the script typeface to discriminate the quantities calculated from the unit-cell model from the above BCA estimates. An important difference between them, even if no shear is applied, is that the BCA conventionally considers a straight tube, whereas the unit-cell model allows tubes to bend if this lowers the total equilibrium free energy, which balances contributions from confinement *and* bending. In Section 4, we find that the average tube width thereby grows by a factor  $\overline{\mathcal{R}}(0)/\overline{R} \approx 1.4$  in the quiescent solution, and even further, with the coefficient  $b_{\mathcal{R}} \approx 0.14$ , upon shearing. The comparison of Equations (4) and (5) thus suggests that the nonlinear shear-softening of entangled polymer solutions and the associated rheological stresses are predominantly caused by non-affine tube deformations with only minor contributions from shear alignment. In view of the above-established flattening of  $S(\gamma)$  at large strains, this statement is likely to hold beyond the range of validity of the asymptotic result in Equation (5).

Similarly, we can use the unit-cell model to quantify how shearing affects tube bending. For the mean curvature of the tube backbone we find for small deformations:

$$\overline{\mathcal{C}}(\gamma)/\overline{\mathcal{C}}(0) \sim 1 + b_{\mathcal{C}}\gamma^2. \quad (6)$$

with  $\overline{\mathcal{C}}(0) \approx 1.4(L_p\overline{L}_e/2)^{-1/2}$ , where  $(L_p\overline{L}_e/2)^{-1/2}$  is the mean curvature of a wormlike chain confined to a straight tube segment of length  $\overline{L}_e/2$ , the coefficient  $b_{\mathcal{C}} \approx 0.037$  is obtained. Its small positive value indicates that, on average and for moderate strains, the effect of filament buckling slightly exceeds that of filament stretching.

The average curvature of the tube can also be quantified by a tube persistence length  $l_t$ , conveniently inferred from the Odijk relation  $\overline{L}_e^3 = 4^3\overline{\mathcal{R}}^2l_t$  between entanglement length and tube width [49]. For a straight tube,  $l_t$  is equal to the bare intrinsic persistence length  $L_p$  of the enclosed test polymer. However, as already pointed out above, the unit cell model predicts a substantial renormalization, even without shear, because it allows the tube to bend spontaneously to minimize the unit-cell free energy, in qualitative accord with the persistence-length renormalization due to molecular crowding found in recent model simulations [50]. Quantitatively, we find  $l_t(0) = [\overline{R}/\overline{\mathcal{R}}(0)]^2L_p \approx 0.56L_p$ , in line with our above finding  $\mathcal{C}(0) \approx 1.4(L_p\overline{L}_e/2)^{-1/2}$ , which can thus be rewritten as  $\mathcal{C}(0) \approx (l_t(0)\overline{L}_e/2)^{-1/2}$ . Our own simulations cannot reach high enough densities to make this effect discernible. If we extend the Odijk relation to the case of a sheared solution, namely  $\overline{\mathcal{L}}_e(\gamma)^2 = 4^3\overline{\mathcal{R}}(\gamma)^2l_t(\gamma)$ , and replace  $\overline{\mathcal{L}}_e(\gamma)$  by its equilibrium value  $\overline{L}_e$  (which is a good approximation for moderate strains), we find for the renormalization of the tube persistence length under shear

$$l_t(\gamma)/L_p \sim [\overline{R}/\overline{\mathcal{R}}(\gamma)]^2 = [\overline{R}/\overline{\mathcal{R}}(0)]^2 (1 + b_{\mathcal{R}}\gamma^2)^{-2}. \quad (7)$$

So, some polymers stretch and others buckle upon shearing, but, overall, buckling wins and the average tube persistence length decreases, in line with the increasing curvature, found above.

A more comprehensive characterization than by mean values is possible by statistical distribution functions. In contrast to the marginal effects that we obtained from tube alignment, above, we now find the distributions to be quite sensitive to the non-affine shear deformations predicted by the unit-cell model. Rephrasing the result in terms of the reduced tube-radius distribution  $p_{\gamma}(r) = \overline{\mathcal{R}}(\gamma)P_{\gamma}[r\overline{\mathcal{R}}(\gamma)]$  yields a master curve onto which the appropriately normalized experimental data should collapse, independently of the actin concentration. For the curvature distribution, we apply the same procedure to arrive at a reduced curvature distribution  $p_{\gamma}(c)$ .

The predicted influence of shear on the master curves corresponding to  $p_{\gamma}(r)$  and  $p_{\gamma}(c)$  is illustrated in Figure 2. It reveals that  $p_{\gamma}(r)$  develops broad tails at small arguments as the strain



$\gamma$  increases, whereas  $p_\gamma(c)$  becomes more sharply peaked around its average (normalized to 1) and develops a tail at large arguments. The emergence of the tails can be traced back to so-called hairpin conformations (thermodynamically suppressed strongly contorted unit cell configurations [20,21]), as schematically sketched as insets in Figure 2. They are pulled tight under shearing, which accounts for the increasingly bimodal structure developing for large strains  $\gamma$  in both distributions, but is found to have only negligible impact onto the mean tube parameters.

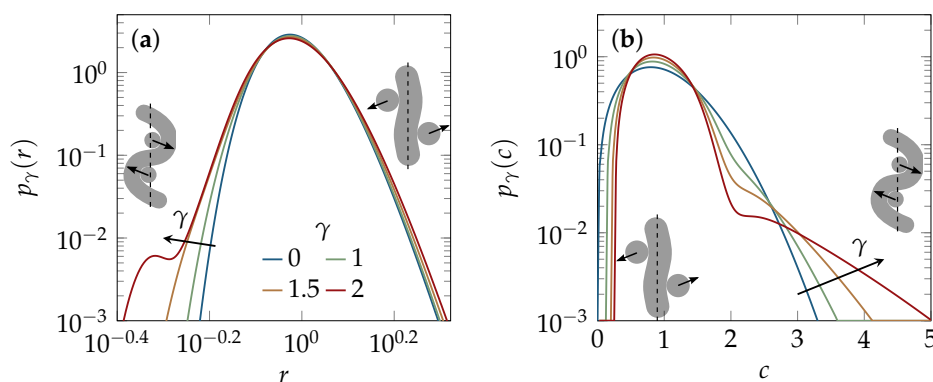


**Figure 2.** How shear affects packing structure in the unit-cell model [21]. In contrast to the most probable tube conformations, rare hairpin configurations are buckled and pulled tighter by increasing shear (as sketched in the insets). They are responsible for the tails emerging upon increasing strain  $\gamma$  in the concentration-independent master curves of the reduced probability distribution functions (a)  $p_\gamma(r) \equiv \bar{\mathcal{R}}(\gamma)P[r\bar{\mathcal{R}}(\gamma)]$  for the tube width and (b)  $p_\gamma(c) \equiv \bar{\mathcal{C}}(\gamma)P[c\bar{\mathcal{C}}(\gamma)]$  for the tube curvature.

### 2.3. Experiments and Simulations

The details of our simulations and experiments can be found in Section 4. Briefly, the simulations use a hybrid Monte-Carlo/Brownian-Dynamics algorithm, developed by Ramanathan and Morse [51–53], who kindly provided us with the source code of their program, to sample over topologically allowed states of a solution of wormlike chains. In this algorithm a sequence of Monte-Carlo steps, which respect the mutual uncrossability of colliding chains, is drawn from the stochastic dynamics of each chain, as obtained by solving a corresponding Langevin equation. The polymers were given a preferential orientation at initialization, i.e., before the uncrossability constraints and Brownian motion were switched on.

In the experiments, the thermal motion of a fluorescently labeled actin filament in the meshwork of unlabeled neighbor filaments is tracked over a fixed time span, long enough to identify the shape of the confinement tube. Two different setups were used to prepare the samples: a large micro chamber and a narrow capillary yielding almost isotropic and nematically ordered solutions, respectively. Varying the polymer concentration, this approach provides the dependence of the tube width on the alignment strength  $S$ , because the flow-induced ordering depends on the concentration—denser solutions yielding stronger alignment, see Figure 3b. The measured relation between the average tube width and alignment displayed in Figure 3a is consistent with the simulations and the BCA-prediction.

Beyond the mean tube width, we also measured the distribution of tube widths. As shown in Figure 4, the rescaled data for all concentrations and  $S$ -values fall on a master curve, as predicted by the extended BCA.



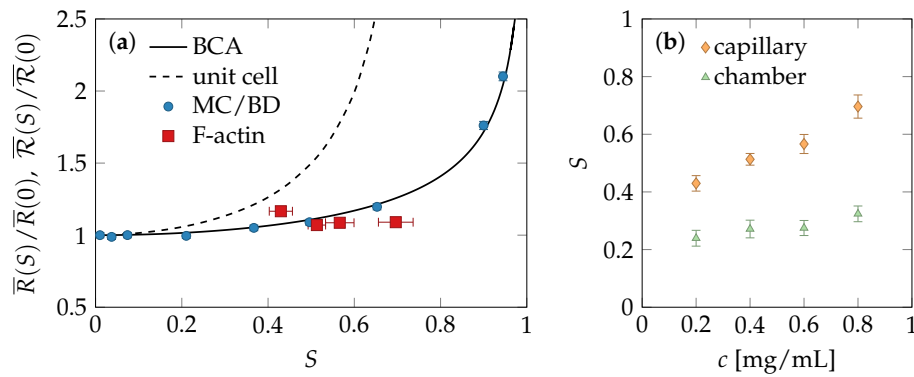


**Figure 3.** Nematic alignment and tube deformation. (a) Dependence of the mean tube radius  $\bar{R}$  on the nematic order as predicted by the binary-collision approximation (BCA) calculation, Equation (2), and the unit-cell model. The four experimental data points correspond to four different F-actin concentrations  $c$ . Our Monte-Carlo/Brownian-Dynamics (MC/BD) simulations of pre-aligned polymer solutions and F-actin experiments show no sign of the strong strain-induced tube dilation predicted by the unit-cell model but agree with the BCA predictions for moderately pre-aligned tubes, corresponding to shear alignment by a strain of about  $\gamma = 1.5 \dots 2.5$ . We interpret this as an indication that the average tube deformations had mostly relaxed between the cessation of shear and the start of the measurements, while the inflicted shear alignment was largely conserved. Note that the statistical errors of the tube size is very small ( $\approx 1\%$ ) for both the experiments and the simulations; (b) Polymer solutions were prepared in two different sample geometries for each  $c$ , a narrow capillary and a wider micro chamber, to get strongly sheared networks and weakly sheared reference samples, yielding values for  $\bar{R}(S)$  and  $\bar{R}(S \approx 0)$ , respectively. Their ratio is shown in panel (a) against the values for  $S$  in the capillary.

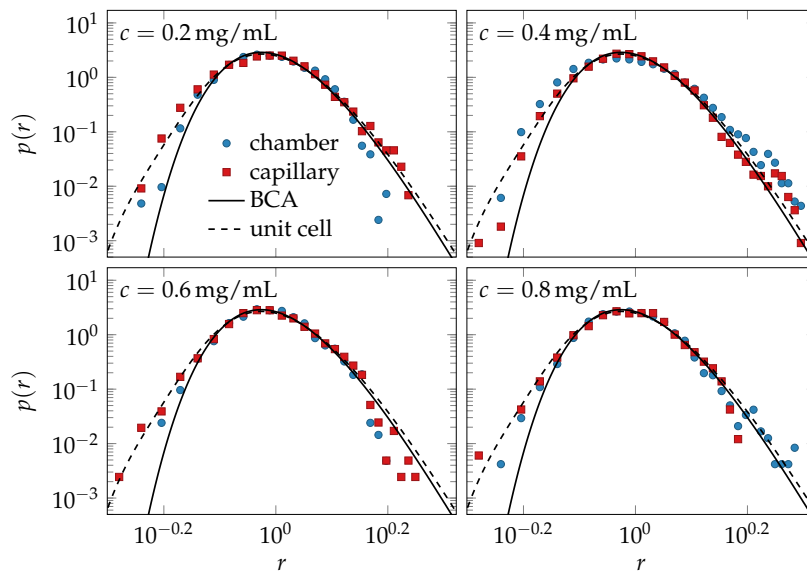


**Figure 4.** Reduced tube-width distribution: differently prepared F-actin experiments collapse onto a single master curve  $p(r) = \bar{R}P(r\bar{R})$ , independent of both concentration and the degree of nematic order of the solution. The scaling and the shape of the equilibrium master curve, Equation (12), are predicted by the tube model, evaluated in the binary-collision approximation (BCA). Its deformation due to shearing is estimated using the unit-cell model. Small deviations between the data and the equilibrium theory are consistent with the predicted effect of a remnant strain  $\gamma = 1.5$  (dashed lines) and interpreted as indicative of long-lived deformations of rare hairpin configurations.

#### 2.4. Comparison of Theory and Data

Our theoretical, experimental, and numerical findings all suggest that moderate tube-segment alignment only weakly influences the tube size and its distribution and therefore excite only weak restoring stresses. Curiously, all our experimental data seem to fall into regime of moderate alignment, up to  $S \approx 0.5$  where the tube radius is almost independent of  $S$ , cf. Figure 3. The experimental data support the predictions obtained from both the simulations of the prealigned fiber solutions and the affine phantom model and BCA prediction: the detected alignment is compatible with an average tube width equal to its equilibrium value.

The shear strain  $\gamma$  imposed on the actin solution cannot directly be controlled, in our setup, but from the recorded filling speeds of the capillary, it should be similar for all analyzed actin concentrations. By the time of the measurement, the solution was no longer actively sheared, only the final shear strain was maintained. According to Equation (3), the observed weak alignment corresponding to nematic order of strength  $S \approx 0.4 \dots 0.7$  is consistent with remnant shear strains  $\gamma \approx 1.5 \dots 2.5$  and reflects the predicted difficulty to achieve any stronger shear alignment with such strains. At the same time, the measured tube-radius data show no sign of the sizeable increase of the mean tube radius  $\overline{R}(S)$  predicted by the unit-cell model as a consequence of tube deformations. A plausible explanation could be that the tube deformations had already been undone by the associated restoring stresses at the time of the measurements, whereas the negligible restoring stresses associated with the experimentally observed moderate tube alignment allowed the latter to persist. Indeed, having no discernible effect on the tube conformations, these stresses should not appreciably exceed the thermal energy per tube volume.

Another effect on the packing structure that should arguably be long-lived and experimentally detectable is the change in the tube-width and curvature distributions caused by the shearing of hairpins (Figure 2). Hairpin configurations are topologically prevented from relaxing into more typical configurations without first disentangling from their tubes. They are preserved and even stabilized upon shearing, and their effects onto the shapes of the tube-width and curvature distributions are independent of the average values of the tube width and curvature. Hence, they also should relax on a very slow time scale, and their deformation by shear and its characteristic fingerprint in the distributions in Figure 2 (relative enhancement of the fraction of small tube radii and large tube curvatures) should be largely preserved after cessation of shear, when the average tube width and curvature have already relaxed. Indeed, as demonstrated in Figure 4, the frequency of small tube widths is found to be increased compared to the prediction of the equilibrium model (solid lines). Excellent agreement of theory and data for the tube-width distribution is obtained by choosing a plausible value for the remnant strain  $\gamma = 1.5$ , consistent with the observed tube alignment in Figure 3, according to Equation (3). Despite this very favorable agreement, some issues remain to be resolved. Our computer simulations seem to indicate a tendency of the BCA to systematically underestimate the fraction of narrow tubes, even in equilibrium solutions (Figure 5 of the methods section). A thorough investigation of this issue is currently hampered by computational limitations and experimental difficulties. The measured tube width distributions have a tendency to weakly broaden within the observable finite-time windows, presumably because the ideal limit of strong entanglement is difficult to achieve in practice (especially in computer simulations).

### 3. Conclusions

The mechanical properties of entangled solutions of semiflexible polymers depend crucially on the response of the mesoscopic architecture to external perturbations. We have analyzed the impact of two such perturbations: an imposed affine nematic ordering and a proper shear deformation that induces a similar degree of nematic alignment but also additional, non-affine strains. By measuring the tube-shaped cages of labeled test polymers after cessation of shear, we found that initially isotropic solutions developed moderate nematic order by shear alignment, which persisted after the shearing had stopped. Besides this shear-alignment, which is comparable

to what one would expect from a purely affine model, shearing was predicted to cause non-affine local tube deformations (Figure 3) and leave a characteristic fingerprint in the tube-width and backbone-curvature distributions (Figure 2). We estimated both effects using the unit-cell approach by Fernández [21]. We could not detect the expected average tube deformations, experimentally, presumably because they had been driven back by the associated restoring forces, at the time of measurement. However, our data for the reduced tube-width distribution could well be fitted by the unit-cell model, assuming a finite remnant strain consistent with the observed tube alignment (Figure 4). The theory identifies a small fraction of topologically protected hairpins as the main source of the observed deviations from the equilibrium distributions. Similarly, literature data for the microstructure of F-actin solutions [17,54] seem consistent with a sizeable influence of shear on the curvature distribution  $p_\gamma(c)$ , although the very large strains imposed in Reference [17] prohibit a direct comparison.

In summary, our experimental and numerical data can be reconciled with the predictions of the unit-cell model if one accepts that the predicted average tube dilation and tube buckling upon shearing is energetically costly and relaxes quickly, so that it is not detectable after cessation of shear, whereas moderate tube alignment and hairpin deformations induce no sizeable (global) stresses and are therefore longer-lived, hence detectable. With this interpretation, our comparison of theory and experiment yielded consistent results but calls for further investigations. It would be particularly interesting to test the predicted faster relaxation of the average tube width and curvature as opposed to the shear alignment and hairpin effects with a higher time resolution as possible in our setup. A careful analysis of the evolution of curvature distributions upon application of finite large strains would also be very desirable.

## 4. Materials and Methods

### 4.1. Experiments

Actin was isolated from rabbit skeletal muscle, purified, and polymerized following standard procedures [48] to gain F-actin solutions of polymer concentrations  $c$  in the range from 0.2 to 0.8 mg/mL. These values correspond to dimensionless polymer length concentrations  $\rho L_p \approx 2300$  to 9200, based on the typical value  $L_p = 17 \mu\text{m}$  of the persistence length and the estimate  $\rho/c \approx 40 \mu\text{m}^{-2}/(\text{mg/mL})$  obtained from the molecular structure of the actin filaments [43].

The filaments were labeled with TRITC-Phalloidin (Sigma Aldrich, Taufkirchen, Germany) and mixed gently with unlabeled filaments at a ratio of 1:1000. We used two different sample geometries for each concentration, a narrow capillary (0.1 mm  $\times$  2 mm  $\times$  50 mm, CM Scientific Ltd., West Yorkshire, UK) and a large chamber (8 mm  $\times$  8 mm  $\times$  5 mm, Lab-Tek Chambers, Nalge Nunc International, New York, NY, USA), yielding nematically ordered and almost isotropic polymer networks, respectively. Two-dimensional confocal microscope (LSM510, Carl Zeiss, Jena, Germany; objective C-Apochromat 63 $\times$ /1.2 W korr; 543 nm laser and long pass filter 560 nm) images of a fluorescently labeled filament were recorded every second during a time span of 150 s, superimposed, and analyzed to measure the tube width, i.e., the space explored by the fluctuating polymer, similar to previous studies [48]. Due to the large number of data points that we collected, the statistical errors for the mean tube width, as obtained from a standard Jackknife method, are on the order of 1%. Filament orientations (i.e., order parameters) were obtained from three-dimensional stacks of images with voxel sizes chosen according to optical resolution and Nyquist's sampling theorem.

### 4.2. Simulations

We use a hybrid Monte-Carlo/Brownian-dynamics algorithm proposed by Ramanathan and Morse [51–53] to simulate networks of entangled wormlike chains that have zero thickness but can not cross each other. The Brownian dynamics of each bead-rod polymer in the solution is computed by numerically integrating the corresponding Langevin equations. Each time step a trial

move is computed for one randomly chosen polymer and steric interactions between filaments are implemented by rejecting the trial move if it would lead to a cut through a neighbor filament.

To mimic the shear alignment observed in the experiments we implement nematic order in the simulations by an external field  $-h \cos(\gamma)$  that favors nematic alignment with an external director. The field acts during the initialization phase when the polymers are generated and placed in the simulation box in their free equilibrium states. After the system is initialized, the field is turned off and the system evolves thermally— similar to what happens in experiments right after preparation. At the end of each simulation run, we measure the order parameter

$$S = \frac{1}{2N_{\text{rod}}} \sum_{i=1}^{N_{\text{rod}}} (3 \cos^2 \theta_i - 1) \tag{8}$$

of the network by averaging the orientations of the  $N_{\text{rod}}$  polymer segments. The direction of each polymer segment is characterized by the angle  $\theta_i$  between a rod that connects two neighboring monomer beads and the externally imposed director. Following Reference [52], we determine the time-dependent tube radius  $R(t)$  from the reptation-corrected MSD,

$$R(t)^2 = \frac{1}{N(T-t)} \sum_{i=1}^N \int_0^{T-t} d\tilde{t} d_i(\tilde{t}, \tilde{t} + t)^2, \tag{9}$$

where  $N$  is the number of molecules,  $T$  the total simulation time, and  $d_i(\tilde{t}, \tilde{t} + t)$  gives the closest approach between the chain’s middle bead at time  $\tilde{t} + t$  and the contour of this chain at time  $\tilde{t}$ . The  $S$ -dependent equilibrium mean tube radius  $\bar{R}(S)$  is then obtained assuming that  $R(t) = \bar{R}(S)f(t/\tau_e)$  can be written in terms of a universal scaling function  $f$  [51], where the so-called entanglement time  $\tau_e \propto \bar{R}(S)^{8/3}$  itself depends on the mean tube width.

The data shown in Figure 4 were obtained for solutions that contained 1296 chains of length  $L = L_p$  in a cubic simulation box of edge length  $1.2L$ , yielding a dimensionless polymer length concentration of  $\rho L_p^2 = 750$  and an entanglement length on the order of  $L_e \approx 0.2L_p$  according to Equation (11). The simulation time was set to one half the rotational diffusion time of a straight rod of length  $L$ , which corresponds to about  $40\tau_e$  for the used polymer concentration. The measured order parameter  $S$  was found to remain almost constant during the whole simulation time.

Figure 5 compares the reduced distribution of the tube widths obtained from isotropic solutions of various concentrations with the BCA prediction.

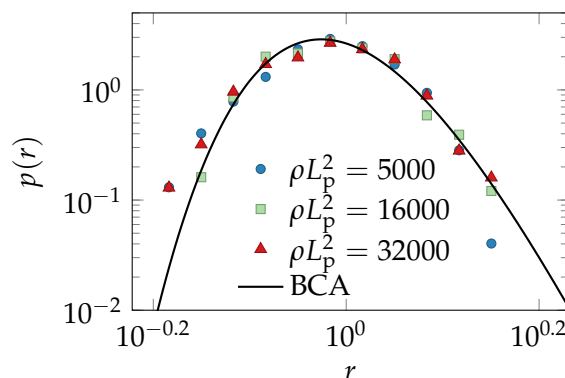


**Figure 5.** Reduced tube-width distribution obtained from the hybrid Monte-Carlo/Brownian-dynamics computer simulations [51–53]. As expected from the BCA prediction, data for various polymer length concentrations  $\rho$  collapse onto a single master curve.

### 4.3. Binary Collision Approximation (BCA)

We tackle the complicated many-body problem of an entangled network of semiflexible polymers using the binary collision approximation (BCA) [43], which can easily be extended to nematically ordered networks. A representative test polymer is modeled as a wormlike chain (WLC) of persistence length  $L_p$ . Its collisions with other polymers in the solution are accounted for as far as these can be represented by independent pair interactions. Collective many-body effects are summarily included on a mean-field level by confining all polymers to cylindrical harmonic cages by adding a term  $\bar{\phi}r_{\perp}^2/2$  to the WLC-Hamiltonian. Balancing the bending and confinement free energy contributions, the tube radius, defined as the average transverse displacement  $\bar{R}^2 \equiv (2L)^{-1} \int_0^L ds \langle r_{\perp}^2(s) \rangle$  of the test chain, and the entanglement length  $\bar{L}_e \equiv \phi^{-1} \bar{R}^{-2}$ , which characterizes the mean distance between tube–tube collisions along a tube backbone, follow from a straightforward calculation as

$$\bar{R} = 2^{-3/4} L_p^{-1/8} \bar{\phi}^{-3/8} \quad \text{and} \quad \bar{L}_e = 2^{3/2} L_p^{1/4} \bar{\phi}^{-1/4}, \tag{10}$$

respectively. It was proposed by Morse [43] that the mean tube strength  $\bar{\phi}$  can be determined self-consistently within the BCA as an average over all possible polymer–polymer configurations. The strategy is to describe the steric interaction of two colliding chains in the solution as a function of the size of the tube each chain is confined to. The calculation is eventually closed by identifying the average of the so obtained pair interaction as the mean-field tube potential. More precisely, the collision geometry of the two polymer segments that fluctuate around their straight primitive paths is described in terms of their relative orientation and separation  $x$  (i.e., their closest approach). The strength  $\phi_{\pm}(x)$  of the harmonic confinement potential is obtained as the second-order Taylor coefficient of the potential of mean force  $F_{\pm}(x)$  (“BCA potential”),  $\phi_{\pm}(x) \propto \partial_x^2 F_{\pm}(x)$ . The latter is of pure entropic origin and given as the negative logarithm of the partition sum of a pair of polymers, each dressed by its own tube, in either a topologically open (subscript “+”) or entangled (“−”) configuration. (See also the sketch in Figure 2 of Reference [44].) This differentiation is necessary, because the number of states for two bendable polymers is not completely determined by the positions and orientations of their primitive paths, as it would be the case for straight rigid rods [48]. From the average over all colliding segment pairs one obtains the relation  $\bar{\phi} = \alpha_0 \rho / \bar{R}$  that links  $\bar{\phi}$  to the polymer contour-length concentration  $\rho$  and the mean tube radius  $\bar{R}$ . Together with Equation (10), this procedure yields the self-consistent BCA solutions

$$\bar{R} = (4\alpha_0 \rho)^{-3/5} L_p^{-1/5} \quad \text{and} \quad \bar{L}_e = (\alpha_0 \rho / 8)^{-2/5} L_p^{1/5} \tag{11}$$

of the mean tube radius and the entanglement length, respectively, with a numerical coefficient  $\alpha_0 \approx 0.50$  [44].

In Reference [44,48], the above theory for an average tube was generalized to the so-called segment-fluid approximation that gives access to the distribution  $P(\phi)$  of tube strengths, which can vary along the test chain. Its predicted statistics of tube-radius fluctuations was found to be in good agreement with experimental data, allowing for a decent global fit for various actin concentrations. The central idea behind the segment-fluid model is to introduce a canonical ensemble of  $N + 1$  independent entanglement segments of length  $L$ , each dressed by an individual tube associated with its own value of  $\phi$ . The segment-averaged mean field  $\bar{\phi}$  felt by the test polymer as a whole, is thus obtained as an average over the  $N$  collision partners. In general, any higher order moment  $\bar{\phi}^k$  can be computed similarly, to estimate the complete tube-strength distribution  $P(\phi)$ . Glaser et al. [44,48] showed that the distribution  $P(\phi)$  can be approximated to very good accuracy by a Gamma distribution with mean  $\bar{\phi} = \alpha_0 \rho / \bar{R}$  and variance  $\bar{\phi}^2 - \bar{\phi}^2 = \beta_0 \rho / (L \bar{R}^3)$ , where  $\beta_0 \approx 0.094$ . Within the tube-segment approach, the relation between network-averaged tube width and tube strength, given by Equation (10), is replaced by a similar relation for the fluctuating quantities  $R$

and  $\phi$ , which allows to convert  $P(\phi)$  directly into the tube-width distribution  $P(R)$ . Rescaling the tube radius by its mean, a concentration-independent scaling form of the distribution [44]

$$p(r) = \bar{R}P(r\bar{R}) \propto r^{-19.1}e^{-6.11r^{-8/3}} \tag{12}$$

ensues. Here, the magnitude  $\bar{r}^2 = \bar{R}^2/\bar{R}^2$  of the fluctuations is completely determined by the value of the combination  $(L/L_e)\alpha_0/\beta_0$ , and the scaled length  $L/L_e \approx 1.3$  of the tube segment is obtained by comparing  $\bar{r}^2$  with a corresponding fluctuation-response estimate, which is derived for a polymer exposed to an external force that is self-consistently identified with the confinement force. The latter calculation reveals that  $L/L_e$  itself depends only on the ratio  $\alpha_0/\beta_0$ . Following the same lines that lead to the tube-width distribution, we can use the local version of Equation (10) to derive the distribution  $P(L_e)$  of the entanglement length from  $P(\phi)$ . Again, one obtains that the reduced distribution  $p(l_e) = \bar{L}_eP(l_e\bar{L}_e)$  depends only on the value of  $(L/L_e)\alpha_0/\beta_0$  and takes the universal form

$$p(l_e) \propto l_e^{-28.0}e^{-6.14l_e^{-4}}. \tag{13}$$

We now extend the BCA to nematically ordered polymer solutions, characterized by the standard order parameter as defined in Equation (1). Repeating the calculations outlined in Reference [44] with this generalized orientational segment distribution, we find that the mean  $\bar{\phi}$  and the variance  $\bar{\phi}^2 - \bar{\phi}^2$  of the tube strength take the same form as their isotropic-solution analogs, given in the text above Equation (12), but now with the functions

$$\alpha(S) = \alpha_0I(S) \quad \text{and} \quad \beta(S) = \beta_0I(S), \tag{14}$$

that replace the numerical coefficients  $\alpha_0$  and  $\beta_0$ , respectively, which yields the expressions for the mean tube radius and the mean entanglement length given in Equation (2). Here,

$$I(S) = (4/\pi) \int d\mathbf{u}_1 d\mathbf{u}_2 f_S(\mathbf{u}_1)f_S(\mathbf{u}_2)|\mathbf{u}_1 \times \mathbf{u}_2| \tag{15}$$

denotes the normalized packing entropy of the solution. For low nematic order,  $S \ll 1$ , the distribution  $f_S(\mathbf{u})$  can be expanded up to linear order in  $S$ , for which the asymptotic proportionality  $I(S) - 1 \propto S^2 + \mathcal{O}(S^3)$  follows from the normalization of  $f_S(\mathbf{u})$  and the definition of  $S$ . It reveals that  $I(S)$ , and thus  $\bar{R}(S)$ , varies only weakly with  $S$ , as long as the solution is not too strongly ordered. To make these dependencies more quantitative, we have to specify the distribution function  $f_S(\mathbf{u})$ . Since we expect its exact functional form not to be crucial, we choose Onsager’s trial function  $f_a(\theta) = a \cosh(a \cos \theta)/(4\pi \sinh a)$  that was originally applied to solutions of rigid rods [45] and covers the wanted generic features of the distributions. Here,  $a$  is related to the order parameter via  $S = 1 - 3a^{-1} \coth a + 3a^{-2}$ , and  $\theta = \cos^{-1}(\mathbf{u} \cdot \mathbf{d})$  is the angle between the direction of the tube segment and the nematic axis. As shown by Onsager, this trial function yields  $I(S) = 2 I_2(2a)/\sinh^2 a$ , where  $I_2$  denotes the modified Bessel function of the first kind. Replacing  $\alpha_0$  in Equation (11) by its order-dependent extension  $\alpha(S)$ , Equation (14), we obtain Equation (2) for the mean tube radius and entanglement length of the nematically ordered system, where the weak-order asymptotics in Equation (2) follow from  $S \sim a^2/15$  together with  $I(S) \sim 1 - a^4/360$ .

#### 4.4. Affine Strain Alignment

To estimate the tube-segment orientation in a sheared solution, we consider a solution of straight inflexible (phantom) rods that follow an externally applied shear strain  $\gamma$  affinely. We describe



the latter in terms of the deformation matrix  $\Lambda_\gamma$ , so that the initial distribution  $f_0(\mathbf{u})$  of the rod orientations  $\mathbf{u}$  is changed to

$$f_\gamma(\mathbf{u}) = \left| \frac{d\mathbf{u}_\gamma}{d\mathbf{u}} \right|^{-1} f_a[\mathbf{u}_\gamma^{-1}(\mathbf{u})], \quad \text{with } \mathbf{u}_\gamma(\mathbf{u}) = \frac{\Lambda\mathbf{u}}{|\Lambda\mathbf{u}|}, \tag{16}$$

where  $\mathbf{u}_\gamma : S^{d-1} \rightarrow S^{d-1}$ , as well as its inverse  $\mathbf{u}_\gamma^{-1}(\mathbf{u}) = \Lambda^{-1}\mathbf{u}/|\Lambda^{-1}\mathbf{u}|$ , is an automorphism of the sphere of dimension  $d - 1$ . Since the expressions for  $d = 3$  become quite lengthy, we first start with  $d = 2$ , which already illustrates how shearing induces nematic ordering.

#### 4.4.1. Two-Dimensional Solution

In two dimensions, the direction  $\mathbf{u} = (\cos \varphi, \sin \varphi)$  of a rod in the solution depends only on the angle  $\varphi$  between  $\mathbf{u}$  and the  $x$ -axis. Applying the simple shear deformation

$$\Lambda = \begin{pmatrix} 1 & 0 \\ \gamma & 1 \end{pmatrix} \tag{17}$$

of strain  $\gamma$ , the particle orientation becomes  $\mathbf{u}_\gamma = (\cos \varphi_\gamma, \sin \varphi_\gamma)$  with

$$\varphi_\gamma = \arctan \left( \frac{\gamma \cos \varphi + \sin \varphi}{\cos \varphi} \right) \tag{18}$$

If we assume the system to be isotropic before the deformation,  $f_0(\varphi) = 1/(2\pi)$ , we obtain a shear-induced dependence

$$f_\gamma(\varphi) = \frac{1}{2\pi} \left| \frac{d\varphi_\gamma}{d\varphi} \right| = \frac{1}{2\pi} \frac{\sec^2 \varphi}{1 + (\gamma - \tan \varphi)^2} \tag{19}$$

of the angular distribution function on  $\varphi$ . As  $\gamma$  increases,  $f_\gamma(\varphi)$  turns into a double-peaked distribution for the ordered system, as illustrated in Figure 1b. The nematic order parameter  $S(\gamma) = 2\lambda_1 - 1$ , associated to the distribution  $f_\gamma$ , is determined by the largest eigenvalue  $\lambda_1$  of the second-rank ordering tensor

$$\int d\varphi f_\gamma(\varphi) \mathbf{u}\mathbf{u} = \frac{1}{4 + \gamma^2} \begin{pmatrix} 2 & \gamma \\ \gamma & 2 + \gamma^2 \end{pmatrix}, \tag{20}$$

which yields

$$S(\gamma) = \frac{\gamma}{\sqrt{4 + \gamma^2}}, \tag{21}$$

shown in Figure 1a. The corresponding eigenvector gives the director

$$\mathbf{d}(\gamma) \propto \begin{pmatrix} \sqrt{4 + \gamma^2} - \gamma \\ 2 \end{pmatrix} \tag{22}$$

(or nematic axis) of the nematic solution.

#### 4.4.2. Three-Dimensional Solution

Simple shear of the form

$$\Lambda = \begin{pmatrix} 1 & 0 & 0 \\ 0 & 1 & 0 \\ \gamma & 0 & 1 \end{pmatrix} \tag{23}$$

leaves the azimuthal angle  $\varphi_\gamma = \varphi$  at its initial value and changes the polar angle as

$$\theta_\gamma = \arccos \left( \frac{\cos \theta + \gamma \cos \varphi \sin \theta}{\sqrt{\sin^2 \theta + (\cos \theta + \gamma \cos \varphi \sin \theta)^2}} \right). \tag{24}$$

This leads to the strain-dependent angular distribution

$$\begin{aligned} f_\gamma(\varphi, \theta) \sin \theta &= \frac{1}{4\pi} \left| \frac{\partial(\varphi_{-\gamma}, \theta_{-\gamma})}{\partial(\varphi, \theta)} \right| \sin \theta_{-\gamma} \\ &= \frac{2 \sin \theta}{\pi} \left[ 4 + \gamma^2 - \gamma^2 \cos(2\theta) - 2\gamma^2 \cos(2\varphi) \sin^2 \theta + 4\gamma \cos \varphi \sin^2(2\theta) \right]^{-3/2} \end{aligned} \tag{25}$$

of an initially isotropic three-dimensional solution,  $f_0 = 1/(4\pi)$ . Note that  $f_\gamma(\mathbf{u})$  is not axially symmetric with respect to the director  $\mathbf{d}$ , but is characterized by biaxial order, which is typically quantified in terms of the second-rank ordering tensor. For our purpose, however, it suffices to estimate the degree of shear-induced alignment by the scalar order parameter  $S$  as follows. For given strain  $\gamma$ , it exhibits a maximum at  $\{\varphi_\gamma^*, \theta_\gamma^*\}$  with  $\varphi_\gamma^* = 0$  and

$$\theta_\gamma^* = \arctan \left( \frac{1}{2} \sqrt{4 + \gamma^2} - \frac{\gamma}{2} \right), \tag{26}$$

thus determining to the director  $\mathbf{d}(\gamma) = (\sin \theta_\gamma^*, 0, \cos \theta_\gamma^*)$ , which exactly corresponds to Equation (22) for the director of the sheared two-dimensional solution. As the distribution  $f_\gamma(\varphi, \theta)$  is not rotationally symmetric with respect to  $\mathbf{d}(\gamma)$ , an analytical expression for  $S(\gamma)$  cannot be derived. For small deformations, however, one obtains

$$\int d\varphi f_\gamma(\varphi) \mathbf{u}\mathbf{u} \sim \frac{1}{3} \mathbb{1} + \frac{\gamma}{5} (\mathbf{e}_1 \mathbf{e}_3 + \mathbf{e}_3 \mathbf{e}_1) \tag{27}$$

to linear order in  $\gamma$ , where  $\mathbf{e}_1$  and  $\mathbf{e}_3$  denote the unit vectors parallel to the  $x$  and  $z$  axis, respectively. From its largest eigenvalue  $\lambda_1 = 1/3 + \gamma/5$  we obtain the linear scaling relation for  $S(\gamma) = (1/2)(3\lambda - 1)$ , given in Equation (3). In Figure 1, this asymptotic relation is compared with the numerically obtained  $S(\gamma)$ , which reveals that it provides a good approximation up to  $\gamma \approx 1$ .

#### 4.5. Unit-Cell Approach

The non-affine tube deformation caused by a macroscopically imposed simple shear deformation is estimated using the unit-cell approach by Fernández et al. [21]. Namely, we minimize the free energy of a test tube clamped between two neighbor tubes that change their positions affinely with the applied strain  $\gamma$ , thereby exerting a force on the test tube, which bends accordingly. To treat large polymer deformations exactly, the polymer segment is modeled as an Euler-Bernoulli beam. Then, the tube backbone contour is obtained for strains  $\gamma$  up to  $\approx 2$  by solving the equation of elastica with forces acting on the collision points between the test tube and its confining neighbors. Assuming that the deformation happens in a quasi-static fashion, lateral friction is neglected and the test polymer remains equilibrated in its tube. The value of the constraining forces is determined by minimizing the test tube’s free energy comprising bending and confinement contributions. Following Reference [21], Figure 6 illustrates the “test tube” of the unit-cell model clamped between two neighboring tubes. Affine shearing of the polymer solution translates to an affine displacement of the confining tubes (whether the centers or contact points with the test tube are displaced does not matter much). Due to the mutual balance of enthalpic (backbone bending) and entropic (tube size) contributions to the free energy, shearing induces a strongly non-affine local polymer deformation, in this model. Averaging over a representative set of shear geometries, the deformation results in a



dilation of the tube upon shear, which gives rise to a nonlinear softening at large strains, for a broad range of polymer concentrations and initial (equilibrium) tube conformations.

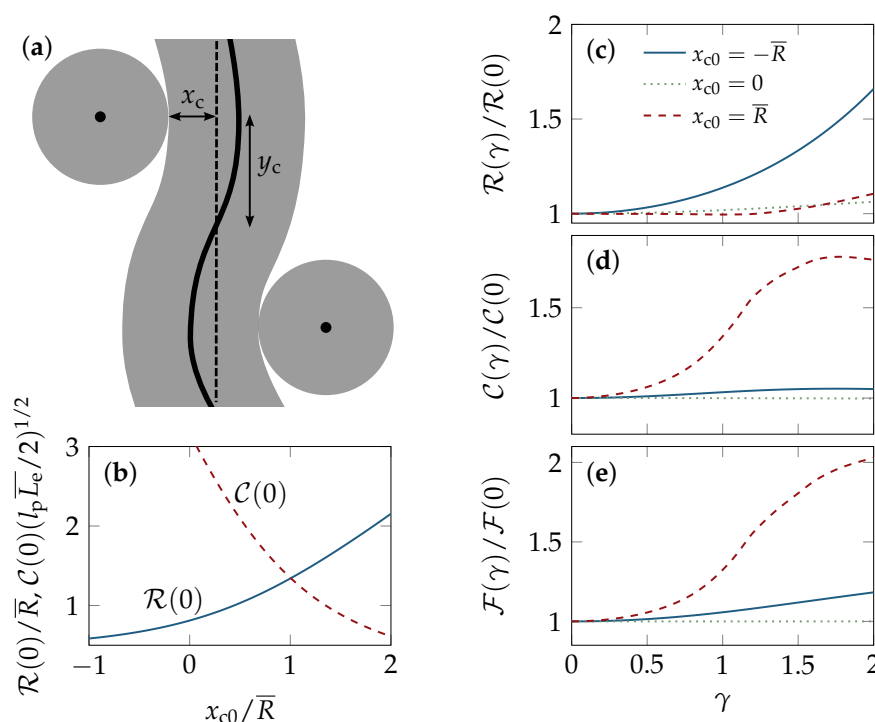


**Figure 6.** Unit-cell model by Fernández et al. [21]. (a) The test tube is deformed by two confining tubes (Sketch adapted from Reference [21]); (b) The zero-strain values of the average tube radius  $\bar{\mathcal{R}}(\gamma = 0)$  and the mean curvature  $\bar{\mathcal{C}}(\gamma = 0)$  varies with the unit-cell conformation, which is characterized by the deflection  $x_{c0}$ . Shearing of the network is mimicked by an affine displacement of the contact points with (or centers of) the confining tubes. There is a trade-off between bending and confinement, since a more strongly bent conformation allows for a wider tube, which, on average, gives rise to a strain-induced tube dilation and bending, quantified by (c) the average tube radius  $\bar{\mathcal{R}}(\gamma)$  and (d) the mean curvature  $\bar{\mathcal{C}}(\gamma)$  with strain  $\gamma$ ; (e) The total free energy  $\mathcal{F}(\gamma)$  increases upon shearing as required by mechanical stability. All curves were computed numerically from the full non-linear theory.

For moderate shear deformations, the model equations can be linearized and solved analytically. Starting point is the deflection  $x_c + \mathcal{R}$  of the tube backbone due to the force  $f$  between the colliding tubes, as given by Equation (9a) of Reference [21]. For small  $y_c^2 f / L_p$ , where  $2y_c$  is the distance between the tube–tube collisions along the backbone (see the sketch in Figure 6), the deflection becomes  $x_c + \mathcal{R} \sim y_c^3 f / (3L_p)$ , which serves as a relation for the modified tube radius  $\mathcal{R}$ . Note that positive deflections  $x_c > 0$  correspond to hairpin conformations. This yields the total free energy as the sum

$$\mathcal{F} \sim y_c^3 f^2 / (6L_p) + L_p^{-1/3} y_c [(2/3) y_c^3 f / L_p - 2x_c]^{-2/3} \tag{28}$$

of the linearized bending free energy, i.e., expanded to lowest order in  $f$ , and the confinement free energy. Within the linearized theory, the lateral deflection  $x_c + \mathcal{R} \sim y_c^3 f / (3L_p)$  is varied to minimize  $\mathcal{F}$ , so that the tube-deforming force  $f$  is determined by the equilibrium condition  $\partial_f \mathcal{F} = 0$ . If the backbone is only weakly bent,  $y_c^3 f / (L_p |x_c|) \ll 1$ , this condition can be expanded to

$$\frac{10y_c^3 f}{9L_p |x_c|} \sim -1 + \sqrt{1 + (10/27)(4\bar{\mathcal{R}}/|x_c|)^{8/3}}. \tag{29}$$

Inserted into the expression for the tube radius, we obtain its strain dependence  $R(\gamma)/R(0) \sim 1 + b_R \gamma^2$ , Equation (5), with the zero-strain value

$$\overline{R}(\gamma = 0)/|x_{c0}| \sim \frac{7}{10} + \frac{3}{10} \sqrt{1 + (10/27)(4\overline{R}/|x_{c0}|)^{8/3}}, \tag{30}$$

where  $x_{c0}$  and  $y_{c0}$  denote the collision coordinates for the unsheared solution. Following Reference [21], we here set  $y_{c0} = \overline{L}_e/2$  and used that  $\overline{L}_e = 4L_p^{1/3}\overline{R}^{2/3}$ , according to Equation (10). Besides the width of the tube, we characterize its conformation in terms of the mean curvature  $\overline{C}$ , defined through the average

$$\overline{C}^2 \equiv \frac{1}{2y_c} \int_0^{y_c} ds [\mathbf{r}''(s)]^2 \tag{31}$$

along the backbone contour  $\mathbf{r}(s)$  of the tube segment. Note that  $y_c L_p \overline{C}^2$  is nothing but the bending energy of the tube segment (in natural units) as it appears in the unit-cell model. With the weak-force scaling of Equation (29), a similar calculation as for  $\overline{R}(\gamma)$  yields the asymptotic scaling  $\overline{C}(\gamma)/C(0) \sim 1 + b_C \gamma^2$ , Equation (6), with

$$\overline{C}(\gamma = 0) \sim \frac{9|x_{c0}|/\overline{R}}{20\sqrt{6L_p\overline{L}_e}} \left[ -1 + \sqrt{1 + (10/27)(4\overline{R}/|x_{c0}|)^{8/3}} \right]. \tag{32}$$

Comparing the asymptotic scaling relations with the numerically solved full model, we find the quadratic strain dependencies in Equations (5) and (6) to be in good agreement with the full model. However, as the above weak-force criterion does not hold for typical model parameters, the zero-strain values  $\overline{R}(\gamma = 0)$  and  $\overline{C}(\gamma = 0)$  and the coefficients  $b_R$  and  $b_C$  obtained from the full model can deviate substantially from their asymptotic estimates given here. Their dependence on the ratio  $x_{c0}/\overline{R}$  between the unperturbed tube deflection and the width of a straight equilibrium tube is shown in Figure 6. With  $x_{c0} = -\overline{R}$ , for instance, we have  $y_c^3 f/(L_p|x_{c0}|) \approx 2$  and, consequently, the asymptotic solutions  $\overline{R}(\gamma = 0) \sim 1.9\overline{R}$  and  $\overline{C}(\gamma = 0) \sim 0.39(L_p\overline{L}_e/2)^{-1/2}$  of the linear model markedly differ from the numerically obtained predictions  $\overline{R}(\gamma = 0) \approx 1.3\overline{R}$  and  $\overline{C}(\gamma = 0) \approx 1.4(L_p\overline{L}_e/2)^{-1/2}$  of the full model, see Figure 6b. Notably,  $b_C$  can actually become negative as illustrated in Figure 6d.

We note that we quantify the geometry of the straight tube by means of the BCA predictions for  $\overline{R}$  and  $\overline{L}_e$ , given in Equation (11), whereas the entanglement length in Reference [21] was defined as  $\overline{L}_e = (L_p/\overline{\phi})^{1/4}$ , which differs from Equation (10) by the numerical prefactor  $2^{3/2}$ . The slightly larger values for  $\overline{L}_e$  and  $y_{c0}$  used here have consequences for both the geometry and stability of the ground state of the unit cell, as described so far, which predicts an instability against shearing when the aspect ratio  $|x_{c0}|/y_{c0}$ , or, equivalently, the ratio  $|x_{c0}|/\overline{R}$ , exceeds a certain threshold value. In this regime the total model free energy decreases upon straining, as the test tube is widened to an unrealistically large volume that violates the constraint set by the imposed polymer concentration. As shown in Reference [21], this artifact of the simplified unit-cell geometry can be cured by accounting for the so-called ‘‘Doi–Kuzuu effect’’ [55], which relates the number of contacts between the tubes to the applied deformation. Upon large deformations, the test tube makes new lateral contacts with previously spatially separated tubes, which limits the lateral expansion to physically reasonable bounds and can effectively be accounted for by a renormalization of the unit cell parameters as a function of the strain. With this important amendment, the ground state is always stable and robust to moderate parameter changes. The resulting strain-dependent tube radius, curvature, and (clearly stable) total free energy are depicted in Figure 6, using typical values  $L_p = 17 \mu\text{m}$  and  $\rho = 20 \mu\text{m}^{-2}$  for the persistence length and the polymer length concentration, respectively, in Equation (11). The latter correspond to semi-dilute F-actin solutions of concentration  $c = 0.5 \text{ mg/mL}$ , based on the estimate  $\rho/c \approx 40 \mu\text{m}^{-2}/(\text{mg/mL})$  obtained from the molecular structure of the actin filaments [43].

It is worth noting that the Doi-Kuzuu effect affects so-called hairpin configurations (thermodynamically suppressed strongly contorted unit cell configurations [20,21]) differently from the typical configurations. We keep track of this by the factor  $-x_c/|x_c|$  in the second term of the differential equation

$$y_c'(\gamma) = y_{c0}\lambda_y'(\gamma) - 4(x_c/|x_c|)(y_c^2R/\xi^2)\lambda_x'(\gamma) - 4(y_c^2/\xi^2)R'(\gamma) \tag{33}$$

that determines the longitudinal deformation of the unit cell (Equation (18) of Reference [21]). The first term on the right hand side represents the affine stretch by a factor  $\lambda_y(\gamma)$ , the last term corrects for the volume change of the unit-cell due to tube dilation/contraction. The second term accounts for the transversely approaching/distancing of the tube segments that follow the stretch factor  $\lambda_x(\gamma)$ , which effectively decreases/increases the distance  $2y_c$  between the collision points. For a hairpin configuration, characterized by  $x_c > 0$ , neighboring tubes are pushed aside, corresponding to an increasing  $y_c$ . It should also be noted that, apart from this topological distinction, the correction is of mean-field type. This restriction could tend to iron out a physically meaningful heterogeneous response of the polymer (tube) network. Beyond the mean-field approximation, unstable unit-cells might still exist locally and give rise to spontaneous network heterogeneities (without invoking any enthalpic attractions or crosslinkers). In a stationary shear flow, these might play an important role for the nucleation of shear bands, a phenomenon that is known to occur in densely entangled solutions of flexible polymers [56] and that was recently observed for entangled F-actin solutions [16]. It would be interesting to see, whether such effects could be grasped with the theory by pushing the treatment of the Doi-Kuzuu effect beyond the mean-field approximation.

Finally, we estimate the non-affine contributions to the nematic order parameter  $S$ , within the unit-cell approach. Unfortunately, finding the exact deformation field from the complex response of the tube backbone is not a straightforward task. To simplify the computation, we therefore follow Reference [21] and consider only a discrete set of test-tube segments with orientations along the three main stretch directions or principal axes of the simple shear deformation. Under the assumption that the average tube deformation can be described by a deformation tensor  $\Lambda_\gamma = \Lambda_\gamma^a + \Lambda_\gamma^n$  that we decompose into its affine and non-affine contribution, respectively, we can approximately reconstruct the non-affine contribution  $\Lambda_\gamma^n$  from the three principle shear transformations. We first relate these transformations for the stretching and compression along the principal axes of the affine deformation with the lab-frame coordinates. We denote these principal directions (i.e., the normalized eigenvectors of the affine Cauchy deformation tensor  $(\Lambda_\gamma^a)^T\Lambda_\gamma^a$ ) by  $\mathbf{v}_i$ , and the corresponding stretch factors (the eigenvalues) by  $\lambda_i$ . The index convention is that  $i = 1, 2, 3$  represent the stretch, compression, and neutral axis, respectively. Note that  $\mathbf{v}_i$  gives the direction *before* the shear deformation and yields the orientation  $\mathbf{w}_i \equiv \lambda_i^{-1}\Lambda_\gamma^a\mathbf{v}_i$  after an affine deformation  $\Lambda_\gamma^a$  has been applied. For a given point  $\mathbf{r}_0$  in the lab frame, the model now takes its principal-axes coordinates  $\mathbf{v}_i \cdot \mathbf{r}_0$  before the deformation and computes its principal-axes coordinates  $\mathbf{w}_i \cdot \mathbf{r}_\gamma$  at strain  $\gamma$ . With the above introduced decomposition into an affine and a non-affine contribution to the deformation tensor,  $\mathbf{r}_\gamma = (\Lambda_\gamma^a + \Lambda_\gamma^n) \cdot \mathbf{r}_0$ , we obtain

$$\mathbf{w}_i \cdot \mathbf{r}_\gamma = \lambda_i\mathbf{v}_i \cdot \mathbf{r}_0 + \sum_j \mathbf{w}_i \cdot (\Lambda_\gamma^n \cdot \mathbf{v}_j\mathbf{v}_j \cdot \mathbf{r}_0). \tag{34}$$

The unit operator  $\mathbb{1} = \sum_j \mathbf{v}_j\mathbf{v}_j$  was inserted to reintroduce the coordinates  $\mathbf{v}_j \cdot \mathbf{r}_0$ . This equation must be solved for the nine components of  $\Lambda_\gamma^n$ , which is indeed possible if we insert the end-to-end vector of the tube segments for  $\mathbf{r}_0$  and  $\mathbf{r}_\gamma$  and exploit the available information for all three principal axes ( $i = 1, 2, 3$ ). Here, another technical detail of the unit-cell model has to be taken into account: fixing the (unperturbed) tube direction to  $\mathbf{v}_i$  yields two possible unit-cell conformations, depending on the orientation of the trihedron built by the three principal axes. We average over these two geometries to obtain the mean change of the tube segment orientation that we can

use in Equation (34). With the full deformation tensor  $\Lambda_\gamma = \Lambda_\gamma^a + \Lambda_\gamma^n$  at hand, the non-affine strain dependence  $S(\gamma)$  of the nematic order parameter is readily computed by applying the same procedure as in Section 4.4 for the purely affine deformation. Combining  $S(\gamma)$  and  $\overline{\mathcal{R}}(\gamma)$  predicted by the unit-cell approach, we eventually obtain the order-dependent mean tube radius  $\overline{\mathcal{R}}(S)$  that is shown in Figure 1.

**Acknowledgments:** We thank David Morse for kindly providing us with the source code of the computer simulations. We thank Roland Springer and Georg Dreissen for help with digital image processing and Bernd Hoffmann, Erik Noetzel, Nils Hersch, and Lukas Bethlehem (all ICS-7) for actin purification. We acknowledge support from the German Research Foundation (DFG) and Universität Leipzig within the program of Open Access Publishing.

**Author Contributions:** Marc Lämmel and Klaus Kroy developed the theory; Marc Lämmel extended and analyzed the simulations; Evelin Jaschinski and Rudolf Merkel conceived and designed the experiments; Evelin Jaschinski performed the experiments; Evelin Jaschinski and Marc Lämmel analyzed the data.

**Conflicts of Interest:** The authors declare no conflict of interest.

## Abbreviations

The following abbreviations are used in this manuscript:

WLC	Wormlike chain
BCA	Binary collision approximation
MC/BD	Monte Carlo/Brownian dynamics

## References

1. Kollmannsberger, P.; Fabry, B. Linear and nonlinear rheology of living cells. *Annu. Rev. Mater. Res.* **2011**, *41*, 75–97.
2. Pritchard, R.H.; Shery Huang, Y.Y.; Terentjev, E.M. Mechanics of biological networks: From the cell cytoskeleton to connective tissue. *Soft Matter* **2014**, *10*, 1864–1884.
3. Bausch, A.R.; Kroy, K. A bottom-up approach to cell mechanics. *Nat. Phys.* **2006**, *2*, 231–238.
4. Storm, C.; Pastore, J.J.; MacKintosh, F.C.; Lubensky, T.C.; Janmey, P.A. Nonlinear elasticity in biological gels. *Nature* **2005**, *435*, 191–194.
5. Janmey, P.A.; McCulloch, C.A. Cell mechanics: Integrating cell responses to mechanical stimuli. *Annu. Rev. Biomed. Eng.* **2007**, *9*, 1–34.
6. Kasza, K.E.; Rowat, A.C.; Liu, J.; Angelini, T.E.; Brangwynne, C.P.; Koenderink, G.H.; Weitz, D.A. The cell as a material. *Curr. Opin. Cell Biol.* **2007**, *19*, 101–107.
7. Shin, J.H.; Gardel, M.L.; Mahadevan, L.; Matsudaira, P.; Weitz, D.A. Relating microstructure to rheology of a bundled and cross-linked F-actin network in vitro. *Proc. Natl. Acad. Sci. USA* **2004**, *101*, 9636–9641.
8. Lieleg, O.; Claessens, M.M.A.E.; Bausch, A.R. Structure and dynamics of cross-linked actin networks. *Soft Matter* **2010**, *6*, 218–225.
9. Kurniawan, N.A.; Enemark, S.; Rajagopalan, R. The role of structure in the nonlinear mechanics of cross-linked semiflexible polymer networks. *J. Chem. Phys.* **2012**, *136*, 065101.
10. De Gennes, P.G. *Scaling Concepts in Polymer Physics*; Cornell University Press: Ithaca, NY, USA, 1979.
11. Doi, M.; Edwards, S.F. *The Theory of Polymer Dynamics*; Oxford University: New York, NY, USA, 1988; Volume 73.
12. Pearson, D.; Herbolzheimer, E.; Grizzuti, N.; Marrucci, G. Transient behavior of entangled polymers at high shear rates. *J. Polym. Sci. B Polym. Phys.* **1991**, *29*, 1589–1597.
13. Mhetar, V.; Archer, L. Nonlinear viscoelasticity of entangled polymeric liquids. *J. Nonnewton. Fluid. Mech.* **1999**, *81*, 71–81.
14. Marrucci, G. Dynamics of entanglements: A nonlinear model consistent with the Cox-Merz rule. *J. Nonnewton. Fluid Mech.* **1996**, *62*, 279–289.
15. Graham, R.S.; Likhtman, A.E.; McLeish, T.C.B.; Milner, S.T. Microscopic theory of linear, entangled polymer chains under rapid deformation including chain stretch and convective constraint release. *J. Rheol.* **2003**, *47*, 1171–1200.

16. Kunita, I.; Sato, K.; Tanaka, Y.; Takikawa, Y.; Orihara, H.; Nakagaki, T. Shear banding in an F-Actin solution. *Phys. Rev. Lett.* **2012**, *109*, 248303.
17. Kirchenbuechler, I.; Guu, D.; Kurniawan, N.A.; Koenderink, G.H.; Lettinga, M.P. Direct visualization of flow-induced conformational transitions of single actin filaments in entangled solutions. *Nat. Commun.* **2014**, *5*, 5060.
18. Falzone, T.T.; Blair, S.; Robertson-Anderson, R.M. Entangled F-actin displays a unique crossover to microscale nonlinearity dominated by entanglement segment dynamics. *Soft Matter* **2015**, *11*, 4418–4423.
19. Gurmessa, B.; Fitzpatrick, R.; Falzone, T.T.; Robertson-Anderson, R.M. Entanglement density tunes microscale nonlinear response of entangled Actin. *Macromolecules* **2016**, *49*, 3948–3955.
20. Morse, D.C. Viscoelasticity of Concentrated Isotropic Solutions of Semiflexible Polymers. 3. Nonlinear Rheology. *Macromolecules* **1999**, *32*, 5934–5943.
21. Fernandez, P.; Grosser, S.; Kroy, K. A unit-cell approach to the nonlinear rheology of biopolymer solutions. *Soft Matter* **2009**, *5*, 2047–2056.
22. Morse, D.C. Viscoelasticity of tightly entangled solutions of semiflexible polymers. *Phys. Rev. E* **1998**, *58*, R1237–R1240.
23. Semmrich, C.; Storz, T.; Glaser, J.; Merkel, R.; Bausch, A.R.; Kroy, K. Glass transition and rheological redundancy in F-actin solutions. *Proc. Natl. Acad. Sci. USA* **2007**, *104*, 20199–20203.
24. Xu, J.; Tseng, Y.; Wirtz, D. Strain hardening of actin filament networks: Regulation by the dynamic cross-linking protein  $\alpha$ -actinin. *J. Biol. Chem.* **2000**, *275*, 35886–35892.
25. Semmrich, C.; Larsen, R.J.; Bausch, A.R. Nonlinear mechanics of entangled F-actin solutions. *Soft Matter* **2008**, *4*, 1675–1680.
26. Broedersz, C.P.; MacKintosh, F.C. Modeling semiflexible polymer networks. *Rev. Mod. Phys.* **2014**, *86*, 995–1036.
27. Thorpe, M. Continuous deformations in random networks. *J. Non-Cryst. Solids* **1983**, *57*, 355–370.
28. Heussinger, C.; Frey, E. Floppy modes and nonaffine deformations in random fiber networks. *Phys. Rev. Lett.* **2006**, *97*, 105501.
29. Wyart, M.; Liang, H.; Kabla, A.; Mahadevan, L. Elasticity of floppy and stiff random networks. *Phys. Rev. Lett.* **2008**, *101*, 215501.
30. Sharma, A.; Licup, A.J.; Jansen, K.A.; Rens, R.; Sheinman, M.; Koenderink, G.H.; MacKintosh, F.C. Strain-controlled criticality governs the nonlinear mechanics of fibre networks. *Nat. Phys.* **2016**, *12*, 584–587.
31. Huisman, E.M.; Storm, C.; Barkema, G.T. Frequency-dependent stiffening of semiflexible networks: A dynamical nonaffine to affine transition. *Phys. Rev. E* **2010**, *82*, 061902.
32. Kang, H.; Wen, Q.; Janmey, P.A.; Tang, J.X.; Conti, E.; MacKintosh, F.C. Nonlinear elasticity of stiff filament networks: Strain stiffening, negative normal stress, and filament alignment in fibrin gels. *J. Phys. Chem. B* **2009**, *113*, 3799–3805.
33. Vader, D.; Kabla, A.; Weitz, D.; Mahadevan, L. Strain-induced alignment in collagen gels. *PLoS ONE* **2009**, *4*, 1–12.
34. Harasim, M.; Wunderlich, B.; Peleg, O.; Kröger, M.; Bausch, A.R. Direct observation of the dynamics of semiflexible polymers in shear flow. *Phys. Rev. Lett.* **2013**, *110*, 108302.
35. Huber, B.; Harasim, M.; Wunderlich, B.; Kröger, M.; Bausch, A.R. Microscopic origin of the non-newtonian viscosity of Semiflexible polymer solutions in the semidilute regime. *ACS Macro Lett.* **2014**, *3*, 136–140.
36. Sussman, D.M.; Schweizer, K.S. Microscopic theory of topologically entangled fluids of rigid macromolecules. *Phys. Rev. E* **2011**, *83*, 061501.
37. Lang, P.S.; Obermayer, B.; Frey, E. Dynamics of a semiflexible polymer or polymer ring in shear flow. *Phys. Rev. E* **2014**, *89*, 022606.
38. Feng, J.; Levine, H.; Mao, X.; Sander, L.M. Alignment and nonlinear elasticity in biopolymer gels. *Phys. Rev. E* **2015**, *91*, 042710.
39. Foucard, L.C.; Price, J.K.; Klug, W.S.; Levine, A.J. Cooperative buckling and the nonlinear mechanics of nematic semiflexible networks. *Nonlinearity* **2015**, *28*, R89.
40. Alvarado, J.; Mulder, B.M.; Koenderink, G.H. Alignment of nematic and bundled semiflexible polymers in cell-sized confinement. *Soft Matter* **2014**, *10*, 2354–2364.
41. Münster, S.; Jawerth, L.M.; Leslie, B.A.; Weitz, J.I.; Fabry, B.; Weitz, D.A. Strain history dependence of the nonlinear stress response of fibrin and collagen networks. *Proc. Natl. Acad. Sci. USA* **2013**, *110*, 12197–12202.

42. Morse, D.C. Viscoelasticity of concentrated isotropic solutions of semiflexible polymers. 1. Model and stress tensor. *Macromolecules* **1998**, *31*, 7030–7043.
43. Morse, D.C. Tube diameter in tightly entangled solutions of semiflexible polymers. *Phys. Rev. E* **2001**, *63*, 031502.
44. Glaser, J.; Kroy, K. Tube-width fluctuations of entangled stiff polymers. *Phys. Rev. E* **2011**, *84*, 051801.
45. Onsager, L. The effects of shape on the interaction of colloidal particles. *Ann. N. Y. Acad. Sci.* **1949**, *51*, 627–659.
46. Sussman, D.; Schweizer, K. Microscopic theory of the tube confinement potential for liquids of topologically entangled rigid macromolecules. *Phys. Rev. Lett.* **2011**, *107*, 1–4.
47. Szamel, G. Reptation as a dynamic mean-field theory: Study of a simple model of rodlike polymers. *Phys. Rev. Lett.* **1993**, *70*, 3744–3747.
48. Glaser, J.; Chakraborty, D.; Kroy, K.; Lauter, I.; Degawa, M.; Kirchgeßner, N.; Hoffmann, B.; Merkel, R.; Giesen, M. Tube width fluctuations in F-Actin solutions. *Phys. Rev. Lett.* **2010**, *105*, 037801.
49. Odijk, T. The statistics and dynamics of confined or entangled stiff polymers. *Macromolecules* **1983**, *16*, 1340–1344.
50. Schöbl, S.; Sturm, S.; Janke, W.; Kroy, K. Persistence-length renormalization of polymers in a crowded environment of hard disks. *Phys. Rev. Lett.* **2014**, *113*, 238302.
51. Ramanathan, S. Study of Dynamics and Viscoelasticity in Entangled Solutions of Semiflexible Polymers by Brownian Dynamics Simulations. Ph.D. Thesis, University of Minnesota, Minneapolis, MN, USA, 2006.
52. Ramanathan, S.; Morse, D.C. Simulations of dynamics and viscoelasticity in highly entangled solutions of semiflexible rods. *Phys. Rev. E* **2007**, *76*, 010501.
53. Ramanathan, S.; Morse, D.C. Brownian dynamics algorithm for entangled wormlike threads. *J. Chem. Phys.* **2007**, *126*, 094906.
54. Romanowska, M.; Hinsch, H.; Kirchgeßner, N.; Giesen, M.; Degawa, M.; Hoffmann, B.; Frey, E.; Merkel, R. Direct observation of the tube model in F-actin solutions: Tube dimensions and curvatures. *Europhys. Lett.* **2009**, *86*, 26003.
55. Doi, M.; Kuzuu, N.Y. Nonlinear elasticity of rodlike macromolecules in condensed state. *J. Polym. Sci. B Polym. Phys.* **1980**, *18*, 409–419.
56. Larson, R.; Desai, P.S. Modeling the rheology of polymer melts and solutions. *Annu. Rev. Fluid Mech.* **2015**, *47*, 47–65.



© 2016 by the authors; licensee MDPI, Basel, Switzerland. This article is an open access article distributed under the terms and conditions of the Creative Commons Attribution (CC-BY) license (<http://creativecommons.org/licenses/by/4.0/>).

## Viscoelastic response

Viscoelasticity is a salient feature of biological matter. It refers to the complex rheological response that exhibits both solid- and fluid-like characteristics, depending on the probed time scale or the applied shear rate: on short times (high frequencies), these systems behave like an elastic solid; on long times (low frequencies), like a viscous fluid. As mentioned in Chap. 6, some characteristics of the viscoelastic response of cells or tissue can be sufficiently reproduced by reduced model systems of tightly entangled stiff polymers [40, 102]. They therefore provide an excellent framework to investigate the mesoscale mechanisms underlying the diverse rheology of the biological materials.

One can build upon the above discussion and extend the analysis of the various relaxation processes at work by their associated characteristic time scales. They are outlined and briefly discussed in Sec. 8.1. Starting point is, once again, the concept of the static confinement tube as described in the previous chapter. As already alluded to there, the limitations of this model become however evident at long times, when the topological entanglements are released, thereby rendering the tube itself dynamic. Some of the theoretical attempts to account for such confinement transients are reviewed in Sec. 8.2. The subsequent Secs. 8.3 and 8.4 address the solutions' viscoelastic linear and nonlinear response, respectively. Based on the surveyed experimental observations and theoretical attempts, we will hypothesize that sticky (or frictional) contacts between the entangled polymers may be responsible for some of the unexpected observations, especially the pronounced rate-dependent softening–stiffening transition [45]. The idea of the sticky contacts suggests an apparent similarity between the purely entangled solutions and (transiently) crosslinked polymer networks. The latter is therefore discussed in Sec. 8.5. In a recently developed model, we combined the concept of a transient confinement tube with the sticky polymer contacts to obtain the viscoelastic response of an entangled stiff-polymer solution. It captures the above mentioned softening–stiffening transition, chiefly, because it distributes the macroscopic deformation among soft bending modes and stiff stretching modes. Although this work is still in progress, I present its actual status in an Appendix to this chapter, in order to document the concrete realization of some of the ideas that are merely sketched in the main text.

## 8.1 Time scales

In the following, we briefly go through the relaxation processes relevant for the biopolymer solutions. On very short times, the dynamics is not influenced by confinement effects, and one regains the free-polymer behavior briefly sketched in Sec. 6.1. On long enough time and length scales, in contrast, the topological entanglements dominate the relaxation processes. The crossover between these two regimes is given by entanglement time [6, 99].

$$t_e = (\zeta_{\perp}/k_B T)L_e^4/L_p. \quad (8.1)$$

It is the equilibration time for the bending modes of a polymer that is confined to a homogeneous tube<sup>1</sup>. Assuming that these short modes have already been equilibrated (*i.e.*, for  $t > t_e$ ), longitudinal deformations relax over times

$$t_L^{\parallel} \approx (\zeta/k_B T)L^2L_e^3/L_p^2 \quad (8.2)$$

as obtained from the diffusion of the contour-length density (stored in the chain undulations) over a length  $L$  (in the stiff-polymer limit) [86]. For tightly entangled solutions with  $L_e L_p \ll L^2$ , the separation  $t_e \ll t_L^{\parallel}$  underlying this estimate is indeed a valid assumption. It however breaks down in the stiff-polymer limit  $L_p/L \rightarrow \infty$ , where  $L_e/L$  remains finite. For this limit, Morse [86] argued that the longitudinal relaxation time is given by the time needed for the tension to propagate along the whole polymer, which he approximated as  $(\zeta/k_B T)L^8/L_p^5$ . This estimate, however, neglects the influence of hydrodynamic (longitudinal) friction [48, 79], which in fact can have a significant impact on the dynamic single-polymer response: in order for a steplike stretch deformation of the polymer to relax, the outer parts of the polymer are pulled towards its center through the viscous solvent [79]. The characteristic time needed for the tension to relax to zero across the whole filament, which is confined to a harmonic tube potential (see Sec. 7.2), was estimated by Thüroff *et al.* [103] as

$$t_{\text{tens}} \approx (\zeta/k_B T)L^4L_e^2/(2L_p^3). \quad (8.3)$$

Due to the confinement, only modes up to wavelength  $L_e$  equilibrate after such a release event, which makes this relaxation time in entangled solutions shorter than for a free polymer [48, 49]. At times beyond  $t_{\text{tens}}$ , longitudinal friction becomes negligible, and the dynamics is determined by the transverse confinement due to topological entanglements.

In the classical reptation model, where the confinement tube is assumed to remain invariant at all probed time scales, changing the filaments' orientations requires them to leave their tubes. With a typical time scale on the order of the time a filament needs to reptate (*i.e.*, diffuse longitudinally) its own contour length, such tube disengagement is the slowest relaxation process of the entangled polymer solutions. Applying the Sutherland-Einstein relation to the reptation diffusivity [50], this time is estimated as

$$t_{\text{rep}} = (\zeta/k_B T)L^3. \quad (8.4)$$

<sup>1</sup>For the (static) tube model, with Hamiltonian given in Eq. (7.3), the Langevin dynamics of a WBR becomes

$$\zeta_{\perp} \partial_t \mathbf{r}_{\perp}(s, t) = -\kappa \partial_s^4 \mathbf{r}_{\perp}(s, t) - \phi \mathbf{r}_{\perp} + \xi_{\perp}(s, t),$$

from which one readily obtains  $\text{MSD}_{\perp} \propto (L_e^3/\ell_p)[1 - \Gamma(3/4, t/t_e)/\Gamma(3/4)]$  with  $L_e = (\kappa/\phi)^{1/4}$  and Eq. (8.1) for  $t_e$ .



If  $L_p < L$ , the filament orientation can relax quicker, because reptating a distance  $L/2$  already changes the orientation of the filament center according to the tangent–tangent correlation  $\langle \mathbf{r}'(L/2) \cdot \mathbf{r}'(0) \rangle \approx 1 - L/2L_p$ , see Eq. (6.4). This corresponds to a variation  $\langle \Delta\theta^2 \rangle \approx L/L_p$  of the angle  $\Delta\theta$  between the tangents before and after the reptation step of length  $L/2$ . The filament orientation is thus randomized after a time  $t_{\text{rot}}$  (*i.e.*, after  $t_{\text{rot}}/t_{\text{rep}}$  reptation steps), when  $\langle \Delta\theta^2 \rangle t_{\text{rot}}/t_{\text{rep}} \approx 1$ , hence [41]

$$t_{\text{rot}} \approx (\zeta/k_B T) L^2 L_p. \quad (8.5)$$

This scaling was confirmed by experiments with carbon nanotubes diffusing in porous agarose networks [104] and by recent Brownian dynamics simulations of polymer solutions in the loosely entangled stiff-chain limit [90]. For semidilute entangled solutions of semiflexible polymers, Lang and Frey [90] however found that the polymer orientation can relax even faster via releasing topological constraints, a mechanism that is neglected in the traditional reptation model. (Also for entangled solutions of flexible polymers, such constraint-release events were recently identified to play an important role for the dynamics [105–107].) The release renders the confinement tubes themselves transient and allows bending modes of the semiflexible polymers to relax significantly faster than for a topologically frozen network. From their simulations, Lang and Frey found the collective releasing mechanism to yield a relaxation time

$$t_{\text{rel}} \approx 10^{-4} (\zeta/k_B T) \rho L^5 \quad (8.6)$$

for the bending modes of a test filament. They provided solid evidence that the correlated motion of the test filament and the surrounding tube-forming filaments is indeed responsible for this new relaxation time, while they could not present a sound theoretical explanation for its actual form. Comparing the constraint-release time in Eq. (8.6) with the usual reptation time for a topologically frozen network in Eq. (8.4), we obtain  $t_{\text{rel}}/t_{\text{rep}} \approx 10^{-4} \rho L^2$ , which implies that correlated disentanglement is markedly faster than single-chain reptation only if  $\rho L^2 < 10^4$ , *i.e.*, if the solutions are not too dense. For semidilute F-actin solutions ( $\rho \approx 40 \mu\text{m}^{-1}$ ,  $L \approx 10 \dots 20 \mu\text{m}$  [88, 108]), typical values of this dimensionless concentration are in fact on the order of the crossover value  $10^4$ , while the highest concentrations used in the simulations by Lang and Frey are not larger than  $\rho L^2 \approx 10^{2.6}$ . It thus remains unclear whether collective constraint-release processes are essential for the dynamics of tightly entangled biopolymer solutions or if tube disengagement sets in before. Assuming their relevance, Eq. (8.6) can be used to derive the time scale for the terminal stress relaxation of the solution. Namely, since bending-mode relaxation during the time  $t_{\text{rel}}$  goes along with a change  $\langle \Delta\theta^2 \rangle \approx L/L_p$  of the filament orientation, Eq. (8.6) yields a typical relaxation time  $t_{\text{rel}}/\langle \Delta\theta^2 \rangle \approx 10^{-4} (\zeta/k_B T) \rho L^4 L_p$  for the filament orientation [90] [*cf.*, the arguments leading to Eq. (8.5)].

The scaling behavior of the relaxation times introduced in Eqs. (8.3)–(8.6) and their typical values estimated for semidilute F-actin solutions are summarized in Table 8.1. Although these very rough estimates have to be interpreted with some caution, two interesting qualitative findings should persist: first, terminal stress relaxation of these tightly entangled biopolymer solutions is not necessarily facilitated by the correlated release of topological constraints and the dynamic tube renewal as described by Lang and Frey, since its predicted relaxation time is comparable to that of pure single-chain reptation in a frozen network topology. Second, the tension that is built up by steplike stretch deformation of the filaments relaxes at relatively long times (few seconds) and can thus significantly contribute to the nonlinear response. The

relaxation process	time scale	F-actin [s]
bending equilibration [86, 99]	$t_e \propto L_e^4/L_p$	$4 \cdot 10^{-1}$
contour-length diffusion [86]	$t_L^{\parallel} \propto L^2 L_e^3/L_p^2$	1
tension relaxation	$t_{\text{tens}} \propto L^4 L_e^2/L_p^3$ [103]	2
constraint release [90]	$t_{\text{rel}} \propto \rho L^4 L_p$	$6 \cdot 10^2$
randomize orientation [41]	$t_{\text{rot}} \propto L^2 L_p$	$2 \cdot 10^3$
reptation (tube disengagement) [86]	$t_{\text{rep}} \propto L^3$	$10^3$

Table 8.1: Relaxation processes and associated time scales for “tightly entangled” solutions of semiflexible polymers. The order-of-magnitude estimates for F-actin are obtained from Eqs.(8.3)–(8.6) with  $\rho = 40 \mu\text{m}^{-2}$ ,  $L = 10 \mu\text{m}$ ,  $L_p = 17 \mu\text{m}$ , and  $\zeta/k_B T \approx 2\pi\eta_s \approx 1.5 \text{ s}/\mu\text{m}^3$  [83, 88, 108–110]. Note that, for these values, (nonlinear) tension relaxation is predicted to take much longer than equilibrating bending modes in the tube. The estimates further suggest terminal stress relaxation to be determined by single-chain reptation, while the correlated constraint-release mechanism described by Lang and Frey [90] yields shorter time scales.

same holds for the time needed to build up the tension when filaments are pulled transversely at the entanglement points [82]. Despite the recent progress in theoretically describing both the collective constraint-release mechanism [90] and the transverse-longitudinal coupling via hydrodynamic friction [81, 82, 103], their impact on the viscoelastic response of tightly entangled biopolymer solutions is still poorly understood. Indeed, there is various experimental evidence for a transient rather than a frozen network topology, as outlined in the next section. There I also briefly review the very recent theoretical attempts to account for the collective relaxation processes and the ensuing transient caging effects.

## 8.2 Dynamic tube

It is worth recalling that Morse’s EMA and ENA approaches [88] (see Sec. 7.2) aim at effectively capturing collective relaxation processes of the entangled polymer network. As mentioned above, this raises the question, whether the concept of a static tube (and the notion of the tube width and its statistics) is well justified at all. And it is clearly a matter of time scales and their (possibly absent) separation: over times longer than  $t_{\text{rot}}$ , global collective relaxation processes will render the confinement tube eventually transient. The rough estimate in Table 8.1 indicates that this static–dynamic crossover takes place at delay times of a few minutes for typical biopolymer solutions, like entangled F-actin, and could thus be visible in standard experiments. And indeed, some data support the idea of a dynamic rather than a static tube. First, the transverse MSD of a tagged polymer is rarely found to saturate at  $t > t_e$ , but rather continues to grow in a creep-like manner [17, 18], approximately as  $\text{MSD}_{\perp}(t \gg t_e) \propto \ln t$ , corresponding to a logarithmic tail in the dynamic structure factor [45], and an approximate power-law modulus at low frequencies [15]. This is the same long-time behavior as obtained from computer simulations of entangled semiflexible polymers by Lang and Frey [90] and, earlier, by Ramanathan and Morse [93]. Second, the distribution of the transverse fluctuations  $|\mathbf{r}_{\perp}(t) - \mathbf{r}_{\perp}(0)|$  feature pronounced exponential tails at sufficiently long times  $t$ , as shown by Wang *et al.* [92], who recorded actin-filament trajectories

over five to ten minutes. This is in strong contrast to the (close-to) Gaussian statistics expected for a static confinement cage. At short times, the shape of the confinement potential and the ensuing tube-width distributions obtained by Dichtl and Sackmann [69] and Glaser *et al.* [19] from time series of maximum duration of 30 s and 2.5 min, respectively, are instead in better agreement with the concept of the static tube, even resembling the theoretically predicted deviations from Gaussian statistics [89]. This agreement supports the estimate in Table 8.1, namely that the constraint-release dynamics becomes important only on longer time scales.

As mentioned above, the effective medium approaches can be used to mimic large-scale/long-time relaxation processes in the entangled polymer network on a rather abstract level. The idea is that the transverse fluctuations of a test polymer are confined to a dynamic tube, which itself is embedded in an elastic medium. The long-time behavior is then determined by the tube dynamics that follows the relaxation of the medium. For tube fluctuation modes that are still much shorter than  $L$  and  $L_p$ , the surrounding medium might be described by a two-dimensional membrane that is pierced by the tube, whereas three-dimensional deformations of the medium become important at longer scales [111]. The two different embeddings of codimensions two and three yield a logarithmic,  $\text{MSD}_\perp(t) \propto \ln(t/t_e)$ , and an algebraic growth,  $\text{MSD}_\perp(t) \propto \text{const.} - \text{erf}(t/t_e)(t/t_e)^{-1/2}$ , for the transverse polymer fluctuations, respectively [112] (here, the entanglement time  $t_e$  represents the shortest relaxation time of the effective medium, it is used to regularize the continuum theory; see the Appendix at the end of this chapter). The logarithmic tails of the dynamic structure factor obtained from light scattering experiments for F-actin solutions [45] suggest that the two-dimensional effective medium indeed provides a reasonable approximation to the collective network dynamics on such intermediate time scales.

The phenomenology of the long-time dynamics of the entangled polymer solutions [45] and the microscopic explanation via collective relaxation modes and the ensuing transient caging effects due to topological entanglements reveal an analogy of these systems with classic glass-forming colloidal suspensions [113]. This motivated Kroy and Glaser to put forward the so-called glassy wormlike chain model [114, 115], where the relaxation time of long-wavelength bending modes are slowed down exponentially, the underlying picture being that the polymer is subjected to a rough effective free-energy landscape with a hierarchy of free-energy barriers that represent the topological entanglements on a coarse-grained level. Penalizing long-wavelength modes by means of such an Arrhenius energy [116] that scales with the number of entanglements per chain gives rise to the logarithmic long-time  $\text{MSD}_\perp(t) \propto \ln t$ , in agreement with what is commonly observed for biopolymer solutions.

The classical approach to capture the glassy dynamics that emerges from transient caging effects in colloidal solutions, similar to the picture of a dynamic tube, is the mode-coupling theory [117]. It was however shown by Miyazaki and Yethiraj [118] that the conventional two-point mode-coupling approximation cannot be applied to dense solutions of rods, where caging must be traced back to topological entanglements rather than to simple excluded-volume effects. This requires four-point correlations to be taken into account. Within the low-density limit for the rod-rod direct correlation function, the so extended mode-coupling scheme becomes equivalent to the kinetic-theory approach by Szamel [119, 120]. Szamel's theory describes the translational Brownian dynamics (neglecting rotational diffusion) of a tagged rod in a semidilute solution in terms of a hierarchy of  $n$ -particle Smoluchowski equations, which is closed (nonperturbatively) at the level of the two-particle distribution via an effective diffusion tensor. Conceptually, the underlying diagrammatic expansion up to pairwise interactions is in the same spirit as the BCA

proposed by Morse [88] to compute the static entanglement free energy. Later on, Schweizer and Sussman extended Szamel's framework to compute the notably large anharmonic contributions to the dynamic confinement potential [121, 122] and to investigate the influence of rod alignment and step deformation on the dynamic caging effect [123]. Most interestingly, they showed that the confinement potential exhibits logarithmic tails at large displacements, which they found to be in good agreement with the experimental data for F-actin solutions by Wang *et al.* [92], although the underlying rigid-rod approach fails to predict the correct concentration dependence of the (short-time) mean tube width. In order to apply the theory to solutions of flexible polymers, they divided the polymers' primitive paths into rodlike segments that follow an ideal random walk, with topological entanglements being represented on the level of the collisions of the segments [124]. This, of course, ignores bending free-energy contributions and correlations of the segment orientations along the polymer, which are, however, believed to be essential to the mechanics of tightly entangled solutions of stiff polymers [6]. So far, no attempt has been proposed to overcome this limitation. One plausible remedy might be to dress the bare hard-core repulsion between the rodlike polymer segments with the soft BCA interaction that correctly captures the topologically impeded bending modes of the two colliding stiff-polymer segments (see Ref. [89]).

### 8.3 Linear response

The liquid–solid hybrid nature of a viscoelastic material is most conveniently quantified by its linear response to a time-dependent straining protocol  $\boldsymbol{\gamma}(t)$ . Often, this protocol is given by an oscillatory shear deformation  $\boldsymbol{\gamma}(t) = \boldsymbol{\gamma}_0 \cos(\omega t)$  of small (formally vanishing) amplitude  $\boldsymbol{\gamma}_0$  and given frequency  $\omega$ . The stress tensor  $\boldsymbol{\sigma}(t)$  is related to the strain rate tensor  $\dot{\boldsymbol{\gamma}}(t)$  via the dynamic linear modulus  $G(t)$  as

$$\boldsymbol{\sigma}(t) = \int_{-\infty}^t d\tilde{t} G(t - \tilde{t}) \dot{\boldsymbol{\gamma}}(\tilde{t}) \quad (8.7)$$

After Fourier transforming this equation, the convolution turns into a product,  $\boldsymbol{\sigma}_\omega = G(\omega) \boldsymbol{\gamma}_\omega$ , where  $\boldsymbol{\sigma}_\omega = \int_{-\infty}^{\infty} dt \boldsymbol{\sigma}(t) e^{i\omega t}$  and  $\boldsymbol{\gamma}_\omega = \int_{-\infty}^{\infty} dt \boldsymbol{\gamma}(t) e^{i\omega t}$  are the standard Fourier transforms of stress and strain, respectively, and where

$$G(\omega) = G'(\omega) + iG''(\omega) = i\omega \int_0^{\infty} dt G(t) e^{-i\omega t} \quad (8.8)$$

denotes the frequency-dependent complex modulus. Its real and imaginary parts  $G'(\omega)$  and  $G''(\omega)$  provide the storage and loss modulus, which characterize the elastic and viscous contribution to the linear response, respectively. For an elastic solid with modulus  $k$ , one has  $G(t) = k$  and the complex modulus reduces to  $G(\omega) = G'(\omega) = k$ ; for a liquid of viscosity  $\eta$ ,  $G(t) = 2\eta\delta(t)$  and thus  $G(\omega) = iG''(\omega) = i\omega\eta$ .

At high frequencies  $\omega \gg t_e^{-1}$ , the topological entanglements are not probed by an applied deformation and one recovers the single-chain response  $G'(\omega) \propto G''(\omega) \propto \omega^{3/4}$ , whereby the solid-like elastic contributions dominate,  $G'(\omega) > G''(\omega)$ . As detailed in Sec. 6.1.3, the 3/4 power-law scaling is expected from the transverse bending response of a wormlike chain [66, 68], but also for affine longitudinal stretch deformations, where tension propagation can be neglected (as opposed to pulling/release in a quiescent solvent) [79, 81, 84, 85]. Since the free-energy

contribution due to tension is much larger than that for bending, Morse [86] argued that the high-frequency regime is dominated by the stretch response. However, force-balance arguments, along the lines of the floppy-mode picture established for crosslinked polymer networks [125], rather suggest nonaffine deformations at the polymer scale, where bending modes take up most of the macroscopic strain, while longitudinal deformations are strongly suppressed. Compared to the affine-stretch prediction, this nonaffinity thus yields a softer response and a different concentration dependence of the modulus [14, 126, 127]— $G_0 \propto \rho^{7/5}$  vs.  $G_0 \propto \rho^{11/5}$  according to the tube model, Eq. (7.2), for bending and stretching, respectively.

That nonaffine bending contributions dominate the mechanics of the entangled solutions, at least at moderate frequencies, is indeed supported by experiments with bundled semiflexible polymer networks by Lieleg *et al.* [27], who found  $G_0$  to exhibit two scaling regimes as a function of the crosslinker–actin molar concentration ratio  $R$ . For  $R < 0.01$ , their data agree with a bending-dominated scaling  $G_0 \propto \rho^{1.3}$ , independent of  $R$ , thereby resembling purely entangled solutions, while a stretch-dominated regime  $G_0 \propto \rho^{2.4}$  is entered for  $R > 0.01$ . The critical crosslinker concentration  $R \approx 0.01$  is thereby expected to mark the onset of bundling and, thus, of interfilament binding. A similar transition from a bending- to a stretching-dominated regime with increasing (pre-)strain has been observed in collagen networks [128]. This strongly suggests that the linear response of the entangled solutions is indeed dominated by filament bending rather than stretching. That the nonaffine contributions become increasingly suppressed with increasing frequency is suggested by various computational models for crosslinked polymer networks [129–132]. As we will outline in Sec. 8.5.5, the crossover frequency, as predicted by these models, is however beyond the frequencies accessible to typical rheometric experiments. It is thus not yet clear to what degree nonaffinities contribute to the observed high-frequency response of biopolymer solutions and whether it is dominated by bending or stretching contributions.

For deformation rates around the entanglement frequency,  $\omega \sim t_e^{-1}$ , the topological confinement determines the response, leading to an approximate plateau  $G'(\omega) \approx G_0$  for the storage modulus. As described in the previous section, the confinement is released at times longer than  $t_e$ , so that  $G'(\omega)$  again decreases with decreasing frequency  $\omega \ll t_e^{-1}$ . This gives rise to the low-frequency power-law regime obtained in purely entangled biopolymer solutions<sup>2</sup> [15, 45], whose onset depends on the underlying relaxation process—for instance, tube disengagement via reptation or correlated constraint release, as discussed in Sec. 8.1.

I would like to end this section with a few remarks about the experimental techniques that are usually employed to study the viscoelastic response of biopolymer solutions. The bulk rheology of a solution is traditionally measured via macroscopic deformations, typical examples being oscillatory shear mentioned at the beginning of this section. While these experiments provide information about the global rheological properties, microrheology techniques have been extensively used in the past to get a more detailed picture of the processes at the level of the polymeric packing structure [137, 138]. In these experiments, spherical micron-size beads are either actively pulled (using magnetic or optical tweezers, for instance) or they passively diffuse through the medium. For the latter, single- and two-point techniques have been developed, where the fluctuations of a single tracer particle or the correlations between two of them are

<sup>2</sup>For living cells [40, 102] and some reconstituted actin gels [133], the power-law regime is found to be extended over all frequencies, with a marked plateau regime being absent. This observation is usually traced back to the combination of bond kinetics [9, 134] and stiff-polymer physics, which is argued to feature broad distributions of length, time or energy scales that yield the observed power-law rheology [135, 136].

recorded. The wanted response functions are then deduced from the data via the fluctuation–dissipation theorem [73]. Single-point microrheology probes the dynamics of an entangled polymer solution on a very local scale, yielding an extended plateau regime for  $G'(\omega < t_e^{-1})$ . Two-point approaches, in contrast, resolve correlated collective dynamics, better reproducing the bulk response, with a low-frequency power-law scaling of  $G(\omega)$  as obtained in macroscopic-rheometry experiments [18]. The differences between local and bulk properties, which are reflected in the one- and two-point measurements, emerge as a consequence of the polymers' mesoscale packing structure. It was shown by Sonn-Segev *et al.* [139] that a large contrast between the (frequency-dependent) bulk viscosity  $\eta_b = G(\omega)/i\omega$  and the solvent viscosity  $\eta_s$  leads to a marked increase of the characteristic length scale at which the bulk response becomes dominant. More precisely, the (longitudinal) displacement correlations between two tracer particles decay as  $r^{-3}$  for particle distances  $r < r_c$  before the asymptotic  $r^{-1}$  decay takes over. The dynamic crossover distance  $r_c \approx (\eta_b/\eta_s)\xi$  separates the relative flow between the polymer network and the solvent in the vicinity of the driven bead from the asymptotic collective (Stokes) flow further away [140]. It can be notably larger than the mesh size  $\xi$ . The larger  $r_c$ , the larger is the difference between locally and globally probed mechanical properties of the solution. From this perspective, the observation that deviations between one- and two-point microrheology become more pronounced as the filament length is increased [18] is consistent with the experimentally found positive correlation between filament length and plateau bulk modulus  $G_0 \propto \eta_b \propto r_c$  [14], although this length dependence is not yet convincingly understood on a molecular level—note that the tube model predicts  $G_0$  to be independent of  $L$ , see Eq. (7.2).

Limited to the (near-)equilibrium regime, passive microrheology techniques can only provide information about the linear response, while analyzing the nonlinear behavior requires to strain the solution actively. This regime is the subject of the next section.

## 8.4 Nonlinear response

The nonlinear response to an applied finite shear strain  $\gamma$  is often characterized by the differential shear modulus  $K(\gamma) = d\sigma/d\gamma$ . It gives immediate information whether the solution becomes stiffer ( $dK/d\gamma > 0$ ) or softer ( $dK/d\gamma < 0$ ) upon shearing. The tube-model prediction for the nonlinear response of an entangled semiflexible-polymer solution was first derived by Morse [87], who assumed that the tube follows the strain affinely and that the deformation is slow enough that the polymer's unconfined bending modes are always equilibrated. He showed that this approach yields a strain-softening response. Similar behavior was obtained by Fernández *et al.* [101] from a unit-cell approach that allows for nonaffine tube deformations. The theoretical prediction of strain softening has however been challenged by the more complex phenomenology found in experiments with F-actin solutions, namely a transition from strain softening to stiffening upon changing various parameters, like solvent or ambient conditions or the shear rate [45, 46, 141]. To observe this transition in macroscopic-deformation experiments, inelastic flow has to be reduced, which can be done using short stress or strain-rate pulses [45, 46]. Very recently, Robertson-Anderson and coworkers reported a similar rate-dependent transition from active microrheology measurements of entangled DNA [142] and F-actin [143–146]. These authors used optical tweezers in combination with fluorescence microscopy to apply a local strain to the solutions while recording the resulting force that acts on the bead and the surrounding deformation/flow

field. They observed a short-term stiffening response, followed by a softening and a subsequent viscous-flow regime. The viscous regime was found to exhibit shear thinning, while the stiffening was found to be more pronounced as the strain rate [143] or the concentration [145] was increased, in agreement with the earlier bulk-rheology observations [45, 46, 141], although the values of the local and global strain rates used in the two setups differ strongly, thus making a quantitative comparison of the different experimental techniques forbiddingly complicated.

The softening–stiffening transition is very similar to what is observed in transiently crosslinked biopolymer solutions [9], where it is expected to arise from the interplay between the bond kinetics and the stiff-polymer physics [26]. For purely entangled solutions, sticky (or frictional) interactions between the filaments [147, 148] have thus been put forward as a possible explanation for the observed softening–stiffening transition [114, 115]. This idea is also supported by active microrheology experiments by Dichtl and Sackmann [44], who used magnetic tweezers to pull a bead, to which they attached a (fluorescently labeled) test filament, through an entangled F-actin solution. Applying a sequence of force pulses to the bead, they observed that the test filament remained stuck in a “pinched state” during a few successive pulses before it was released again and continued to follow the driving force. This suggests that network heterogeneities together with transient interfilament frictional coupling plays an important role for the mechanical properties of the biopolymer solutions. And it implies that the linear modulus increases with increasing filament length (via the number  $L/L_e$  of filament contacts, *i.e.*, entanglement points). The observed softening–stiffening transition with increasing deformation rate might then be explained either by a rate-dependent friction [147, 148] or by the viscoelastic single-polymer stretch response together with the softening response of the tube deformations (see the Appendix at the end of this chapter).

The analogy of the softening–stiffening crossover with the glass transition [45] brings us back to the glassy wormlike chain model and the dynamic-tube approaches reviewed in Sec. 8.2. While these theoretical attempts already hint at the mechanisms that are responsible for the observed phenomenology, a comprehensive explanation on the basis of the solutions’ microstructure is still lacking. So far, it is not clear whether transverse–longitudinal coupling via the solvent [82] plays an important role for the solutions’ nonlinear stiffening response. It might in fact provide a promising alternative mechanism to the inter-chain friction.

## 8.5 Crosslinked-network models

From the discussion in the previous sections we learned that the purely entangled semiflexible-polymer solutions share some phenomenological similarities with (transiently) crosslinked polymer networks, most prominently the softening–stiffening transition, but also the observations that the plateau modulus of entangled solutions of F-actin and DNA-helix tubes increases with increasing filament length [14] and, most surprisingly, with increasing persistence length [52, 53] (see Sec. 7.1.2). This suggests to compare the entangled stiff-polymer solutions with rigidly crosslinked polymer networks—promising a deeper understanding of the influence of network heterogeneities and the nonaffine microscale response to an applied macroscopic deformation [149]. In the following, I summarize the main theoretical progress made in this field during the last years. For a more comprehensive discussion of the various computational approaches proposed in the literature I would like to refer the reader to the excellent review by Broedersz and MacKintosh [7].

Besides viscoelasticity, a second paramount characteristic of the mechanics of biological matter is inelasticity. It refers to the partly reversible damage of crosslinked polymer networks during deformation and differs from ordinary plastic (*i.e.*, irreversible) response due to rebinding of unbound crosslinks. When crosslinks start to break under load, rigid networks can become liquid-like and start to flow. Bond kinetics and the ensuing inelasticity will not be discussed in the following. A comprehensive overview of its phenomenology and various theoretical modeling attempts together with an extensive reference list of the relevant literature can be found in the recent review article by Gralka and Kroy [134]. The current understanding of the behavior of yield-stress materials in soft condensed matter has recently been gathered and extensively discussed by Bonn *et al.* [150].

### 8.5.1 Affine network models

Most early theoretical attempts to describe the viscoelastic response of biopolymer solutions rest on the assumption of a homogeneous strain field at all length scales, where each chain follows the macroscopic deformation affinely [62, 84, 85, 151, 152]. For crosslinked networks, the affine models attribute the response to the stretch deformation of the filament segments of length  $L_s$  between consecutive crosslinks. The so predicted plateau value  $G_0 \approx 6\rho k_B T L_p^2 / L_s^3$  for the linear modulus [similar to the stretching energy scale given in Eq. (7.2), where  $L_s$  is replaced by the entanglement length  $L_e$ ] and the stress dependence  $K \propto \sigma^{3/2}$  for the differential modulus, characterizing strain stiffening, has been found to be in very good agreement with experimental data obtained from crosslinked (and bundled) F-actin [133, 153–155], intermediate filaments [156–158], fibrin gels [159], pectin [152, 160, 161], and synthetic hydrogels [162].

### 8.5.2 Nonaffinity

Despite their apparent success, affine network approaches were soon challenged by the insight that nonaffine bending modes are energetically favored, at least at moderate deformation rates and amplitudes, as already mentioned in Sec. 8.3. Since the total elastic energy of an affinely strained semiflexible-polymer network can be lowered via relaxing stretching modes at the cost of the cheaper bending modes, Heussinger and Frey concluded that an affine deformation field is always unstable [163, 164]. This is particularly important for strongly polydisperse networks, with a nonvanishing fraction of very short segments. As the entropic tension of a chain segment decays as  $L_p^2 / L^3$  with the segment length  $L_s$  [see the force-extension for a WLC in Eq. (6.5)] the polydisperse networks can build up large residual stresses under purely affine strain fields.

A number of theoretical attempts to account for nonaffine effects make use of a unit cell that follows the strain affinely while the polymer fibers that pass through this cell are allowed to minimize the cell's deformation free energy via nonaffine contributions [101, 126, 127, 161, 165–167]. As the unit cell usually represents either a cube of edge length given by the network's mesh size  $\xi$  or an entanglement element given by a tube segment of length  $L_e$  [101, 126], heterogeneities and correlations at the level of the filament length  $L$  are neglected. That nonaffinity on the scale  $L$  plays an important role for the mechanics of stiff-polymer networks was however shown for computationally solved whole-network models. First insight came from athermal so-called Mikado models, where rods are placed randomly on a plane to form a two-dimensional network, whose response to a macroscopic low-frequency strain is obtained by numerically minimizing its



overall elastic energy that comprises bending and stretching contributions of the filaments [168–170]. Later studies have used lattice based network models to further elaborate on this [7, 171]. In the athermal, purely mechanical limit, often employed in these approaches, the filaments' stretch response is either modeled by that of an elastic beam or fiber of fixed (one-dimensional Young's) modulus  $\mu$ , whereas entropic contribution that are expected for semiflexible polymers at finite temperature are neglected. To account for such entropic effects, the modulus  $\mu \propto k_B T L_p^2 / L_s^3$  obtained for a WLC segment of length  $L_s$ , Eq. (6.5), can be used for the considered low-frequency deformations where all bending modes are assumed to remain equilibrated. The strongly length-dependent  $\mu$  makes these thermal networks more sensitive to polydispersity and randomness than the purely mechanical networks with  $\mu = \text{const.}$  [164, 172].

The athermal Mikado networks revealed an interesting crossover behavior. For infinitely long filaments, bending modes were found to be suppressed, while the stretching modes dominated the affine elastic response. For filaments of finite length, in contrast, an elastic regime was identified that is dominated by soft nonaffine bending deformations, and which crosses over to an affine stretch-dominated regime once a critical density or a critical filament length are exceeded. Wilhelm and Frey [168] interpreted the nonaffine–affine (bend–stretch) transition in terms of a rigidity percolation, with a critical density  $\rho_c$  of the filament network that determines the transition point. Their scaling-law prediction for the elastic modulus yields the affine/nonaffine limit for  $\sqrt{\kappa/\mu}(\rho - \rho_c)$  much larger/smaller than unity. Here,  $\kappa$  is the filaments' bending rigidity and  $\mu$  their length-independent stretch modulus.<sup>3</sup> For two- and three-dimensional lattice-based models, this idea was later substantiated by Broedersz *et al.* [173], who identified two transition points. First, a high-density threshold is found, given by the classical Maxwell isostatic connectivity threshold, when bending is switched off ( $\kappa = 0$ ) [174–176]. The networks' rigidity is then controlled by their connectivity (rather than the polymer concentration, which neglects the above mentioned stabilization effect for longer filaments). The soft–rigid crossover corresponds to the jamming transition for granular materials [176–178]. At the isostatic point, the networks become critical and exhibit diverging nonaffine fluctuations and a diverging length scale; the elastic modulus takes the role of the order parameter [7]. As bending contributions are switched on ( $\kappa > 0$ ), a second threshold emerges discontinuously at a lower density (*i.e.*, lower connectivity), which marks the onset of network rigidity. The isostatic threshold at higher connectivity becomes smeared out, representing the bending–stretching transition found in the Mikado model. The bending rigidity thus plays the role of an applied field or coupling that shifts the critical point (discontinuously) to a lower connectivity, once it is switched on [7]. Subisostatic networks at the margins of mechanical stability can be made rigid by additional weak interactions [175], viscous damping due to the solvent [129–131], internal and external stresses [179–181], externally applied strains [182, 183], and thermal fluctuations [172, 184].

---

<sup>3</sup>An alternative interpretation of the mechanical response of the Mikado networks was proposed by Head *et al.* [169, 170]. They argued that the total elastic energy of the network is minimized by relaxing the stretch contributions at the ends of a test filament of total length  $L$ , at the cost of exciting softer bending modes of the filaments to which the test filament is connected. The nonaffine–affine transition is then characterized by the length  $L_{\text{NA}} \approx L_s (L_s / \sqrt{\kappa/\mu})^\nu$  (with  $\nu = 2/5$  for dense networks) over which the test filament's stretch contributions relax,  $L_{\text{NA}} \ll L$  corresponding to the bending-dominated nonaffine regime,  $L_{\text{NA}} \gg L$  to the stretching-dominated affine regime. Shortcomings of this approach are, however, that the exponent  $\nu$  does not seem to be universal (for less dense networks, simulations yield  $\nu = 1/3$ ) and that it does not capture the correct behavior ( $G_0 \rightarrow 0$ ) at the rigidity threshold [7].

### 8.5.3 Floppy-mode theory

Based on the insight gained from the Mikado model approaches, Heussinger, Frey, and coworkers [125, 185] developed a floppy-mode theory, from which they estimated the contribution of nonaffine zero-energy deformation modes to the elastic response of such networks, when the filaments have a vanishing bending rigidity. A qualitatively similar behavior is expected whenever the bending modes remain much softer than stretching modes, as it is the case for the biopolymer networks. The basic idea underlying the floppy-mode approach is that the amplitude of transverse bending deformations does not scale with the segment length  $L_s$  but with the total length  $L$  of the filament, in order to avoid stretching of the other filaments to which they are connected.<sup>4</sup> This yields a bending energy per segment of the form  $\kappa L^2/L_s^3$  to lowest (*i.e.*, harmonic) order in the transverse deformation amplitude, corresponding to a static modulus

$$G_0 \propto c\kappa L^3/L_s^4 \propto \kappa L^2 \rho^{1+4/(d-1)} \quad (8.9)$$

in  $d$  dimensions, where  $L_s \propto \rho^{-1/(d-1)}$ . This scaling, with  $L_s$  representing the mean segment length, is only valid if the segment-length distribution is peaked around the mean, as it is the case for lattice based models [171, 186]. For the two-dimensional Mikado models, however, the distances between intersecting filaments follows an exponential distribution, yielding a diverging average bending energy when all segments would contribute equally. Heussinger and Frey thus introduced a cutoff mode, based on the insight that too short floppy modes cease to be floppy. So, they argued that the bending energy of the shortest fiber segment that contributes to the overall elastic energy is on the same order as the floppy-mode energy of a whole filament, such that bent shorter segments can relax by exciting floppy modes. This yields a static modulus for the two-dimensional Mikado network of the form  $G_0 \propto \kappa L^4 \rho^7$ , in good agreement with the simulations [168].

Equation (8.9) provides an interesting answer to the question whether bending or stretching dominates the network mechanics. It is clear that the modulus is bounded from above by its affine stretch-dominated limit  $G \approx \rho\mu$ . This limit is thus reached, when  $L$  in Eq. (8.9) for the nonaffine modulus exceeds the critical value  $L_{\text{NA}} \propto L_c^2 \sqrt{\mu/\kappa} \propto \rho^{-2/(d-1)} \sqrt{\mu/\kappa}$  at the nonaffine–affine (bend–stretch) transition. Deviations of this prediction from the numerically obtained Mikado-model scaling  $L_{\text{NA}} \propto L_c^{1+\nu} \sqrt{\mu/\kappa}$  with  $\nu = 0.3 \dots 0.4$  [169, 170], may be a consequence of the strongly polydisperse fiber-segment lengths, as opposed to the (three-dimensional) lattice-based models. For the latter, floppy-mode counting, similar to Maxwell’s [187, 188] classical estimate for the rigidity threshold for central-force interactions (here, extended to three-node constraints due to the non-zero bending stiffness), can be employed to predict the numerical values of the critical network density at the bend–stretch transition as a function of the network dimension and the lattice geometry [7, 173].

---

<sup>4</sup>Averaging out the relative angle between two connected filaments, one obtains that the transverse deflection  $\delta r_{\perp}$  of a test filament follows the distance  $\Delta R_{\text{c.m.}}$  between the centers of mass of the two connected filaments,  $\delta r_{\perp} \propto \Delta R_{\text{c.m.}}$ . Assuming that the distance  $\Delta R_{\text{c.m.}}$  between the centers of mass of two connected filaments follows the strain  $\gamma$  affinely, this yields  $\delta r_{\perp} \propto \Delta R_{\text{c.m.}} \propto \gamma L$ , where we used  $\Delta R_{\text{c.m.}} \approx (V/N)^{1/d} \propto (L^d/2)^{1/d} \propto L$  for the distance between the  $N = 2$  crosslinked filaments whose centers of mass must both be located in a cylinder of volume  $V \propto L^d$ , in  $d$  dimensions [185].

### 8.5.4 Nonlinear response

In the nonlinear response regime, permanently crosslinked networks exhibit strain stiffening, once some critical strain amplitude  $\gamma_c$  is exceeded [155, 182]. From the affine mean-field picture, one expects stiffening to set in when the end-to-end distance  $\approx L - L^2/6L_p$ , Eq. (6.6), of the polymer segment is stretched to a length  $\gamma_c L_s$  at which the bending fluctuations of the polymer are pulled taut, thus [7]

$$\gamma_c \approx L_s/6L_p. \quad (\text{affine theory}) \quad (8.10)$$

The two-dimensional Mikado models [168–170] and three-dimensional crosslinked-network simulations [189, 190] showed that the nonaffine contributions to the response become increasingly suppressed with increasing strain  $\gamma$ . For the network models, the onset of the stiffening has thus been interpreted as a strain-induced transition from the soft nonaffine bending-dominated regime to the stiff affine stretching-dominated one [191]. Within the floppy-mode theory, transverse deflections of a bent filament scale as  $\gamma L$  and go along with an axial deformation of a segment on the order of  $\delta_{\perp}^2/L_s$  [27]. Nonlinear contributions are assumed to become noticeable once bending ( $\kappa\gamma^2 L^2/L_s^3$ ) and stretching ( $\mu\gamma^4 L^4/L_s^3$ ) contribute similarly to the total elastic energy, thus [7]

$$\gamma_c \approx \sqrt{\kappa/\mu}/L = L_p^{-1/2} L_s^{3/2} L^{-1}, \quad (\text{floppy-mode theory}) \quad (8.11)$$

where the second relation is obtained for the entropic semiflexible-polymer modulus  $\mu = \kappa L_p/L_s^3$ . Note that the floppy-mode theory predicts the linear-response regime to vanish as the filaments become infinitely long ( $L \gg L_s$ , with fixed  $L_p$ ).

In contrast to most elastic materials, biopolymer networks are usually found to contract or build up negative normal stresses in response to a uniaxial extension or shear, respectively [192]. This nonlinear effect is due to the nonlinear and asymmetric force-extension relation, which can arise either from the entropic polymer response or from collective buckling of the athermal filaments under compression [Majumdar2017, 185, 193]. It thus crucially depends on the strain-induced filament reorientation and ensuing alignment [96, 189, 194, 195]. The latter can also importantly contribute to the stiffening. Based on their simulations of two- and three dimensional crosslinked fiber networks, Huismann, Onck, van Giessen, and coworkers related the negative normal stresses to the nonaffine network rearrangements that govern the gradual transition from a bending- to a stretching-dominated regime as  $\gamma$  increases [189, 191]. Later, the same group identified stress-chains in the simulated networks, which they argued to be responsible for the stiffening, namely, at smaller strains, when these chains are pulled out and, at larger strains, when the stress-chains are reoriented [196]. Again, they obtained the former regime to be bending-dominated, the latter stretching-dominated. A similar behavior was recently obtained by Amuasi *et al.* [197] from simulations of semiflexible-polymer networks—with a slightly different interpretation though. These authors found the tensile filaments to be pulled into the stretch direction by the (many) surrounding polymers, the latter thereby building up large stresses that are stored in their bending modes. In this order—first reorientation, then pulling out undulations—the two response regimes seem in fact more plausible. They lead to an intermediate non-affine bending-dominated stiffening ( $K \sim e^{\sigma L/G_0}$ ), which turns into the affine stretch-dominated regime ( $K \sim \sigma^{3/2}$ ) at large strains.

### 8.5.5 Network dynamics and viscoelasticity

In the above, we only reviewed the quasi-stationary, purely elastic ( $\omega = 0$ ) response of the polymer networks. The linear viscoelastic response of a random spring network has been investigated by Tighe [129] and Yucht *et al.* [130]. They described the dynamics of the end nodes of a spring segment deterministically, driven by the axial harmonic force and by a viscous solvent that follows the strain affinely. Recall that in the absence of bending contributions these networks exhibit a rigidity transition in the zero-frequency limit ( $\omega = 0$ ), characterized by a continuously vanishing elastic shear modulus as the network connectivity approaches the isostatic point [173, 174]. As the frequency is increased ( $\omega > 0$ ), this critical point, which separates fluid from solid-like behavior, expands into a critical region where loss and storage moduli are comparable [ $G''(\omega) \approx G'(\omega)$ ]. One thus obtains three regimes: a low-connectivity fluid-like, a high-connectivity solid-like, and an intermediate critical phase.

In the (very) high-frequency limit, the viscous drag between the affinely deforming solvent and the network dictates the response. It then becomes affine, independent of the network connectivity [130]. Balancing tension and drag on a fiber segment of length  $L_s$ , the nonaffine–affine crossover frequency is given by  $\omega_{\text{NA}} = (\mu/k_{\text{B}}TL_s)/(4\pi\eta_s a)$ , with  $\mu$  being the stretch modulus,  $\eta_s$  the solvent viscosity, and  $a$  the hydrodynamic size of the network nodes. However, if this crossover behavior at  $\omega_{\text{NA}}$  is applicable to typical biopolymer experiments is questionable. While the solvent-dominated regime ( $\omega_{\text{NA}} > \omega$ ) is characterized by a linear scaling  $G''(\omega) \sim \eta_s \omega$  for the loss modulus, most experimental data for biopolymer networks feature the semiflexibility scaling  $G'(\omega) \propto G''(\omega) \propto \omega^{3/4}$  for the fastest accessible rates. Solvent contributions are then expected to become paramount at even higher frequencies, beyond what is experimentally accessible.<sup>5</sup> For slower deformations ( $\omega < \omega_{\text{NA}}$ ), nonaffine contributions were shown to become increasingly pronounced with decreasing frequency. Nonaffine deformations would then also play an important role at all experimentally accessible frequencies.

In a recent study, Dennison and Stark [131] confirmed the above findings using an elaborate hybrid molecular-dynamics/multiparticle-collision-dynamics simulation technique. It allowed them to account for thermal fluctuations of the network and to explicitly incorporate hydrodynamic interactions (via fictitious fluid particles). In agreement with earlier work by Dennison *et al.* [184], the thermal fluctuations were found to stabilize networks at and below the critical point, as long as the frequency is not so large that the fluid character takes over. As a general observation, stronger hydrodynamic interactions led to an increased frequency dependence of the linear modulus, a faster relaxation, and a more affine response.

The bending contributions to the viscoelastic response of crosslinked networks were recently discussed by Rizzi *et al.* [132]. They used a computational approach very similar to the one proposed by Yucht *et al.* [130], but with length-dependent moduli for the fiber segments, as expected for (athermal) slender elastic beams. From their—somewhat preliminary—simulations, Rizzi *et al.* found the soft nonaffine bending modes to be successively suppressed as  $\omega$  increases. This observations was, however, not worked out systematically and a convincing explanation how the nonaffin/affine response is influenced by the interplay of the viscous solvent and the

<sup>5</sup>For typical biopolymer networks, the nonaffine–affine crossover frequency is expected to be on the order of  $600 \text{ s}^{-1}$ , beyond the limits of macrorheometry, but accessible to microrheological techniques [15]. This estimate is obtained for the entropic semiflexible-polymer modulus  $\mu \approx k_{\text{B}}TL_p^2/L_s^3$  and the values  $4\pi\eta_s \approx 3 \text{ s}$  for water and  $L_p \approx 17 \text{ }\mu\text{m}$ ,  $L_s \approx 2 \text{ }\mu\text{m}$ ,  $a \approx 10 \text{ nm}$  for crosslinked semidilute F-Actin.

frequency-dependent stretching and bending contributions of the polymer network is still lacking.

An extension of the floppy-mode theory to the frequency-dependent dynamic response was recently established by Plagge *et al.* [198]. These authors used an effective-medium approximation [185], where the energy contained in a floppy mode of given amplitude is balanced with the average bending-energy contributions of the test filament and floppy-mode contributions of the attached neighboring (“effective-medium”) filaments. Expanding the floppy-mode energy to harmonic order in the deformation amplitude, a self-consistent equation for the stiffness of the effective medium can be derived. Plagge *et al.* solved it numerically to compute the frequency-dependent microrheological modulus  $g(\omega)$  from the nonaffine response of the test filament. In a second step, they introduced transient crosslinks to this model on a coarse-grained level, namely by connecting the viscoelastic single-chain element with a dashpot of viscosity  $\eta_{cl}$  (along the lines of a standard Maxwell element). The overall microrheological modulus  $\bar{g}(\omega)$  then follows from  $1/\bar{g}(\omega) = 1/g(\omega) + 1/(i\omega\eta_{cl})$ . This yields a Maxwell-like peak for the loss modulus, which is thus assumed to represent the terminal stress relaxation due to the transient crosslinks that need to break before the system can flow. Such a low-frequency peak in  $G''(\omega)$  has been observed for transiently crosslinked biopolymer networks [27, 31, 136] and is characteristic for purely entangled biopolymer solutions [11, 15, 199]. For the latter, it is traced to the long-time relaxation processes, like tube disengagement and collective constraint release, discussed in Sec. 8.2 (see, e.g., Ref. [67]). Plagge *et al.* further used their model to address the nonlinear response of the crosslinked networks. To this end, they introduced crosslinks with a load-dependent unbinding rate, which allowed them to reproduce the rate-dependent softening–stiffening transition discussed in Sec. 8.4.

### 8.5.6 Conclusions and implications for entangled biopolymer solutions

Now the question is, of course, to what extent insights that have been gained from the crosslinked polymer networks carry over to the entangled biopolymer solutions. Here, I give a short list of some suggestive analogies between the two systems and their possible implications for future theoretical work. The drawn conclusions are, however, of somewhat speculative character and should be taken with some caution.

1. In the absence of crosslinks, both soft bending and slippage at the entanglement points contribute to the floppy modes, suggesting a markedly nonaffinity response.
2. The positive correlation between the plateau modulus  $G_0$  and filament length  $L$  [14] might be explained along the lines of the rigidity transition [168]. This, however, seems to require sticky/frictional polymer contacts in order for a percolated network to be formed.
3. Such frictional interactions (arguably, together with some finite prestrain) may also explain the increase of  $G_0$  with increasing persistence length  $L_p$  [52, 53].
4. The crosslinked networks exhibit a rigidity transition as the connectivity [168–170, 173] (*i.e.*, concentration and/or fiber length), fiber bending rigidity [173, 175], shear rate [129, 130], or some finite (pre)strain [182, 200] are increased. This is to some extent similar to the nonlinear softening–stiffening transition observed for F-actin solutions as the polymer concentration, filament length, shear rate, salt concentration are increased or the temperature is decreased (corresponding to an increased persistence length) [45, 46].

5. At high frequencies, hydrodynamic interactions might suppress nonaffinities and facilitate the excitation of stretch modes, yielding a stiffer response [130].

Interpreting these similarities can be problematic because of various complications. Simple geometric arguments, for instance, forbid axial stretch deformations to be exited to linear order in the strain. However, it seems plausible that local prestresses in the entangled (but sticky) biopolymer solutions are inevitable created during sample preparation. They can give rise to a linear coupling between the transverse and longitudinal deformation of a filament. This is what we tacitly assumed in our approach proposed in the Appendix.

An alternative starting point might be to combine Morse's tube model [6] with Heussinger's floppy mode theory [125]. The backbone and shape of the tube would then respond nonaffinely. Following Fernandez *et al.* [101] (see also Ref. [96], appended to Chap. 7), the overall free energy per tube segment comprises bending and confinement contributions. But, since the transverse deflections are assumed to scale linearly with the filament length, according to the floppy mode theory, the bending contributions would dominate the linear response, yielding a plateau modulus  $G_0$  of the form given in Eq. (8.9). From such a nonaffine response one thus expects  $G_0$  to increase both with increasing filament length  $L$  and with increasing persistence length  $L_p$  (the value of the exponent for the latter depending on the actual form of the segment length), without the necessity of sticky polymer contacts. The softening–stiffening transition might then be explained along the same lines. Namely, not in terms of a transition from a bending-dominated to a stretching-dominated regime, but due to the reorientation of some tubes (of length  $L$ ) into the mean stretch direction. The strongly increasing number of exited bending modes of the neighboring transverse tubes that pull on the rotating tubes is then responsible for the stiffening response, similar to what was obtained by Amuasi *et al.* [197] for the crosslinked networks. It is plausible that this pulling–reorientation mechanism requires a minimum polymer concentration, tube (*i.e.*, filament) length, tube bending modulus (which increases with increasing shear rate), etc., thereby providing an explanation of the softening–stiffening transition observed for entangled biopolymers.

Definite answers surely require further experimental and theoretical studies. Here, computer simulations seem particularly promising as they allow for a systematic analysis of the various deformation modes and the influence of parameters like filament length, persistence length, and stickiness on the mechanical properties of the solutions. With the computational power available today, we are however just at the edge of resolving the dynamics of the tightly entangled solutions. The recent effort by Lang and Frey [90] provides an impressive example, with reduced concentration  $L_p^2\rho$  on the order of  $10^4$  and simulation times long enough to investigate the (transient) confinement, although the filament length used in their simulations seems to be too short to apply their interpretation to typical F-actin experiments [see the remarks below Eq. (8.6)]. The limitations become even more visible as one tries to take hydrodynamic interactions into account. This was recently done by Nikoubashman and Howard [201], who used a hybrid molecular-dynamics/multiparticle-collision-dynamics algorithm to simulate semidilute polymer solutions together with a solvent represented by fictitious fluid particles. With  $L_p^2\rho \leq 250$  these solutions are however not tightly entangled; and, in order to keep the monomer number low, they used a polymer aspect ratio  $a/L \approx 10^{-2}$  that is much larger than for F-actin (on the order of  $10^{-3}$ ). Breaking these limits might nevertheless be possible in the near future with the help of massively parallel algorithms processed on modern graphics processing units (see, *e.g.*, Ref. [202]).

# Appendix





# Analytical model for the viscoelastic response of stiff polymer solutions

Marc Lämmel and Klaus Kroy\*

*Institut für Theoretische Physik, Universität Leipzig, Postfach 100920, 04009 Leipzig, Germany*

(Dated: August 31, 2018)

A central task in biomechanics is to establish a physical understanding of the unique mechanical properties of living cells and tissues in terms of the material properties of their polymeric constituents. We propose an analytical model for the linear and nonlinear viscoelastic shear response of solutions of stiff polymers. It integrates locally non-affine bending deformations as captured by a hybrid tube/effective-medium model with transient polymer stretching and elucidates the crucial role of the polymer length for the macroscopic mechanical response.

## I. INTRODUCTION

The insight that packing structure, phase behavior, and mechanics of semidilute polymer solutions is determined by highly correlated fluctuations, akin to those at a critical point, marks a historical paradigm shift in polymer physics [1]. But for stiff biopolymers, such as those responsible for the remarkable mechanical properties of your own cells and tissue [2–4], the necessity to pay attention to small self-affine fluctuations around the straight ground state seems less compelling than in the case of their much floppier synthetic relatives. First theoretical evidence for the relevance of nonaffine contributions for the mechanics to such stiff-polymer systems was provided by thorough studies of idealized “mikado” models [5–7] and random or lattice-based fiber networks [8, 9]. Their mechanical response to a macroscopic strain is determined by bending and stretching contributions of the filaments to the overall mechanical free energy of the network [5–7]. For polymers close to the rod limit, these two deformation modes become very distinct—stiff polymers bend much easier than they stretch or buckle. The strong free-energy separation was employed to formulate a floppy-mode theory that tries to account for some of the soft bending fluctuations of the stiff polymers in a network [10, 11]. It has on the other hand been argued that the two deformation modes give rise to two different types of networks of stiff polymers [12]: softer ones dominated by fluctuations and entanglements and described by the tube model of semiflexible polymers [13, 14]; and stiffer ones dominated by (transient) crosslinks, commonly described by an affine rubber-like network model [15]. As an experimental criterion the absence or presence of stiffening in the nonlinear shear response has been proposed [12], whereby strain stiffening is usually traced back to stretch deformations of polymers that are aligned into the strain direction [16]. Later on, experimental progress has revealed that the issue is even more subtle, however, and that even pure F-actin solutions stiffen under prestress if inelastic flow is minimized, with the degree of stiffening changing continuously as a

function of system parameters (such as polymer length, concentration, and shear rate) and ambient conditions (*e.g.*, temperature and ionic strength) [17, 18]. A similar transition from softening to stiffening with increasing deformation rate was recently observed from active one-point microrheology measurements [19]. The rapidly relaxing (and relatively weak) stiffening reflected by these data should however be interpreted carefully, since such locally probed rheology can differ strongly from the bulk response [20]. A first attempt towards a theoretical description of the linear and nonlinear viscoelastic response of semiflexible-polymer solutions was recently proposed by Plagge *et al.* [21], who extended the earlier static versions of the two-dimensional mikado models to account for thermal fluctuations and reversible crosslinks.

Besides the softening–stiffening fingerprint in the nonlinear rheology, recent experimental observations in the linear regime also challenge the widely accepted theoretical concepts. A thorough analysis of entangled solutions of semiflexible DNA helix tubes, whose stiffness can be tuned through their diameter, provides clear evidence that even the linear rheology deviates qualitatively from the theoretically expected scaling laws for pure solutions and is rather reminiscent of (transiently) crosslinked networks [22]. Similar deviations have been observed for reconstituted biopolymer solutions, where the ionic strength of the buffer had been varied to alter the filaments’ persistence length [23]. It is hard to see how these fundamental effects could be integrated into any of the prevailing schemes, which have moreover been criticized for their *ad hoc* affine assumptions [11]. Finally, the widespread observation of effective power-law rheology of the cytoskeleton [24] suggests that neither the tube model nor the affine network model represents an appropriate approach to describe the viscoelastic passive rheology of living cells. Instead, the concept of inter-molecular friction seems to be a recurrent property responsible for a great part of the above outlined phenomenology, as it notoriously intensifies the hindrance and caging effects at the contact (or “entanglement”) points of the chains in solution [25], closely akin to a transiently crosslinked gel. The latter analogy is also theoretically suggested from the pertinence of binding site models that relate mesoscopic friction to the formation and rupture of microscopic bonds, *i.e.*, of transient crosslinks [26, 27].

In the following, we outline an approach to the lin-

---

\* Corresponding author.

Electronic address: [klaus.kroy@uni-leipzig.de](mailto:klaus.kroy@uni-leipzig.de)

ear and nonlinear viscoelastic response of entangled solutions of stiff polymers that overcomes several of the limitations of previous attempts. Among them is the assumption of affinity of the longitudinal polymer deformations down to the entanglement scale. It is dictated by a twofold application of the phenomenological tube concept in the conventional theory [13, 28]. The first (uncritical) application serves to estimate the transverse confinement and deformation free energy of a test polymer by entanglements, which yields a contribution  $G_{\perp}$  to the shear modulus. Additionally, a tube-like confining potential is also assumed to represent the caging of the test polymer during transient longitudinal stretching. On this basis the second, affine contribution  $G_{\parallel}$  is derived in the same way as for crosslinked networks with entanglements playing the role of crosslinks. We here relax this latter constraint by embedding the tube into a soft viscoelastic medium that effectively represents its transient environment. Hence the relaxation of long wavelength modes of the polymers is not *a priori* blocked by the tube but merely strongly slowed down. A conceptually similar effective medium approach has been proposed earlier by Morse [29]. Its qualitative scenario is very much akin to the one underlying the so-called glassy wormlike chain (GWLC) model [30, 31] that effectively liberates the tube to wander between energetically equivalent configurations separated by free energy barriers. Based on the transient-tube picture, a second profound modification of the conventional approach becomes possible, namely to allow for some frictional coupling between the stiff longitudinal deformation modes and the overall affine background deformation for polymers of finite length.

As detailed in Sec. III, these two modifications allow us to unite elements of the conventional viscoelastic tube and network models on a new basis and, at the same time, resolve the opposition between these models and the ubiquitous observations of apparent power-law rheology. Additionally, the crucial role played by (zero-energy) floppy modes and the polymer length in this regard is revealed. The theory provides predictions for the full frequency-dependent linear and nonlinear dynamic response. It further offers a plausible explanation for the above mentioned experimentally observed nontrivial concentration (and persistence-length) dependence of the quasi-stationary response that is in apparent conflict with the traditional tube model.

The rest of the paper is organized in three succinct sections, with the focus on conceptual aspects and technical details deferred to four appendices. Section II introduces the constituent parts of the model. Its predictions for the linear and nonlinear viscoelastic response are presented in Sec. II. We conclude with a summary in Sec. IV, where we briefly discuss possible applications and extensions of the presented work.

## II. MODEL

As a starting point, consider a quasi-static periodic shear deformation, fast enough that the entangled network topology can be regarded as approximately fixed, but slow enough that it does not couple longitudinally to the polymers, which have a finite contour length  $L$ . Hence, the polymers can maintain their stiff longitudinal modes equilibrated inside their tube-like cages, while the latter suffer from transverse deformations (squeezing and bending). Under such circumstances the network may be modeled as an effective homogeneous elastic solid embedded into a viscous solvent, with its osmotic compressibility and shear elasticity resulting essentially from the tube-like lateral confinement of the thermal contour undulations of the polymers. Based on this intuitive picture, the tube model of semiflexible polymers [13, 32, 33] yields a linear plateau modulus  $G_0^{\perp} = \rho k_B T / L_e$ . Here  $\rho$  is the contour length concentration and  $L_e = 3.0 \rho^{-2/5} \ell_p^{1/5}$  the entanglement length. We relate the frequency dependence  $G_{\perp}(\omega) = G_0^{\perp} / \chi_{\perp}(\omega)$  of the linear shear modulus to the dynamics of a stiff chain that is confined to a dynamic tube that itself is embedded in an elastic medium [29]. The overall dynamics is then obtained as the superposition

$$\chi_{\perp}(\omega) = \chi_{\text{STA}}(\omega) + \chi_{\text{EMA}}(\omega) \quad (1)$$

of the static-tube (STA) and the elastic-medium (EMA) contributions. The elastic medium accounts for the tube relaxation on intermediate times scales, larger than the entanglement time  $\omega_e^{-1}$ , which is typical relaxation time for the bending fluctuations of the confined polymer, but short enough that the tube fluctuation modes are still much shorter than the polymer length. The latter assumption suggests to describe the elastic medium as a two-dimensional membrane that is pierced by the tube (see Fig. 1a), whereas three-dimensional deformations of the medium become important for tube deformations comparable to the polymer length. Explicit expressions for the two contributions  $\chi_{\text{STA}}(\omega)$  and  $\chi_{\text{EMA}}(\omega)$  are derived in Appendices A and B, respectively. Equation (1) combines the chain dynamics at high frequencies, as derived from the static-tube approach (STA), with the relaxation of the surrounding network at low frequencies, obtained from the elastic-medium approach (EMA). The resulting crossover of the hybrid STA/EMA model is illustrated in Figs. 1b and 1c for the transverse MSD of a test chain in the solution and the linear shear modulus, respectively.

For the general case, where coupling of the effective medium to the longitudinal modes has to be taken into account, the total shear stress amplitude  $\sigma_{\omega}$  for a macroscopic periodic shear deformation of frequency  $\omega$  and strain amplitude  $\gamma_{\omega}$  is decomposed into the “transverse” effective medium contribution  $G_{\perp}(\omega)\gamma_{\omega}$  and a “longitudinal” single-polymer contribution  $G_{\parallel}(\omega)\gamma_{\omega}^{\parallel}$  [34]:

$$\sigma_{\omega} = G(\omega)\gamma_{\omega} = G_{\perp}(\omega)\gamma_{\omega} + G_{\parallel}(\omega)\gamma_{\omega}^{\parallel} \quad (2)$$

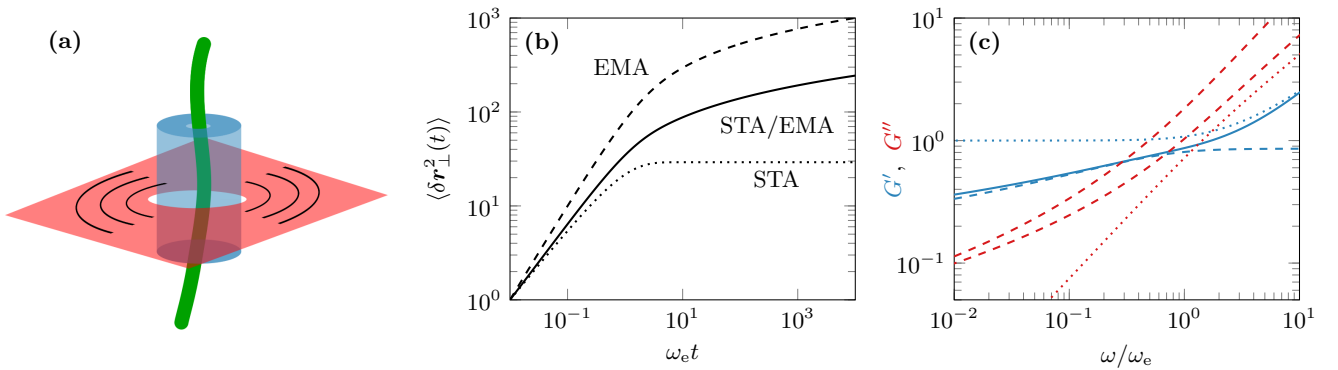


FIG. 1. Transient tube model for entangled stiff-polymer solutions. (a) Transverse fluctuations of a test chain (green) are confined to a tube-like cage (blue) formed by neighboring filaments; the (one-dimensional) tube is embedded into a two-dimensional elastic medium that represents the surrounding solution. (b,c) Combining the static tube (STA, dotted lines) with the two-dimensional elastic medium approach (EMA, dashed lines) yields a hybrid response (STA/EMA, solid lines) that is characterized by logarithmic long-time tails for the transverse MSD  $\langle \delta r_{\perp}^2(t) \rangle$ , corresponding to the logarithmic scaling of the linear storage and loss modulus  $G'(\omega)$  and  $G''(\omega)$  for low frequencies, very much reminiscent of frequently observed power-law rheology.

The frequency dependence  $G_{\parallel}(\omega) = G_0^{\parallel}/\chi_{\parallel}(\omega)$  with  $G_0^{\parallel} = 6\rho k_{\text{B}}T\ell_p^2/L_e^3$  is taken from the stretch response of a wormlike chain of length  $L_e$  [35] (see App. D). Now, our central idea is that the effective medium should be treated as a viscoelastic solvent that pulls on the longitudinal stretching modes of the individual polymers if the solution is sheared at higher frequency. It “buffers” the macroscopic excitation of the stiff modes featuring in the affine network models, so that  $\gamma_{\omega}^{\parallel} \leq \gamma_{\omega}$  (see Fig. 2a). Note that the stretching modes are excited in the linear regime, in contrast to the floppy-mode picture, where stretching contributes to second order only [10, 21, 36]. For the fully coupled or “crosslinked” case, one expects the effective medium to take up the deformation mismatch  $\gamma_{\omega} - \gamma_{\omega}^{\parallel}$ . To linear order, force balance then requires

$$\Gamma G_{\perp}(\omega)(\gamma_{\omega} - \gamma_{\omega}^{\parallel}) = G_{\parallel}(\omega)\gamma_{\omega}^{\parallel}. \quad (3)$$

Since the stress contributions of the effective-medium chains add up to the total tension felt by the test polymer of length  $L$ , the coupling parameter is expected to be of the form [37]

$$\Gamma = \Gamma_0(L/L_e)^2, \quad (4)$$

with an effective friction coefficient  $\Gamma_0$ . For frictional polymer contacts, one expects  $\Gamma_0$  to depend logarithmically on the shear rate [27], but, for simplicity, we neglect such a possible dependence in the following.

To generalize the model, we additionally want to allow for some slippage  $s\gamma_{\omega}$  with  $s \leq 1$  between the effective medium and the test polymer, which we anticipate to become most important in merely physically entangled solutions subjected to high strains and stresses. Hence,

substituting  $(1-s)\gamma_{\omega}$  for  $\gamma_{\omega}$  in the force balance, Eq. (3), the full constitutive equation reads

$$\frac{\gamma_{\omega}^{\parallel}}{\gamma_{\omega}} = \frac{1-s}{1 + G_{\parallel}(\omega)/[\Gamma G_{\perp}(\omega)]}. \quad (5)$$

In the limit of very stiff polymers,  $G_{\parallel}(\omega) \gg \Gamma G_{\perp}(\omega)$ , the effective medium takes up all the strain,  $\gamma_{\omega}^{\parallel} \sim 0$ , whereas the usual affine deformation rule  $\gamma_{\omega}^{\parallel} \sim \gamma_{\omega}$  is recovered in the long-polymer or strong-coupling limit  $G_{\parallel}(\omega) \ll \Gamma G_{\perp}(\omega)$ . Note, however, that the total shear modulus  $G(\omega)$ , as defined in Eq. (2), does not converge to the conventional form in the latter case, but rather to a hybrid mixture of the effective medium and the single-chain predictions.

### III. RESULTS

#### A. Linear response

To convey a general impression of the theory, we first consider its prediction

$$G(\omega) = G_{\perp}(\omega) + \frac{(1-s)G_{\parallel}(\omega)}{1 + G_{\parallel}(\omega)/[\Gamma G_{\perp}(\omega)]} \quad (6)$$

for the linear shear modulus.

Figure 2b illustrates the dependence of the plateau modulus  $G_0$ , which we identify with the linear elastic modulus at the entanglement frequency,  $G_0 \equiv G'(\omega_e)$ , on the concentration and the length of the polymers. A good approximation to the full expressions used in this plot can be obtained by substituting  $G_0^{\perp}$  for  $G_{\perp}(\omega_e)$  and

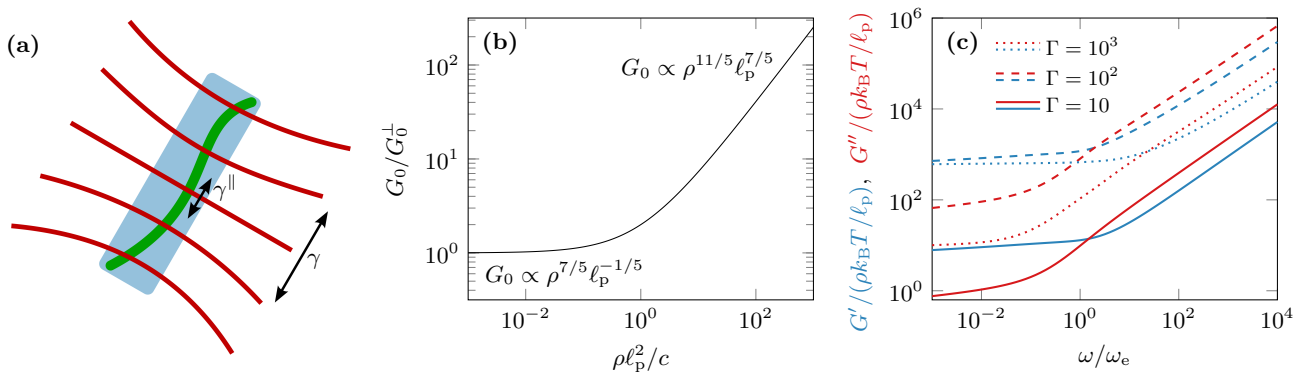


FIG. 2. Linear shear response. (a) The macroscopic deformation  $\gamma$  is shared among the bent background polymers (red), whose transverse fluctuations follow the transient tube model (STA/EMA, see Fig. 1), and the test polymer (green) that is longitudinally stretched by a strain  $\gamma^{\parallel}$ . (b) The plateau modulus  $G_0 \equiv G'(\omega_e)$  as a function of the reduced polymer concentration  $\rho\ell_p^2$ , computed from Eq. (6) with  $s = 0$ , echoes the two contributions to the network's rheology: a bending-dominated dilute/flexible regime ( $\rho\ell_p^2 \ll c$ ) where  $G_0/(k_B T \rho/\ell_p) \propto (\rho\ell_p^2)^{2/5}$  and a stretch-dominated dense/stiff regime ( $\rho\ell_p^2 \gg c$ ) where  $G_0/(k_B T \rho/\ell_p) \propto (\rho\ell_p^2)^{6/5}$ . (c) Frequency-dependent storage and loss modulus  $G'(\omega)$  and  $G''(\omega)$  for various coupling strengths  $\Gamma$ .

$G_0^{\parallel}$  for  $G_{\parallel}(\omega_e)$  in Eq. (6):

$$G_0/G_0^{\perp} \approx 1 + (\rho\ell_p^2/c)^{4/5} \quad (7)$$

Here, we identified the characteristic reduced concentration  $c$ , which decreases monotonically with the polymer length  $L$  according to

$$c^{4/5} = \frac{2/3}{1-s} \left( 1 + \frac{6\ell_p^2}{\Gamma_0 L^2} \right). \quad (8)$$

For dilute systems of more flexible polymers,  $\rho\ell_p^2 \ll c$ , Eq. (7) yields the tube-model prediction  $G_0 \sim G_0^{\perp}$ , while the stretching contributions dominate the dense/stiff regime,  $\rho\ell_p^2 \gg c$ , where  $G_0 \sim G_0^{\parallel}$ , such that

$$G_0/k_B T \propto \begin{cases} \rho^{7/5} \ell_p^{1/5}, & (\rho\ell_p^2 \ll c) \\ c^{-4/5} \rho^{11/5} \ell_p^{7/5}. & (\rho\ell_p^2 \gg c) \end{cases} \quad (9)$$

As recently reviewed by Tassieri [23], similar scaling regimes have been observed for pure entangled solutions of *in vitro* reconstituted F-actin [38], intact cardiac thin filaments [39], and DNA helix tubes [22]. The intermolecular friction and stickiness mentioned in the introduction might serve as a possible mechanism underlying such gel-like rheology despite the absence of any crosslinker molecules. The positive correlation between of  $G_0$  and the polymer length  $L$  predicted by Eq. (7), in particular the crossover from a length-independent  $G_0$  (for  $\rho\ell_p^2 \ll c$ ) to the quadratic scaling  $G_0 \propto L^2$  (for  $\rho\ell_p^2 \gg c$ ) as the filaments become longer, has also in agreement with experiments of pure F-actin solutions [33, 40] and cross-linked actin networks [41]. The data of Ref. [41] moreover suggest the shape of  $G_0(L)$  to turn from convex to concave as the rigidity of the

crosslinks increases, as also expected from our model, namely from  $d^2 G_0/dL^2 \propto 1 - (\Gamma_0/2)(L/\ell_p)^2$ , if we assume that the coupling strength decreases with increasing crosslink rigidity, such that  $d^2 G_0/dL^2 > 0$  for flexible and  $d^2 G_0/dL^2 < 0$  for rigid crosslinks, corresponding to  $\Gamma_0 < 2(\ell_p/L)^2$  (*i.e.*, weak coupling) and  $\Gamma_0 > 2(\ell_p/L)^2$  (strong coupling), respectively.

We next turn to the frequency dependence of the linear response. With typical *in vitro* solutions of F-actin in mind [42, 43], we set  $\ell_p = 17 \mu\text{m}$  and  $\rho = 10^4 \ell_p^{-2} \approx 40 \mu\text{m}^{-2}$  [29] in Fig. 2c. This plot depicts the real and imaginary parts  $G'(\omega)$  and  $G''(\omega)$  of  $G(\omega)$  for various filament lengths  $L$ , which reproduces not only the general shape but also the dependence on polymer length measured in macroscopic rheology (see, *e.g.*, the data by Hinner and Sackmann reproduced in Ref. [29], in particular the widening of the gap between  $G'(\omega)$  and  $G''(\omega)$  at high frequencies for short polymer lengths) and two-point microrheology [44]. Passive one-point microrheological measurements with small beads can plausibly not excite the longitudinal modes contributing to  $G(\omega)$  efficiently [20] and have indeed convincingly be explained by assuming a coupling via transverse single-polymer modes to the effective medium background alone [44].

## B. Nonlinear response

Next, we explore the potential of the model to account for complex features in the nonlinear rheology of stiff polymers and consider the frequency-dependent differential modulus  $K(\omega, \gamma) = d\sigma_{\omega}/d\gamma$ , which is nothing but the linear modulus  $G(\omega, \sigma_{\omega})$  at a prestress  $\sigma_{\omega}$  built up during the deformation of strain  $\gamma$  (at shear rate  $\dot{\gamma} = \omega/2\pi$ ). The prestress enters via the backbone tension  $f_{\omega} = 15|\sigma_{\omega}|/\rho$



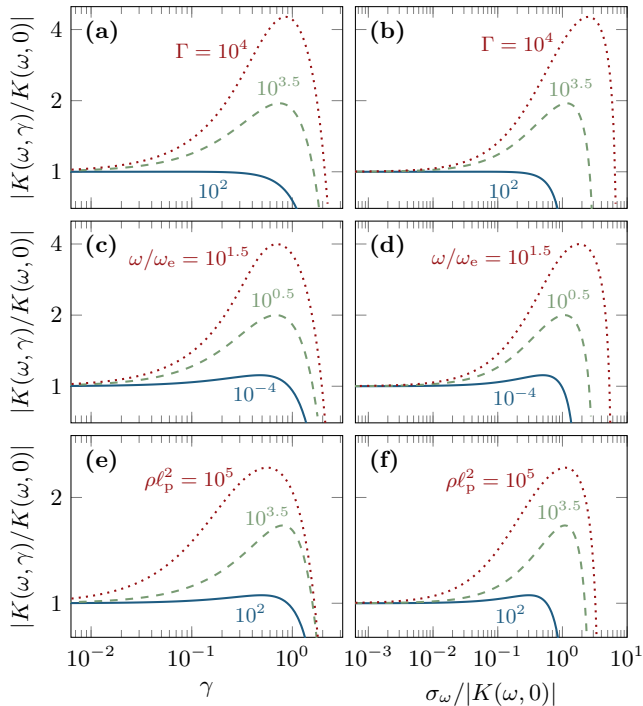


FIG. 3. Nonlinear shear response. Differential shear modulus  $K(\omega, \gamma)$ , obtained from Eq. (11), as a function of the strain  $\gamma$  and stress  $\sigma_\omega$  for various polymer lengths  $L$  (a,b; with  $\omega/\omega_e = 10^{-2}$  and  $\rho\ell_p^2 = 10^4$ ), various strain rates  $\dot{\gamma} = \omega/2\pi$  (c,d; with  $\Gamma = 10^3$  and  $\rho\ell_p^2 = 10^4$ ), and polymer concentrations  $\rho$  (e,f; with  $\Gamma = 10^{0.3}(\rho\ell_p^2)^{4/5}$  and  $\omega/\omega_e = 10^{-2}$ ).

of the stretched test polymer [35] (see App. D). At moderate strain amplitudes and low shear rates, the nonlinear response of the network can be traced back to the (quasi-stationary) tube deformations, which provoke strain softening [45, 46]. Within our approach, such softening is delegated to the effective medium, *i.e.*, the transverse response of the test chain. We here take the strain dependence  $K_\perp(\omega = 0, \gamma) \approx e^{-0.3\gamma^{2.5}}$  of the differential modulus for a quasi-stationary deformation from Ref. [45], where it was obtained from the tangential contraction of a test chain in an affinely deformed tube. It is multiplied to  $G_\perp(\omega)$ , which amounts to replacing

$$G_\perp(\omega) \mapsto K_\perp(\omega = 0, \gamma)G_\perp(\omega) \quad (10)$$

in Eq. (6). To compute the differential modulus  $K(\omega, \gamma) = G[\omega, \sigma_\omega(\gamma)]$  from the so extended linear modulus at prestress  $\sigma_\omega(\gamma)$ , we numerically integrate

$$\frac{d\sigma_\omega}{d\gamma} = G[\omega, \sigma_\omega(\gamma)] \quad (11)$$

using a standard Euler scheme. The nontrivial strain and stress dependence of  $K(\omega, \gamma)$  and the softening–stiffening crossover with increasing polymer length, shear rate, and polymer concentration displayed in Fig. 3 is in very good

FIG. 4. Strain  $\gamma$  (a–c) and stress  $\sigma$  (d–f) at the onset of the stiffening ( $\gamma_c, \sigma_c$ ; blue solid lines) and at the maximum of the differential shear modulus  $|K(\gamma, \omega)|$  ( $\gamma_{\max}, \sigma_{\max}$ ; red dashed lines) as a function of the coupling strength  $\Gamma \propto (L/L_e)^2$  (a,d; with  $\omega/\omega_e = 10^{-2}$  and  $\rho\ell_p^2 = 10^4$ ), the shear rate  $\dot{\gamma} = \omega/2\pi$  (b,e; with  $\Gamma = 10^3$  and  $\rho\ell_p^2 = 10^4$ ), and the reduced polymer concentration  $\rho\ell_p^2$  (c,f; with  $\Gamma = 10^{0.3}(\rho\ell_p^2)^{4/5}$  and  $\omega/\omega_e = 10^{-2}$ ).

agreement with experimental observations for F-actin solutions (see, *e.g.*, Fig. 4 of Ref. [17] and Fig. 5 of Ref. [18]). A subtle point in the measurement of  $K(\omega, \gamma)$  is to avoid too much inelastic flow [47]. For this reason it is not appropriate to apply a stationary prestress, and one has to resort to some sort of pulsed protocols, instead [17]. Otherwise the stiffening is wiped out by excessive slippage, which results from the fact that stiff polymer segments of length much shorter than their persistence length can hardly be stretched at all. To account for the strong slippage, we have set  $s = 0.95$  for the plots in Fig. 3. With smaller values the onset of the stiffening would occur at correspondingly smaller strains  $\gamma$ , as illustrated in Fig. 4 for the critical strain  $\gamma_c$  and stress  $\sigma_c$ , which we define through  $|\sigma_c| = 1.1|K(\omega, 0)|\gamma_c$  [48]. While the stiffening of  $K(\omega, \gamma)$  at intermediate values of the prestress is a consequence of the coupling to the stiff longitudinal modes, its breakdown at even larger prestress is due to the effective medium collapse at large strains, predicted by the nonlinear tube model [45, 46]. This underscores the importance of fluctuations on the entanglement scale even in the strong coupling regime, where one might naively expect the theory to be completely dominated by the longitudinal modes. Note that the yielding sets in at decreasingly smaller strains  $\gamma_c$  as the shear rate and/or polymer concentration become larger, as shown in Figs. 4b & c, although with an increasingly larger peak value  $|K(\omega, \gamma_c)|$  (not shown). This behavior might be a consequence of the linear approximation to the force balance, Eq. (3), which neglects any second-order stretch forces built up by the effective-medium chains. The influence of the latter should thus be investigated in a future study that extends the theory proposed here.

In Fig. 4, we show the strain and stress values  $\gamma_{\max}$  and  $\sigma_{\max}$  at which  $|K(\omega, \gamma)|$  takes its maximum. Again, we find these predictions to be in good agreement with experiments of pure [17, 18] and (flexibly) crosslinked [41, 49, 50] F-actin, actin-bundle networks [51], and collagen gels [48]. The length dependence of  $\gamma_c$  shown in Fig. 4a, for instance, is similar to the data in Ref. [41], although our model does not explicitly account for breaking of crosslinks under load, which is certainly the case in these experiments. Such inelastic effects become particularly apparent for the length dependence of the yield stress  $\sigma_{\max}$ . For bonds that break under a critical tension  $f_c$ , the force balance argument used in Eq. (3) yields a linear scaling  $\sigma_{\max} \propto (L/L_e)f_c$ , as indeed found in Ref. [41]. The numerical solution of our model, which delegates

FIG. 5. Strain-softening/-stiffening regimes as a function of the scaled coupling strength  $\Gamma(\rho\ell_p)^{-4/5} \propto (L/\ell_p)^2$  and the shear rate  $\dot{\gamma}$ . The curves separate the two regimes for three different polymer concentrations (see legend), where stiffening is exhibited when the actual stress exceeds the linear prediction by more than 10%, *i.e.*, when  $|\sigma| \geq 1.1|K(\omega, \gamma = 0)|\gamma$  for some  $\gamma \geq \gamma_c$ .

yielding to the soft tube deformations only, instead follows the approximate scaling  $\sigma_{\max} \propto L^{4/3}$ , in the stiffening regime (Fig. 4, for  $\Gamma > 10^3$ ). Within our approach, inelastic contributions may be introduced through a stress-dependent fraction of closed crosslinks [21, 51–54], represented by a stress-dependent coupling parameter  $\Gamma$ .

#### IV. SUMMARY AND CONCLUSIONS

We have developed an analytically tractable model for the linear and nonlinear viscoelastic response of entangled solutions of stiff biopolymers. Our approach combines an extended version of the tube model for semiflexible polymer solutions that properly captures the transverse bending fluctuations beyond the lifetime of the tube itself (*i.e.*, beyond the entanglement time) with the non-affine stretch response of the individual polymers. The linear frictional coupling between soft bending and stiff stretching modes at the entanglement points yields a nontrivial dependence of the linear shear modulus on the polymer concentration and persistence length, providing a plausible explanation for experimentally found scaling laws that are in apparent conflict with the standard tube-model predictions [23]. We also provided solid evidence that our approach correctly captures the nonlinear response, as illustrated for the dependence of the differential shear modulus on the polymer length, shear rate, and polymer concentration. Within the proposed theory, this rich phenomenology is derived from a linear microrheological element, determined by the force balance in Eq. , whereby nonlinearities enter via strain-softening of a quasi-statically deformed tube and a finite prestress built up during a macroscopic deformation. An interesting question to be answered in a future study is thus how nonlinear effects at the microscopic level, like second-order longitudinal stretching of the effective-medium chains, would alter this picture. Another potential extension of the presented framework is to explicitly account for strain-induced (or imposed) polymer alignment [48, 55, 56] at the level of the coarse-grained force balance in Eq. (3), which we expect to provide a similar contribution to the stiffening as, for instance, recently discussed by Amuasi *et al.* [57] based on computer simulations of quasi-statically deformed crosslinked polymer solutions. These authors found the tensile filaments to be pulled into the stretch direction by the (many) surrounding polymers, which thereby build up large stresses that are stored in their bending modes. This leads to an early

non-affine bending-dominated stiffening ( $|K| \sim e^{\sigma L/G_0}$ ), before the affine stretch-dominated regime ( $K \sim \sigma^{3/2}$ ) at large strains becomes visible. In addition, adjacent polymers that are aligned in parallel as the network is strained may exhibit an increased probability to form entanglement points along their contours [58]. Finally, we would like to note that the inter-chain coupling could also depend on the shear rate. While the logarithmic dependence of the friction force between contacting polymers on the sliding velocity suggests  $\Gamma \propto \ln \omega$  [27], an explicit model for transient crosslinks may resort to load-dependent bond kinetics with  $\Gamma$  being proportional to the fraction of closed bonds [21, 54].

#### ACKNOWLEDGMENTS

We thank Pablo Fernández for fruitful discussions during the early stages of this work. M.L. acknowledges the financial support from the European Union through the European Social Funds (ESF program “Wissens- und Know-How-Transfer”) and the graduate school “Leipzig School of Natural Sciences – Building with Molecules and Nano-objects (BuildMoNa)”.

#### Appendix A: Static tube approach (STA)

We consider a semidilute solution of stiff polymers over a time span short enough that the entangled network topology can be regarded as fixed and the confinement tubes, representing the caging effect due to neighboring network chains, as approximately static. The dynamics of a test chain in solution can then be modeled by the (overdamped) Langevin equation [59]

$$\zeta_{\perp} \partial_t \mathbf{r}_{\perp} = -\kappa \partial_s^4 \mathbf{r}_{\perp} + f \partial_s^2 \mathbf{r}_{\perp} - \phi \mathbf{r}_{\perp} + \boldsymbol{\xi}_{\perp} \quad (\text{A1})$$

for a weakly bending wormlike chain, described by the transverse deviations  $\mathbf{r}_{\perp} \equiv \mathbf{r}_{\perp}(s, t)$  of its contour of length  $L$  from the straight ground state at position  $s \in [0, L]$  along the contour and time  $t$ . The solvent friction coefficient  $\zeta_{\perp}$  per unit length is related to the Gaussian thermal noise  $\boldsymbol{\xi}_{\perp}$  by the fluctuation-dissipation theorem  $\langle \boldsymbol{\xi}_{\perp}(s, t) \boldsymbol{\xi}_{\perp}(s', t') \rangle = 2k_B T \zeta_{\perp} \delta(s-s') \delta(t-t')$ , with the Boltzmann constant  $k_B$  and temperature  $T$ . The coefficients  $\kappa = k_B T \ell_p$ ,  $f$ , and  $\phi$  denote the bending rigidity ( $\ell_p$  being the persistence length), the backbone tension, and the strength of the harmonic confinement potential that represents the tube, respectively. Assuming hinged ends (*i.e.*, both the transverse excursion  $\mathbf{r}_{\perp}$  the curvature  $\partial_s^2 \mathbf{r}_{\perp}$  at the ends  $s = 0$  and  $s = L$  vanish), one can expand  $\mathbf{r}_{\perp}(s, t) = \sum_{k=1}^{\infty} \mathbf{r}_k^{\perp}(t) \sin(\pi k s/L)$  into eigenmodes and integrate Eq. (A1) to obtain, *e.g.*, the MSD

$$\begin{aligned} \langle \delta \mathbf{r}_{\perp}^2(t) \rangle &\equiv \int_0^L \frac{ds}{L} \langle [\mathbf{r}_{\perp}(s, t) - \mathbf{r}_{\perp}(s, 0)]^2 \rangle \\ &= \frac{4L^3}{\pi^4 \ell_p} \sum_{k=1}^{\infty} \frac{1 - \exp(-\omega_k t)}{k^4 + k^2 f/f_e + (L/L_e)^4}, \end{aligned} \quad (\text{A2})$$

where  $\omega_k = \omega_L[k^4 + k^2 f/f_e + (L/L_e)^4]$ , with  $\omega_L = \pi^4 \kappa / (\zeta_\perp L^4)$ , is the inverse characteristic relaxation time of the  $k$ -th mode,  $L_e = \pi(\ell_p/\phi)^{1/4}$  the entanglement length (to keep the expressions short, we introduce this definition, differing from  $L_e = 2\sqrt{2}(\ell_p/\phi)^{1/4}$  usually used in the literature), and  $f_e = \pi^2 \kappa / L^2$  the Euler force. Replacing the sum in Eq. (A2) by an integral, one obtains the MSD

$$\langle \delta \mathbf{r}_\perp^2(t) \rangle \propto (L_e^3/\ell_p) [1 - \Gamma(3/4, \omega_e t) / \Gamma(3/4)] \quad (\text{A3})$$

of an unstretched (*i.e.*,  $f = 0$ ) chain in a static tube. It exhibits a crossover around the entanglement time  $\tau_e \equiv \omega_e^{-1} = \zeta_\perp L_e^4 / (\pi^4 \kappa)$  from an initial growth close to the scaling  $\langle \delta \mathbf{r}_\perp^2(t) \rangle \sim t^{3/4}$  of a free chain towards a saturation regime at large times,  $\langle \delta \mathbf{r}_\perp^2(t \gg \omega_e^{-1}) \rangle \sim \sqrt{2} L_e^3 / \ell_p$ , as shown in Fig. 1.

The Fourier transform  $\langle \delta \mathbf{r}_\perp^2(\omega) \rangle$  of the MSD is directly related to the imaginary part of the susceptibility  $\chi(\omega) = \chi'(\omega) + i\chi''(\omega)$  by the fluctuation-dissipation theorem  $\chi''(\omega) = -\omega \langle \delta \mathbf{r}_\perp^2(\omega) \rangle / (2k_B T)$ . Using the Kramers–Kronig relations the complex response function is obtained as [30]

$$\chi_{\text{STA}}(\omega) = \sum_{k=1}^{\infty} \frac{(2\sqrt{2}/\pi)(L/L_e)^3}{[k^4 + k^2 f/f_e + (L/L_e)^4](1 + i\omega/\omega_k)}, \quad (\text{A4})$$

here normalized to  $\chi_{\text{STA}}(0) = 1$  (as before, after replacing the sum by an integral). Its inverse  $G_{\text{STA}}(\omega) = G_0^\perp / \chi_{\text{STA}}(\omega)$  provides the contribution of the polymer network (*i.e.*, without the solvent contribution) to the dynamic shear modulus [35]. The real and imaginary part  $G'_{\text{STA}}(\omega)$  and  $G''_{\text{STA}}(\omega)$  of  $G_{\text{STA}}(\omega)$  are plotted in the right panel of Fig. 1.

## Appendix B: Effective medium approach (EMA)

The equation of motion (in the overdamped limit, corresponding to low network densities) for an in-plane deformation  $\mathbf{u} \equiv \mathbf{u}(\mathbf{x}, t)$  (no bending) of a thin two-dimensional plate at position  $\mathbf{x}$  reads [60, 61]

$$\zeta \partial_t \mathbf{u} = \frac{Eh}{2(1+\nu)} \Delta \mathbf{u} + \frac{Eh}{2(1-\nu)} \nabla(\nabla \cdot \mathbf{u}) + \boldsymbol{\xi}, \quad (\text{B1})$$

where  $\zeta$  denotes the friction coefficient per area,  $E$  the Young's modulus, and  $h$  the thickness of the plate. The Gaussian thermal noise  $\boldsymbol{\xi}$  obeys  $\langle \boldsymbol{\xi}(\mathbf{x}, t) \boldsymbol{\xi} \rangle = 2k_B T A \zeta \delta(\mathbf{x}) \delta(t)$ , with  $A$  being the surface area of the plate. Fourier transforming Eq. (B1) one finds that  $\mathbf{u}_q$  can be decomposed into a longitudinal (*i.e.*, rotation free) component  $\mathbf{u}_q^l$  that points into the direction of  $\mathbf{q}$  and a transverse (divergence free) component  $\mathbf{u}_q^t$ , which both solve a diffusion equation  $\partial_t \mathbf{u}_q^{l,t} = -D_{l,t} q^2 \mathbf{u}_q^{l,t} + \boldsymbol{\xi}_q^{l,t} / \zeta$  with the diffusion constants  $D_l = Eh / [\zeta(1 - \nu^2)]$  and  $D_t = Eh / [2\zeta(1 - \nu)]$ . We thus obtain the mean squared

displacement as

$$\langle \delta \mathbf{u}^2(t) \rangle = \frac{1}{A} \int_{|\mathbf{q}| < q_c} \frac{d\mathbf{q}}{(2\pi)^2} \left[ \langle |\mathbf{u}_q^l|^2 \rangle (1 - e^{-D_l q^2 t}) + \langle |\mathbf{u}_q^t|^2 \rangle (1 - e^{-D_t q^2 t}) \right], \quad (\text{B2})$$

with the amplitudes  $\langle |\mathbf{u}_q^l|^2 \rangle = k_B T A / (\zeta D_l q^2)$  and  $\langle |\mathbf{u}_q^t|^2 \rangle = k_B T A / (\zeta D_t q^2)$ . The high-wavenumber cutoff  $q_c$ , also required to regularize the three-dimensional elastic network theory [61], originates from the underlying microscopic length scale of the polymer network, below which the deformations are suppressed. It should thus be traced back to, *e.g.*, the mesh size of a meshwork of rigid rods or the entanglement length of the semiflexible polymer solution.

For the sake of simplicity and in order to compare this approach with other models and experimental observations, we now set both the longitudinal and the transverse relaxation time of the elastic continuum equal to an entanglement time  $1/\omega_e$ , *i.e.*,  $D_l q^2 = D_t q^2 = \omega_e$ , and obtain the MSD

$$\langle \delta \mathbf{u}^2(t) \rangle = \frac{k_B T}{2\pi \zeta D} [\gamma_E + \ln(\omega_e t) - \text{Ei}(-\omega_e t)], \quad (\text{B3})$$

where  $\text{Ei}(x) = -\int_{-x}^{\infty} ds \exp(-s)/s$  is the exponential integral. For large  $t$ , the MSD of the two-dimensional elastic medium thus grows logarithmically and does not saturate, as it is the case, for, *e.g.*, the transverse MSD of a polymer confined to a static tube, as illustrated in the left panel of Fig. 1. The Fourier transform  $\langle \delta \mathbf{u}^2(\omega) \rangle$  yields, via the fluctuation-dissipation theorem  $\tilde{\chi}_{\text{EMA}}''(\omega) = -\omega \langle \delta \mathbf{u}^2(\omega) \rangle / (2k_B T)$  together with the Kramers–Kronig relations, the susceptibility  $\tilde{\chi}_{\text{EMA}}(\omega) = \tilde{\chi}_{\text{EMA}}'(\omega) + i\tilde{\chi}_{\text{EMA}}''(\omega)$ ,

$$\chi_{\text{EMA}}(\omega) = \frac{\ln(1 + \omega_e^2/\omega^2) + i[\pi - 2 \arctan(\omega/\omega_e)]}{2^{-5/8} \sqrt{\pi^2 + 4(\ln 2)^2}} \quad (\text{B4})$$

where we dropped the dimensionful factor (as indicated by the tilde) and normalized it to  $|\chi_{\text{EMA}}(\omega_e)| = |\chi_{\text{STA}}(\omega_e)|$ . The latter follows from balancing the contribution  $G_{\text{EMA}}(\omega) = G_0^\perp / \chi_{\text{EMA}}(\omega)$  of the polymer network (without the solvent contribution) to the dynamic shear modulus with the tube modulus at  $\omega = \omega_e$  via  $|G_{\text{EMA}}(\omega_e)| = |G_{\text{STA}}(\omega_e)|$ . As a consequence of the infinitely growing MSD, the two-dimensional EMA yields a scaling  $G_{\text{EMA}}(\omega) \propto 1/\ln(\omega/\omega_e)$  at low frequencies, rather reminiscent of power-law rheology (with small exponent), and does not exhibit a plateau modulus, since  $G_{\text{EMA}}(\omega \rightarrow 0) = 0$ .

## Appendix C: STA/EMA hybrid

An obvious hybrid model combining the static tube model that correctly captures the WLC dynamics at high

frequencies with the effective medium approach that accounts for collective network effects dominating the long time response, is given by [61]

$$\langle \delta \mathbf{r}_\perp^2(t) \rangle = \langle \delta \mathbf{r}_\perp^2(t) \rangle_{\text{STA}} + \langle \delta \mathbf{u}^2(t) \rangle_{\text{EMA}} \quad (\text{C1})$$

and the corresponding susceptibility  $\chi_\perp(\omega)$  given in Eq. (1). A similar hybrid model, named elastic network approximation, was proposed by Morse [29], who added up the square roots of the MSDs to obtain an estimate for the tube diameter. The idea of the Eq. (C1) is that the polymer is confined to a tube, which is not static but undergoes deformations due to permanent network rearrangement. This is illustrated in Fig. 1, where we compare both the MSD and the microscopic shear modulus with the corresponding static tube and elastic medium results.

#### Appendix D: Stretch response of a WBR

We outline the calculation of the end-to-end response function  $\chi_\parallel(\omega)$  of a free WBR as proposed by Gittes and MacKintosh [35] and extent it to non-zero backbone tension  $f$ . Within the WBR approximation, the stored length is estimated as

$$\delta \ell(t) = \frac{1}{2} \int_0^L ds [\mathbf{r}'_\perp(t, s)]^2 \quad (\text{D1})$$

and the MSD  $\langle \delta \ell^2(t) \rangle \equiv \langle [\delta \ell(t) - \delta \ell(0)]^2 \rangle$  becomes

$$\langle \delta \ell^2(t) \rangle = \frac{\pi^4}{16L^2} \sum_{k,m} k^2 m^2 [\langle \mathbf{r}_k^\perp(0)^2 \mathbf{r}_m^\perp(0)^2 \rangle - \langle \mathbf{r}_k^\perp(0)^2 \mathbf{r}_m^\perp(t)^2 \rangle] \quad (\text{D2})$$

with the same eigenmode decomposition  $\mathbf{r}_\perp(s, t) = \sum_{k=1}^\infty \mathbf{r}_k^\perp(t) \sin(\pi k s / L)$  used in Eq. (A2). Using Wick's theorem,  $\langle \mathbf{r}_k^\perp(0)^2 \mathbf{r}_m^\perp(t)^2 \rangle = \langle \mathbf{r}_k^\perp(0)^2 \rangle^2 + 2 \langle \mathbf{r}_k^\perp(0) \mathbf{r}_m^\perp(t) \rangle^2$ , and equipartition,  $\langle (\mathbf{r}_k^\perp)^2 \rangle = 4L^3 / [\ell_p \pi^4 (k^4 + k^2 f / f_e)]$ , one arrives at

$$\langle \delta \ell^2(t) \rangle = \frac{L^4}{\pi^4 \ell_p^2} \sum_{k=1}^\infty \frac{k^4 [1 - \exp(-2\omega_k t)]}{[k^4 + k^2 f / f_e + (L/L_e)^4]^2}. \quad (\text{D3})$$

Applying the FDT and Kramers-Kronig relations to its Fourier transform  $\langle \delta \ell^2(\omega) \rangle$ , yields the susceptibility (c.f. App. A)

$$\chi_\parallel(\omega) = \sum_k \frac{(8\sqrt{2}/\pi)(L_e/L)^3 k^4}{[k^4 + k^2 f / f_e + (L/L_e)^4]^2 (1 - i\omega / 2\omega_k)}. \quad (\text{D4})$$

and the linear shear modulus

$$G_\parallel(\omega) = G_0^\parallel / \chi_\parallel(\omega), \quad (\text{D5})$$

with the plateau modulus  $G_0^\parallel \equiv G_\parallel(\omega = 0) = \rho k_B T \ell_p^2 / L_e^3$  for polymer segments of length  $L = L_e$ , as used in our model. Again, we approximate the sum in Eq. (D4) by an integral and normalize the susceptibility to  $\chi_\parallel(0) = 1$ .

- 
- [1] P.-G. De Gennes, *Scaling concepts in polymer physics* (Cornell university press, 1979).
- [2] K. E. Kasza, A. C. Rowat, J. Liu, T. E. Angelini, C. P. Brangwynne, G. H. Koenderink, and D. A. Weitz, *Cell structure and dynamics*, *Curr. Opin. Cell Biol.* **19**, 101 (2007).
- [3] B. D. Hoffman and J. C. Crocker, *Annu. Rev. Biomed. Eng.* **11**, 259 (2009).
- [4] P. Kollmannsberger and B. Fabry, *Annu. Rev. Mater. Res.* **41**, 75 (2011).
- [5] J. Wilhelm and E. Frey, *Phys. Rev. Lett.* **91**, 108103 (2003).
- [6] D. A. Head, A. J. Levine, and F. C. MacKintosh, *Phys. Rev. Lett.* **91**, 108102 (2003).
- [7] D. A. Head, A. J. Levine, and F. C. MacKintosh, *Phys. Rev. Lett.* **91**, 108102 (2003).
- [8] O. Stenull and T. C. Lubensky, *arXiv:cond-mat/1108.4328* (2011).
- [9] C. P. Broedersz and F. C. MacKintosh, *Rev. Mod. Phys.* **86**, 995 (2014).
- [10] C. Heussinger and E. Frey, *Phys. Rev. Lett.* **97**, 105501 (2006).
- [11] C. Heussinger, B. Schaefer, and E. Frey, *Phys. Rev. E* **76**, 031906 (2007).
- [12] M. L. Gardel, J. H. Shin, F. C. MacKintosh, L. Mahadevan, P. Matsudaira, and D. A. Weitz, *Science* **304**, 1301 (2004).
- [13] D. C. Morse, *Phys. Rev. E* **58**, R1237 (1998).
- [14] D. C. Morse, *Macromolecules* **31**, 7030 (1998).
- [15] F. C. MacKintosh, J. Käs, and P. A. Janmey, *Phys. Rev. Lett.* **75**, 4425 (1995).
- [16] P. R. Onck, T. Koeman, T. van Dillen, and E. van der Giessen, *Phys. Rev. Lett.* **95**, 178102 (2005).
- [17] C. Semmrich, T. Storz, J. Glaser, R. Merkel, A. R. Bausch, and K. Kroy, *Proc. Natl. Acad. Sci. U.S.A.* **104**(51), 20199 (2007).
- [18] C. Semmrich, R. J. Larsen, and A. R. Bausch, *Soft Matter* **4**, 1675 (2008).
- [19] T. T. Falzone, S. Blair, and R. M. Robertson-Anderson, *Soft Matter* **11**, 4418 (2015).
- [20] A. Sonn-Segev, A. Bernheim-Groswasser, H. Diamant, and Y. Roichman, *Phys. Rev. Lett.* **112**, 088301 (2014).
- [21] J. Plagge, A. Fischer, and C. Heussinger, *Phys. Rev. E* **93**, 062502 (2016).
- [22] T. Schuldt, J. Schnauß, T. Händler, M. Glaser, J. Lorenz, T. Golde, J. A. Käs, and D. M. Smith, *Phys. Rev. Lett.* **117**, 197801 (2016).
- [23] M. Tassieri, *Macromolecules* **50**, 5611 (2017).



- [24] B. Fabry, G. N. Maksym, J. P. Butler, M. Glogauer, D. Navajas, and J. J. Fredberg, *Phys. Rev. Lett.* **87**, 148102 (2001).
- [25] M. A. Dichtl and E. Sackmann, *Proc. Natl. Acad. Sci. U.S.A.* **99**, 6533 (2002).
- [26] M. Srinivasan and S. Walcott, *Phys. Rev. E* **80**, 046124 (2009).
- [27] A. Ward, F. Hilitski, W. Schwenger, D. Welch, A. W. C. Lau, V. Vitelli, L. Mahadevan, and Z. Dogic, *Nat. Mater.* **14**, 583 (2015).
- [28] F. Gittes, B. Schnurr, P. D. Olmsted, F. C. MacKintosh, and C. F. Schmidt, *Phys. Rev. Lett.* **79**, 3286 (1997).
- [29] D. C. Morse, *Phys. Rev. E* **63**, 031502 (2001).
- [30] K. Kroy and J. Glaser, *New J. Phys.* **9**, 416 (2007).
- [31] J. Glaser, O. Hallatschek, and K. Kroy, *The European physical journal. E, Soft matter* **26**, 123 (2008).
- [32] H. Isambert and A. C. Maggs, *Macromolecules* **29**, 1036 (1996).
- [33] B. Hinner, M. Tempel, E. Sackmann, K. Kroy, and E. Frey, *Phys. Rev. Lett.* **81**, 2614 (1998).
- [34] The transverse deformation is determined by the strain  $\gamma_\omega - \gamma_\omega^\parallel$  taken up by the effective medium only. With  $G_\parallel(\omega) \gg G_\perp(\omega)$ , this yields Eq. (2):  $\sigma_\omega = G_\perp(\omega)\gamma_\omega + [G_\parallel(\omega) - G_\perp(\omega)]\gamma_\omega^\parallel \simeq G_\perp(\omega)\gamma_\omega + G_\parallel(\omega)\gamma_\omega^\parallel$ .
- [35] F. Gittes and F. MacKintosh, *Phys. Rev. E* **58**, R1241 (1998).
- [36] M. Wardetzky, *Soft Matter* **11**, 343 (2014).
- [37] C. P. Broedersz, C. Storm, and F. C. MacKintosh, *Phys. Rev. E* **79**, 061914 (2009).
- [38] M. Tassieri, R. M. L. Evans, L. Barbu-Tudoran, G. N. Khaname, J. Trinick, and T. A. Waigh, *Phys. Rev. Lett.* **101**, 198301 (2008).
- [39] M. Tassieri, R. Evans, L. Barbu-Tudoran, J. Trinick, and T. Waigh, *Biophys. J.* **94**, 2170 (2008).
- [40] F. G. Schmidt, B. Hinner, and E. Sackmann, *Phys. Rev. E* **61**, 5646 (2000).
- [41] K. E. Kasza, C. P. Broedersz, G. H. Koenderink, Y. C. Lin, W. Messner, E. a. Millman, F. Nakamura, T. P. Stossel, F. C. Mackintosh, and D. a. Weitz, *Biophys. J.* **99**, 1091 (2010).
- [42] F. Gittes, B. Mickey, J. Nettleton, and J. Howard, *The Journal of cell biology* **120**, 923 (1993).
- [43] H. Isambert, P. Venier, A. C. Maggs, A. Fattoum, R. Kassab, D. Pantaloni, and M.-F. Carlier, *J. Biol. Chem.* **270**, 11437 (1995).
- [44] J. Liu, M. L. Gardel, K. Kroy, E. Frey, B. D. Hoffman, J. C. Crocker, A. R. Bausch, and D. A. Weitz, *Phys. Rev. Lett.* **96**, 118104 (2006).
- [45] D. C. Morse, *Macromolecules* **32**, 5934 (1999).
- [46] P. Fernández, S. Grosser, and K. Kroy, *Soft Matter* **5**, 2047 (2009).
- [47] P. Fernández and A. Ott, *Phys. Rev. Lett.* **100**, 238102 (2008).
- [48] D. Vader, A. Kabla, D. Weitz, and L. Mahadevan, *PLoS One* **4**, e5902 (2009).
- [49] M. L. Gardel, J. H. Shin, F. C. MacKintosh, L. Mahadevan, P. A. Matsudaira, and D. A. Weitz, *Phys. Rev. Lett.* **93**, 188102 (2004).
- [50] K. Kasza, G. Koenderink, Y. Lin, C. Broedersz, W. Messner, F. Nakamura, T. Stossel, F. MacKintosh, and D. Weitz, *Phys. Rev. E* **79**, 041928 (2009).
- [51] M. Maier, K. W. Müller, C. Heussinger, S. Köhler, W. a. Wall, a. R. Bausch, and O. Lieleg, *Eur. Phys. J. E* **38**, 50 (2015).
- [52] L. Wolff, P. Fernández, and K. Kroy, *New J. Phys.* **12**, 053024 (2010).
- [53] L. Wolff, P. Fernández, and K. Kroy, *PLoS One* **7**, e40063 (2012).
- [54] M. Gralka and K. Kroy, *Biochimica et Biophysica Acta (BBA) - Molecular Cell Research* **1853**, 3025 (2015).
- [55] J. Feng, H. Levine, X. Mao, and L. M. Sander, *Phys. Rev. E* **91**, 042710 (2015).
- [56] M. Lämmel, E. Jaschinski, R. Merkel, and K. Kroy, *Polymers* **8** (2016).
- [57] H. E. Amuasi, C. Heussinger, R. L. C. Vink, and A. Zippelius, *New J. Phys.* **17**, 083035 (2015).
- [58] P. Benetatos, A. von der Heydt, and A. Zippelius, *New J. Phys.* **16**, 113037 (2014).
- [59] O. Hallatschek, E. Frey, and K. Kroy, *Phys. Rev. E* **75**, 031905 (2007).
- [60] L. D. Landau and E. Lifshitz, *Course of Theoretical Physics* **3** (1986).
- [61] K. Kroy and E. Frey, "Scattering in polymeric and colloidal systems," (CRC Press, 1999) Chap. Dynamic Scattering from Semiflexible Polymers, p. 496, 1st ed.



# Bibliography

- [1] J. Howard, *Mechanics of motor proteins and the cytoskeleton* (Sinauer Associates, Inc., 2001).
- [2] D. Boal, *Mechanics of the cell* (Cambridge University Press, 2002).
- [3] P. A. Janmey and C. A. McCulloch, “Cell mechanics: integrating cell responses to mechanical stimuli”, *Annu. Rev. Biomed. Eng.* **9**, 1–34 (2007).
- [4] K. E. Kasza, A. C. Rowat, J. Liu, T. E. Angelini, C. P. Brangwynne, G. H. Koenderink, and D. A. Weitz, “The cell as a material”, *Curr. Opin. Cell Biol.* **19**, 101–107 (2007).
- [5] D. A. Fletcher and R. D. Mullins, “Cell mechanics and the cytoskeleton”, *Nature* **463**, 485–(2010).
- [6] D. C. Morse, “Viscoelasticity of concentrated isotropic solutions of semiflexible polymers. 1. model and stress tensor”, *Macromolecules* **31**, 7030–7043 (1998).
- [7] C. P. Broedersz and F. C. MacKintosh, “Modeling semiflexible polymer networks”, *Rev. Mod. Phys.* **86**, 995–1036 (2014).
- [8] A. R. Bausch and K. Kroy, “A bottom-up approach to cell mechanics”, *Nat. Phys.* **2**(4), 231–238 (2006).
- [9] O. Lieleg, M. M. a. E. Claessens, and A. R. Bausch, “Structure and dynamics of cross-linked actin networks”, *Soft Matter* **6**, 218 (2010).
- [10] R. H. Pritchard, Y. Y. Shery Huang, and E. M. Terentjev, “Mechanics of biological networks: from the cell cytoskeleton to connective tissue”, *Soft Matter* **10**, 1864 (2014).
- [11] R. Ruddies, W. H. Goldmann, G. Isenberg, and E. Sackmann, “The viscoelasticity of entangled actin networks: the influence of defects and modulation by talin and vinculin”, *Eur. Biophys. J.* **22**, 309–321 (1993).
- [12] J. Käs, H. Strey, and E. Sackmann, “Direct imaging of reptation for semiflexible actin filaments”, *Nature* **368**, 226–9 (1994).
- [13] J. Käs, H. Strey, J. Tang, D. Finger, R. Ezzell, E. Sackmann, and P. Janmey, “F-actin, a model polymer for semiflexible chains in dilute, semidilute, and liquid crystalline solutions”, *Biophys. J.* **70**, 609–625 (1996).
- [14] B. Hinner, M. Tempel, E. Sackmann, K. Kroy, and E. Frey, “Entanglement, elasticity, and viscous relaxation of actin solutions”, *Phys. Rev. Lett.* **81**, 2614–2617 (1998).

- [15] F. G. Schmidt, B. Hinner, and E. Sackmann, "Microrheometry underestimates the values of the viscoelastic moduli in measurements on f-actin solutions compared to macrorheometry", *Phys. Rev. E* **61**, 5646–5653 (2000).
- [16] M. L. Gardel, M. T. Valentine, J. C. Crocker, A. R. Bausch, and D. A. Weitz, "Microrheology of entangled f-actin solutions", *Phys. Rev. Lett.* **91**, 158302 (2003).
- [17] M. Keller, R. Tharmann, M. A. Dichtl, A. R. Bausch, and E. Sackmann, "Slow filament dynamics and viscoelasticity in entangled and active actin networks", *Philosophical Transactions of the Royal Society of London A: Mathematical, Physical and Engineering Sciences* **361**, 699–712 (2003).
- [18] J. Liu, M. L. Gardel, K. Kroy, E. Frey, B. D. Hoffman, J. C. Crocker, A. R. Bausch, and D. A. Weitz, "Microrheology probes length scale dependent rheology", *Phys. Rev. Lett.* **96**, 118104 (2006).
- [19] J. Glaser, D. Chakraborty, K. Kroy, I. Lauter, M. Degawa, N. Kirchgeßner, B. Hoffmann, R. Merkel, and M. Giesen, "Tube Width Fluctuations in F-Actin Solutions", *Phys. Rev. Lett.* **105**, 3–6 (2010).
- [20] V. Pelletier, N. Gal, P. Fournier, and M. L. Kilfoil, "Microrheology of microtubule solutions and actin-microtubule composite networks", *Phys. Rev. Lett.* **102**, 188303 (2009).
- [21] M. H. Jensen, E. J. Morris, R. D. Goldman, and D. A. Weitz, "Emergent properties of composite semiflexible biopolymer networks", *BioArchitecture* **4**, 138–143 (2014).
- [22] M. H. Jensen, E. J. Morris, and D. A. Weitz, "Mechanics and dynamics of reconstituted cytoskeletal systems", *Biochimica et Biophysica Acta (BBA) - Molecular Cell Research* **1853**, 3038–3042 (2015).
- [23] O. Lieleg, M. M. A. E. Claessens, Y. Luan, and A. R. Bausch, "Transient binding and dissipation in cross-linked actin networks", *Phys. Rev. Lett.* **101**, 108101 (2008).
- [24] K. E. Kasza, C. P. Broedersz, G. H. Koenderink, Y. C. Lin, W. Messner, E. a. Millman, F. Nakamura, T. P. Stossel, F. C. Mackintosh, and D. a. Weitz, "Actin filament length tunes elasticity of flexibly cross-linked actin networks.", *Biophys. J.* **99**, 1091–100 (2010).
- [25] N. a. Kurniawan, L. H. Wong, and R. Rajagopalan, "Early stiffening and softening of collagen: Interplay of deformation mechanisms in biopolymer networks", *Biomacromolecules* **13**, 691–698 (2012).
- [26] L. Wolff, P. Fernández, and K. Kroy, "Resolving the stiffening-softening paradox in cell mechanics", *PLoS One* **7**, e40063– (2012).
- [27] O. Lieleg, M. M. A. E. Claessens, C. Heussinger, E. Frey, and A. R. Bausch, "Mechanics of bundled semiflexible polymer networks", *Phys. Rev. Lett.* **99**, 088102 (2007).
- [28] O. Lieleg and A. R. Bausch, "Cross-linker unbinding and self-similarity in bundled cytoskeletal networks", *Phys. Rev. Lett.* **99**, 158105 (2007).
- [29] K. Schmoller, O. Lieleg, and A. Bausch, "Structural and viscoelastic properties of actin/filamin networks: cross-linked versus bundled networks", *Biophys. J.* **97**, 83–89 (2009).
- [30] O. Lieleg, J. Kayser, G. Brambilla, L. Cipelletti, and A. R. Bausch, "Slow dynamics and internal stress relaxation in bundled cytoskeletal networks", *Nat. Mater.*, 1–7 (2011).

- [31] K. W. Müller, R. F. Bruinsma, O. Lieleg, A. R. Bausch, W. A. Wall, and A. J. Levine, “Rheology of semiflexible bundle networks with transient linkers”, *Phys. Rev. Lett.* **112**, 238102 (2014).
- [32] M. Maier, K. W. Müller, C. Heussinger, S. Köhler, W. a. Wall, a. R. Bausch, and O. Lieleg, “A single charge in the actin binding domain of fascin can independently tune the linear and non-linear response of an actin bundle network”, *Eur. Phys. J. E* **38**, 50 (2015).
- [33] F. Backouche, L. Haviv, D. Groswasser, and A. Bernheim-Groswasser, “Active gels: dynamics of patterning and self-organization”, *Phys. Biol.* **3**, 264– (2006).
- [34] M. Soares e Silva, M. Depken, B. Stuhmann, M. Korsten, F. C. MacKintosh, and G. H. Koenderink, “Active multistage coarsening of actin networks driven by myosin motors”, *Proc. Natl. Acad. Sci. U.S.A.* **108**, 9408–9413 (2011).
- [35] S. Köhler, V. Schaller, and A. R. Bausch, “Structure formation in active networks”, *Nat. Mater.* **10**, 462– (2011).
- [36] M. P. Murrell and M. L. Gardel, “F-actin buckling coordinates contractility and severing in a biomimetic actomyosin cortex”, *Proc. Natl. Acad. Sci. U.S.A.* **109**, 20820–20825 (2012).
- [37] S. Köhler and A. R. Bausch, “Contraction mechanisms in composite active actin networks”, *PLoS One* **7**, e39869– (2012).
- [38] B. Stuhmann, M. Soares e Silva, M. Depken, F. C. MacKintosh, and G. H. Koenderink, “Nonequilibrium fluctuations of a remodeling in vitro cytoskeleton”, *Phys. Rev. E* **86**, 020901 (2012).
- [39] I. Kirchenbuechler, D. Guu, N. a. Kurniawan, G. H. Koenderink, and M. P. Lettinga, “Direct visualization of flow-induced conformational transitions of single actin filaments in entangled solutions.”, *Nat. Comm.* **5**, 5060 (2014).
- [40] P. Kollmannsberger and B. Fabry, “Linear and nonlinear rheology of living cells”, *Annu. Rev. Mater. Res.* **41**, 75–97 (2011).
- [41] T. Odijk, “The statistics and dynamics of confined or entangled stiff polymers”, *Macromolecules* **16**, 1340–1344 (1983).
- [42] M. Doi, “Effect of chain flexibility on the dynamics of rodlike polymers in the entangled state”, *Journal of Polymer Science: Polymer Symposia* **73**, 93–103 (1985).
- [43] A. N. Semenov, “Dynamics of concentrated solutions of rigid-chain polymers. part 1.-brownian motion of persistent macromolecules in isotropic solution”, *J. Chem. Soc., Faraday Trans. 2* **82**, 317–329 (1986).
- [44] M. A. Dichtl and E. Sackmann, “Microrheometry of semiflexible actin networks through enforced single-filament reptation: frictional coupling and heterogeneities in entangled networks”, *Proc. Natl. Acad. Sci. U.S.A.* **99**, 6533–6538 (2002).
- [45] C. Semmrich, T. Storz, J. Glaser, R. Merkel, A. R. Bausch, and K. Kroy, “Glass transition and rheological redundancy in f-actin solutions”, *Proc. Natl. Acad. Sci. U.S.A.* **104(51)**, 20199–20203 (2007).
- [46] C. Semmrich, R. J. Larsen, and A. R. Bausch, “Nonlinear mechanics of entangled F-actin solutions”, *Soft Matter* **4**, 1675 (2008).

- [47] O. Hallatschek, “Semiflexible polymer dynamics”, PhD thesis (Freie Universität Berlin, Oct. 2004).
- [48] O. Hallatschek, E. Frey, and K. Kroy, “Tension dynamics in semiflexible polymers. i. coarse-grained equations of motion”, *Phys. Rev. E* **75**, 031905 (2007).
- [49] O. Hallatschek, E. Frey, and K. Kroy, “Tension dynamics in semiflexible polymers. ii. scaling solutions and applications”, *Phys. Rev. E* **75**, 031906 (2007).
- [50] M. Doi and S. F. Edwards, *The theory of polymer dynamics*, Vol. 73 (Oxford University Press on Demand, 1988).
- [51] H. Yamakawa, *Modern theory of polymer solutions* (Harper & Row, Publishers, Inc., 1971).
- [52] C. Schuldt, J. Schnauß, T. Händler, M. Glaser, J. Lorenz, T. Golde, J. A. Käs, and D. M. Smith, “Tuning synthetic semiflexible networks by bending stiffness”, *Phys. Rev. Lett.* **117**, 197801 (2016).
- [53] M. Tassieri, “Dynamics of semiflexible polymer solutions in the tightly entangled concentration regime”, *Macromolecules* **50**, 5611–5618 (2017).
- [54] O. Kratky and G. Porod, “Röntgenuntersuchung gelöster fadenmoleküle”, *Recl. Trav. Chim. Pays-Bas* **68**, 1106–1122 (1949).
- [55] L. D. Landau and E. Lifshitz, “Theory of elasticity, vol. 7”, *Course of Theoretical Physics* **3** (1986).
- [56] H. Kleinert, *Path integrals in quantum mechanics, statistics, polymer physics, and financial markets*, 5th ed. (World Scientific, 2009).
- [57] B. Hamprecht, W. Janke, and H. Kleinert, “End-to-end distribution function of two-dimensional stiff polymers for all persistence lengths”, *Phys. Lett. A* **330**, 254–259 (2004).
- [58] S. Mehraeen, B. Sudhanshu, E. F. Koslover, and A. J. Spakowitz, “End-to-end distribution for a wormlike chain in arbitrary dimensions”, *Phys. Rev. E* **77**, 061803 (2008).
- [59] J. F. Marko and E. D. Siggia, “Stretching dna”, *Macromolecules* **28**, 8759–8770 (1995).
- [60] A. V. Dobrynin, J.-M. Y. Carrillo, and M. Rubinstein, “Chains are more flexible under tension”, *Macromolecules* **43**, 9181–9190 (2010).
- [61] J. Wilhelm and E. Frey, “Radial distribution function of semiflexible polymers”, *Phys. Rev. Lett.* **77**, 2581–2584 (1996).
- [62] F. C. MacKintosh, J. Käs, and P. A. Janmey, “Elasticity of semiflexible biopolymer networks”, *Phys. Rev. Lett.* **75**, 4425–4428 (1995).
- [63] M. Muthukumar and S. F. Edwards, “Screening of hydrodynamic interaction in a solution of rodlike macromolecules”, *Macromolecules* **16**, 1475–1478 (1983).
- [64] K. Kroy and E. Frey, “Dynamic scattering from solutions of semiflexible polymers”, *Phys. Rev. E* **55**, 3092–3101 (1997).
- [65] C. H. Wiggins, D. Rivelino, a. Ott, and R. E. Goldstein, “Trapping and wiggling: elastohydrodynamics of driven microfilaments.”, *Biophys. J.* **74**, 1043–60 (1998).
- [66] R. Granek, “From semi-flexible polymers to membranes: anomalous diffusion and reptation”, *J. Phys. II France* **7**, 1761–1788 (1997).

- [67] E. Frey, K. Kroy, and J. Wilhelm, in *Advances in structural biology*, Vol. 5, edited by S. K. Malhotra and J. A. Tuszyński, Advances in Structural Biology Supplement C (JAI, 1999), pp. 135–168.
- [68] F. Amblard, A. C. Maggs, B. Yurke, A. N. Pargellis, and S. Leibler, “Subdiffusion and anomalous local viscoelasticity in actin networks”, *Phys. Rev. Lett.* **77**, 4470–4473 (1996).
- [69] M. A. Dichtl and E. Sackmann, “Colloidal probe study of short time local and long time reptational motion of semiflexible macromolecules in entangled networks”, *New J. Phys.* **1**, 18 (1999).
- [70] E. Farge and A. C. Maggs, “Dynamic scattering from semiflexible polymers”, *Macromolecules* **26**, 5041–5044 (1993).
- [71] R. Götter, K. Kroy, E. Frey, M. Bärmann, and E. Sackmann, “Dynamic light scattering from semidilute actin solutions: a study of hydrodynamic screening, filament bending stiffness, and the effect of tropomyosin/troponin-binding”, *Macromolecules* **29**, 30–36 (1996).
- [72] A. Bernheim-Groswasser, R. Shusterman, and O. Krichevsky, “Fluorescence correlation spectroscopy analysis of segmental dynamics in actin filaments”, *J. Chem. Phys.* **125**, 084903 (2006).
- [73] F. Gittes, B. Schnurr, P. D. Olmsted, F. C. MacKintosh, and C. F. Schmidt, “Microscopic viscoelasticity: shear moduli of soft materials determined from thermal fluctuations”, *Phys. Rev. Lett.* **79**, 3286–3289 (1997).
- [74] J. Xu, A. Palmer, and D. Wirtz, “Rheology and microrheology of semiflexible polymer solutions: actin filament networks”, *Macromolecules* **31**, 6486–6492 (1998).
- [75] M. Tassieri, R. M. L. Evans, L. Barbu-Tudoran, G. N. Khaname, J. Trinick, and T. A. Waigh, “Dynamics of semiflexible polymer solutions in the highly entangled regime”, *Phys. Rev. Lett.* **101**, 198301 (2008).
- [76] A. Palmer, J. Xu, and D. Wirtz, “High-frequency viscoelasticity of crosslinked actin filament networks measured by diffusing wave spectroscopy”, *Rheol. Acta* **37**, 97–106 (1998).
- [77] L. Deng, X. Trepate, J. P. Butler, E. Millet, K. G. Morgan, D. A. Weitz, and J. J. Fredberg, “Fast and slow dynamics of the cytoskeleton”, *Nat. Mater.* **5**, 636 (2006).
- [78] B. Obermayer and E. Frey, “Tension dynamics and viscoelasticity of extensible wormlike chains”, *Phys. Rev. E* **80**, 040801 (2009).
- [79] R. Everaers, F. Jülicher, A. Ajdari, and A. C. Maggs, “Dynamic fluctuations of semiflexible filaments”, *Phys. Rev. Lett.* **82**, 3717–3720 (1999).
- [80] L. Le Goff, F. Amblard, and E. M. Furst, “Motor-driven dynamics in actin-myosin networks”, *Phys. Rev. Lett.* **88**, 018101 (2001).
- [81] T. Hiraiwa and T. Ohta, “Viscoelastic behavior of a single semiflexible polymer chain”, *J. Phys. Soc. Jpn.* **77**, 023001 (2008).
- [82] B. Obermayer and O. Hallatschek, “Coupling of transverse and longitudinal response in stiff polymers”, *Phys. Rev. Lett.* **99**, 098302 (2007).
- [83] L. Le Goff, O. Hallatschek, E. Frey, and F. Amblard, “Tracer studies on f-actin fluctuations”, *Phys. Rev. Lett.* **89**, 258101 (2002).

- [84] D. C. Morse, “Viscoelasticity of tightly entangled solutions of semiflexible polymers”, *Phys. Rev. E* **58**, R1237–R1240 (1998).
- [85] F. Gittes and F. MacKintosh, “Dynamic shear modulus of a semiflexible polymer network”, *Phys. Rev. E* **58**, R1241–R1244 (1998).
- [86] D. C. Morse, “Viscoelasticity of concentrated isotropic solutions of semiflexible polymers. 2. linear response”, *Macromolecules* **31**, 7044–7067 (1998).
- [87] D. C. Morse, “Viscoelasticity of concentrated isotropic solutions of semiflexible polymers. 3. nonlinear rheology”, *Macromolecules* **32**, 5934–5943 (1999).
- [88] D. C. Morse, “Tube diameter in tightly entangled solutions of semiflexible polymers”, *Phys. Rev. E* **63**, 031502 (2001).
- [89] J. Glaser and K. Kroy, “Tube-width fluctuations of entangled stiff polymers”, *Phys. Rev. E* **84**, 051801 (2011).
- [90] P. Lang and E. Frey, “Disentangling entanglements in biopolymer solutions”, *Nat. Comm.* **9**, 494 (2018).
- [91] M. Romanowska, H. Hinsch, N. Kirchgeßner, M. Giesen, M. Degawa, B. Hoffmann, E. Frey, and R. Merkel, “Direct observation of the tube model in f-actin solutions: tube dimensions and curvatures”, *Europhys. Lett.* **86**, 26003 (2009).
- [92] B. Wang, J. Guan, S. M. Anthony, S. C. Bae, K. S. Schweizer, and S. Granick, “Confining potential when a biopolymer filament reptates”, *Phys. Rev. Lett.* **104**, 118301 (2010).
- [93] S. Ramanathan and D. Morse, “Simulations of dynamics and viscoelasticity in highly entangled solutions of semiflexible rods”, *Phys. Rev. E* **76**, 4–7 (2007).
- [94] I. Lauter, “Untersuchung mechanischer und dynamischer eigenschaften von polymerisierten aktinlösungen”, PhD thesis (Rheinischen Friedrich-Wilhelms-Universität Bonn, 2011).
- [95] E. Jaschinski, “Experimentelle Untersuchung der Lokalisationsröhre von Aktinfilamenten in halbverdünnten Lösungen in Abhängigkeit von der Gegenionkonzentration und der Vororientierung in drei Dimensionen Dissertation”, PhD thesis (Rheinischen Friedrich-Wilhelms-Universität Bonn, 2014).
- [96] M. Lämmel, E. Jaschinski, R. Merkel, and K. Kroy, “Microstructure of sheared entangled solutions of semiflexible polymers”, *Polymers* **8** (2016).
- [97] L. Onsager, “the Effects of Shape on the Interaction of Colloidal Particles”, *Ann. N. Y. Acad. Sci.* **51**, 627–659 (1949).
- [98] A. Khokhlov and A. Semenov, “Liquid-crystalline ordering in the solution of long persistent chains”, *Physica A* **108**, 546–556 (1981).
- [99] H. Isambert and A. C. Maggs, “Dynamics and Rheology of Actin Solutions”, *Macromolecules* **29**, 1036–1040 (1996).
- [100] M. Tassieri, R. Evans, L. Barbu-Tudoran, J. Trinick, and T. Waigh, “The self-assembly, elasticity, and dynamics of cardiac thin filaments”, *Biophys. J.* **94**, 2170–2178 (2008).
- [101] P. Fernández, S. Grosser, and K. Kroy, “A unit-cell approach to the nonlinear rheology of biopolymer solutions”, *Soft Matter* **5**, 2047–2056 (2009).



- [102] B. D. Hoffman and J. C. Crocker, “Cell mechanics: dissecting the physical responses of cells to force”, *Annu. Rev. Biomed. Eng.* **11**, 259–288 (2009).
- [103] F. Thüroff, B. Obermayer, and E. Frey, “Longitudinal response of confined semiflexible polymers”, *Phys. Rev. E* **83**, 021802 (2011).
- [104] N. Fakhri, F. C. MacKintosh, B. Lounis, L. Cognet, and M. Pasquali, “Brownian motion of stiff filaments in a crowded environment”, *Science* **330**, 1804 (2010).
- [105] S. Q. Wang, S. Ravindranath, Y. Wang, and P. Boukany, “New theoretical considerations in polymer rheology: Elastic breakdown of chain entanglement network”, *J. Chem. Phys.* **127** (2007) 10.1063/1.2753156.
- [106] S.-Q. Wang, Y. Wang, S. Cheng, X. Li, X. Zhu, and H. Sun, “New experiments for improved theoretical description of nonlinear rheology of entangled polymers”, *Macromolecules* **46**, 3147–3159 (2013).
- [107] Z. Wang, C. N. Lam, W.-R. Chen, W. Wang, J. Liu, Y. Liu, L. Porcar, C. B. Stanley, Z. Zhao, K. Hong, and Y. Wang, “Fingerprinting molecular relaxation in deformed polymers”, *Phys. Rev. X* **7**, 031003 (2017).
- [108] S. Kaufmann, J. Käs, W. H. Goldmann, E. Sackmann, and G. Isenberg, “Talin anchors and nucleates actin filaments at lipid membranes a direct demonstration”, *FEBS Lett.* **314**, 203–205 (1992).
- [109] H. Isambert, P. Venier, A. C. Maggs, A. Fattoum, R. Kassab, D. Pantaloni, and M.-F. Carrier, “Flexibility of actin filaments derived from thermal fluctuations. effect of bound nucleotide, phalloidin, and muscle regulatory proteins”, *J. Biol. Chem.* **270**, 11437–11444 (1995).
- [110] J. He, J. Viamontes, and J. X. Tang, “Counterion-induced abnormal slowdown of f-actin diffusion across the isotropic-to-nematic phase transition”, *Phys. Rev. Lett.* **99**, 068103 (2007).
- [111] F. Ziemann, “Untersuchung der lokalen viskoelastischen eigenschaften von zellen und zellmodellen mit einem magnetkugel-mikrorheometer (“magnetic tweezers”)”, PhD thesis (Technische Universität München, 1997).
- [112] K. Kroy and E. Frey, “Scattering in polymeric and colloidal systems”, in, edited by W. Brown and K. Mortensen, 1st ed. (CRC Press, 1999) Chap. Dynamic Scattering from Semiflexible Polymers, p. 496.
- [113] L. Berthier and G. Biroli, “Theoretical perspective on the glass transition and amorphous materials”, *Rev. Mod. Phys.* **83**, 587–645 (2011).
- [114] K. Kroy and J. Glaser, “The glassy wormlike chain”, *New J. Phys.* **9**, 416 (2007).
- [115] J. Glaser, O. Hallatschek, and K. Kroy, “Dynamic structure factor of a stiff polymer in a glassy solution.”, *The European physical journal. E, Soft matter* **26**, 123–36 (2008).
- [116] P. Sollich, F. Lequeux, P. Hébraud, and M. E. Cates, “Rheology of soft glassy materials”, *Phys. Rev. Lett.* **78**, 2020–2023 (1997).
- [117] W. Götze, *Complex dynamics of glass-forming liquids: a mode-coupling theory* (Oxford University Press, 2008).

- [118] K. Miyazaki and A. Yethiraj, “Entanglement effects in mode coupling theories of polymers”, *J. Chem. Phys.* **117**, 10448–10451 (2002).
- [119] G. Szamel, “Reptation as a dynamic mean-field theory: study of a simple model of rodlike polymers”, *Phys. Rev. Lett.* **70**, 3744–3747 (1993).
- [120] G. Szamel and K. S. Schweizer, “Reptation as a dynamic mean-field theory: Self and tracer diffusion in a simple model of rodlike polymers”, *J. Chem. Phys.* **100**, 3127 (1994).
- [121] D. Sussman and K. Schweizer, “Microscopic Theory of the Tube Confinement Potential for Liquids of Topologically Entangled Rigid Macromolecules”, *Phys. Rev. Lett.* **107**, 1–4 (2011).
- [122] D. Sussman and K. Schweizer, “Microscopic theory of topologically entangled fluids of rigid macromolecules”, *Phys. Rev. E* **83**, 1–11 (2011).
- [123] D. M. Sussman and K. S. Schweizer, “Microscopic Theory of Quiescent and Deformed Topologically Entangled Rod Solutions: General Formulation and Relaxation after Nonlinear Step Strain”, *Macromolecules* **45**, 3270–3284 (2012).
- [124] D. Sussman and K. Schweizer, “Microscopic Theory of Entangled Polymer Melt Dynamics: Flexible Chains as Primitive-Path Random Walks and Supercoarse Grained Needles”, *Phys. Rev. Lett.* **109**, 1–5 (2012).
- [125] C. Heussinger and E. Frey, “Floppy modes and nonaffine deformations in random fiber networks”, *Phys. Rev. Lett.* **97**, 105501 (2006).
- [126] K. Kroy and E. Frey, “Force-extension relation and plateau modulus for wormlike chains”, *Phys. Rev. Lett.* **77**, 306–309 (1996).
- [127] R. Satcher and C. Dewey, “Theoretical estimates of mechanical properties of the endothelial cell cytoskeleton”, *Biophys. J.* **71**, 109–118 (1996).
- [128] A. M. Stein, D. A. Vader, D. A. Weitz, and L. M. Sander, “The micromechanics of three-dimensional collagen-i gels”, *Complexity* **16**, 22–28 (2011).
- [129] B. P. Tighe, “Dynamic critical response in damped random spring networks”, *Phys. Rev. Lett.* **109**, 168303 (2012).
- [130] M. G. Yucht, M. Sheinman, and C. P. Broedersz, “Dynamical behavior of disordered spring networks”, *Soft Matter* **9**, 7000–7006 (2013).
- [131] M. Dennison and H. Stark, “Viscoelastic properties of marginal networks in a solvent”, *Phys. Rev. E* **93**, 022605 (2016).
- [132] L. G. Rizzi, S. Auer, and D. A. Head, “Importance of non-affine viscoelastic response in disordered fibre networks”, *Soft Matter* **12**, 4332–4338 (2016).
- [133] M. L. Gardel, F. Nakamura, J. H. Hartwig, J. C. Crocker, T. P. Stossel, and D. A. Weitz, “Pre-stressed f-actin networks cross-linked by hinged filamins replicate mechanical properties of cells”, *Proc. Natl. Acad. Sci. U.S.A.* **103**, 1762–1767 (2006).
- [134] M. Gralka and K. Kroy, “Inelastic mechanics: a unifying principle in biomechanics”, *Biochimica et Biophysica Acta (BBA) - Molecular Cell Research* **1853**, 3025–3037 (2015).
- [135] J. Glaser and K. Kroy, in *Biopolymers*, edited by M. Elnashar (InTech, 2010).

- [136] C. Broedersz, M. Depken, N. Yao, M. Pollak, D. Weitz, and F. MacKintosh, “Cross-Link-Governed Dynamics of Biopolymer Networks”, *Phys. Rev. Lett.* **105**, 1–4 (2010).
- [137] F. MacKintosh and C. Schmidt, “Microrheology”, *Current Opinion in Colloid & Interface Science* **4**, 300–307 (1999).
- [138] T. M. Squires and T. G. Mason, “Fluid mechanics of microrheology”, *Annu. Rev. Fluid Mech.* **42**, 413–438 (2010).
- [139] A. Sonn-Segev, A. Bernheim-Groswasser, H. Diamant, and Y. Roichman, “Viscoelastic response of a complex fluid at intermediate distances”, *Phys. Rev. Lett.* **112**, 088301 (2014).
- [140] H. Diamant, “Response of a polymer network to the motion of a rigid sphere”, *Eur. Phys. J. E* **38**, 32 (2015).
- [141] J. Xu, Y. Tseng, and D. Wirtz, “Strain hardening of actin filament networks: regulation by the dynamic cross-linking protein  $\alpha$ -actinin”, *J. Biol. Chem.* **275**, 35886–35892 (2000).
- [142] C. D. Chapman and R. M. Robertson-Anderson, “Nonlinear microrheology reveals entanglement-driven molecular-level viscoelasticity of concentrated dna”, *Phys. Rev. Lett.* **113**, 098303 (2014).
- [143] T. T. Falzone, S. Blair, and R. M. Robertson-Anderson, “Entangled f-actin displays a unique crossover to microscale nonlinearity dominated by entanglement segment dynamics”, *Soft Matter* **11**, 4418–4423 (2015).
- [144] T. T. Falzone and R. M. Robertson-Anderson, “Active entanglement-tracking microrheology directly couples macromolecular deformations to nonlinear microscale force response of entangled actin”, *ACS Macro Lett.* **4**, 1194–1199 (2015).
- [145] B. Gurmessa, R. Fitzpatrick, T. T. Falzone, and R. M. Robertson-Anderson, “Entanglement density tunes microscale nonlinear response of entangled actin”, *Macromolecules* **49**, 3948–3955 (2016).
- [146] B. Gurmessa, S. Ricketts, and R. M. Robertson-Anderson, “Nonlinear actin deformations lead to network stiffening, yielding, and nonuniform stress propagation”, *Biophys. J.* **113**, 1540–1550 (2017).
- [147] M. Srinivasan and S. Walcott, “Binding site models of friction due to the formation and rupture of bonds: State-function formalism, force-velocity relations, response to slip velocity transients, and slip stability”, *Phys. Rev. E* **80**, 046124 (2009).
- [148] A. Ward, F. Hilitski, W. Schwenger, D. Welch, A. W. C. Lau, V. Vitelli, L. Mahadevan, and Z. Dogic, “Solid friction between soft filaments”, *Nat. Mater.* **14**, 583 (2015).
- [149] B. A. DiDonna and T. C. Lubensky, “Nonaffine correlations in random elastic media”, *Phys. Rev. E* **72**, 066619 (2005).
- [150] D. Bonn, M. M. Denn, L. Berthier, T. Divoux, and S. Manneville, “Yield stress materials in soft condensed matter”, *Rev. Mod. Phys.* **89**, 035005 (2017).
- [151] A. C. Maggs, “Two plateau moduli for actin gels”, *Phys. Rev. E* **55**, 7396–7400 (1997).
- [152] C. Storm, J. J. Pastore, F. C. MacKintosh, T. C. Lubensky, and P. A. Janmey, “Nonlinear elasticity in biological gels”, *Nature* **435**, 191–194 (2005).

- [153] M. L. Gardel, J. H. Shin, F. C. MacKintosh, L. Mahadevan, P. Matsudaira, and D. A. Weitz, “Elastic behavior of cross-linked and bundled actin networks”, *Science* **304**, 1301– (2004).
- [154] J. H. Shin, M. L. Gardel, L. Mahadevan, P. Matsudaira, and D. A. Weitz, “Relating microstructure to rheology of a bundled and cross-linked f-actin network in vitro”, *Proc. Natl. Acad. Sci. U.S.A.* **101**, 9636–9641 (2004).
- [155] R. Tharmann, M. M. A. E. Claessens, and A. R. Bausch, “Viscoelasticity of isotropically cross-linked actin networks”, *Phys. Rev. Lett.* **98**, 088103 (2007).
- [156] Y.-C. Lin, N. Y. Yao, C. P. Broedersz, H. Herrmann, F. C. MacKintosh, and D. A. Weitz, “Origins of elasticity in intermediate filament networks”, *Phys. Rev. Lett.* **104**, 058101 (2010).
- [157] Y.-C. Lin, C. P. Broedersz, A. C. Rowat, T. Wedig, H. Herrmann, F. C. MacKintosh, and D. A. Weitz, “Divalent cations crosslink vimentin intermediate filament tail domains to regulate network mechanics”, *J. Mol. Biol.* **399**, 637–644 (2010).
- [158] N. Y. Yao, C. P. Broedersz, Y.-C. Lin, K. E. Kasza, F. C. MacKintosh, and D. A. Weitz, “Elasticity in ionically cross-linked neurofilament networks”, *Biophys. J.* **98**, 2147–2153 (2010).
- [159] I. K. Piechocka, R. G. Bacabac, M. Potters, F. C. MacKintosh, and G. H. Koenderink, “Structural hierarchy governs fibrin gel mechanics”, *Biophys. J.* **98**, 2281–2289 (2010).
- [160] E. Schuster, L. Lundin, and M. A. K. Williams, “Investigating the relationship between network mechanics and single-chain extension using biomimetic polysaccharide gels”, *Macromolecules* **45**, 4863–4869 (2012).
- [161] J.-M. Y. Carrillo, F. C. MacKintosh, and A. V. Dobrynin, “Nonlinear elasticity: from single chain to networks and gels”, *Macromolecules* **46**, 3679–3692 (2013).
- [162] P. H. J. Kouwer, M. Koepf, V. A. A. Le Sage, M. Jaspers, A. M. van Buul, Z. H. Eksteen-Akeroyd, T. Woltinge, E. Schwartz, H. J. Kitto, R. Hoogenboom, S. J. Picken, R. J. M. Nolte, E. Mendes, and A. E. Rowan, “Responsive biomimetic networks from polyisocyanopeptide hydrogels”, *Nature* **493**, 651 (2013).
- [163] C. Heussinger and E. Frey, “Stiff polymers, foams, and fiber networks”, *Phys. Rev. Lett.* **96**, 017802 (2006).
- [164] C. Heussinger and E. Frey, “Role of architecture in the elastic response of semiflexible polymer and fiber networks”, *Phys. Rev. E* **75**, 011917 (2007).
- [165] H. Jerry Qi, C. Ortiz, and M. C. Boyce, “Mechanics of biomacromolecular networks containing folded domains”, *J. Eng. Mater. Technol.* **128**, 509–518 (2006).
- [166] J. S. Palmer and M. C. Boyce, “Constitutive modeling of the stress–strain behavior of f-actin filament networks”, *Acta Biomater.* **4**, 597–612 (2008).
- [167] F. Meng and E. M. Terentjev, “Nonlinear elasticity of semiflexible filament networks”, *Soft Matter* **12**, 6749–6756 (2016).
- [168] J. Wilhelm and E. Frey, “Elasticity of stiff polymer networks”, *Phys. Rev. Lett.* **91**, 108103 (2003).

- [169] D. A. Head, A. J. Levine, and F. C. MacKintosh, “Deformation of cross-linked semiflexible polymer networks”, *Phys. Rev. Lett.* **91**, 108102 (2003).
- [170] D. A. Head, A. J. Levine, and F. C. MacKintosh, “Deformation of cross-linked semiflexible polymer networks”, *Phys. Rev. Lett.* **91**, 108102 (2003).
- [171] O. Stenull and T. C. Lubensky, “Simple lattice model for biological gels”, arXiv:cond-mat/1108.4328 (2011).
- [172] M. C. Wigbers, F. C. MacKintosh, and M. Dennison, “Stability and anomalous entropic elasticity of subisostatic random-bond networks”, *Phys. Rev. E* **92**, 042145 (2015).
- [173] C. P. Broedersz, X. Mao, T. C. Lubensky, and F. C. MacKintosh, “Criticality and isostaticity in fibre networks”, *Nat. Phys.* **7**, 983–988 (2011).
- [174] S. Arbabi and M. Sahimi, “Mechanics of disordered solids. i. percolation on elastic networks with central forces”, *Phys. Rev. B* **47**, 695–702 (1993).
- [175] M. Wyart, H. Liang, A. Kabla, and L. Mahadevan, “Elasticity of floppy and stiff random networks”, *Phys. Rev. Lett.* **101**, 215501 (2008).
- [176] A. J. Liu and S. R. Nagel, “The jamming transition and the marginally jammed solid”, *Annual Review of Condensed Matter Physics* **1**, 347–369 (2010).
- [177] M. van Hecke, “Jamming of soft particles: geometry, mechanics, scaling and isostaticity”, *J. Phys.: Condens. Matter* **22**, 033101 (2010).
- [178] A. Baule, F. Morone, H. J. Herrmann, and H. A. Makse, “Edwards statistical mechanics for jammed granular matter”, *Rev. Mod. Phys.* (2017).
- [179] C. P. Broedersz and F. C. MacKintosh, “Molecular motors stiffen non-affine semiflexible polymer networks”, *Soft Matter* **7**, 3186–3191 (2011).
- [180] M. Sheinman, C. P. Broedersz, and F. C. MacKintosh, “Actively stressed marginal networks”, *Phys. Rev. Lett.* **109**, 238101 (2012).
- [181] A. J. Licup, S. Münster, A. Sharma, M. Sheinman, L. M. Jawerth, B. Fabry, D. A. Weitz, and F. C. MacKintosh, “Stress controls the mechanics of collagen networks”, *Proc. Natl. Acad. Sci. U.S.A.* **112**, 9573–9578 (2015).
- [182] A. Sharma, A. J. Licup, K. A. Jansen, R. Rens, M. Sheinman, G. H. Koenderink, and F. C. MacKintosh, “Strain-controlled criticality governs the nonlinear mechanics of fibre networks”, *Nat. Phys.* **12**, 584 (2016).
- [183] M. Vahabi, A. Sharma, A. J. Licup, A. S. G. van Oosten, P. A. Galie, P. A. Janmey, and F. C. MacKintosh, “Elasticity of fibrous networks under uniaxial prestress”, *Soft Matter* **12**, 5050–5060 (2016).
- [184] M. Dennison, M. Sheinman, C. Storm, and F. C. MacKintosh, “Fluctuation-stabilized marginal networks and anomalous entropic elasticity”, *Phys. Rev. Lett.* **111**, 095503 (2013).
- [185] C. Heussinger, B. Schaefer, and E. Frey, “Nonaffine rubber elasticity for stiff polymer networks”, *Phys. Rev. E* **76**, 031906 (2007).
- [186] C. Broedersz, M. Sheinman, and F. MacKintosh, “Filament-Length-Controlled Elasticity in 3D Fiber Networks”, *Phys. Rev. Lett.* **108**, 3–7 (2012).

- [187] J. C. Maxwell, “On the calculation of the equilibrium and stiffness of frames”, *Phil. Mag.* **27**, 294–299 (1864).
- [188] X. Mao and T. C. Lubensky, “Maxwell lattices and topological mechanics”, *Annual Review of Condensed Matter Physics* **9**, 413–433 (2018).
- [189] E. M. Huisman, T. van Dillen, P. R. Onck, and E. Van der Giessen, “Three-dimensional cross-linked f-actin networks: relation between network architecture and mechanical behavior”, *Phys. Rev. Lett.* **99**, 208103 (2007).
- [190] N. A. Kurniawan, S. Enemark, and R. Rajagopalan, “The role of structure in the nonlinear mechanics of cross-linked semiflexible polymer networks.”, *J. Chem. Phys.* **136**, 065101 (2012).
- [191] P. R. Onck, T. Koeman, T. van Dillen, and E. van der Giessen, “Alternative explanation of stiffening in cross-linked semiflexible networks”, *Phys. Rev. Lett.* **95**, 178102 (2005).
- [192] P. A. Janmey, M. E. McCormick, S. Rammensee, J. L. Leight, P. C. Georges, and F. C. MacKintosh, “Negative normal stress in semiflexible biopolymer gels”, *Nat. Mater.* **6**, 48 (2006).
- [193] E. Conti and F. C. MacKintosh, “Cross-linked networks of stiff filaments exhibit negative normal stress”, *Phys. Rev. Lett.* **102**, 088102 (2009).
- [194] D. Vader, A. Kabla, D. Weitz, and L. Mahadevan, “Strain-induced alignment in collagen gels.”, *PLoS One* **4**, e5902 (2009).
- [195] J. Feng, H. Levine, X. Mao, and L. M. Sander, “Alignment and nonlinear elasticity in biopolymer gels”, *Phys. Rev. E* **91**, 042710 (2015).
- [196] G. Žagar, P. R. Onck, and E. van der Giessen, “Two fundamental mechanisms govern the stiffening of cross-linked networks”, *Biophysical Journal* **108**, 1470–1479 (2015).
- [197] H. E. Amuasi, C. Heussinger, R. L. C. Vink, and A. Zippelius, “Nonlinear and heterogeneous elasticity of multiply-crosslinked biopolymer networks”, *New J. Phys.* **17**, 083035 (2015).
- [198] J. Plagge, A. Fischer, and C. Heussinger, “Viscoelasticity of reversibly crosslinked networks of semiflexible polymers”, *Phys. Rev. E* **93**, 062502 (2016).
- [199] M. Keller, J. Schilling, and E. Sackmann, “Oscillatory magnetic bead rheometer for complex fluid microrheometry”, *Review of Scientific Instruments* **72**, 3626–3634 (2001).
- [200] J. Feng, H. Levine, X. Mao, and L. M. Sander, “Nonlinear elasticity of disordered fiber networks”, *Soft Matter* **12**, 1419–1424 (2016).
- [201] A. Nikoubashman and M. P. Howard, “Equilibrium dynamics and shear rheology of semiflexible polymers in solution”, *Macromolecules* **50**, 8279–8289 (2017).
- [202] J. Glaser, T. D. Nguyen, J. A. Anderson, P. Lui, F. Spiga, J. A. Millan, D. C. Morse, and S. C. Glotzer, “Strong scaling of general-purpose molecular dynamics simulations on gpus”, *Computer Physics Communications* **192**, 97–107 (2015).

## Acknowledgments

The way towards the new insight documented in this thesis has often been delighting and enriching, but sometimes also stressful and demanding. Going this way was only possible with the help and support of numerous friends and colleagues.

First, I would like to thank Prof. Klaus Kroy for giving me the opportunity to work on various exciting and relevant topics of modern physics. I gratefully acknowledge his never-ending patience, the friendly working atmosphere in his group, and his extensive concrete support. Further, I would like to thank Daniel Rings, from whom I benefited a lot during the work on my Diploma thesis and during the first years of my PhD studies. A special thanks goes to Anne Meiwald, without her kind help the cooperation with our colleagues from Israel would have been less intense and surely less successful. Finally, I would like to thank various colleagues and friends for numerous intense and fruitful discussions and inspirations, to name some of them: Jens Glaser, Evelin Jaschinski, Rudolf Merkel, Johannes Wagner, Frauke Gräter, Sven Auschra, Mona Guthardt, Kamil Dzikowski, Maik Weßling, Dmytro Mishagli, Alexandre Valance, Luc Oger, Hezi Yizhaq, Itzhak Ktra, Haim Tsoar, and Eres Schmerler.

Schließlich möchte ich mich bei meiner Familie für die liebevolle Unterstützung bedanken.

## Author contributions

All the projects and studies I outlined in this thesis were done in close collaboration with my supervisor Klaus Kroy. The work on aeolian sand transport dates back to my Diploma thesis, where I developed a first version of the two-species formalism. With the beginning of my PhD, I started my studies on biopolymer systems. There, I greatly benefited from the work by Jens Glaser and from the numerous fruitful and inspiring discussions with Evelin Jaschinski and her supervisor Rudolf Merkel. I extended Jens' theory to account for the nematic microstructure of the solutions and investigated the influence of shear-induced polymer alignment, which we used to interpret Evelin's experimental observations. Ever since, I have very much enjoyed sharing my passion with other students and colleagues. The work on the splash model, for instance, started as a Bachelor project of Maik Weßling and was then continued by Kamil Dzikowski, a RISE student from Lancaster (UK). I later consolidated this model, refined and extended it to also predict the statistics of the splashed bed grains, and analyzed it extensively. This finally led to a joint project with Luc Oger and Alexandre Valance from Rennes (France), who provided us with simulation and experimental data to which I compared our theory. The progress we made there, provided me with the key insight needed to finish the work on the analytic mesoscale model for aeolian sand transport, which I initially started in close collaboration with Anne Meiwald. She is also responsible for the progress during the early stages of the work on megaripple formation, a joint project with colleagues from Israel (Hezi Yizhaq, Haim Tsoar, Itzhak Ktra, and Eres Schmerler), who provided us with field data and helped us with our own measurements. Based on an idea by Klaus, I developed and analyzed the sorting model that we put forward to explain the origin of the megaripples.